

MULTI-PHYSICS MODELING AND SIMULATION OF PHOTOVOLTAIC DEVICES AND  
SYSTEMS

By

Timofey Golubev

A DISSERTATION

Submitted to  
Michigan State University  
in partial fulfillment of the requirements  
for the degree of

Physics – Doctor of Philosophy

2020

## **ABSTRACT**

### **MULTI-PHYSICS MODELING AND SIMULATION OF PHOTOVOLTAIC DEVICES AND SYSTEMS**

By

Timofey Golubev

Physics-based computational modeling is an essential aspect of research and development of new photovoltaic (PV) technologies. For example, PV modeling allows us to improve our understanding of device physics, evaluate the potential of new device architectures prior to experimentation, and predict the energy production of PV systems. This dissertation describes the development of improvements to PV modeling at both the device and system levels, as well as the application of these models to obtain new insights into device physics and PV system performance.

The first half of this thesis focuses on solar cell modeling using the drift-diffusion approach. Investigations into numerical instabilities of a drift-diffusion model for bilayer organic solar cells are described, and techniques for improving convergence behavior are presented. The drift-diffusion approach is then adapted for planar perovskite solar cells, validated against literature results, and utilized to understand a new experimental result involving the impact of ultrathin fullerene layers on device performance. The second half of this thesis expands our modeling to PV systems. Here, we focus on the effects of temperature and soiling (accumulation of particulate matter on PV module surfaces) on PV system energy production. A general semi-physical model for predicting annual PV soiling losses is developed and integrated with open-source PV performance models and commercial algorithms for PV system cleaning schedule optimization. Additionally, the potentials of machine learning approaches to soiling modeling are discussed and a proof-of-concept is demonstrated. In order to consider the impact of temperature on PV module performance, a coupled thermal-electrical modeling approach is developed by combining temperature-dependent equivalent circuit models with a commercial heat transfer solver. This approach also allows for predicting energy production of PV modules or films installed on irregular surfaces, such as vehicles. Application of the coupled thermal-electrical approach to simulation of residential rooftop and vehicle-integrated

PV systems is demonstrated. Overall, this work has resulted in an improved understanding of the numerical methods necessary to ensure stability of drift-diffusion codes, insight into the role of fullerenes in perovskite solar cells, and the development of modeling approaches that can aid in PV system engineering and improve accuracy in PV system energy production forecasting.

Copyright by  
TIMOFEY GOLUBEV  
2020

## ACKNOWLEDGEMENTS

I am deeply grateful for the support I have received during my graduate career. First, I would like to thank my advisor, Phillip Duxbury, for his guidance on both my thesis research projects and general career planning. Thank you for providing me an opportunity to work on very interesting photovoltaics research and encouraging me to pursue an internship, which later turned into a permanent position.

I also wish to thank my Ph.D. guidance committee members: Andrew Cristlieb, Richard Lunt, Morten Hjorth-Jensen, Hui-Chia Yu, and Pengpeng Zhang. I thank Richard Lunt for providing me the opportunity to collaborate on perovskite solar cells research. I thank Morten Hjorth-Jensen for his great computational physics course that helped me discover a passion for computational physics research, as well as encouragement and support during a difficult time of my graduate studies when I was struggling to find a thesis advisor and topic that would allow me to pursue this passion. I thank Pengpeng Zhang for being my advisor during my 2nd and 3rd years of graduate school and providing an opportunity to do some interesting experimental research, as well as her patience and support when I realized that I prefer computational research. My experience as an experimentalist has certainly made me a better scientist, since it has given me a hands-on understanding of experimental physics. I thank Andrew Christlieb and Hui-Chia Yu for general thesis advice and support.

I would like to thank Non Thongprong for helping me get started with drift-diffusion modeling, Diany Li for performing the experiments for the perovskite devices that I modeled, and Reza Loloee for his constant technical support during my time as an experimentalist. I am grateful to Ryan Jones from Enlighten Energy for providing the opportunity to work on PV soiling research and technical advice on the project. I also would like to thank Mark Hepokoski and Corey Packard from ThermoAnalytics for providing advice and supporting the coupled thermal-electrical PV modeling project, as well as their encouragement to finish my thesis. I acknowledge financial support for my graduate studies and research from Michigan State University, the U.S. Department of Education

GAANN fellowship, Enlighten Energy, and ThermoAnalytics.

I would like to express gratitude to Vladimir Zelevinsky for his excellent theoretical physics lectures and Kim Crosslan for support with all of the various paperwork and organizational aspects of being a graduate student. I would like to thank Alexey Yamilov for being my undergraduate research advisor and first introducing me to programming and computational physics. I am thankful to all of my undergraduate and graduate school professors for the knowledge and skills that they taught me, which provided a solid foundation for my research work. Also, I would like to thank my colleagues at ThermoAnalytics for making my work experience enjoyable, and allowing me to maintain a good work/Ph.D-research balance for the last 1.5 years.

I am grateful to all the graduate students who started graduate school with me in 2014 and accompanied me in course work, research, and recreational activities: Andrew Tan, Bakul Agarwal, Xingze Mao, Joe Williams, Crispin Contreras, John Bower, Bryan Isherwood, Victor Aguilar, Hao Lin, Tenzin Rubga, Safwan Shanab, and more. I would like to extend my thanks to all the members of the Foot-Pounds soccer team, which I was glad to be a part of. I am also very thankful to Xi Dong, who was my labmate for a few months before I switched to computational research, and became a great friend and fishing companion. Our fishing trips gave me much-needed breaks from the challenges and stress of graduate school. Finally, I would like to thank my parents and grandmother for their love and support throughout my life.

## TABLE OF CONTENTS

LIST OF TABLES . . . . .	ix
LIST OF FIGURES . . . . .	xi
CHAPTER 1 INTRODUCTION . . . . .	1
1.1 Motivation . . . . .	1
1.2 Solar Cell Devices . . . . .	2
1.3 Photovoltaic Device Modeling . . . . .	5
1.3.1 Equivalent Circuit Approach . . . . .	6
1.3.2 Drift-Diffusion Approach . . . . .	8
1.4 Photovoltaic System Modeling . . . . .	13
1.5 Outline . . . . .	15
<b>I Drift-Diffusion Modeling of Solar Cells</b>	<b>17</b>
CHAPTER 2 IMPLEMENTING DRIFT-DIFFUSION MODELS . . . . .	18
2.1 1D Drift-Diffusion Equations . . . . .	18
2.2 Discretization . . . . .	19
2.3 Iteration Schemes . . . . .	22
2.3.1 Gummel Method . . . . .	22
2.3.2 Newton-Raphson Method . . . . .	24
2.4 Model Verification . . . . .	28
2.4.1 Single-Carrier Device in Space-Charge-Limited Current Regime . . . . .	28
2.4.2 Two-Carrier Device . . . . .	31
2.5 Conclusions . . . . .	33
CHAPTER 3 IMPROVING CONVERGENCE OF A DRIFT-DIFFUSION MODEL FOR BILAYER ORGANIC SOLAR CELLS . . . . .	34
3.1 DD-BI Model . . . . .	35
3.2 Convergence Improvements . . . . .	40
3.2.1 Convergence Acceleration through Pulay Mixing . . . . .	41
3.2.2 Newton vs. Gummel Iterative Methods . . . . .	42
3.2.3 Slotboom Variables Approach . . . . .	45
3.3 Conclusions . . . . .	46
CHAPTER 4 DRIFT DIFFUSION MODELING OF PEROVSKITE SOLAR CELLS . . . . .	48
4.1 Numerical Model . . . . .	48
4.2 Model Validation . . . . .	50
4.3 Understanding the Impact of $C_{60}$ at the Interface of Perovskite Solar Cells . . . . .	53
4.4 Conclusions . . . . .	65

## II Modeling of Photovoltaic Systems 66

CHAPTER 5	IMPROVING PV SYSTEM SOILING LOSS PREDICTIONS	68
5.1	Background	68
5.2	Semi-Physical Modeling of Soiling Accumulation	71
5.2.1	Background	72
5.2.2	Limitations of Existing Models	82
5.2.3	Developing a General Soiling Accumulation Model	85
5.3	Effect of Rainfall	91
5.4	Incidence Angle Modifier due to Soiling	94
5.5	Combining Incidence Angle Modifier with Soiling Accumulation Models	97
5.6	Model Validation	100
5.7	Integration into Commercial Software	103
5.8	Predicting Soiling with Machine Learning	113
5.8.1	Introduction to MLR and ANN	114
5.8.2	Soiling Mass Accumulation	116
5.8.3	Soiling Loss	122
5.9	Conclusions	126
CHAPTER 6	COUPLED THERMAL-ELECTRICAL MODELING OF INTEGRATED PV SYSTEMS	128
6.1	Empirical Models	128
6.2	Physical Thermal-Electrical Model	133
6.2.1	Introduction and Motivation	133
6.2.2	Methods	135
6.2.3	Model Validation	148
6.2.4	Comparison with Empirical Models	153
6.3	Example Applications	155
6.3.1	Building Rooftop PV Systems	155
6.3.2	Vehicle-Integrated Solar Panels	158
6.3.3	PV-Battery Systems	165
6.3.4	Other Applications	169
6.4	Conclusions	170
CHAPTER 7	CONCLUSIONS AND OUTLOOK	171
7.1	Conclusions	171
7.2	Outlook	173
APPENDICES		176
APPENDIX A	PV SOILSAYER SOFTWARE DESCRIPTION	177
APPENDIX B	PV MODULE DATASHEETS	201
BIBLIOGRAPHY		205



## LIST OF TABLES

Table 4.1: Complete set of parameters used for the model. References for parameters obtained from literature are listed. . . . .	56
Table 5.1: Empirical parameters of the Guo et al. model. . . . .	84
Table 5.2: Daily rainfall adjustments needed to account for measured soiling ratio time-series for NREL Site 3. . . . .	101
Table 5.3: Daily rainfall adjustments needed to account for measured soiling ratio time-series for NREL Site 11. . . . .	102
Table 5.4: Variability of forecast for a site in Lamont, CA (NREL Site 11 from [124]) when using different weather prediction resources. . . . .	111
Table 5.5: Comparison of ANN and MLR performance when different numbers of features (environmental variables) are used for model training. . . . .	120
Table 5.6: Statistical metrics comparing MLR and ANN model performance when using a dataset generated with the semi-physical soiling model without the resuspension term. . . . .	122
Table 6.1: SAPM temperature model coefficients. . . . .	130
Table 6.2: Errors of empirical models for results shown in Figure 6.1. . . . .	131
Table 6.3: Errors of empirical models for entire year using default parameters. . . . .	132
Table 6.4: Errors of empirical models' results shown in Figure 6.2. . . . .	133
Table 6.5: Errors for one year of module temperatures predicted by empirical models using fitted parameters. . . . .	133
Table 6.6: Physical properties of the solar module. . . . .	148
Table 6.7: Electrical parameters of the solar module. . . . .	149
Table 6.8: Physical properties of the CdTe solar module. . . . .	151
Table 6.9: Derived equivalent circuit parameters of the First Solar 4 Series FS-4122-3 solar module. . . . .	152

Table A.1: SAPM temperature model coefficients. . . . .	182
Table A.2: Spectral mismatch modifier coefficients. . . . .	183
Table A.3: Sample albedo values. From [129]. . . . .	186
Table A.4: Default annual losses in PVWatts for reference. . . . .	189

## LIST OF FIGURES

Figure 1.1: Diagram of the energetics, and drift and diffusion currents at the p-n junction of a solar cell. Adapted from [8]. . . . .	3
Figure 1.2: General JV curve showing the main parameters used to describe a solar cell's performance. Adapted from [9]. . . . .	4
Figure 1.3: Equivalent circuit of an ideal solar cell (a) and a solar cell with losses modeled with series and shunt resistance (b). Adapted from [13]. . . . .	7
Figure 2.1: Two Gummel iteration approaches. Approach b) is used in this study. . . . .	23
Figure 2.2: Flow chart of the main steps in the Newton-Raphson method. . . . .	27
Figure 2.3: Comparison of results from drift-diffusion model of an arbitrary single-carrier device under SCLC conditions with Mott-Gurney analytical equations. a) Current density versus voltage. b) The electric field distribution through the thickness of a device under high voltage. . . . .	30
Figure 2.4: Drift-diffusion (DD) model results for JV curves of a hole-only device with varying sizes of injection barriers compared with the Mott-Gurney equation. . . . .	31
Figure 2.5: Results from drift-diffusion models of single-layer, two-carrier devices: one with uniform mobilities (a-d) and another with 100x larger hole mobility than electron mobility (e-i). . . . .	32
Figure 3.1: Basic architecture (a) and energy level alignment (b) of a bilayer solar cell. Adapted from [32]. . . . .	35
Figure 3.2: Carrier densities at short-circuit (a) and open-circuit (b) conditions for the bilayer device. . . . .	36
Figure 3.3: Recombination and generation processes at the bilayer interface. Adapted from [15]. . . . .	37
Figure 3.4: The hole density at a point close to the interface inside the device (which exact point does not matter) is plotted versus the number of iterations of the Gummel loop. a) A converging solution, which occurs when the mixing factor is sufficiently small for the applied voltage. b) A solution that cannot converge. . . . .	40

Figure 3.5: Comparison of convergence behaviors between Gummel and Newton methods. a) Mixing factor needed to achieve convergence. b) Number of iterations required to converge. . . . .	44
Figure 4.1: Device structure of planar heterojunction perovskite solar cell modeled by Sherkar et al. [47]. . . . .	50
Figure 4.2: Simulated JV curves for different carrier mobilities in perovskite layer from this work (a), and Sherkar et al. (b). . . . .	51
Figure 4.3: Simulated JV curves for different trap densities at HTL/perovskite interface (a, b) and ETL/perovskite interface (c, d). Results from this work's model (a, c) are compared with results from Sherkar et al. (b, d). . . . .	52
Figure 4.4: Simulated JV curves for different injection barriers at the anode and cathode ( $\phi_a$ and $\phi_c$ respectively) on the JV curve from this work's model (a), and from Sherkar et al. (b). . . . .	53
Figure 4.5: Energy levels and thicknesses of the device layers with the rectangles representing the bandgap of the material. The levels were found from a combination of literature values and fitting of the numerical model (more details in Table 4.1). The levels within the BCP bandgap are gap-states due to diffusion of Ag into BCP. . . . .	54
Figure 4.6: Carrier photogeneration rate profile for the device without $C_{60}$ as determined from the transfer-matrix optical model using the sum over wavelengths 350-750 nm. Position is displayed relative to the beginning of the HTL (PEDOT:PSS) layer. . . . .	57
Figure 4.7: Comparison of the JV curve results from the experiment and numerical model. . . . .	58
Figure 4.8: JV curves showing the effects of perovskite/BCP interface carrier mobility (a) with ETL trap density set to $6 \times 10^{20} \text{ m}^{-3}$ and trap density (b) on the 0 nm device with perovskite/BCP interface mobility set to $2 \times 10^{-9} \text{ m}^2/\text{Vs}$ (the same value as for the 20 nm $C_{60}$ device). All other parameters were kept the same as in Table 4.1. . . . .	59
Figure 4.9: Charge carrier densities for the simulated devices with 0 nm, 1 nm, and 20 nm $C_{60}$ under illumination at zero applied bias. The perovskite/ $C_{60}$ and $C_{60}$ /BCP interfaces are marked by dotted black lines. The parameters used are listed in Table 4.1. . . . .	61

Figure 4.10: The effect of using an energetic barrier for electron extraction instead of a low effective mobility region at the perovskite/BCP interface of devices without C <sub>60</sub> . The fit to experiment that was achieved when using a low mobility region is shown for comparison. . . . .	62
Figure 4.11: Charge carrier densities for device with 0 nm C <sub>60</sub> under illumination at 0.7 V (a) and 0.9 V (b) applied bias. The parameters used are listed in Table 4.1. . . . .	64
Figure 4.12: The effect of variation of the HOMO/LUMO of the HTL/ETL on the JV curve of the device with 0 nm C <sub>60</sub> . The fit to experiment is included for comparison. . . . .	65
Figure 5.1: Soiling is a complex problem with many influencing factors over a large range of size and time scales. Environmental parameters are shown in blue, microscopic soiling processes are shown in green, and controllable influencing factors related to plant design and maintenance strategies are in orange. Adapted from [85]. . . . .	73
Figure 5.2: Schematic of particle dry deposition model resistance analogy. Adapted from [96]. . . . .	76
Figure 5.3: Schematic of deposition due to particle impaction. Adapted from [100]. . . . .	79
Figure 5.4: One year of hourly soiling rates predicted by the Guo et al. model with (a) and without (b) the resuspension term. . . . .	85
Figure 5.5: Attachment probability as a function of a) particle diameter (with wind speed of 1 m/s and relative humidity of 70%) and b) wind speed (with particle diameter of 15 μm and relative humidity of 50%). . . . .	87
Figure 5.6: Wind-induced velocity as a function of a) wind speed (for 10 μm particles in 40% relative humidity) and b) relative humidity (for 50 μm particles at 2 m/s wind speed). . . . .	88
Figure 5.7: Resuspension flux versus wind speed for RH 40%. . . . .	89
Figure 5.8: Net soiling mass accumulation flux at 40% RH, 50 μg/m <sup>3</sup> PM10 concentration, and 20° tilt angle. . . . .	90
Figure 5.9: Comparison of hourly soiling mass accumulation rates for Riverside, CA as predicted by the Guo et al. model (a) and the improved model proposed in this thesis (b). . . . .	90
Figure 5.10: Reduction in soiling losses due to rainfall. This plot is from Enlighten Energy's PV SoilSayer software, which contains an implementation of the soiling model described here. . . . .	93

Figure 5.11: Empirical angular loss factors for direct (a), diffuse (b), and albedo (c) irradiance as functions of angle of incidence for two angular loss coefficients ( $a_r$ ). . . . .	97
Figure 5.12: Hourly soiling loss profile over a single day for two different panels: a "no clean" panel that was never cleaned and a "clean" panel that is periodically cleaned according to a cleaning cycle. This plot is from Enlighten Energy's PV SoilSayer software, which contains an implementation of the soiling model described here. . . . .	99
Figure 5.13: Comparison of model predictions with NREL Site 3 (Calipatria, California) when using precipitation data provided by NREL (a) and when using modified rainfall data (b). . . . .	101
Figure 5.14: Comparison of model predictions with NREL Site 11 (Lamont, California) measured data when using precipitation data provided by NREL (a) and when using modified rainfall data (b). . . . .	102
Figure 5.15: Flow-chart of the approach used to incorporate the soiling loss models that were developed in this work into PV SoilSayer. . . . .	104
Figure 5.16: Beginning of PV SoilSayer results report, showing the forecast inputs and comparison of the predicted annual energy production and soiling losses for a system that is never cleaned ("No Clean" case) versus a system that is cleaned according to an optimized cleaning schedule ("Clean" case). . . . .	106
Figure 5.17: Optimal manual cleaning dates and soiling rates results page from a sample PV SoilSayer forecast. . . . .	107
Figure 5.18: Visualization of soiling losses and energy production from a sample PV SoilSayer forecast. The sharp reductions in soiling loss correspond to manual and rainfall cleanings of the panels. . . . .	108
Figure 5.19: Visualization of soiling and energy production for a single month from a sample PV SoilSayer forecast. A manual cleaning event occurs from June 13 to June 22, reducing the soiling loss on the "Clean" panel and increasing the difference between "Clean" and "No Clean" panel energy production. . . . .	109
Figure 5.20: AC soiling loss with oscillations caused by inverter clipping. . . . .	110
Figure 5.21: AC soiling loss for same forecast as Figure 5.20, but without inverter clipping. . . . .	111
Figure 5.22: Comparison of soiling time-series predictions for a site in Lamont, CA (NREL Site 11 from [124]) when using different weather prediction resources. . . . .	112

Figure 5.23: Diagram of an ANN. From [134]. . . . .	115
Figure 5.24: Heatmap of Pearson correlation coefficients between environmental variables and predicted soiling rate. . . . .	117
Figure 5.25: Heatmap of Spearman correlation coefficients between environmental variables and predicted soiling rate. . . . .	118
Figure 5.26: Comparison of hourly soiling rates predicted by MLR and ANN models to rates predicted by the semi-physical model (with resuspension) that they were trained on. Only data points from the testing set are shown. . . . .	121
Figure 5.27: Comparison of hourly soiling rates predicted by MLR and ANN models to rates predicted by the semi-physical model (without resuspension) that they were trained on. Only the test data points are shown. . . . .	122
Figure 5.28: Heatmap of Spearman correlation coefficients between ten-day moving averages of soiling and environmental variables measured at a PV power plant in California. . . . .	123
Figure 5.29: Comparison of Kimber, MLR, and ANN models' ability to fit the training data (measured soiling and environmental parameters for 2019). . . . .	124
Figure 5.30: Comparison of Kimber, MLR, and ANN models' ability to predict soiling in 2020, when trained on data from 2019. Statistical metrics for two different prediction periods are shown: February 25 through June 16, and April 23 through June 16. . . . .	125
Figure 6.1: Comparison of empirical models using default parameters. . . . .	131
Figure 6.2: Comparison of empirical models with parameters fitted using least-squares optimization. . . . .	132
Figure 6.3: Five-parameter equivalent circuit representation of a solar cell. Adapted from [145]. . . . .	137
Figure 6.4: Flow chart of the Cubas et al. procedure to find the equivalent circuit parameters. . . . .	140
Figure 6.5: Flow chart of the improved equivalent circuit parameters extraction method. . . . .	142
Figure 6.6: Example of results from our modified parameter extraction tool. a) Convergence behavior as the ideality factor guess is incremented. b, c) IV curves generated during the iterative process, with the optimized ones plotted in red. Fill factor decreases as ideality factor increases. d) Values of optimal parameters for this run. . . . .	143

Figure 6.7: Flow chart of the calculations at each time step of the coupled thermal-electric PV model. . . . .	147
Figure 6.8: TAItherm prediction of cell temperature variation with a) irradiance, b) air temperature, and c) wind speed. . . . .	149
Figure 6.9: One day simulation results for a) cell temperature, b) current, c) efficiency, d) silicon bandgap, e) modified ideality factor, and f) diode saturation current. . . . .	150
Figure 6.10: Example of the effect of cell temperature on a) IV curve and b) power production. . . . .	151
Figure 6.11: Comparison of one day of modeled and measured First Solar Series 4 CdTe module temperature and short-circuit current. . . . .	153
Figure 6.12: Comparison of cell temperature versus irradiance predictions under 1 m/s and 5 m/s wind. . . . .	154
Figure 6.13: Comparison of cell temperature versus air temperature and wind speed predictions. . . . .	154
Figure 6.14: Comparison of cell temperature predictions versus wind speed and irradiance made with a fitted PVsyst model ( $\eta_m=18\%$ , $\alpha = 0.9$ , $u_c = 23.2$ , $u_v = 7.4$ ) and TAItherm. . . . .	155
Figure 6.15: TAItherm house model with roof-mounted solar panel. . . . .	156
Figure 6.16: PV rooftop system simulation results for a typical day in July in Phoenix, Arizona. Predicted power (a) and efficiency (b) with and without considering temperature-induced losses. . . . .	156
Figure 6.17: Predicted PV energy production with and without including soiling losses. a) Daily DC power. b) Monthly DC energy production. . . . .	157
Figure 6.18: a) Soiling coefficients used as input. b) Transmission and angular losses due to soiling calculated by the thermal-electrical model. Daily rainfall totals are shown with blue bars. . . . .	158
Figure 6.19: TAItherm Jeep model with roof-mounted solar panel. . . . .	159
Figure 6.20: Comparison of a single day of modeled vehicle-integrated solar panel power (a) and efficiency (b) when different factors affecting PV performance are considered (irradiance dependence only, irradiance and angle dependence, and irradiance, angle, and temperature dependence). . . . .	160



Figure 6.21: a) TPV UV-vis spectrum for front illumination. Data from [163]. b) Incident angle modifier for a conventional thin film PV and one that is optimized for improved angle-dependence. Data from [147]. . . . .	163
Figure 6.22: a) Predicted total annual energy production in five U.S. cities for three different vehicle-integrated PV systems: TPVs covering entire surface of the vehicle, TPVs only used in windows, and a conventional silicon PV roof module. b) Predicted monthly energy production for the TPV system that covers the entire surface of the vehicle. . . . .	164
Figure 6.23: Schematic of the thermal-electrical battery model. $Q$ is the heat generated by the battery, calculated in terms of Joule heating (electrical losses) within the battery equivalent circuit and entropic heating (heat from chemical reactions in the battery). Adapted from [165]. . . . .	166
Figure 6.24: Flow diagram of the battery life prediction model. ("Eqc" stands for "equivalent circuit".) . . . . .	167
Figure 6.25: a) Battery charge/discharge current over a single summer day. Positive current is defined as charging. b) State of charge of the 30 Ah battery due to the current profile in a). . . . .	168
Figure 6.26: Relative resistance (a) and capacity (b) of the 30 Ah and 60 Ah batteries. Values are relative to those of a brand-new battery. . . . .	168
Figure 6.27: PV-battery and battery management system modeling approach. . . . .	169
Figure A.1: Weather Resource UI. . . . .	178
Figure A.2: System Design UI. . . . .	179
Figure A.3: Inverter partial-load efficiency curve. Adapted from [181]. . . . .	181
Figure A.4: Array types. Adapted from [183]. . . . .	184
Figure A.5: Ground cover ratio. Adapted from [183]. . . . .	185
Figure A.6: PV System Losses UI. . . . .	187
Figure A.7: Monthly energy production chart example. . . . .	189
Figure A.8: Soiling loss calculation/upload options. . . . .	190
Figure A.9: Soiling Loss Calculator UI. . . . .	191

Figure A.10: DC Loss Over a Dry Period UI. . . . . 191

Figure A.11: Daily Soiling Rates UI. . . . . 192

Figure A.12: Angular Losses UI. . . . . 193

Figure A.13: Rainfall Parameters UI. . . . . 195

Figure A.14: Sample Monthly Average Soiling Losses Output. . . . . 195

Figure A.15: Clean Cycle Configuration UI. . . . . 196

Figure A.16: Optimal Clean Cycle UI. . . . . 197

Figure A.17: Clean Based on Specific Thresholds UI. . . . . 199

Figure A.18: Clean Based on Specified Cycle UI. . . . . 200

# CHAPTER 1

## INTRODUCTION

### 1.1 Motivation

Fossil fuel energy sources have been a fundamental driver of industrialization and the resulting technological, economic, and social progress. However, fossil fuels are finite with predictions expecting worldwide reserves of oil, natural gas, and coal to be depleted in 50, 51, and 132 years respectively [1]. Additionally, fossil fuels are the dominant source of greenhouse gases, which are causing climate change [2]. The Intergovernmental Panel on Climate Change (IPCC) predicts that without significant emissions reductions, annual carbon dioxide emissions would rise to over 100% above 2010 levels by 2050, which is likely to cause a rise in global temperatures of 4°C from pre-industrial levels. Such a temperature rise is expected to cause serious groundwater shortages, more severe weather events, decreased agricultural production, and loss of critical ecosystem functions. The IPCC predicts that it is possible to limit the global temperature increase to 2°C if carbon dioxide emissions drop to 66% below 2010 levels by 2050 [3]. A rapid transition to clean renewable energy sources is essential to maintain the standard of living in developed countries, allow for the continued development of the rest of the world, and reduce the effects of greenhouse gas emissions.

With the increasing concerns and education about fossil fuels, renewable energy usage has been expanding worldwide. Sunlight is the most abundant renewable resource. There is more energy in the sunlight striking the earth's surface in two hours than the annual worldwide energy consumption [4]. In 2018, increases in solar power production capacity accounted for over 53% of the total new net capacity of all renewable sources [5]. The growth in photovoltaics (PV) energy has been supported by improved technologies that have led to increasing efficiencies and rapidly falling costs [6]. There is still an immense opportunity for growth since PV energy currently supplies only 2.6% of the global electricity demand [7]. In order to effectively expand PV technologies, it is necessary not just to install more solar panels, but also to continue to improve power generation

efficiencies and reduce manufacturing costs. These improvements can be made in two different categories. One area of potential improvement is to develop better solar cell materials and devices that are more efficient and less expensive to produce. The second area where improvements can be made is at the PV module and system level, by reducing losses due to the environmental conditions such as high temperatures and reduction in absorbed irradiance due to soiling (i.e. particulate matter) accumulation.

Physics and computational modeling are an essential part of the research and development of PV devices and systems. Computational modeling allows us to explain experimental observations and test new designs before investing time and financial resources into conducting experiments. Developing models for solar cell devices that can explain experimental observations requires a strong understanding of solar cell device physics. Consideration of semiconductor physics, optics, heat transfer, weather, and soiling is necessary to realistically model solar modules that are outside of controlled laboratory conditions. Therefore, accurate modeling of PV technologies in real-world conditions is a complex multi-physics problem whose solution requires the combination of electrical, thermal, and environmental models. This dissertation describes the development of improvements to PV modeling at both the device and system levels, as well as the application of these models to obtain new insights into device physics and PV system performance.

## **1.2 Solar Cell Devices**

A solar cell is a two-terminal semiconductor device that generates current and voltage when under illumination. The basic components of a solar cell are two electrodes (at least one of which allows transmission of light) and a solar irradiance absorber (also known as the *active layer*), which is made of a semiconductor. The working principle is based on the photovoltaic effect where photons of energy greater than the bandgap of the absorber layer excite electrons from the valence band (VB) to the conduction band (CB), leaving behind holes in the VB. Holes are the absence of an electron and behave like a particle, which is positively charged and has an effective mass that reflects its ability to move through a material. Due to an energy level difference between

the cathode and anode work functions, a solar cell has a built-in electric potential. The electric potential causes the photogenerated free electrons and holes (also known as *charge carriers*, or simply *carriers*) to separate and move on-average in opposite directions to the positive and negative contacts, thus generating a current. Charge carriers also move due to diffusion, which describes the tendency of particles to move from higher to lower concentration. The net current in the device has contributions from carrier drift due to the electric potential and carrier diffusion due to the particle concentration gradient (Figure 1.1). The mechanism of separation of the carriers is dependent on the materials and architecture of the cell. The accumulation of electrons and holes at the electrodes results in the generation of a voltage, which counteracts the built-in potential. Once the voltage due to charge accumulation at the contacts becomes high enough to cancel both the drift and diffusion currents, there will be zero current in the solar cell. The voltage at which this occurs is called the open-circuit voltage ( $V_{oc}$ ). Beyond  $V_{oc}$ , current flows in the opposite direction, and the solar cell no longer produces electrical energy.

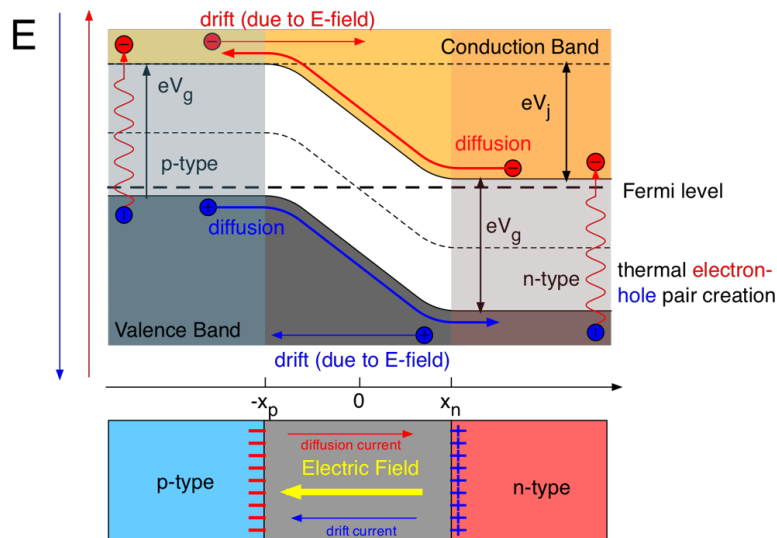


Figure 1.1: Diagram of the energetics, and drift and diffusion currents at the p-n junction of a solar cell. Adapted from [8].

The performance of a solar cell can be described in terms of a generated current density ( $J$ ) versus voltage ( $V$ ) curve (commonly known as *JV curve*), as shown in Figure 1.2. The *JV curve* has several parameters that are used to characterize a device's performance: short-circuit current

density ( $J_{sc}$ ), open-circuit voltage ( $V_{oc}$ ), and fill factor ( $FF$ ). The short-circuit current is the current which flows when the voltage between the electrodes is zero, or equivalently when the device is short-circuited. This current depends strongly on the photon absorption rate in the active layer. In the ideal case,  $J_{sc}$  is equal to the photocurrent ( $J_{ph}$ ); in other words, all of the photogenerated electrons and holes reach the electrodes. The open-circuit voltage is the maximum voltage that a solar cell can produce or the voltage that develops inside the cell when the two electrodes are isolated.  $V_{oc}$  is the zero of the JV curve. A solar cell will have the highest efficiency if it is operated at the  $J$  and  $V$  that gives maximum power output, where power is defined by  $P = JV$ . The fill factor is defined as the ratio  $P_{max}/J_{sc}V_{oc}$  and represents the "squareness" of the JV curve. Power conversion efficiency is the ratio between the maximum generated power and the incident power

$$PCE = \frac{P_{max}}{P_{inc}} = \frac{J_{sc}V_{oc}FF}{P_{inc}} \quad (1.1)$$

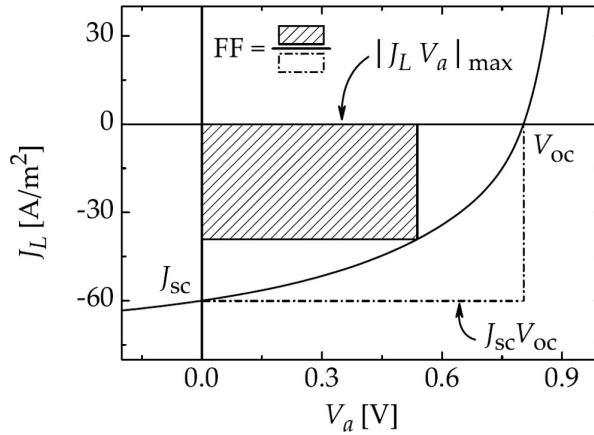


Figure 1.2: General JV curve showing the main parameters used to describe a solar cell's performance. Adapted from [9].

To maximize efficiency, the  $J_{sc}$ ,  $V_{oc}$ , and  $FF$  should be maximized. Qualitatively, this means that an ideal solar cell will have a high absorption rate of photons with all of the generated charge carriers reaching the electrodes without loss. In practice, we can describe four main criteria for an efficient solar cell. First, the absorbing layer's bandgap must be small enough so that the photons from solar radiation have enough energy to excite the electrons. Simultaneously, the bandgap

should be large enough to prevent carrier recombination. Second, the absorber layer should be thick enough to absorb a significant amount of light. However, this thickness is limited to the finite diffusion lengths of charge carriers in the material. Therefore, an active layer that has high carrier mobilities is beneficial. Third, the cell's layers should have suitable energy bands so that both the electrons and holes encounter no energy barriers as they travel to their contacts. Finally, the losses during transport of the generated carriers to the electrodes should be minimized. These losses can occur due to carriers recombining with defects and impurities in the active layer and at the interfaces between layers [10].

Solar cell technologies are often classified into three generations. First-generation solar cells are silicon-based and dominate the market. Second-generation solar cells are based on thin-film technologies such as cadmium telluride (CdTe), copper indium gallium diselenide (CIGS), and thin-film amorphous silicon. Third-generation solar cells are based on semiconducting organic molecules, inorganic nanoparticles, or organic-inorganic hybrid materials, and generally manufactured through solution-processing. Prominent examples are organic and perovskite solar cells. Some advantages of third-generation solar cells are reduced manufacturing costs due to low temperature and vacuum-free fabrication and the possibility of roll-to-roll printing. They are also light, flexible, and can be made semi-transparent [11]. The commercial market is currently dominated by first-generation solar cells, but this may soon change as third-generation PV technologies advance to commercially-viable products. The device modeling portion of this dissertation focuses on the emerging third-generation solar cells, while the system-level modeling portion concentrates mostly on the first and second-generation solar cells that are commonly used today commercially.

### **1.3 Photovoltaic Device Modeling**

As briefly described above, many aspects need to be optimized in order to design efficient solar cells. Experimentally optimizing all of these aspects is time-consuming and can be costly. Computational modeling can help rapidly test possible combinations of materials and device architectures for ones that have the greatest potential of producing high-performance solar cells.

Also, comparing experimental results to simulations based on the physics equations improves our understanding of the mechanisms that affect the device performance. Computational modeling has been used since the 1950s to study the physical properties of semiconductor devices, including solar cells. Many PV device models are based on the fitting of experimental JV curves to an equivalent circuit equation. More detailed and physics-based approaches are based on various simplifications of the Boltzmann transport equation. One of the most popular and efficient approaches is the drift-diffusion model, which involves numerically solving equations for the electric potential and currents in the device in a self-consistent loop. The equivalent circuit and drift-diffusion approaches are introduced in the next two sections.

### 1.3.1 Equivalent Circuit Approach

Equivalent circuit modeling is a widely used approach for describing the electrical behavior of solar cell devices. This approach uses equivalent circuit equations based on the Shockley diode equation, which describes the ideal recombination current from diffusion and recombination of carriers at the p-n junction (a diode) [12]. The Shockley diode equation for current ( $I$ ) in a diode as a function of applied voltage ( $V_a$ ) is

$$I(V_a) = I_o \left[ \exp\left(\frac{eV_a}{k_B T}\right) - 1 \right] \quad (1.2)$$

where  $I_0$  is the saturation-current (thermal generation current at zero applied bias),  $e$  is the elementary charge,  $k_B$  is the Boltzmann constant, and  $T$  is the device temperature. The thermal generation current is the current due to drift of the minority carriers (electrons in the p-type region and holes in the n-type region) across the junction.

The simplest model of a solar cell treats it as an equivalent circuit composed of an ideal diode and a current source that are connected in parallel, as shown in Figure 1.3a. The relationship between current and voltage is described by adding a photocurrent term to the Shockley diode equation

$$I(V_a) = I_o \left[ \exp\left(\frac{eV_a}{k_B T}\right) - 1 \right] - I_{ph} \quad (1.3)$$



In practice, a solar cell has losses which can be described by adding a series resistance ( $R_s$ ) and a shunt (or parallel) resistance ( $R_p$ ), as shown in Figure 1.3b. The series resistance describes the losses related to non-infinite mobilities of the charge carriers and imperfect contacts between the active layer and electrodes. The parallel resistance determines the leakage current, which is the current that does not flow through the electrodes and can be due to pinholes between the layers in the cell that provide an alternate path for the current. The charges that flow through the leakage path will not contribute to the powering of the device or charging of the battery that the solar cell is connected to.

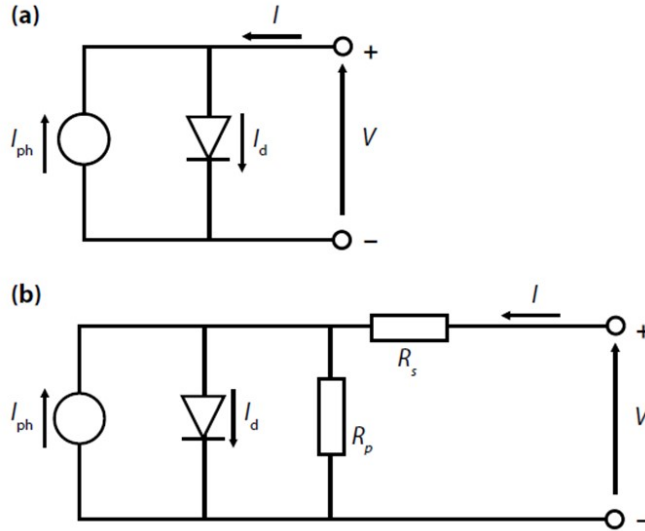


Figure 1.3: Equivalent circuit of an ideal solar cell (a) and a solar cell with losses modeled with series and shunt resistance (b). Adapted from [13].

A non-dimensional constant,  $a$ , called the ideality factor, is added to the Shockley diode term to account for deviation of the diodes from Shockley diffusion theory [14]. Recognizing  $e/k_B T$  as the thermal voltage ( $V_T$ ), this more realistic equivalent circuit can be described by

$$I(V) = I_o \left[ \exp\left(\frac{(V - IR_s)}{aV_T}\right) - 1 \right] + \frac{V - IR_s}{R_p} - I_{ph} \quad (1.4)$$

For a high-performance solar cell,  $R_s$  should be small, and  $R_p$  should be large. Other equivalent circuit models have been developed, such as the ones for organic heterojunctions [15, 16]. The effect of temperature on device performance can be included by considering its effect on the parameters of the equivalent circuit equation. An advantage of equivalent circuit modeling is that it is a simple approach with low computational expense and reasonable accuracy, as long as the equations are fitted to experimental data. Equivalent circuit modeling of solar cells with consideration of the effects of temperatures is described in Chapter 6.

### 1.3.2 Drift-Diffusion Approach

While using equivalent circuit equations allows for a quick fitting of experimental current-voltage curves and some understanding of the physical parameters, it does not give a deep physical insight into the mechanisms occurring inside the device. In order to understand the device physics, it is necessary to perform simulations which explicitly treat the electrodynamics, charge generation, separation, and recombination processes. The most general equation for transport in semiconducting devices is the semi-classical Boltzmann transport equation (BTE), which describes the time evolution of a seven-dimensional particle distribution function  $f(\vec{r}, \vec{t}, t)$  [17].

$$\frac{\partial f}{\partial t} + \vec{v} \cdot \nabla_r f + \vec{F} \cdot \nabla_p f = \left( \frac{\partial f}{\partial t} \right)_{collisions} \quad (1.5)$$

The distribution function represents the probability for a particle to occupy position  $\vec{r}$  with momentum  $\vec{p}$  at time  $t$ . By definition, integrating  $f$  over all momenta gives the particle density at position  $\vec{r}$ , and further integrating over all positions gives the total number of particles  $N$  in the system. (Note that this equation is often written in terms of wavenumber  $\vec{k}$ , which is related to particle momentum through the de Broglie relation  $\vec{p} = \hbar \vec{k}$ ).

The collisions term on the right-hand side describes scattering in and out of a momentum state. The probability of scattering of particles out of a momentum state  $\vec{p}$  to a momentum  $\vec{p}'$  is defined as  $S(\vec{p}, \vec{p}')$ . The total number of scattering events from  $\vec{p}$  to  $\vec{p}'$  is given by the transition probability multiplied by the probability distribution function. The net change in  $f(\vec{p})$  due to scattering is the

difference between scattering of particles into state  $\vec{p}$  and scattering of particles out of state  $\vec{p}$ . For each state  $\vec{p}$ , we sum the contributions to scattering from all other states  $\vec{p}'$ .

$$\left(\frac{\partial f}{\partial t}\right)_{collisions} = \sum_{\vec{p}'} \left[ f(\vec{p}')S(\vec{p}', \vec{p}) - f(\vec{p})S(\vec{p}, \vec{p}') \right] \quad (1.6)$$

However, we should correct for the Pauli Exclusion Principle which states that only one particle can occupy a given state at a given time (ignoring spin). To account for exclusion, the transition rate probability is multiplied by the probability that the state is not occupied ( $1 - f$ ), giving

$$\left(\frac{\partial f}{\partial t}\right)_{collisions} = \sum_{\vec{p}'} \left[ (1 - f(\vec{p}))S(\vec{p}', \vec{p}) - f(\vec{k})(1 - f(\vec{p}'))S(\vec{p}, \vec{p}') \right] \quad (1.7)$$

In the limit of small  $d\vec{p}$ , the sum can be converted to an integral, making the BTE an integro-differential equation

$$\frac{\partial f}{\partial t} + \vec{v} \cdot \nabla_r f + \vec{F} \cdot \nabla_p f = \int_{\vec{p}'} [(1 - f(\vec{p}))S(\vec{p}', \vec{p}) - f(\vec{k})(1 - f(\vec{p}'))S(\vec{p}, \vec{p}')] d\vec{p}' \quad (1.8)$$

With seven partial derivatives of the distribution function on the left-hand side, and a scattering integral on the right-hand side, the general BTE is very difficult and computationally expensive to solve. Simplifications of the BTE can be derived through the Method of Moments, where the BTE is multiplied by a moment generating function [18]. Moments of different orders can be taken, with the order of the moment determined by the power of the momentum in the moment generating function. Every moment of the BTE generates a new transport equation. A moment  $M_\phi$  is defined in terms of the moment-generating function  $\phi(\vec{p})$  as

$$M_\phi = \frac{1}{V} \int \phi(\vec{p}) f(\vec{r}, \vec{p}, t) d\vec{p} \quad (1.9)$$

where the  $1/V$  is to cancel out the volume that arises from taking the three-dimensional integral.

The moment-generating functions for the zeroth, first, and second moments are

$$\phi^0 = 1, \phi^1 = \vec{p}, \phi^2 = p^2 \quad (1.10)$$

Taking an  $n$ th order moment of the BTE, we have

$$\frac{\partial}{\partial t} \left[ \frac{1}{V} \int \phi^n f d\vec{p} \right] + \nabla_r \cdot \frac{1}{V} \int \vec{v} f \phi^n d\vec{p} + \frac{1}{V} \int \phi^n \vec{F} \cdot \nabla_p f d\vec{p} = \frac{1}{V} \int \phi^n Q(f) d\vec{p} \quad (1.11)$$

where we used  $\vec{v} \cdot \nabla_r f = \nabla_r \cdot (\vec{v} f)$  and the scattering term of the BTE was denoted as  $Q(f)$  for brevity. The third term of the left-hand side can be simplified by integration by parts

$$\frac{\vec{F}}{V} \cdot \int \phi^n \cdot \nabla_p f dp d^2 p = \frac{\vec{F}}{V} \cdot \left[ \int \phi^n f \Big|_{p=-\infty}^{p=\infty} d^2 p - \int f \frac{\partial \phi}{\partial p} d\vec{p} \right] \quad (1.12)$$

The first term on the right-hand side equals zero since the distribution function must go to zero at infinite momentum. Thus, we have the following equation for the  $n$ th moment of the BTE

$$\frac{\partial}{\partial t} \left[ \frac{1}{V} \int \phi^n f d\vec{p} \right] + \nabla_r \cdot \frac{1}{V} \int \vec{v} f \phi^n d\vec{p} - \frac{F}{V} \cdot \int f \frac{\partial \phi}{\partial p} d\vec{p} = \frac{1}{V} \int \phi^n Q(f) d\vec{p} \quad (1.13)$$

By taking the zeroth and first moments of the BTE, one can derive the continuity and drift-diffusion equations (respectively) which are used for drift-diffusion modeling [17, 19].

To derive the continuity equation, we evaluate the first moment of the BTE by substituting  $\phi = 1$  into Equation 1.13 which yields

$$\frac{\partial}{\partial t} \left[ \frac{1}{V} \int f d\vec{p} \right] + \nabla_r \cdot \frac{1}{V} \int \vec{v} f d\vec{p} = \frac{1}{V} \int Q(f) d\vec{p} \quad (1.14)$$

Note that this is simply taking the mean of the BTE over momentum space. In semiconductors, the mean effect of collisions results in generation and recombination of charge carriers. Therefore, the zeroth moment of the collision term is the net carrier density generation rate  $U_\rho$ . We recognize the first term on the left-hand side as the time derivative of the density distribution of particles in space. We recognize the integral in the second term on the left-hand side as a particle density flux

$$\int \vec{v} f d\vec{p} = \rho \vec{v} \equiv \vec{\Phi}_\rho \quad (1.15)$$

Applying these simplifications, we have

$$\frac{\partial \rho}{\partial t} = U_\rho - \nabla_r \cdot \vec{\Phi}_\rho \quad (1.16)$$

This is the continuity equation which describes a general conservation law, where  $\rho$  is some quantity per unit volume,  $\vec{\Phi}_\rho$  is the flux of that quantity, and  $U_\rho$  is the generation rate of that quantity per unit time per unit volume. In the context of semiconductor device modeling, the continuity equation is a carrier mass conservation law, stating that the rate of change in carrier density is equal to the

net carrier generation rate minus the divergence of the particle flux. Rewriting the particle flux in terms of an electrical current density divided by the charge of the carriers (where  $e$  denotes the elementary charge), we get the continuity equations for electrons ( $n$ ) and holes ( $p$ ) that are used for semiconductor device modeling

$$\frac{\partial p}{\partial t} = U_p - \frac{1}{e} \nabla_r \cdot \vec{J}_p \quad \text{and} \quad \frac{\partial n}{\partial t} = U_n + \frac{1}{e} \nabla_r \cdot \vec{J}_n \quad (1.17)$$

To derive the drift-diffusion equation, we evaluate the first moment of the BTE by substituting  $\phi = \vec{p} = m\vec{v}$  into Equation 1.13 and dividing all terms by  $m$

$$\frac{\partial}{\partial t} \left[ \frac{1}{V} \int \vec{v} f d\vec{p} \right] + \nabla_r \cdot \frac{1}{V} \int \vec{v} \vec{v} f d\vec{p} - \frac{\vec{F}}{mV} \cdot \int f d\vec{p} = \frac{1}{V} \int \vec{v} Q(f) d\vec{p} \quad (1.18)$$

We recognize the integrals in the first term and third terms on the left-hand side as a particle density flux  $\vec{\Phi}_\rho$  and particle density distribution  $\rho$ , respectively. Therefore, we have

$$\frac{\partial \vec{\Phi}_\rho}{\partial t} + \nabla_r \cdot \frac{1}{V} \int \vec{v} \vec{v} f d\vec{p} - \frac{\vec{F}}{m} \rho = \frac{1}{V} \int \vec{v} Q(f) d\vec{p} \quad (1.19)$$

The second term can be simplified as follows.

$$\begin{aligned} \nabla_r \cdot \frac{1}{V} \int \vec{v} \vec{v} f d\vec{p} &= \frac{1}{V} \left[ \int \nabla_r \cdot \vec{v} \vec{v} f d\vec{p} \right] \\ &= \frac{1}{V} \left[ \int \vec{v} \vec{v} \cdot \nabla_r f d\vec{p} \right] \\ &= \frac{1}{V} \left[ \int v_i^2 \nabla_r f d\vec{p} \right] \\ &= \langle v_i^2 \rangle \nabla_r \rho \end{aligned} \quad (1.20)$$

where we have assumed an isotropic velocity distribution ( $\langle v_x^2 \rangle = \langle v_y^2 \rangle = \langle v_z^2 \rangle \equiv \langle v_i^2 \rangle$ ). Next we use the equipartition theorem for a single component of velocity

$$\frac{1}{2} m v_i^2 = \frac{1}{2} k_B T \quad (1.21)$$

where  $k_B$  is the Boltzmann constant and  $T$  is the temperature. Therefore,

$$\langle v_i^2 \rangle \nabla_r \rho = \frac{k_B T}{m} \nabla_r \rho \quad (1.22)$$

The right-hand side collision term of Equation 1.19 can be simplified by using the relaxation time approximation (RTA), where one replaces the scattering integral by  $(f^0 - f)/\tau$ , where  $f^0$  is the equilibrium particle distribution, and  $\tau$  is a time-constant called the relaxation time, which defines the time it takes the system to relax to its equilibrium state after being perturbed by collisions [17].

Thus we have

$$\int \vec{v}Q(f)d\vec{p} = \int \vec{v}\frac{(f^0 - f)}{\tau}d\vec{p} = \rho\frac{\langle\vec{v}_0\rangle - \langle\vec{v}\rangle}{\tau} \quad (1.23)$$

where  $\langle\vec{v}\rangle$  represents the average velocity of the ensemble of particles. By definition, the average velocity of the ensemble at equilibrium is zero, therefore

$$\int \vec{v}Q(f)d\vec{p} = -\rho\frac{\langle\vec{v}\rangle}{\tau} = -\frac{\vec{\Phi}_\rho}{\tau} \quad (1.24)$$

Combining Equations 1.19, 1.22, and 1.24, we have

$$\frac{\partial\vec{\Phi}_\rho}{\partial t} + \frac{k_B T}{m}\nabla_r\rho - \frac{\vec{F}}{m}\rho = -\frac{\vec{\Phi}_\rho}{\tau} \quad (1.25)$$

In the context of semiconductors, the particle density flux can be written in terms of an electrical current density divided by the elementary charge. For holes ( $p$ ) and electrons ( $n$ ), we have

$$\vec{\Phi}_p = \frac{\vec{J}_p}{e} \quad \text{and} \quad \vec{\Phi}_n = -\frac{\vec{J}_n}{e} \quad (1.26)$$

The force is due to the electric field so we can use  $\vec{F} = e\vec{E}$ . Substituting these quantities and rearranging Equation 1.25, we get

$$\tau\frac{\partial\vec{J}_p}{\partial t} + \vec{J}_p = \frac{e^2\tau}{m}\vec{E}p - e\tau\frac{k_B T}{m}\nabla_r p \quad \text{and} \quad \tau\frac{\partial\vec{J}_n}{\partial t} + \vec{J}_n = \frac{e^2\tau}{m}\vec{E}n + e\tau\frac{k_B T}{m}\nabla_r n \quad (1.27)$$

Now we substitute the definition of carrier mobility ( $\mu = e\tau/m$ ) and the Einstein relation for the diffusion coefficient ( $D = \mu k_B T/e$ ), yielding

$$\tau\frac{\partial\vec{J}_p}{\partial t} + \vec{J}_p = e\mu_p\vec{E}p - eD_p\nabla_r p \quad \text{and} \quad \tau\frac{\partial\vec{J}_n}{\partial t} + \vec{J}_n = e\mu_n\vec{E}n + eD_n\nabla_r n \quad (1.28)$$

For drift-diffusion modeling, the time derivative of the current density is usually neglected. The final drift-diffusion equations for holes and electrons are

$$\vec{J}_p = ep\mu_p\vec{E} - eD_p\nabla_r p \quad \text{and} \quad \vec{J}_n = en\mu_n\vec{E} + eD_n\nabla_r n \quad (1.29)$$

These equations describe the contributions to electrical currents in the device. The first term describes carrier drift due to the built-in electric field, and the second term describes carrier diffusion due to the concentration gradient (see Figure 1.1). These equations are usually coupled with Poisson's equation to solve for the electric field.

Drift-diffusion modeling has been widely used for semiconductor device simulation due to being computationally inexpensive and accurate for many situations. For solar cells, drift-diffusion modeling allows us to understand the carrier dynamics (generation, transport, recombination, and extraction) as well as simulate practical efficiency by accounting for various recombination losses in multilayer devices. Recently, there has been work on developing models that are a more accurate approximation of the BTE by taking higher-order moments (e.g. hydrodynamics and energy transport equations), including quantum effects, or even directly solving the full BTE [18, 20, 21]. Some devices, such as nanoscale transistors where the carriers can behave ballistically and quantum effects become important, need these more sophisticated and computationally expensive methods. However, in most solar cells, the carriers experience enough resistance to make their motion diffusive. Also, most solar cells have active layers that are thick enough that quantum confinement effects are not significant. Therefore drift-diffusion modeling, while being one of the simplest models in the hierarchy of semiconductor device models [19], remains accurate for most PV devices. Chapters 2-4 of this dissertation are focused on drift-diffusion modeling.

## **1.4 Photovoltaic System Modeling**

One of the main goals of PV system modeling is to predict annual energy production in order to size a PV system to the energy demand and estimate return-on-investment. Unlike device models, which are generally focused on device performance under standard laboratory test conditions, models of PV systems must consider the realistic environmental conditions. For example, solar modules in hot and sunny locations may have a significantly lower efficiency than when measured in the lab. Solar modules in locations with less directly normal irradiance will produce less power than if a global average solar irradiance is assumed. Since weather cannot be reliably predicted a year in

advance, such models use what is known as Typical Meteorological Year (TMY) weather data. The TMY data represents the median weather conditions (based on a set of weather parameters) for a location for a given historical time frame (30 years is the most common) and can be a combination of measured and modeled data [22].

Solar irradiance, ambient temperature, and wind speed are the three most important parameters from the TMY data for PV modeling. Incident irradiance is the main factor that determines energy production. The combination of incident irradiance, ambient temperature, and wind speed allows to estimate the module temperatures, and therefore, the associated thermal losses. The system's orientation with respect to the sun throughout the day is also important since device efficiency is higher under directly normal irradiance. Even the impact of particulate matter (e.g. dust, dirt, pollutants) accumulating on the panels must be considered, as it can lead to significant losses in energy production. The process of particulate matter accumulating on PV modules is known as *soiling*. Losses due to soiling (known as *soiling losses*) are significant enough in some areas of the world that PV systems must be regularly cleaned to maintain their profitability. Such cleaning should be optimized to balance the cost of cleaning with the cost of energy lost due to a certain level of soiling. The importance of soiling on PV systems has only recently been realized, and the topic is not yet well understood. Chapter 5 discusses the development of improvements to current soiling loss estimation techniques. While not the focus of this dissertation, other losses affecting a PV system's performance are those due to mismatch (electrical loss due to slight differences between connected modules), resistance in the wires, shading of solar irradiance (e.g. by nearby buildings, trees, or hills/mountains), snow, light-induced degradation, and losses in the direct-current to alternating-current inverter.

For standard PV installations (e.g. free-standing modules or rooftop systems), accounting for the system's orientation with respect to the sun is a relatively straightforward trigonometry problem, and module temperature can be estimated through empirical equations. This is no longer the case when modeling emerging PV system technologies such as the integration of PV modules or films onto irregular surfaces such as vehicles. Estimation of incident irradiance and cell temperature for



PVs integrated into irregular surfaces is discussed in Chapter 6.

## 1.5 Outline

The central focus of this dissertation is multi-physics modeling and simulation of PV devices and systems. The first part (**Chapters 2-4**) focuses on electrical modeling of PV devices, which can help our understanding of the physics of new solar cells and aid their development. The second part (**Chapters 5-6**) focuses on the modeling of PV systems, such as rooftop modules and utility-scale power plants.

In **Chapter 2**, I present an introduction to the numerical methods for solving the drift-diffusion equations. I also demonstrate that the drift-diffusion results are consistent with the analytical expression for current in single-carrier devices in the space-charge-limited current regime. In **Chapter 3**, I describe investigations into the numerical properties of a drift-diffusion model for bilayer organic solar cells (DD-BI model) that was developed by Non Thongprong and Kanokkorn Pimcharoen, who are Ph.D. alumni from our research group. Initially, I investigated the numerical instabilities which were often encountered when running the DD-BI. In order to further study these stability issues and more effectively prototype improvements, I re-implemented the Fortran code in Matlab, and then developed and investigated several variations of the iterative scheme, some of which resulted in improved convergence. After acquiring an understanding of the drift-diffusion modeling techniques and their numerical properties, I developed a drift-diffusion model for perovskite solar cells, which are one of the most promising emerging PV technologies. **Chapter 4** focuses on drift-diffusion modeling of perovskite solar cells and analysis of the fundamental physics to explain experimentally measured current-voltage curves. I describe the adaptation of the drift-diffusion model for perovskites and validation of the model by comparison to literature results. Finally, I converted the code into C++ for significantly improved performance and applied the model to help explain a new experimental result where it was found that ultrathin fullerene layers can have a drastic impact on a particular planar perovskite solar cell architecture. C++,

Matlab, and Python examples of the drift-diffusion codes that I developed are available<sup>1</sup>.

**Chapter 5** describes the development of PV energy production forecasting models that consider environmental conditions and soiling losses. I propose improvements over existing soiling loss models where several semi-physical models for soiling accumulation and a model for the angular reflection due to soiling are combined. Additionally, I demonstrate the potential of using a machine learning approach to soiling modeling. In a research and development collaboration with PV startup Enlighten Energy Ltd., the semi-physics soiling models were combined with the PV system performance models provided by the open-source Python package PVLIB to create PV SoilSayer, a new commercial web-based software tool. PV SoilSayer predicts a power plant's yearly energy production, losses due to soiling, and calculates optimized cleaning schedules. The simulation results were compared with experimental data collected at large solar power plants. **Appendix A** describes PV SoilSayer in more detail.

**Chapter 6** describes the development of coupled thermal-electrical PV models by integrating temperature-dependent equivalent circuit solar cell models with a commercial heat-transfer software (TAITherm). I analyze the effects of temperature and irradiance on PV device performance. Additionally, I describe the development of an improved algorithm for determining equivalent circuit model parameters. Then I discuss several practical multi-physics PV applications that can be simulated with the models developed in this dissertation. These include residential roof-mounted PV systems, vehicle-integrated transparent photovoltaics, and PV-battery systems.

**Chapter 7** presents the conclusions of this dissertation and an outlook on potential future research directions.

---

<sup>1</sup><https://github.com/tgolubev>

## **PART I**

### **Drift-Diffusion Modeling of Solar Cells**

## CHAPTER 2

### IMPLEMENTING DRIFT-DIFFUSION MODELS

#### 2.1 1D Drift-Diffusion Equations

Steady-state one-dimensional modeling along the thickness dimension is often sufficient to represent a solar cell [17]. In the device, the electric potential ( $\psi$ ) is due to the free electrons ( $n$ ) and free holes ( $p$ ) and is described by the 1D Poisson equation

$$\frac{\partial^2}{\partial x^2}\psi(x) = \frac{q}{\epsilon}[n(x) - p(x)] \quad (2.1)$$

where  $q$  is the elementary charge (always positive) and  $\epsilon$  is the dielectric constant. The above equation assumes that  $\epsilon$  is constant within each layer of the device. Defining  $x = 0$  as the anode and  $x = L$  as the cathode, the boundary conditions for the electric potential are

$$\psi(L) - \psi(0) + V_{ext} = V_{bi} \quad (2.2)$$

where  $V_{ext}$  is the externally applied bias and  $V_{bi}$  is the built-in potential, which is defined as  $(W_c - W_a)/q$  where  $W_c$  and  $W_a$  are the cathode and anode work functions respectively.

The current density is separated for electrons and holes ( $J_n$  and  $J_p$ , respectively) and related to the net free carrier generation rate,  $U(x)$ , by the continuity equations

$$\frac{\partial J_n}{\partial x}(x) = -qU(x) \quad \text{and} \quad \frac{\partial J_p}{\partial x}(x) = qU(x) \quad (2.3)$$

The equations to find  $U$  generally involve charge recombination and dissociation rates and will vary depending on the solar cell device that is being modeled.

The current densities are also related to the electric potential and charge carrier densities through the drift-diffusion equations

$$J_n = -qn\mu_n \frac{\partial \psi}{\partial x} + qD_n \frac{\partial n}{\partial x} \quad J_p = qp\mu_p \frac{\partial \psi}{\partial x} - qD_p \frac{\partial p}{\partial x} \quad (2.4)$$

where  $D_{n(p)}$  is the diffusion coefficient and  $\mu_{n(p)}$  is the charge carrier mobility. Usually the Einstein relation  $D = \mu V_t$  is used, where  $V_t = k_B T / q$  is called the thermal voltage.

The boundary conditions for the charge densities at the anode are

$$n(0) = N_c \exp\left(-\frac{E_{gap} - \phi_a}{V_t}\right) \quad \text{and} \quad p(0) = N_v \exp\left(-\frac{\phi_a}{V_t}\right), \quad (2.5)$$

where  $N_c$  and  $N_v$  are the density of states of the conduction and valence bands respectively,  $E_{gap}$  is the active layer bandgap, and  $\phi_a$  is the injection barrier at the anode. Similarly, for the cathode

$$n(L) = N_v \exp\left(-\frac{\phi_c}{V_t}\right) \quad \text{and} \quad p(L) = N_c \exp\left(-\frac{E_{gap} - \phi_c}{V_t}\right), \quad (2.6)$$

where  $\phi_c$  is the injection barrier at the cathode. The drift-diffusion and current continuity equations are usually combined.

## 2.2 Discretization

In order to solve these equations numerically, we need to choose a discretization scheme. For 1D simulations of solar cells, a square mesh can be used so finite-difference discretization is appropriate. The Poisson equation is discretized in a straightforward way, using the central-difference approximation for the second derivative

$$\epsilon_i \frac{\psi_{i-1} - 2\psi_i + \psi_{i+1}}{(\delta x)^2} = q(n_i - p_i) \quad (2.7)$$

where  $\delta x$  is the distance between mesh points. The variable  $\psi$  is many orders of magnitudes smaller than  $n$  and  $p$ , which can lead to numerical issues such as rounding errors, overflow, and underflow. This can be avoided by using dimensionless scaled variables  $\psi'_i = \psi / V_t$ ,  $n'_i = n_i / N$ , and  $p'_i = p_i / N$  where  $N$  is of the same order as the density of states of charge carriers. The rescaled Poisson equation is

$$\epsilon_{r,i}(\psi_{i-1} - 2\psi_i + \psi_{i+1}) = \frac{qN(\delta x)^2}{\epsilon_0 V_t} (n'_i - p'_i) \quad (2.8)$$

where  $\epsilon_r = \epsilon / \epsilon_0$  is the relative permittivity. For points  $i$  that are on the interface of two layers with different relative permittivity ( $\epsilon_{r,1}$  and  $\epsilon_{r,2}$ ), we change the left-hand side of the equation to

$$\epsilon_{r,1}\psi'_{i-1} - 2\frac{(\epsilon_{r,1} + \epsilon_{r,2})}{2}\psi'_i + \epsilon_{r,2}\psi'_{i+1} \quad (2.9)$$

To solve for the electric potential at all mesh points, Equation 2.8 is rewritten as a matrix equation

$$\begin{bmatrix} -2\epsilon_{r,1} & \epsilon_{r,2} & 0 & 0 & \cdots & 0 \\ \epsilon_{r,1} & -2\epsilon_{r,2} & \epsilon_{r,3} & 0 & \cdots & 0 \\ \vdots & \vdots & \vdots & \vdots & \ddots & \vdots \\ \vdots & \vdots & \vdots & \vdots & \ddots & 0 \\ 0 & \cdots & \cdots & 0 & \epsilon_{r,L-2} & -2\epsilon_{r,L-1} \end{bmatrix} \begin{bmatrix} \psi'_1 \\ \vdots \\ \vdots \\ \vdots \\ \psi'_{L-1} \end{bmatrix} = C_V \begin{bmatrix} (n'_1 - p'_1) - \epsilon_{r,0}\psi'_0 \\ \vdots \\ \vdots \\ \vdots \\ (n'_{L-1} - p'_{L-1}) - \epsilon_{r,L}\psi'_L \end{bmatrix} \quad (2.10)$$

where  $C_V = qN(\delta x)^2/(\epsilon_0 V_t)$ . We keep the relative permittivity in the matrix to allow treatment of devices with differing dielectric constants in different layers. At the interfaces, the elements will need to be changed according to Equation 2.9. Note that we omit solving for the potential at the endpoints ( $i = 0$  and  $i = L$ ) because it is already defined there by the boundary conditions, which are enforced by moving the terms for the potentials at the endpoints to the right-hand side of the matrix equation. Notice that the matrix is tridiagonal and therefore can be stored as a sparse matrix (storing only the non-zero elements) and solved by using a matrix solving technique such as the straightforward Thomas algorithm or the QR algorithm (available as functions in Matlab and also in the LAPACK library, which can be used with Fortran or C++). One could also use the theorem for inverting a tridiagonal matrix derived by R.A. Usmani [23].

For the continuity equations, one needs to approximate the current in between the mesh points in order to have a result for the derivative of the current on the grid points. Scharfetter and Gummel found that if one estimates the current between mesh points using a simple central-difference method with a step size greater than  $2V_t$ , numerical instability will arise due to the exponential dependence of the charge densities on the electric potential [24]. Since using such a small mesh is computationally expensive, they introduced a method (now known as *Scharfetter-Gummel discretization*) that allows for use of a courser mesh. It reduces numerical instabilities by assuming that  $J_n$ ,  $J_p$ , and  $\partial\psi/\partial x$  are constant between mesh points. Then the drift-diffusion equations for  $n$  and  $p$  between mesh points become differential equations of one variable ( $n$  or  $p$  respectively). For example for the electrons,

we have

$$J_n = q\mu_n V_t \frac{\partial n}{\partial x} - q\mu_n n \frac{\partial \psi}{\partial x} \quad (2.11)$$

The solution of this first-order differential equation is

$$n(x) = -\frac{J_n}{q\mu_n \frac{\partial \psi}{\partial x}} + b \exp\left(\frac{\partial \psi / \partial x}{V_t} x\right) \quad (2.12)$$

We now use the assumption that  $n$  and  $\partial \psi / \partial x$  are the same at neighboring mesh points to write the equation for  $n$  at neighboring points

$$n_i = -\frac{J_{n,i+1/2}}{q\mu_n (\partial \psi / \partial x)_{i+1/2}} + b \exp\left(\frac{(\partial \psi / \partial x)_{i+1/2}}{V_t} x_i\right) \quad (2.13)$$

$$n_{i+1} = -\frac{J_{n,i+1/2}}{q\mu_n (\partial \psi / \partial x)_{i+1/2}} + b \exp\left(\frac{(\partial \psi / \partial x)_{i+1/2}}{V_t} x_{i+1/2}\right) \quad (2.14)$$

Combining these allows to solve for  $b$

$$b = \frac{n_{i+1} + \frac{J_{n,i+1/2}}{q\mu_n (\partial \psi / \partial x)_{i+1/2}}}{\exp((\partial \psi / \partial x)_{i+1/2} / V_t) x_{i+1}} \quad (2.15)$$

Substituting back into Equation 2.13, we solve for  $J_{n,i+1/2}$ , and simplifying we get the Scharfetter-Gummel discretized expression for current

$$J_{n,i+1/2} = \frac{q\mu_{n,i+1}}{\delta x} \left[ B\left(\frac{\delta \psi_{i+1}}{V_t}\right) n_{i+1} - B\left(-\frac{\delta \psi_{i+1}}{V_t}\right) n_i \right] \quad (2.16)$$

where  $\delta \psi_{i+1} \equiv \psi_{i+1} - \psi_i$  and  $B$  is the Bernoulli function  $B(x) = x/(e^x - 1)$ . Rewriting in terms of the dimensionless scaled variables that were introduced earlier ( $\psi'_i = \psi/V_t$ ,  $n'_i = n_i/N$ ), we have

$$J_{n,i+1/2} = \frac{qV_t N \mu_{n,i+1}}{\delta x} [B(\delta \psi'_{i+1}) n'_{i+1} - B(-\delta \psi'_{i+1}) n'_i] \quad (2.17)$$

The discretization proceeds in an analogous way for  $J_{p,i+1/2}$ , resulting in

$$J_{p,i+1/2} = -\frac{qV_t N \mu_{p,i+1}}{\delta x} [B(-\delta \psi'_{i+1}) p'_{i+1} - B(\delta \psi'_{i+1}) p'_i] \quad (2.18)$$

Then, the first order finite-difference approximation can be used to rewrite the continuity equations as

$$\frac{\partial J_{n,i}}{\partial x} = \frac{J_{n,i+1/2} - J_{n,i-1/2}}{\delta x} = -qU_{n,i} \quad (2.19)$$

$$\frac{\partial J_{p,i}}{\partial x} = \frac{J_{p,i+1/2} - J_{p,i-1/2}}{\delta x} = qU_{p,i} \quad (2.20)$$

Finally, the Scharfetter-Gummel discretized expressions for current (Equations 2.17 and 2.18) are substituted into the above two equations to give

$$\mu_{n,i+1}B(\delta\psi'_{i+1})n'_{i+1} - [\mu_{n,i+1}B(-\delta\psi'_{i+1}) + \mu_{n,i}B(\delta\psi'_i)]n'_i + \mu_{n,i}B(-\delta\psi'_i)n'_{i-1} = -\frac{(\delta x)^2}{V_t N}U_{n,i} \quad (2.21)$$

$$\mu_{p,i+1}B(-\delta\psi'_{i+1})p'_{i+1} - [\mu_{p,i+1}B(\delta\psi'_{i+1}) - \mu_{p,i}B(-\delta\psi'_i)]p'_i + \mu_{p,i}B(\delta\psi'_i)p'_{i-1} = \frac{(\delta x)^2}{V_t N}U_{p,i} \quad (2.22)$$

These equations are used to solve for carrier densities at all mesh points by rewriting them as matrix equations, which are analogous to the matrix form of the Poisson equation.

## 2.3 Iteration Schemes

Two main types of iteration schemes are used to self-consistently solve the 1D drift-diffusion equations [17]. One method is the Gummel iteration, where the equations are decoupled and solved separately as three sets of matrix equations: one for the Poisson equation, and two for the drift-diffusion/continuity equations (one for electrons and one for holes) [25]. The other is the Newton-Raphson method (also known as simply Newton's method), which is a general technique used to solve non-linear systems of equations where all of the equations are solved simultaneously using a single matrix.

### 2.3.1 Gummel Method

Flow charts of two general Gummel iteration schemes are shown in Figure 2.1. First, initial guesses for the carrier densities and potential are entered and the discretized Poisson equation is solved. There are two possible approaches: one is to solve for a correction  $\delta\psi$  to the potential (Figure 2.1a); the other is to solve for the new potential directly (Figure 2.1b). In this study, it was found that the first approach does not give any advantage to stability and requires more CPU time due to the additional loop for the Poisson equation. Therefore, the later approach was used in this work.



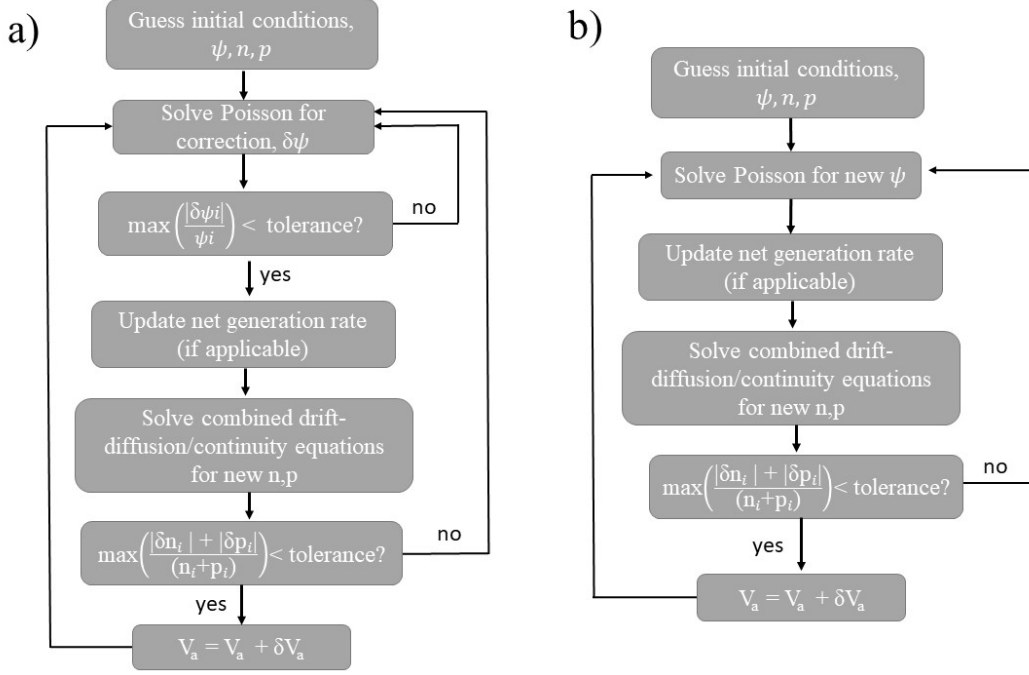


Figure 2.1: Two Gummel iteration approaches. Approach b) is used in this study.

At each iteration, Equation 2.10 is solved first to compute the new value for the electric potential ( $\psi'$ ). Once  $\psi'$  is found, it is used in the continuity/drift-diffusion equations (Equations 2.21 and 2.22) formulated as tridiagonal matrix equations. These equations are solved separately for  $n$  and  $p$ , which are then substituted back into the Poisson equation for the next iteration. The iterations are repeated until the change in  $n$  and  $p$  between two consecutive iterations (*old* and *new*) become less than a set tolerance (e.g.  $10^{-12}$ ). The convergence condition can be written as

$$\max\left(\frac{|n_{new,i} - n_{old,i}| + |p_{new,i} - p_{old,i}|}{n_{old,i} + p_{old,i}}\right) < \text{tolerance} \quad (2.23)$$

Depending on the specific problem, Gummel's method as described above will not always converge. The convergence can be improved by using a weighted average of the solutions from the last two iterations for the initial guess of the following iteration. This technique is called *mixing* or *under-relaxation* and has the effect of decreasing the possibility of solution estimates overshooting the true solution, thus preventing divergence or oscillations in the solution. The simplest mixing is the

linear one, given by

$$n_{new} = wn_{new} + (1 - w)n_{old} \quad (2.24)$$

$$p_{new} = wp_{new} + (1 - w)p_{old} \quad (2.25)$$

$$V_{new} = wV_{new} + (1 - w)V_{old} \quad (2.26)$$

where  $w$  is the mixing factor. Note that the method will also work without mixing of the voltage values but requires more iterations to converge and lower mixing factors.

The Gummel method works well for initial guesses that are far from the true solution, and saves computational power by decoupling the equations. Therefore, this scheme has become very popular for drift-diffusion models. However, convergence is problematic at higher voltages. We find that as the applied bias is increased, we must decrease  $w$ , in order to maintain convergence. When  $V_a$  approaches a solar cell's built-in voltage, the Gummel scheme no longer converges, even when very small  $w$  values are used (e.g.  $10^{-5}$ ). This convergence issue at high biases is known in the literature and is attributed to the strong coupling of the equations at high voltage [17]. If one wants to study the devices at high bias, the suggested solution is to use the fully coupled Newton's method described in the next section.

### 2.3.2 Newton-Raphson Method

Newton's method is based on first-order multivariate Taylor expansion. If we have a function  $f(x_1, x_2, \dots, x_n) \equiv f(\vec{x}) = 0$ , let  $\vec{x}^m$  be an approximation to the exact solution  $\vec{x}$ , and define  $\vec{h} = \vec{x} - \vec{x}^m$  (the error between the approximation and the exact solution), we can write [26].

$$f(\vec{x}) = 0 = f(\vec{x}^m + \vec{h}) = f(\vec{x}^m) + \sum_{j=1}^n h_j \frac{\partial f}{\partial x_j}(\vec{x}^m) + \dots \quad (2.27)$$

If we have a system of  $n$  coupled equations that are all dependent on the same set of  $n$  variables, we can write an equivalent expression in matrix form

$$0 = \begin{bmatrix} f_1(\vec{x}^m) \\ \vdots \\ f_n(\vec{x}^m) \end{bmatrix} + \begin{bmatrix} \frac{\partial f_1}{\partial x_1}(\vec{x}^m) \dots \dots \frac{\partial f_1}{\partial x_n}(\vec{x}^m) \\ \vdots \\ \frac{\partial f_n}{\partial x_1}(\vec{x}^m) \dots \dots \frac{\partial f_n}{\partial x_n}(\vec{x}^m) \end{bmatrix} \begin{bmatrix} h_1 \\ \vdots \\ h_n \end{bmatrix} \quad (2.28)$$

We call the matrix of partial derivatives the Jacobian ( $\mathbf{J}$ ) and can write the equation as  $\mathbf{J}\vec{h}_m = -\vec{f}(\vec{x}_m)$ . Since  $f(\vec{x}_{exact}) = 0$ , the right-hand side of the matrix equation is the error between the approximate and exact solution. An  $m + 1^{th}$  iteration of Newton's method proceeds as follows. First, we compute the Jacobian matrix elements using the solution from the  $m^{th}$  iteration,  $\vec{x}_m$ . Then, we solve the matrix equation for the update vector  $\vec{h}_m$ . Finally, we update the solution by simply adding the update vector to the  $m^{th}$  solution:  $\vec{x}_{m+1} = \vec{x}_m + \vec{h}_m$ . The iterations are repeated until the maximum error  $\vec{f}(\vec{x}_m)$  is less than a desired tolerance condition.

For the drift-diffusion model, we will have a system of  $3L$  coupled equations, where  $n$  is the number of interior mesh points. The equations can be grouped as  $L$  Poisson equations and  $L$  continuity equations for both electrons and holes. The only difference from the equations in Section 2.2 is that we must rearrange them so that one side equals zero as follows

$$F_{V,i} \equiv \psi'_{i-1} - 2\psi'_i + \psi'_{i+1} - C_V[(n'_i + nT'_i) - (p'_i + pT'_i)] = 0$$

$$F_{n,i} \equiv \mu_{n,i}B(-\delta\psi'_i)n'_{i-1} - [\mu_{n,i}B(\delta\psi'_i) + \mu_{n,i+1}B(-\delta\psi'_{i+1})]n'_i + \dots$$

$$\dots + \mu_{n,i+1}B(\delta\psi'_{i+1})n'_{i+1} + CU_{n,i} = 0 \quad (2.29)$$

$$F_{p,i} \equiv \mu_{p,i}B(\delta\psi'_i)p'_{i-1} - [\mu_{p,i}B(-\delta\psi'_i) + \mu_{p,i+1}B(\delta\psi'_{i+1})]p'_i + \dots$$

$$\dots + \mu_{p,i+1}B(-\delta\psi'_{i+1})p'_{i+1} - CU_{p,i} = 0$$

where  $C = (\delta x)^2 / (V_t N)$ .

The Newton's method matrix equation (Equation 2.28) becomes

$$\begin{bmatrix}
 \frac{\partial F_{V,1}}{\partial \psi'_1} & \dots & \frac{\partial F_{V,1}}{\partial \psi'_L} & \frac{\partial F_{V,1}}{\partial n'_1} & \dots & \frac{\partial F_{V,1}}{\partial n'_L} & \frac{\partial F_{V,1}}{\partial p'_1} & \dots & \frac{\partial F_{V,1}}{\partial p'_L} \\
 \vdots & \ddots & \vdots & \vdots & \ddots & \vdots & \vdots & \ddots & \vdots \\
 \frac{\partial F_{V,L}}{\partial \psi'_1} & \dots & \frac{\partial F_{V,L}}{\partial \psi'_L} & \frac{\partial F_{V,L}}{\partial n'_1} & \dots & \frac{\partial F_{V,L}}{\partial n'_L} & \frac{\partial F_{V,L}}{\partial p'_1} & \dots & \frac{\partial F_{V,L}}{\partial p'_L} \\
 \frac{\partial F_{n,1}}{\partial \psi'_1} & \dots & \frac{\partial F_{n,1}}{\partial \psi'_L} & \frac{\partial F_{n,1}}{\partial n'_1} & \dots & \frac{\partial F_{n,1}}{\partial n'_L} & \frac{\partial F_{n,1}}{\partial p'_1} & \dots & \frac{\partial F_{n,1}}{\partial p'_L} \\
 \vdots & \ddots & \vdots & \vdots & \ddots & \vdots & \vdots & \ddots & \vdots \\
 \frac{\partial F_{n,L}}{\partial \psi'_1} & \dots & \frac{\partial F_{n,L}}{\partial \psi'_L} & \frac{\partial F_{n,L}}{\partial n'_1} & \dots & \frac{\partial F_{n,L}}{\partial n'_L} & \frac{\partial F_{n,L}}{\partial p'_1} & \dots & \frac{\partial F_{n,L}}{\partial p'_L} \\
 \frac{\partial F_{p,1}}{\partial \psi'_1} & \dots & \frac{\partial F_{p,1}}{\partial \psi'_L} & \frac{\partial F_{p,1}}{\partial n'_1} & \dots & \frac{\partial F_{p,1}}{\partial n'_L} & \frac{\partial F_{p,1}}{\partial p'_1} & \dots & \frac{\partial F_{p,1}}{\partial p'_L} \\
 \vdots & \ddots & \vdots & \vdots & \ddots & \vdots & \vdots & \ddots & \vdots \\
 \frac{\partial F_{p,L}}{\partial \psi'_1} & \dots & \frac{\partial F_{p,L}}{\partial \psi'_L} & \frac{\partial F_{p,L}}{\partial n'_1} & \dots & \frac{\partial F_{p,L}}{\partial n'_L} & \frac{\partial F_{p,L}}{\partial p'_1} & \dots & \frac{\partial F_{p,L}}{\partial p'_L}
 \end{bmatrix}
 \begin{bmatrix}
 \Delta \psi'_1 \\
 \vdots \\
 \Delta \psi'_L \\
 \Delta n'_1 \\
 \vdots \\
 \Delta n'_L \\
 \Delta p'_1 \\
 \vdots \\
 \Delta p'_L
 \end{bmatrix}
 = -
 \begin{bmatrix}
 F_{V,1} \\
 \vdots \\
 F_{V,L} \\
 F_{n,1} \\
 \vdots \\
 F_{n,L} \\
 F_{p,1} \\
 \vdots \\
 F_{p,L}
 \end{bmatrix}
 \quad (2.30)$$

where  $F_v$ ,  $F_n$ , and  $F_p$  label the Poisson, electron continuity, and hole continuity equations respectively. Many of these derivatives equal zero because the equations for the  $i^{th}$  mesh point depend only on the other variables at the same mesh point and nearest neighbor mesh points (e.g.  $F_{V,2}$  has no dependence on  $n_{20}$ ). Therefore, the Jacobian consists of tridiagonal blocks. For example,  $\partial F_v / \partial \psi'$  results in the Laplacian operator, which can be written in matrix form as

$$\begin{bmatrix}
 -2 & 1 & 0 & 0 & \dots & 0 \\
 1 & -2 & 1 & 0 & \dots & 0 \\
 \vdots & \vdots & \vdots & \vdots & \vdots & \vdots \\
 \vdots & \vdots & \vdots & \vdots & \vdots & 0 \\
 0 & \dots & \dots & 0 & \dots & 1 & -2
 \end{bmatrix}
 \quad (2.31)$$

so this will be the upper-left block of the Jacobian. In order to minimize numerical error, where possible, the derivatives should be taken analytically to yield equations that can be evaluated at

each iteration's solution values. In cases where an analytic expression for the derivative cannot be found, numerical derivatives using central-differences are used as follows

$$\frac{\partial F}{\partial x_i} = \frac{F(x_1, \dots, x_i + \epsilon, \dots, x_n) - F(x_1, \dots, x_i - \epsilon, \dots, x_n)}{2\epsilon} \quad (2.32)$$

where  $\epsilon$  is a small perturbation to the value of  $x_i$ .

Each Newton iteration is more computationally expensive than a Gummel iteration since here we solve a  $3n \times 3n$  matrix instead of an  $n \times n$  matrix. Because Newton's method requires initial guesses relatively close to the real solution, one can use Gummel's method first to establish a better initial guess for input into Newton's method. A flow chart of the main elements of a Newton iteration for solar cell simulation is shown in Figure 2.2.

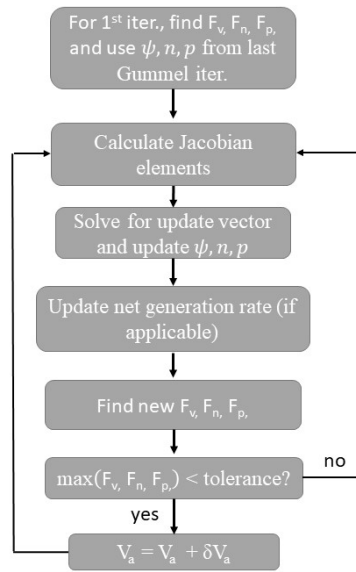


Figure 2.2: Flow chart of the main steps in the Newton-Raphson method.

For the first Newton iteration, at equilibrium conditions, we use the solutions from Gummel's method. First, we calculate the elements of the Jacobian using values of the three functions  $F_V$ ,  $F_n$ , and  $F_p$  from the previous iteration. Next, we solve the matrix equation (Equation 2.30) for the update vector, which we use to update the solutions for  $\psi$ ,  $n$ , and  $p$ . Next, we update the net generation rate. Finally, we recalculate the values of  $F_V$ ,  $F_n$ , and  $F_p$  and check for convergence.

Since these functions should equal zero at the exact solution, the convergence condition is that the values of the functions are less than a tolerance (e.g.  $10^{-12}$ ).

## 2.4 Model Verification

### 2.4.1 Single-Carrier Device in Space-Charge-Limited Current Regime

In order to verify the behavior of our implementations of the drift-diffusion model, the results for a simulation of a single-carrier device in the space-charge-limited current (SCLC) regime were compared with known analytical equations. For these simulations, the influence of carrier traps was neglected. Additionally, since there is only one carrier and traps are ignored, there will be no bimolecular or trap-assisted recombination. Thus, the recombination rate was set to zero in these simulations. An analytical expression for the SCLC of a trap-free single-carrier device with an Ohmic contact, negligible diffusion current, and no photogeneration can be derived from the Poisson-drift-diffusion equations. We will next outline the derivation for a hole-only device (an analogous derivation can be performed for an electron-only device) [27]. The Poisson equation is

$$\frac{\partial^2}{\partial x^2}\psi(x) = -\frac{q}{\epsilon}p(x) \quad (2.33)$$

Since diffusion current is negligible in the SCLC regime (also known as the drift regime), the total hole current is determined solely by the drift contribution

$$J = q\mu p \frac{\partial \psi}{\partial x} \quad (2.34)$$

Rearranging the Poisson equation in terms of  $p$  and substituting into the current equation, we have

$$J = q\mu \left(-\frac{\partial^2 \psi}{\partial x^2}\right) \frac{\epsilon}{q} \frac{\partial \psi}{\partial x} \quad (2.35)$$

We can rewrite the above equation in terms of the electric field ( $\mathcal{E} = -d\psi/dx$ )

$$J = \mu\epsilon \mathcal{E} \frac{\partial \mathcal{E}}{\partial x} = \frac{\mu\epsilon}{2} \frac{\partial(\mathcal{E}^2)}{\partial x} \quad (2.36)$$

or

$$\frac{\partial(\mathcal{E}^2)}{\partial x} = \frac{2J}{\epsilon\mu} \quad (2.37)$$

The general solution is

$$[\mathcal{E}(x)]^2 = ax + b \quad (2.38)$$

Since there is no injection barrier due to the Ohmic contact, the electric field must be zero at  $x = 0$ .

Therefore,

$$\mathcal{E}(x) = \sqrt{ax}^{1/2} \quad (2.39)$$

The potential across the device is given by the integral of the electric field

$$\psi(x) = - \int_0^L \mathcal{E}(x) dx = -\frac{2}{3} \sqrt{ax}^{3/2} + C \quad (2.40)$$

The potential at  $x = 0$  must be 0 due to the Ohmic contact. The potential at  $x = L$  is due to the externally applied voltage,  $V_a$ . Using these boundary conditions, one can find that  $C = 0$  and

$$a = \frac{9 V_a^2}{8 L^3} \quad (2.41)$$

Therefore, we have arrived at the Mott-Gurney equation

$$J = \frac{9}{8} \epsilon \mu \frac{V_a^2}{L^3} \quad (2.42)$$

Note that the same equation applies for electron current in an electron-only device. The Mott-Gurney equation represents the maximal possible current in a semiconductor device and is often used to estimate the carrier mobility of semiconductor materials by fitting the equation to measured JV curves [28]. Combining Equations 2.39 and 2.41, the electric field is

$$\mathcal{E} = \sqrt{\frac{2Jx}{\mu\epsilon}} \quad (2.43)$$

Figure 2.3 shows a comparison of the current density and electric field results of the drift-diffusion simulation of a device in the SCLC regime and the analytical Mott-Gurney equations. We see excellent agreement between the simulation and the analytical expressions in this limit, therefore verifying the correctness of our implementation of the drift-diffusion model. Note that the model was simply set-up to ensure SCLC conditions, and no attempt was made to model a real material. The modeling of real devices is described in the next two chapters.

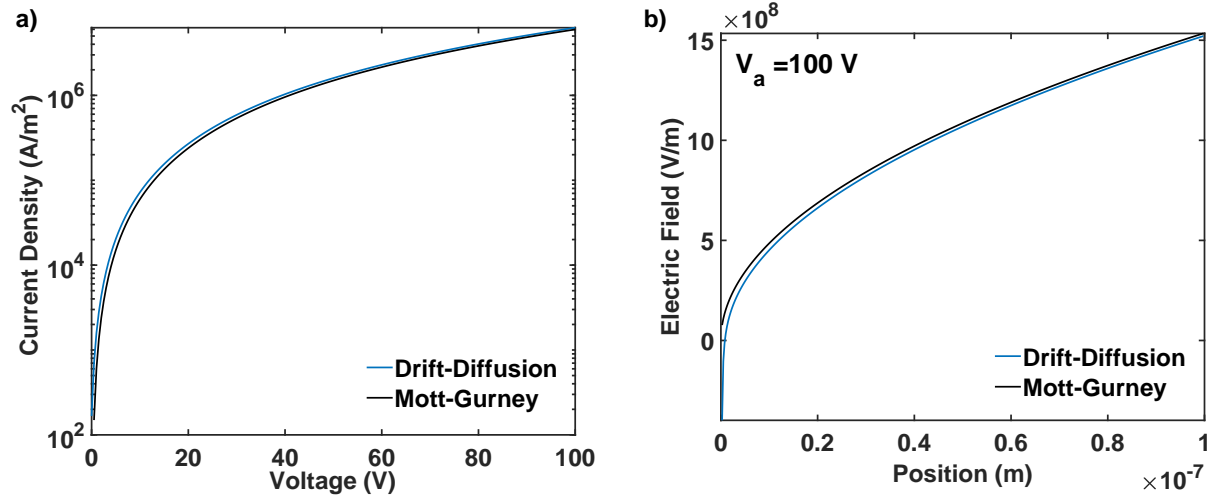


Figure 2.3: Comparison of results from drift-diffusion model of an arbitrary single-carrier device under SCLC conditions with Mott-Gurney analytical equations. a) Current density versus voltage. b) The electric field distribution through the thickness of a device under high voltage.

Figure 2.4 shows the effect of injection barriers ( $\phi_a$ ), which cause the JV behavior to diverge from the SCLC regime. This demonstrates that the approach of fitting JV curves to determine material mobilities will yield inaccurate mobility values if there is a significant injection barrier. (The challenges of determining carrier mobility using analytical expressions for JV curves are discussed in [28]).



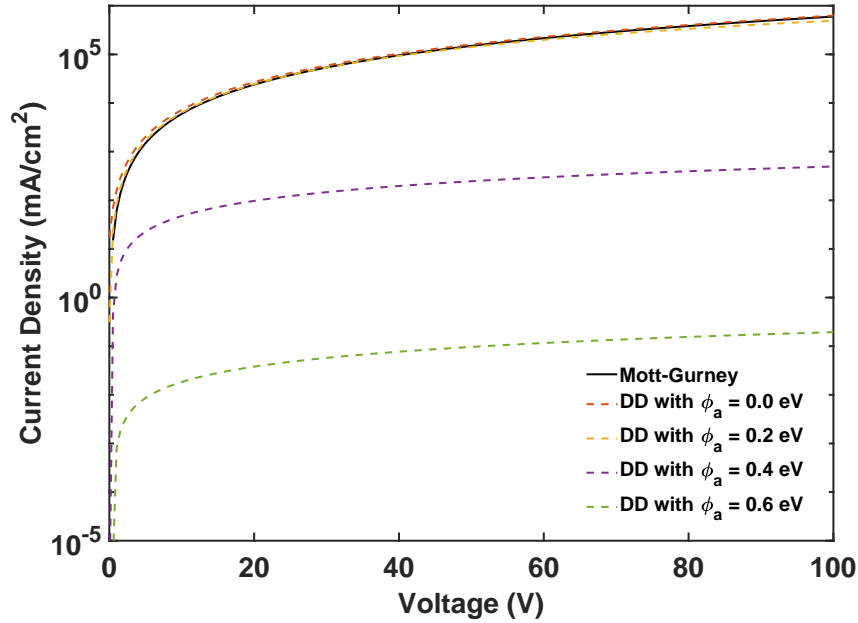


Figure 2.4: Drift-diffusion (DD) model results for JV curves of a hole-only device with varying sizes of injection barriers compared with the Mott-Gurney equation.

## 2.4.2 Two-Carrier Device

A two-carrier (also known as *bipolar*) device supports the transport of both electrons and holes. In a trap-free device, the recombination rate and the locations where it occurs are determined by the probability of electrons and holes finding each other, which is influenced by the carrier mobilities. Figure 2.5(a-d) shows the results of a drift-diffusion simulation of a bipolar device with balanced hole and electron mobilities ( $\mu_p/\mu_n = 1$ ). In this device, the balanced mobilities cause the carrier densities, current densities, electric field, and recombination rate to be distributed symmetrically across the thickness of the device. This symmetry is broken if the mobilities are unbalanced, as shown in Figure 2.5(e-i), where  $\mu_p/\mu_n = 100$ . The higher hole mobilities result in higher carrier density and current for holes than for electrons throughout most of the device. There is a build-up of electrons near the electron-injecting contact due to their low mobility. This causes a higher electric field and a higher recombination rate near the electron contact. These simulation results are qualitatively consistent with previously published results [29].

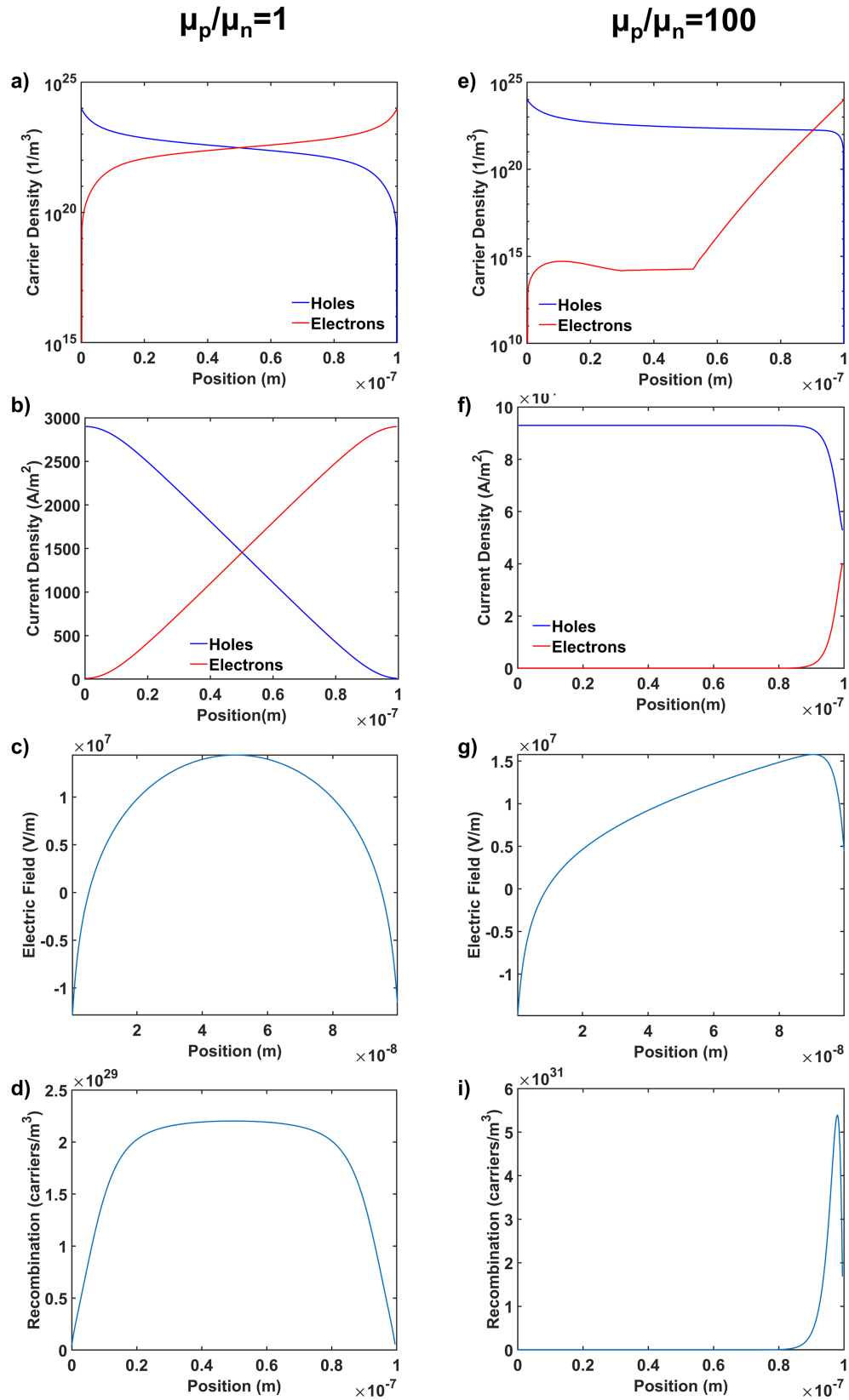


Figure 2.5: Results from drift-diffusion models of single-layer, two-carrier devices: one with uniform mobilities (a-d) and another with 100x larger hole mobility than electron mobility (e-i).

## 2.5 Conclusions

In this chapter, we presented the main numerical methods for solving the 1D drift-diffusion equations. The primary aspect of these methods is to solve the coupled Poisson, drift-diffusion, and continuity equations iteratively until the carrier density profiles converge. We presented two iteration schemes: Gummel's and Newton's method. We also described verification of our implementation of the drift-diffusion model by comparing results from single-carrier device simulations to the Mott-Gurney law. Additionally, we presented example results from simulations of single-layer, two-carrier devices. The two-carrier device results are found to be consistent with our expectations based on an understanding of the device physics. Example Matlab, C++, and Python implementations of the drift-diffusion model are available at <https://github.com/tgolubev>. While the focus of this work is on solar cells, the drift-diffusion model can be applied to a variety of semiconductor devices, including light-emitting diodes (LEDs) and transistors. In the next chapter, we investigate the sometimes problematic convergence behavior of drift-diffusion models and compare the performance of Gummel's and Newton's iterative approaches.

## CHAPTER 3

### IMPROVING CONVERGENCE OF A DRIFT-DIFFUSION MODEL FOR BILAYER ORGANIC SOLAR CELLS

The general drift-diffusion model needs to be modified in order to properly describe the physics in various thin-film solar cells. Here we present an example of this modification for a bilayer organic solar cell (OSC). A bilayer (also known as planar heterojunction) solar cell consists of a donor and acceptor material, charge transport layers, and the contacts (Figure 3.1a). When photons are absorbed by the donor material, this produces excitons (bound excited electron-hole pairs). These excitons can either recombine or dissociate to create free charge carriers, which cause a current in the device. Exciton dissociation is usually described as a two-step process [30]. First, these excitons can diffuse to the donor-acceptor interface where there is a high field due to the energy level offsets between the donor and acceptor materials [31]. At the interface, the field causes the electrons to be transferred from the donor's lowest unoccupied molecular orbital (LUMO) to the acceptor's LUMO, while the holes remain in the donor's highest occupied molecular orbital (HOMO) (Figure 3.1b). These paired charges at the interface are called *polaron pairs* (PPs) or *geminate pairs* or *charge transfer states*. The second step of dissociation is when the charges migrate away from each other due to the built-in field in the device to form free charge carriers. The newly-generated free charge carriers will flow towards the electrodes due to the built-in field. There is also a chance that the PPs recombine since there is a significant Coulomb attraction between the electron and hole in a PP. The competition between recombination and dissociation of PPs is described by rate equations.

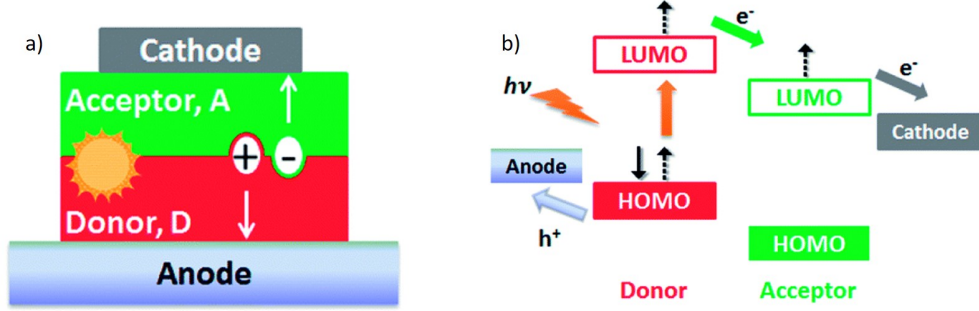


Figure 3.1: Basic architecture (a) and energy level alignment (b) of a bilayer solar cell. Adapted from [32].

### 3.1 DD-BI Model

Two former Ph.D. students in our group, Kanokkorn Pimcharoen and Non Thongprong, developed a 1D drift-diffusion bilayer (DD-BI) model [16, 27] based on the models by Anton Koster [33] and Giebniak, Wiederrecht, Wasielewski, and Forrest (GWFF) [15]. The DD-BI model uses the Gummel method (Figure 2.1b) to solve the Poisson-drift-diffusion system of equations with an added step of recalculating the generation and recombination rates in each iteration.

For simplicity, the mesh size is chosen to be 1 nm, which matches the average separation between electron and hole in PPs at the interface and defines the interface width  $a_0$ . The mesh endpoints are defined to be at 0 and  $L$ , and the interface is defined to be at mesh points  $l$  and  $l + 1$ . Boundary conditions for the potential ( $\psi$ ) and charge densities ( $n$  and  $p$ ) are

$$\psi_L - \phi_0 = V_{bi} - V_a \quad (3.1)$$

$$p_0 = N_{HOMO} \quad p_L = N_{HOMO} \cdot \exp\left(-\frac{E_{LUMO,A} - E_{HOMO,A}}{V_t}\right) \quad (3.2)$$

$$n_L = N_{HOMO} \quad n_0 = N_{LUMO} \cdot \exp\left(-\frac{E_{LUMO,D} - E_{HOMO,D}}{V_t}\right) \quad (3.3)$$

where  $V_{bi}$  is the built-in field (difference between the cathode and anode work functions),  $N_{HOMO}$  and  $N_{LUMO}$  is the density of states of the HOMO and LUMO levels, and  $E$  is the energy level (in eV) of the molecular orbitals, with the subscripts  $A$  and  $D$  denoting the acceptor and donor levels respectively. The smallest value from the boundary conditions is used for the initial values of  $n$  and

$p$  everywhere inside the device. A linear function from  $\psi_0$  to  $\psi_L$  is used for the initial potential. The discretization and solution of the Poisson and drift-diffusion equations is done as described in Sections 2.2 and 2.3.

We also need to consider the energy barriers for carriers crossing the donor-acceptor interface. The energy barriers are simply equal to the energy offsets between the donor and acceptor conduction bands (for electrons) and valence bands (for holes). This can be done by adding the energy barrier height (in dimensionless units) to the numerical derivative of the potential at the interface ( $\delta\psi'_{l+1}$ ) inside of the Bernoulli functions in the continuity equations [34]. Note that since the energy barriers for electrons and holes are different, the  $\delta\psi'$  for holes and electrons in Equations 2.17-2.18 will be different at  $l + 1$ . At applied bias greater than the open-circuit voltage, current flows towards the interface. Since the charge carriers cannot cross the barrier, this leads to an accumulation of carriers of opposite charge at the opposing sides of the interface, which results in both a very high field and a high recombination rate (due to high carrier densities).

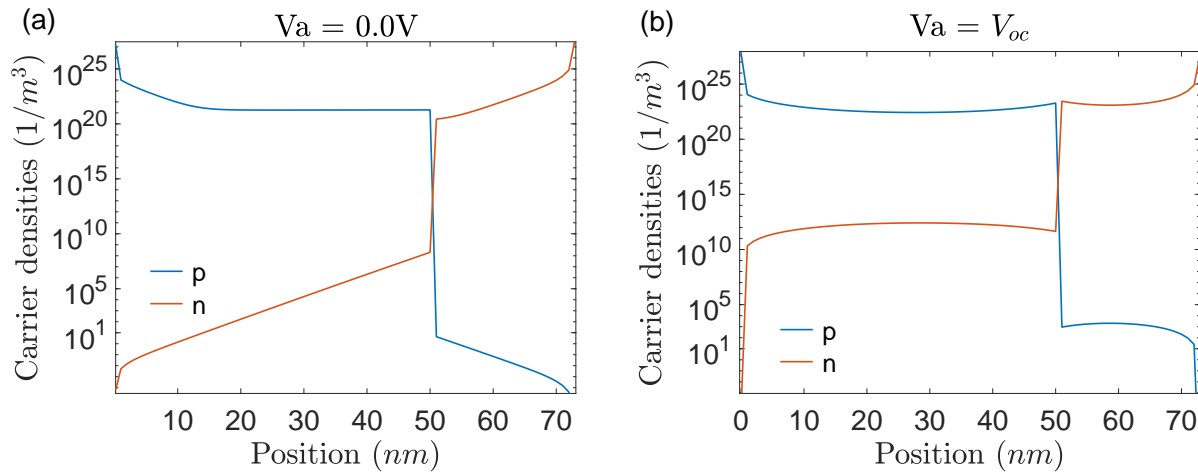


Figure 3.2: Carrier densities at short-circuit (a) and open-circuit (b) conditions for the bilayer device.

Figure 3.2 shows the carrier densities inside the device at short-circuit and open-circuit conditions. The densities at open-circuit conditions increase near the interface due to charge accumulation. There is a larger drop in hole densities than electron densities over the interface since, for this simulation, the energy barrier for holes (difference between the HOMO levels of donor and

acceptor material) was set to be greater than the barrier for electrons (difference between LUMO levels).

The treatment of net generation rate must consider the effects of the bilayer interface. GWWF describe the possible competing processes that can occur at the interface (Figure 3.3) and use detailed balance to derive an expression for the total PP density at the interface ( $\zeta$ ). An exciton current density  $J_x/a_0$  flows to the interface, where  $a_0$  is the separation between the electron and hole in a PP. At the interface, the excitons become PPs where they can either dissociate into free charge carriers with the rate  $k_{PPd}\zeta$  or recombine back into the ground state with the rate  $k_{PPr}\zeta$ . The free charge carriers can recombine back into PPs at the rate  $R$ . Also the PPs can be regenerated from the ground state at the rate  $k_{PPr}\zeta_{eq}$  where  $\zeta_{eq}$  is the PP density in thermal equilibrium (in the dark). Writing a detailed balance equation for these processes, we have

$$\frac{J_x}{a_0} - k_{PPr}(\zeta - \zeta_{eq}) - k_{PPd}\zeta + R = 0 \quad (3.4)$$

Solving for  $\zeta$ , yields

$$\zeta = \frac{J_x/a_0 + k_{PPr}\zeta_{eq} + R}{k_{PPd} + k_{PPr}} \quad (3.5)$$

Once we calculate  $\zeta$ , we can define the net carrier generation rate of electrons ( $U_n$ ) and holes ( $U_p$ ) at the interface as the dissociation rate minus the free carrier recombination rate

$$U_n = U_p = k_{PPd}\zeta - R \quad (3.6)$$

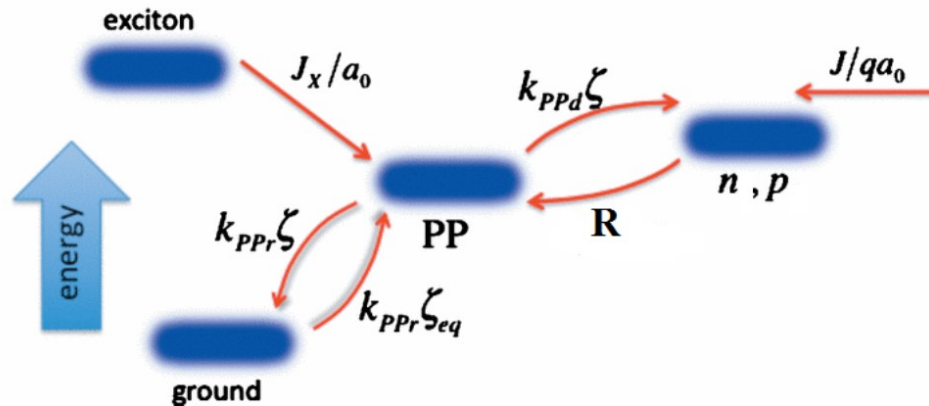


Figure 3.3: Recombination and generation processes at the bilayer interface. Adapted from [15].

In bilayer OSCs, the exciton binding energy is strong; and therefore, we can assume that the thermal dissociation rate of free charge carriers is very small and can be neglected. This means that free carriers are only generated at the interface where there is a strong field that separates the PPs. In our discretization, we define the interface as the region from mesh point  $l$  to mesh point  $l + 1$ . Therefore, our arrays  $U_n(x_i) \equiv U_{n,i}$  and  $U_p(x_i) \equiv U_{p,i}$ , which we use in the continuity equations, only have one non-zero element in each: the element corresponding to mesh point  $l$  for the holes (donor side) and the element corresponding to mesh point  $l + 1$  for the electrons (acceptor side).

In order to calculate  $U_{n(p)}$ , we must have expressions for the various rates in Equation 3.5. In a bilayer OSC, the PP dissociation rate is dependent on the electric field at the interface and can be described by the Onsager-Braun equations [35]

$$k_{PPd} = \frac{3k_{rec} B_1(2\sqrt{-2b})}{4\pi a_0^3 \sqrt{-2b}} e^{-E_b/k_B T}, \quad \text{where} \quad b = \frac{q^3 F_I}{8\pi \epsilon k_B^2 T^2} \quad (3.7)$$

where  $B_1$  is the first-order Bessel function of the first kind,  $F_I = (\psi_{l+1} - \psi_l)/a_0$  is the field at the interface, and  $E_b = q^2/(4\pi\epsilon a_0)$  is the PP binding energy. Note that we define positive field as the field that enhances the dissociation of PPs.  $k_{rec}$  is the Langevin bimolecular recombination coefficient and is given by

$$k_{rec} = \frac{q(\mu_n + \mu_p)}{\epsilon} \quad (3.8)$$

where  $\mu_n$  and  $\mu_p$  are the electron and hole mobilities respectively. For purposes of numerical calculation, the Bessel function is expanded up to the fourth order and Equation 3.7 becomes

$$k_{PPd} = \frac{3k_{rec}}{4\pi a_0^3} e^{-E_b/k_B T} \left[ 1 + b + \frac{b^2}{3} + \frac{b^3}{18} + \frac{b^4}{180} \right] \quad (3.9)$$

The GWWF model improved on these equations by considering the case when the field acts as a barrier to dissociation. When the field points towards the interface, it suppresses the dissociation, and when the field points away from the interface, it enhances the dissociation. This can be described by adding the additional energy  $F_I r_c \cos\theta$  to  $E_b$ , where  $r_c = q^2/(4\pi\epsilon k_B T)$  is the Onsager radius and  $\theta$  is the angle between the vector connecting the PP and the vector normal to the interface. Then the dissociation rate expression is changed by adding this additional energy and integrating



over all possible  $\theta$  values

$$k_{PPd} = \frac{1}{\pi} \int_{-\pi/2}^{\pi/2} \frac{3k_{rec}}{4\pi a_0^3} \exp\left(\frac{-E_b + F_I r_c \cos\theta}{V_t}\right) d\theta \quad (3.10)$$

The integration is only over a semi-circle because, at the interface, the holes will always be on the donor side and electrons on the acceptor side. Note that this equation is only used when the field points in a direction that acts as a barrier to the dissociation. Otherwise, the original Onsager-Braun equation (3.7) is used.

For the recombination of PPs, we use the empirical recombination coefficient equation from paper II of GWWF [36]

$$k_{PPr} = k_{PPr,0} \exp\left(\frac{-qF_I d}{k_B T}\right) \quad (3.11)$$

where  $k_{PPr,0}$  is the coefficient in zero field.

Several models for free carrier recombination can be used. A widely-used model is Shockley-Read-Hall (SRH), which in its simplest form is

$$R_{SRH} = \frac{C_n C_p N_{trap} (np - n_1 p_1)}{C_n (n + n_1) + C_p (p + p_1)} \quad (3.12)$$

where  $n_1$  is the number of electrons in the LUMO band when the electron's quasi-Fermi energy equals the trap energy  $E_t$ , and  $p_1$  is the number of holes in the HOMO band when the hole's quasi-Fermi energy equals  $E_t$ .  $n_1$  and  $p_1$  are given by

$$n_1 = N_{LUMO} \exp\left(-\frac{E_{LUMO} - E_t}{k_B T}\right) \quad \text{and} \quad p_1 = N_{HOMO} \exp\left(-\frac{E_t - E_{HOMO}}{k_B T}\right) \quad (3.13)$$

The quasi-Fermi level is the effective Fermi level for a charge carrier when a semiconductor is not in thermal equilibrium, but the electron population is in equilibrium within the conduction band and the hole population is in equilibrium in the valence band. The "regular" Fermi level is defined as the HOMO level at the temperature of 0 K.

The net carrier generation rates are updated at each iteration as follows. The new voltage (from the solution of the Poisson equation in the case of Gummel's method or solution of the entire system in the case of Newton's method) is used to find the new field at the interface  $F_I$ . The field is then

used to recalculate the PP recombination and dissociation rates,  $k_{PPr}$  and  $k_{PPd}$ . The free carrier recombination rate,  $R$ , is also calculated. Finally  $\zeta$  and  $U_n = U_p$  are calculated using Equations 3.5 and 3.6. The  $U_n$  and  $U_p$  are used in the continuity equations.

### 3.2 Convergence Improvements

In the Fortran implementation of the DD-BI model by Pimcharoen and Thongprong, the solutions for charge densities oscillate from iteration to iteration. The calculation is unable to converge unless mixing (Equation 2.24) is used. With higher applied voltages, progressively smaller mixing factors are required in order to achieve convergence. This is implemented by dividing the mixing factor by two every time the convergence of the Gummel iterations stagnates. Figure 3.4a shows the behavior of a converging solution for carrier density and Figure 3.4b shows the behavior of a solution where the mixing factor is insufficient to achieve convergence. At voltages starting from slightly above the built-in voltage, the algorithm cannot converge at all even with mixing factors as small as  $10^{-5}$ . Another issue related to the instabilities is that at certain voltages, due to very strong oscillations, negative carrier densities are computed.

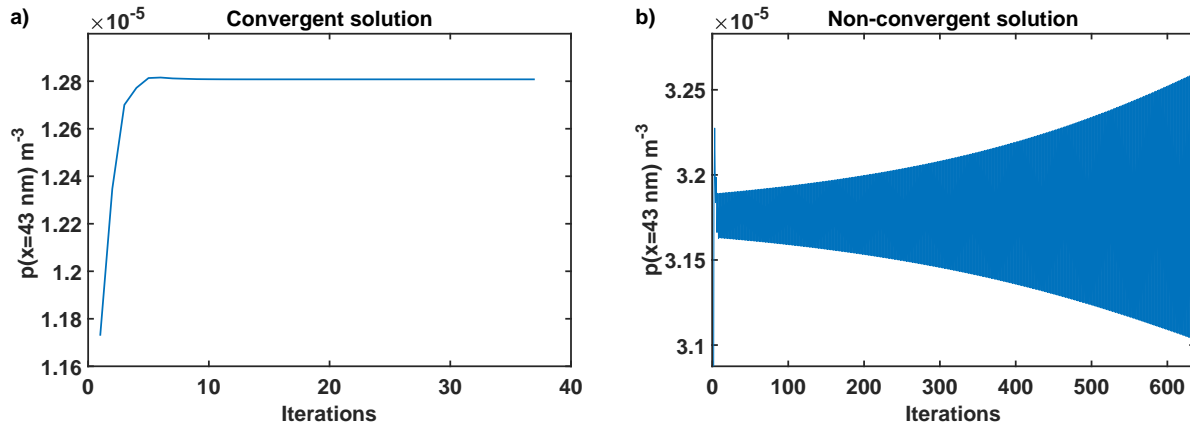


Figure 3.4: The hole density at a point close to the interface inside the device (which exact point does not matter) is plotted versus the number of iterations of the Gummel loop. a) A converging solution, which occurs when the mixing factor is sufficiently small for the applied voltage. b) A solution that cannot converge.

In order to further study these convergence issues, in this work, a Matlab version of the

DD-BI model was implemented. This allowed to take advantage of Matlab's intrinsic matrix-solving functions and confirm that the convergence issues are not due to a mistake in the Fortran implementation. A few improvements to the Gummel iterative method were made and also a version using the Newton-Raphson iterative method was implemented. An improvement to the treatment of negative charge densities is to set each negative element of  $n_{new}$  and  $p_{new}$  to zero. Note that when mixing is applied, the densities after mixing will no longer be zero. This allows for the computation to continue without reducing the mixing factor and repeating the calculations each time there are negatives carrier densities. However, at higher voltages, the convergence stagnates, and the mixing factor still needs to be reduced.

### 3.2.1 Convergence Acceleration through Pulay Mixing

Convergence can be accelerated by applying the Pulay mixing method (also known as *direct inversion in the iterative subspace*), which is widely used for quantum chemistry calculations [37]. Pulay mixing uses a weighted average of several of the previous iterations as the trial solution for the next iteration. Let  $\vec{p}_i$  be the solution at the  $i^{th}$  iteration. We can approximate the solution at iteration  $m + 1$  as a linear combination of the previous trial solutions

$$\vec{p}_{m+1} = \sum_{i=1}^m c_i \vec{p}_i \quad (3.14)$$

Now we expand each trial solution as the exact solution  $\vec{p}_{exact}$  plus the error between the trial and exact solution  $\vec{e}_i$ , so  $\vec{p}_i = \vec{p}_{exact} + \vec{e}_i$ . Substituting into Equation 3.14, we have

$$\vec{p}_{m+1} = \vec{p}_{exact} \sum_{i=1}^m c_i + \sum_{i=1}^m c_i \vec{e}_i \quad (3.15)$$

Therefore, in order for  $\vec{p}_{m+1}$  to be close to the exact solution, we need

$$\sum_{i=1}^m c_i = 1 \quad \text{and} \quad \sum_{i=1}^m c_i \vec{e}_i = 0 \quad (3.16)$$

In other words, we would like to minimize  $\sum_{i=1}^m c_i \vec{e}_i$  under the constraint  $\sum_{i=1}^m c_i = 1$ . This can be done using the Lagrange multiplier method with the Lagrangian

$$\mathcal{L} = \left| \sum_{i=1}^m c_i \vec{e}_i \right|^2 - \lambda \left( \sum_{i=1}^m c_i - 1 \right) \quad (3.17)$$

where  $\lambda$  is the multiplier. Taking the partial derivatives with respect to the coefficients  $c_i$  and  $\lambda$  and setting them to zero results in  $m + 1$  equations, which can be written as a matrix equation

$$\begin{bmatrix} B_{11} & B_{12} & \cdots & B_{1m} & -1 \\ \vdots & \vdots & \ddots & \vdots & \vdots \\ B_{m1} & B_{m2} & \cdots & B_{mm} & -1 \\ -1 & -1 & \cdots & -1 & 0 \end{bmatrix} \begin{bmatrix} c_1 \\ \vdots \\ c_m \\ \lambda \end{bmatrix} = \begin{bmatrix} 0 \\ \vdots \\ 0 \\ -1 \end{bmatrix} \quad (3.18)$$

where  $B_{ij} = \langle \vec{e}_i | \vec{e}_j \rangle$  is the scalar product of the error vectors. Now since we do not know the actual error from exact solution, we approximate it as the change in the trial solution between successive iterations  $\vec{e}_i = \vec{p}_i - \vec{p}_{i-1}$ . Solving the above matrix equation for the  $c_i$  coefficients, we then define the solution at the next iteration as  $p_{m+1} = \sum_i^m c_i \vec{p}_i$ . In practice, only a few previous iterations are used in the sum.

With Pulay mixing, we found that the Gummel scheme requires about 20% fewer iterations to converge than with linear mixing. However, the mixing factors still need to be reduced at higher voltage, and the voltage at which the program no longer converges is the same as when linear mixing is used.

### 3.2.2 Newton vs. Gummel Iterative Methods

Literature claims that the reason for the observed convergence difficulties in drift-diffusion models at higher voltages is due to use of the Gummel method, which decouples the equations [25]. At high voltages, the equations are strongly coupled. For example, a small change in the voltage significantly changes the net generation rates and currents. In the literature, it is recommended to use Newton's method for cases of high applied bias [17]. Here, Newton's method for drift-diffusion was implemented as described in Section 2.3.2 and the convergence properties of the method were investigated. Analytic expressions were used for all of the derivatives in the Jacobian (Equation 2.30), except for the derivatives of the net generation rates, which were found numerically by Equation 2.32.

For Newton's method, a damping (also known as relaxation) factor needs to be used to achieve convergence. The damping factor is simply a number less than one that scales the correction vector in a Newton iteration to prevent oscillating solutions, which can happen when the correction overshoots the value of the true solution. This is analogous to the mixing factors that we used for Gummel's method. For the P3HT:PCBM bilayer device we studied, the  $V_{oc}$  is around 0.69 V, so voltages above this are in a region where the device no longer produces any power. Above 0.69 V, the current now flows into the interface, causing a large build-up of charge. This causes a highly negative recombination rate at the interface, which rapidly becomes more negative with higher voltage. At this point, the device is approaching the breakdown limit, with the current densities at 1.0 V becoming  $1000 \text{ A/m}^2$ . Under these conditions, a physical device would most likely either overheat or the built-up electrons and holes at the interface would have enough energy to overcome the energetic step and spill over into the other half of the device.

Figure 3.5 shows an analysis of the convergence behaviors of the Gummel and Newton methods when applied for the simulation of the bilayer device. We see that both Gummel's and Newton's method can converge with a mixing factor of 60% for low voltages, but Gummel's method requires a reduction of the mixing factor at  $V_a = 0.62 \text{ V}$ . Comparing the number of iterations required for convergence to a tolerance of  $5 \times 10^{-13}$ , we see that the number of iterations is similar for lower voltages, but at higher voltages, Gummel's method requires many more iterations. This is related to the lower mixing factor needed. The numerous spikes occur near the points where the solutions are no longer converging, which are followed by a decrease in the mixing to allow for convergence. Mixing was decreased once there were more than 1000 iterations where the error increased.

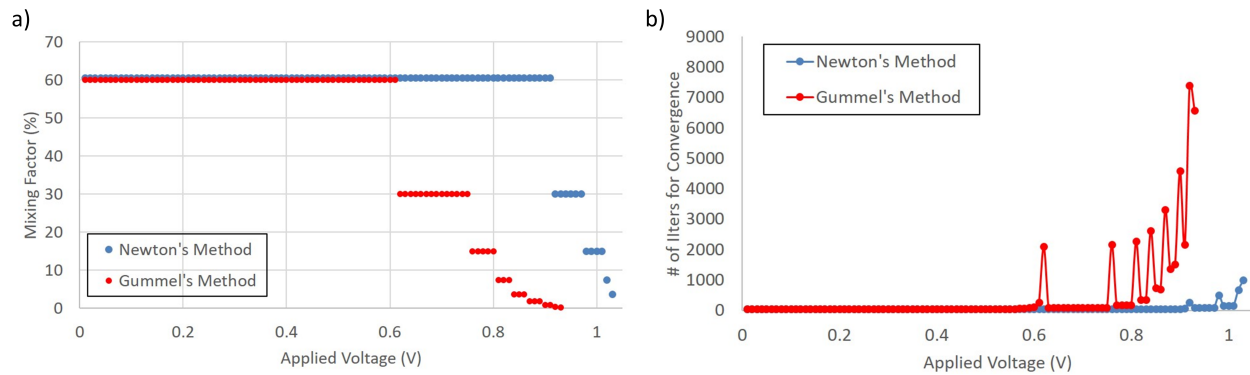


Figure 3.5: Comparison of convergence behaviors between Gummel and Newton methods. a) Mixing factor needed to achieve convergence. b) Number of iterations required to converge.

These models are not computationally expensive, and calculations can be easily done on a standard personal computer (Windows 10 laptop with 8GB RAM and Intel i7-6820HQ CPU at 2.70 GHz base speed and overclocked up to 3.3 GHz). CPU times for the Matlab implementation of these models are reported below. (Implementations in C, C++ or Fortran are expected to be significantly faster). Each iteration of the Gummel method takes only 0.02 – 0.035 seconds. Therefore, even with the large number of iterations required for convergence, an entire calculation of a JV curve sweeping over applied voltages from 0 V to 0.8 V with 0.01 V steps takes only about 4 minutes. For the Gummel method, most of the CPU time per iteration is spent on the recalculation of the net generation rate because this requires evaluation of several non-trivial equations, including integrals that are computed numerically.

Newton's method requires significantly more CPU time per iteration. For the same bilayer model, one Newton iteration takes about 0.25 – 0.65 seconds (lower time for lower voltages). This ten-fold increase over the Gummel method is due to having to calculate all of the partial derivatives for the Jacobian elements and also having to solve a  $3n \times 3n$  matrix instead of three  $n \times n$  matrices. The number of iterations required to converge depends on the damping factor that is used. The same simulation from 0 V to 0.8 V with 0.01 V steps took 794 seconds with Newton's method and 240 seconds with Gummel's method. Thus, for the generation of JV curves within the operating range of a solar cell, Gummel's method is more efficient.

### 3.2.3 Slotboom Variables Approach

During the process of designing ways to improve the algorithm, an alternative approach was investigated which did not yield improved results. Nevertheless, it is overviewed here for completeness of the analysis of possible variations in computational techniques. The Slotboom approach [38] was introduced as an alternative to Scharfetter-Gummel discretization. In this approach, the drift-diffusion equations are rewritten as

$$J_n = qNV_t\mu_n \frac{dF_n}{dx} e^{\psi/V_t} \quad \text{and} \quad J_p = -qNV_t\mu_p \frac{dF_p}{dx} e^{-\psi/V_t} \quad (3.19)$$

where

$$F_n = e^{-\varphi_n/V_t} \quad \text{and} \quad F_p = e^{\varphi_p/V_t} \quad (3.20)$$

and  $\varphi_n$  and  $\varphi_p$  are the electron and hole quasi-Fermi potentials given by

$$\varphi_n = \psi/V_t - \ln(n/N) \quad \text{and} \quad \varphi_p = \psi/V_t + \ln(p/N) \quad (3.21)$$

Note that Equations 3.20 and 3.21 can be combined as

$$F_n = \frac{n}{N} e^{-\psi/V_t} \quad \text{and} \quad F_p = \frac{p}{N} e^{\psi/V_t} \quad (3.22)$$

When discretizing the continuity equations, we get

$$\mu_{n,i+1}(F_{n,i+1} - F_{n,i})e^{\psi_{i+1}/V_t} - \mu_{n,i}(F_{n,i} - F_{n,i-1})e^{\psi_i/V_t} = -\frac{(\delta x)^2}{V_t N} U_{n,i} \quad (3.23)$$

$$\mu_{p,i+1}(F_{p,i+1} - F_{p,i})e^{-\psi_{i+1}/V_t} - \mu_{p,i}(F_{p,i} - F_{p,i-1})e^{-\psi_i/V_t} = -\frac{(\delta x)^2}{V_t N} U_{p,i} \quad (3.24)$$

Therefore, the matrix equations will now be solved for  $F_n$  and  $F_p$  instead of  $n$  and  $p$ . A benefit of this approach over Scharfetter-Gummel discretization is the removal of the approximation using Bernoulli functions, yielding more elegant expressions for the equations. While this is useful for analytical calculations, when attempting to solve these numerically, the  $e^{\psi}$  terms often cause overflow or underflow errors. Note that in the Scharfetter-Gummel method this is avoided because the exponentials are  $e^{\delta\psi}$  (using the difference in potential between neighboring mesh points),

which, provided that the mesh is small enough, will result in a reasonable magnitude exponential. An interesting observation is that if we substitute the expressions for  $F_n$  and  $F_p$  into Equations 3.23 and 3.24, we can get a matrix equation for  $n$  and  $p$  that, while appears similar to the ones from Scharfetter-Gummel's discretization, does not have any Bernoulli functions. The terms generating the matrices will be

$$\mu_{n,i}e^{(\psi'_i-\psi'_{i-1})}n'_{i-1} - (\mu_{n,i+1}e^{(\psi'_{i+1}-\psi'_i)} + \mu_{n,i})n'_i + \mu_{n,i+1}n'_{i+1} = -\frac{(\delta x)^2}{V_i N}U_{n,i} \quad (3.25)$$

$$\mu_{p,i}e^{(\psi'_{i-1}-\psi'_i)}p'_{i-1} - (\mu_{p,i+1}e^{(\psi'_{i+1}-\psi'_i)} + \mu_{p,i})p'_i + \mu_{p,i+1}p'_{i+1} = -\frac{(\delta x)^2}{V_i N}U_{p,i} \quad (3.26)$$

Using these equations for the bilayer device simulation, gave almost identical results (to several decimal places) to those from the Scharfetter-Gummel discretization. There was no significant difference in the convergence properties when compared to using Scharfetter-Gummel discretization. It appears that the Slotboom variables approach is a valid and usable alternative to the discretization as long as one substitutes back the definitions of  $F_n$  and  $F_p$  as done above.

### 3.3 Conclusions

In this chapter, we investigated the impact of several numerical techniques on the convergence behavior of a 1D drift-diffusion model for bilayer organic solar cells. We found that Pulay mixing accelerates the convergence of Gummel iterations by about 20%, but does not resolve the divergences experienced at higher applied voltages. When the coupled Newton's method was used, the model could use higher mixing (relaxation) values and converge at higher applied voltages. This supports the idea that the convergence difficulties are due to a strong coupling of the bilayer drift-diffusion equations at higher applied voltages due to the build-up of space charge at the bilayer interface. In this situation, the decoupled Gummel iteration approach leads to oscillations and instabilities, while Newton's method suppresses such oscillations by solving the entire system simultaneously. The Slotboom variables discretization approach, which avoids the need to use Bernoulli functions, was found to lead to overflow and underflow errors unless the equations are reformulated to solve for the carrier densities. Using the Slotboom variables in this way, gave almost identical simulation



results to the more-traditional Scharfetter-Gummel discretization approach, but did not improve convergence. The results of these investigations can help one select an appropriate discretization and iteration scheme to use for each drift-diffusion problem. Pulay mixing can be used to improve performance, Newton's method is desirable for situations where the equations become highly coupled, and Slotboom variables may be chosen as a way to simplify the implementation of the matrix equations.

## CHAPTER 4

### DRIFT DIFFUSION MODELING OF PEROVSKITE SOLAR CELLS

Perovskite solar cells are thin-film cells based on hybrid halide perovskites, the most common being  $\text{CH}_3\text{NH}_3\text{PbX}_3$  where X is Cl, Br, I, or a mixture of these. They have attracted great interest in recent years [39–43] due to their lower material and production costs, as well as rapid improvements in efficiencies to above 25% [44]. These materials have favorable properties such as a direct bandgap, high absorption coefficients, and high charge mobilities [45, 46]. The devices can be made in both planar heterojunction and bulk heterojunction (also known as mesoporous) architectures. This chapter discusses the application of the drift-diffusion model to planar perovskite solar cells.

A typical planar perovskite solar cell has a perovskite absorber layer sandwiched between an electron transport layer (ETL) and a hole transport layer (HTL). The perovskite layer absorbs light, which results in the photogeneration of free electrons and holes. The charge carriers will diffuse from higher to lower concentration and drift due to the device's built-in electric field. Electrons will, on average, move towards the ETL and holes towards the HTL. The ETL and HTL's primary role is to transport the respective carriers to the electrodes while blocking the opposite carrier type with energy barriers. Holes are unlikely to pass into the ETL and electrons are unlikely to pass into the HTL. This results in very low hole densities in the ETL and very low electron densities in the HTL, which greatly reduces free carrier recombination. Therefore, in the model, we can assume that there is no recombination in the transport layers.

#### 4.1 Numerical Model

To model perovskite solar cell devices, we use a one-dimensional drift-diffusion (1D-DD) approach based on the model reported in Sherkar et al. [47] to self-consistently solve the Poisson, continuity, and drift-diffusion equations using Gummel iterations together with Scharfetter-Gummel discretization, as described in Chapters 2 and 3. The device is discretized into a one-dimensional mesh with a grid size of 0.25 nm, with the anode and cathode located at  $x = 0$  and  $x = L$ ,

respectively. When discretizing the Poisson equation, we use Equation 2.9 for mesh points located at the boundaries between two layers. The dielectric constant of perovskite is generally much higher than that of the transport layer materials, causing a smaller electric field in the perovskite than in the transport layers. The implementation of the energy barriers between layers is done in the same way as in the DD-BI model, namely, by modifying the derivative of the potential  $\delta\psi'$  at the interfaces (see Section 3.1).

A significant difference between perovskites and organic bilayer devices (discussed in Chapter 3) is that perovskites have no donor-acceptor interface where polaron pair formation and separation occurs. In perovskites, the exciton binding energy is on the order of the thermal energy of the carriers [48]; therefore, excitons separate into free charge carriers throughout the device. This means that in simulation, the free carrier generation rate can be treated as directly related to the absorption density of photons without calculating any exciton densities.

Both radiative and non-radiative recombination of carriers decrease device performance. Radiative recombination is the annihilation of an electron from the conduction band with a hole in the valence band, which results in the emission of a photon. Non-radiative recombination (also known as trap-assisted recombination) occurs through a defect or trap, which is an energy level in the bandgap. The trap can capture either an electron or hole (depending on the trap's energy level), which can recombine with a hole in the valence band or an electron in the conduction band, respectively. We include both radiative and non-radiative (trap-assisted) carrier recombination. Radiative recombination is modeled by Langevin bimolecular recombination with the recombination rate given by

$$R_b = k_b(np - n_i^2) \quad (4.1)$$

where  $k_b$  is the bimolecular recombination constant and  $n_i$  is the intrinsic carrier density. Bimolecular recombination is assumed to occur only in the perovskite layer. It is not considered in the transport layers because of the very low density of minority carriers in those layers which makes the recombination rate many orders of magnitude less than in the perovskite. Non-radiative trap assisted recombination is assumed to occur only in 5 nm thick regions inside the perovskite layer

near the HTL and ETL interfaces and is described by the Shockley-Read-Hall equation (3.12). The trap energies are assumed to be located in the middle of the bandgap since this energy gives the most effective recombination [49]. As in Sherkar et al., the traps are assumed to have neutral charge.

## 4.2 Model Validation

The 1D-DD model for planar perovskites was validated by comparing to the literature results from Sherkar et al. The devices studied use gold as the cathode and poly(3,4-ethylenedioxythiophene):poly(styrenesulfonic acid) (PEDOT:PSS) and indium tin oxide (ITO) as the anode. The HTL is negatively doped poly[N,N-bis(4-butylphenyl)-N,N-bis(phenyl)benzidine (polyTPD) and the ETL is positively doped [6,6]-phenyl C<sub>61</sub>-butyric acid methylester (PCBM). Figure 4.1 shows the device architecture.

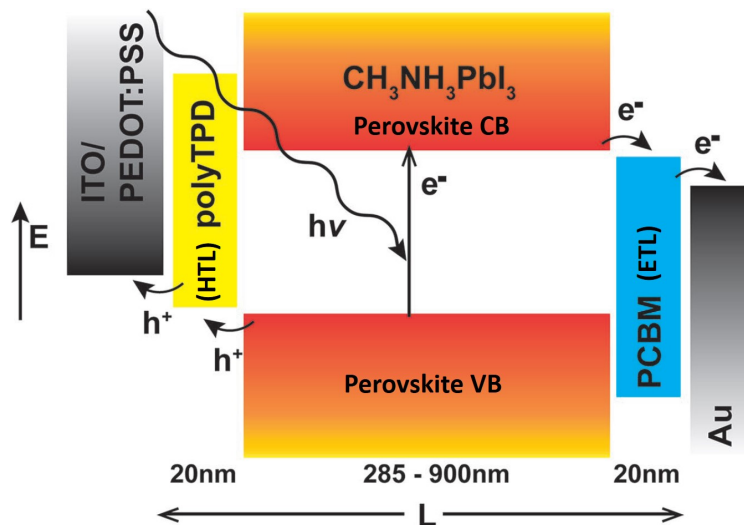


Figure 4.1: Device structure of planar heterojunction perovskite solar cell modeled by Sherkar et al. [47].

The effects of various physical parameters on device performance can be studied with the help of this drift-diffusion device model. From simple physical arguments, we expect an efficient perovskite solar cell to have high carrier mobility in the perovskite layer, low trap densities, good blocking of the minority carrier at the transport layers, a high built-in field, and low injection barriers. High

carrier mobility leads to faster extraction of carriers from the perovskite, which reduces the carrier density and thus reduces recombination. We would also like to have materials with minimum trap densities where trap-assisted recombination could occur. Good blocking of minority carriers by the transport layers prevents recombination near the electrodes. A high built-in field creates a stronger drift current for the separation of electrons and holes in the perovskite layer, which leads to faster charge extraction. We can use our model to test these arguments with numerical experiments.

Figure 4.2 shows the effect of the perovskite mobility on the JV curve and the power conversion efficiency  $\eta$ . The most considerable effect of lower mobility is the reduction of fill factor, which reduces the maximum power output and thus efficiency.  $J_{sc}$  is also reduced with lower mobility since fewer free carriers reach the electrodes. Notice that above a mobility of  $0.5 \text{ cm}^2/\text{Vs}$ , further increasing the mobility does not have much of an effect on the JV curve. This indicates the existence of some mobility threshold that ensures that carriers are able to reach the electrodes.

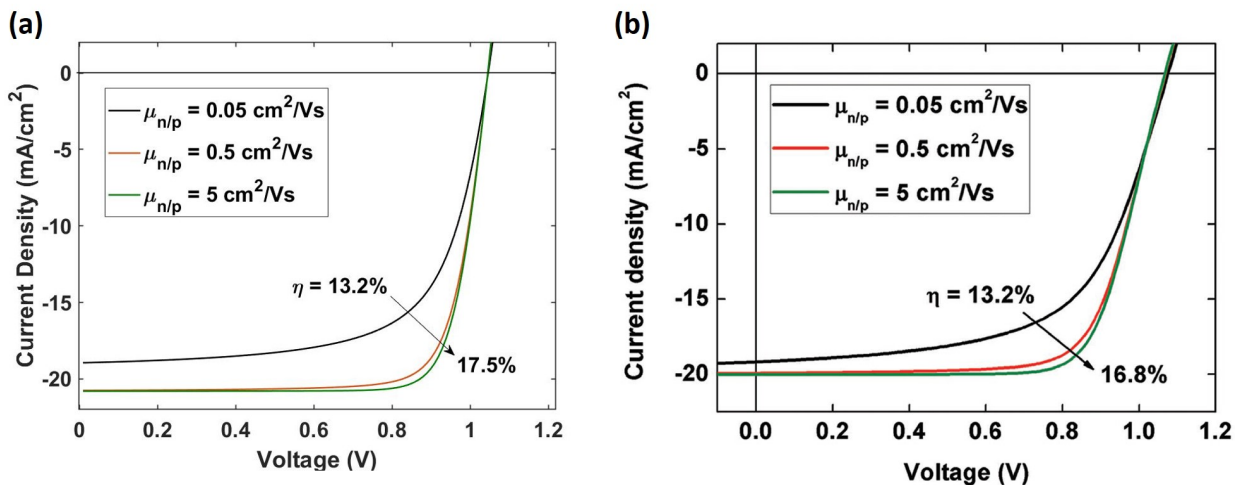


Figure 4.2: Simulated JV curves for different carrier mobilities in perovskite layer from this work (a), and Sherkar et al. (b).

Figure 4.3 shows the effect of trap densities at the HTL/perovskite and perovskite/ETL interfaces. The interfaces are assumed to be 5 nm in width. Note that the surface trap density values are converted to volume trap densities (by dividing by the 5 nm interface width) before use in the Shockley-Read-Hall equation [50]. Higher trap densities reduce fill factor,  $V_{oc}$ , and  $J_{sc}$ . Notice

that the trap density at the perovskite/ETL interface ( $N_{trap}$ ) has a much smaller effect than the traps at the HTL/perovskite interface. This is because the light is incident from the HTL side, and therefore, there is a much higher photogenerated free carrier density near the HTL, so the traps can significantly reduce the free carrier density. Therefore, when designing a perovskite solar cell, choosing materials and manufacturing techniques that reduce traps at the HTL/perovskite interface is important.

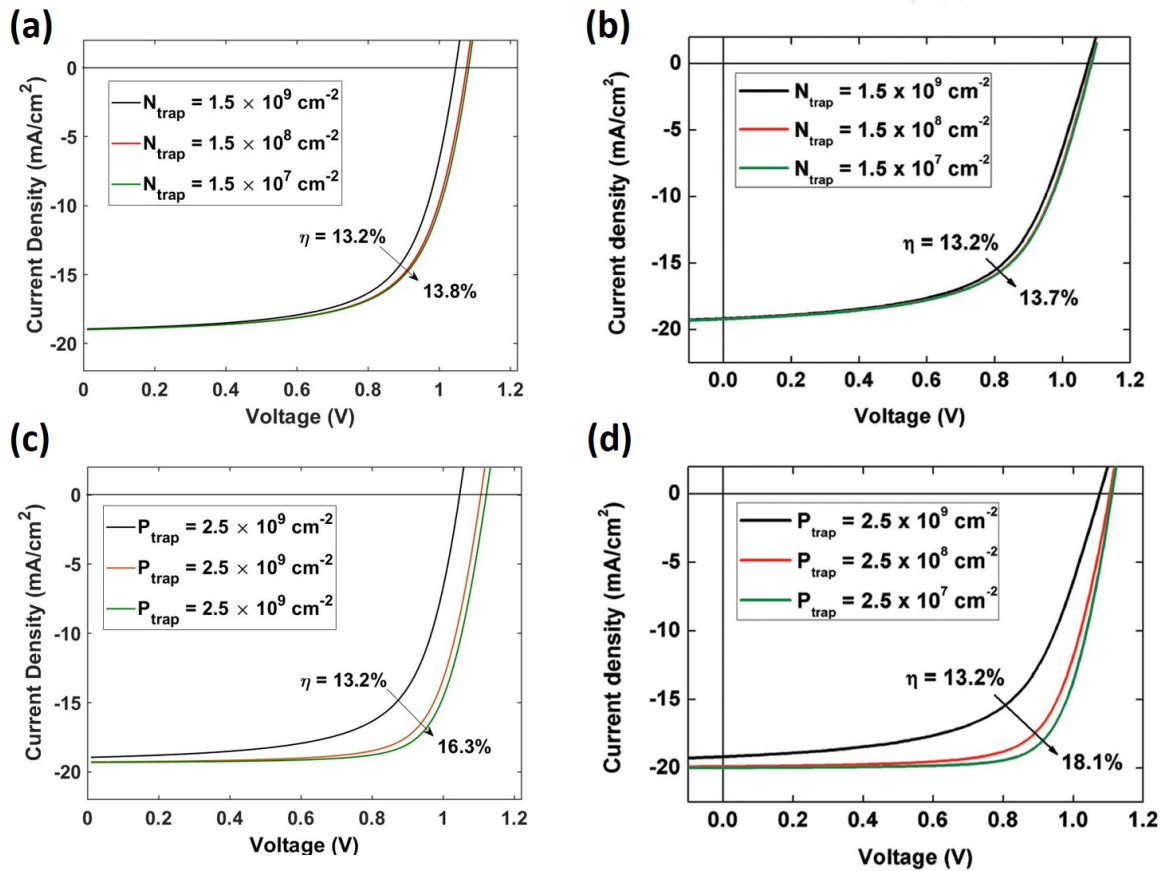


Figure 4.3: Simulated JV curves for different trap densities at HTL/perovskite interface (a, b) and ETL/perovskite interface (c, d). Results from this work's model (a, c) are compared with results from Sherkar et al. (b, d).

The built-in voltage ( $V_{bi}$ ) and electric field are determined by the work function difference between the cathode and anode. Therefore, lowering the injection barriers at the electrodes will increase  $V_{bi}$ . Figure 4.4 shows the effect of injection barriers on the JV curve. As expected, zero injection barriers are predicted to give the best performance.

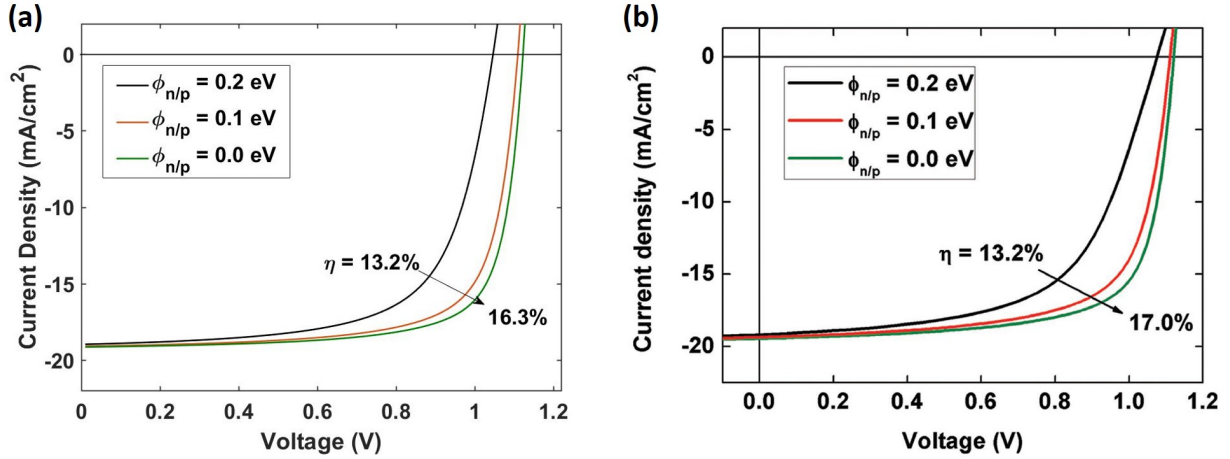


Figure 4.4: Simulated JV curves for different injection barriers at the anode and cathode ( $\phi_a$  and  $\phi_c$  respectively) on the JV curve from this work's model (a), and from Sherkar et al. (b).

In this section, we have confirmed that our 1D-DD model can reproduce results from a validated model in the literature. We have also shown an example of how such a model can be used to understand the effects of carrier mobility, trap density, and injection barriers on device performance. In the next section, we describe the application of this validated 1D-DD model to explain the physics behind experimentally-observed drastic performance differences in perovskite devices with and without fullerene layers.

### 4.3 Understanding the Impact of $C_{60}$ at the Interface of Perovskite Solar Cells

There is increasing interest in the application of fullerene compounds to perovskite photovoltaics [51, 52]. Recently, Liu et al. [53] observed that an ultrathin fullerene ( $C_{60}$ ) layer could have a drastic impact on the performance of planar perovskite solar cells. Through a combination of fluorescence microscopy and impedance spectroscopy, they showed that the main role of the  $C_{60}$  is to efficiently extract electrons from the perovskite film. They demonstrated that even an ultrathin vapor-deposited 1 nm  $C_{60}$  layer works efficiently in the devices, while devices without  $C_{60}$  exhibit poor performance.

The device architecture is as follows. The cells use PEDOT:PSS for the hole transport layer and

bathocuproine (BCP) for the electron transport layer. The devices have a 1 nm, 20 nm, or no C<sub>60</sub> layer between the perovskite and BCP layers. All devices have an 80 nm Ag cathode and 100 nm indium tin oxide (ITO) anode. Figure 4.5 shows the interior layer thicknesses and electronic energy levels of the devices, with the rectangles representing the bandgap of the materials. The energy alignment allows electrons to flow from the perovskite to the cathode and holes to flow from the perovskite to the anode. It has been reported that electrons travel through BCP via gap-states which are thought to be caused by diffusion of the Ag into the BCP layer [54–56]. The energy levels of the gap-states, as predicted by our numerical model, are shown within the BCP rectangle.

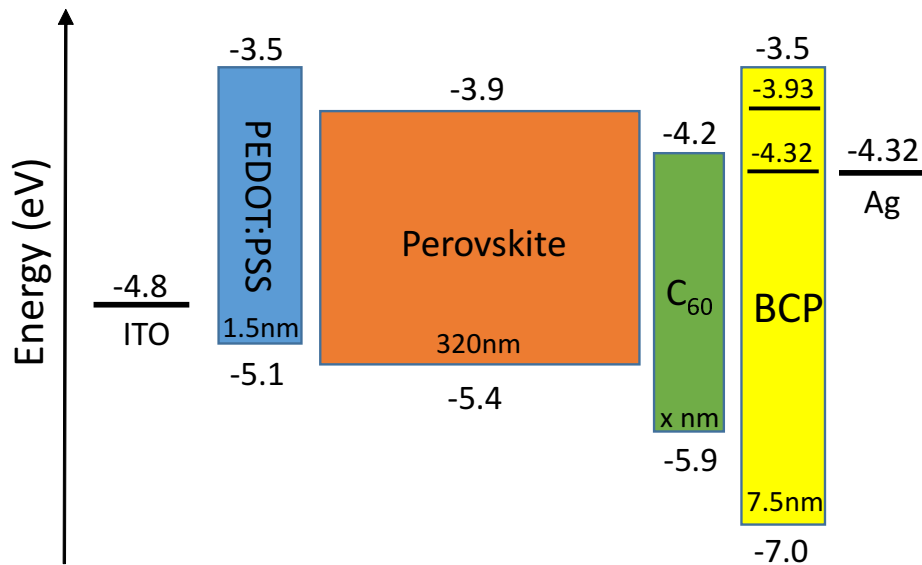


Figure 4.5: Energy levels and thicknesses of the device layers with the rectangles representing the bandgap of the material. The levels were found from a combination of literature values and fitting of the numerical model (more details in Table 4.1). The levels within the BCP bandgap are gap-states due to diffusion of Ag into BCP.

In this work, we provide an explanation for the observed effects of ultrathin C<sub>60</sub> on device performance by use of the drift-diffusion model. The differences in electron extraction with C<sub>60</sub> layer thickness are modeled by a reduced effective carrier mobility in the C<sub>60</sub> layer or at the perovskite/BCP interface (for the devices without C<sub>60</sub>). Our numerical results support the conclusions of Liu et al. regarding the role of C<sub>60</sub> as essential for efficient electron extraction. Based on fitting of the model to the experimental results, the reason for the differences in performance



between the devices with and without C<sub>60</sub> is mostly due to a much lower electron mobility at a perovskite/BCP interface than at a perovskite/C<sub>60</sub> interface. These results help clarify the role of the C<sub>60</sub> layer as part of the ETL in a perovskite solar cell.

Table 4.1 provides the complete set of parameters used for the model with references for parameters taken from literature listed. Less efficient electron transport at the perovskite/BCP interface is modeled by a decreased electron mobility value in a 0.5 nm interface region. For the 1 nm C<sub>60</sub>, less efficient electron transport due to incomplete coverage of C<sub>60</sub> is modeled by a reduced effective mobility for C<sub>60</sub>.

Table 4.1: Complete set of parameters used for the model. References for parameters obtained from literature are listed.

Parameter	Value	Source
Anode (ITO) work function	-4.8 eV	Ref. [57]
HTL (PEDOT) HOMO Level	-5.1 eV	Ref. [58]
HTL (PEDOT) LUMO Level	-3.5 eV	Ref. [58]
Perovskite conduction band minimum	-3.9 eV	Ref. [47, 57, 58]
Perovskite valence band maximum	-5.4 eV	Ref. [47, 57, 58]
ETL (C <sub>60</sub> ) HOMO level	-5.9 eV	Fit
ETL (C <sub>60</sub> ) LUMO level	-4.2 eV	Fit
BCP gap-state levels	-3.93 eV, -4.32 eV	Fit/Ref. [54–56]
BCP HOMO	-7.0 eV	Ref. [59]
Cathode (Ag) work function	-4.32 eV	Ref. [59]/Fit
Density of states (DOS)	$8.1 \times 10^{24} \text{ m}^{-3}$	Ref. [47]
Perovskite relative permittivity	24.1	Ref. [47]
PEDOT:PSS relative permittivity	3.0	Ref. [47]
C <sub>60</sub> relative permittivity	4.25	Ref. [60]
BCP relative permittivity	4.25	Fit
Carrier mobility in perovskite	$10^{-4} \text{ m}^2\text{V}^{-1}\text{s}^{-1}$	Ref. [61]/Fit
Carrier mobility in PEDOT:PSS	$4.5 \times 10^{-6} \text{ m}^2\text{V}^{-1}\text{s}^{-1}$	Ref[62]
Carrier mobility in 20 nm C <sub>60</sub>	$1.6 \times 10^{-4} \text{ m}^2\text{V}^{-1}\text{s}^{-1}$	Ref. [58]
Hole mobility in 1 nm C <sub>60</sub>	$1.6 \times 10^{-4} \text{ m}^2\text{V}^{-1}\text{s}^{-1}$	Ref. [58]
Electron mobility in 1 nm C <sub>60</sub>	$1.6 \times 10^{-5} \text{ m}^2\text{V}^{-1}\text{s}^{-1}$	Fit
Carrier mobility in BCP bulk	$2 \times 10^{-9} \text{ m}^2\text{V}^{-1}\text{s}^{-1}$	Fit
Electron mobility at perovskite/BCP interface	$5 \times 10^{-13} \text{ m}^2\text{V}^{-1}\text{s}^{-1}$	Fit
Maximum charge generation rate	$1.97 \times 10^{28} \text{ m}^{-3}\text{s}^{-1}$	Fit
Electron and hole capture coefficients	$10^{-13} \text{ m}^3\text{s}^{-1}$	Ref. [47]
Bimolecular recombination constant	$6 \times 10^{-17} \text{ m}^3\text{s}^{-1}$	Ref. [47]
HTL/perovskite interface trap density	$5 \times 10^{21} \text{ m}^{-3}$	Ref. [47]
Perovskite/ETL interface trap density	$6 \times 10^{20} \text{ m}^{-3}$	Ref. [47]/Fit
PEDOT:PSS thickness	1.5 nm	Ref. [53]
Perovskite thickness	320 nm	Ref. [53]
BCP thickness	7.5 nm	Ref. [53]
Grid spacing	0.25 nm	

Charge generation profiles were determined using an open-source transfer-matrix optical model [63]. A sample profile for the device without  $C_{60}$  is shown in Figure 4.6.

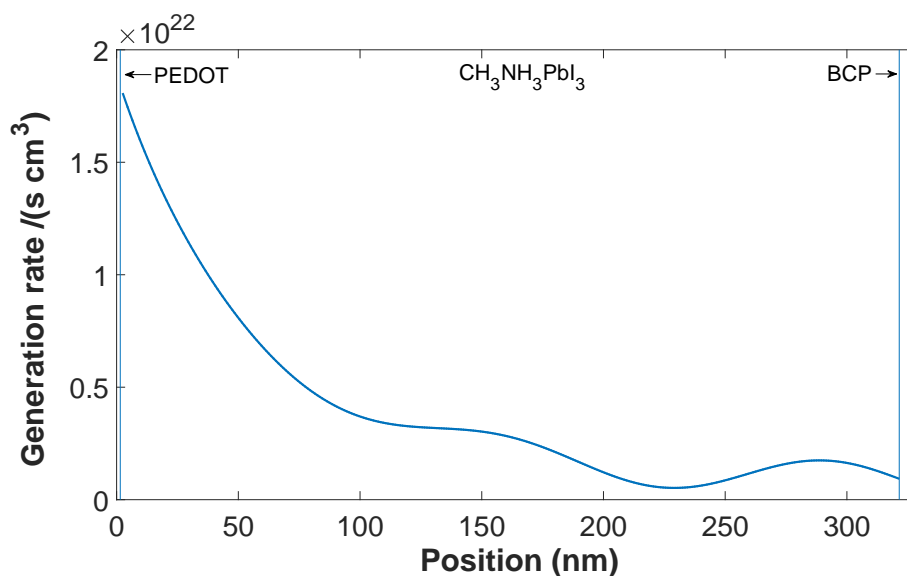


Figure 4.6: Carrier photogeneration rate profile for the device without  $C_{60}$  as determined from the transfer-matrix optical model using the sum over wavelengths 350-750 nm. Position is displayed relative to the beginning of the HTL (PEDOT:PSS) layer.

We find a good agreement between the experimentally measured and numerically predicted current-voltage (JV) curves (Figure 4.7). We see that the  $C_{60}$  layer is essential for good device performance and that a 1 nm  $C_{60}$  layer is sufficient for good performance, with only a small improvement achieved when the layer thickness is increased to 20 nm. The fit to experiment suggests that the electron mobility at a perovskite/ $C_{60}$  interface is significantly higher than at a perovskite/BCP interface (case of no  $C_{60}$ ). This higher mobility models a more efficient extraction of electrons from the perovskite to the ETL.

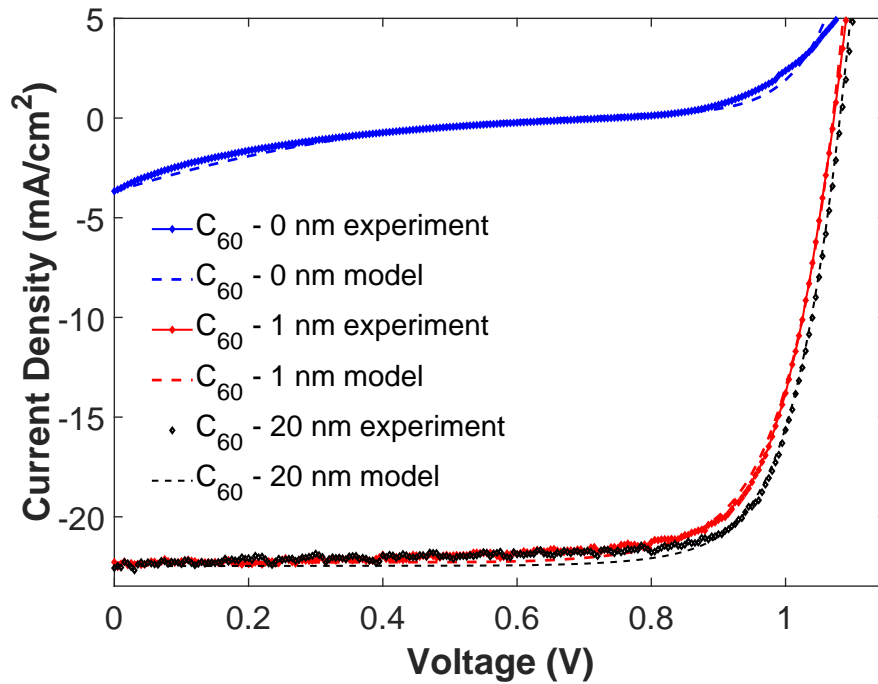


Figure 4.7: Comparison of the JV curve results from the experiment and numerical model.

To determine the reason for the experimentally observed performance loss in the 0 nm  $C_{60}$  devices, the influence of electron mobility and traps at the perovskite/BCP interface was computationally studied (Figure 4.8). For the mobility trials, we set all parameters as in Table 4.1 and only vary the perovskite interface mobility. For testing the effects of the interface trap density, we first raise the perovskite interface mobility to the same value as in the device with 20 nm  $C_{60}$  ( $2 \times 10^{-9} \text{ m}^2/\text{Vs}$ ) to remove the effect of lower mobility, and then vary the trap density. We find that mobility mostly influences the short-circuit current, while trap density mostly influences the open-circuit voltage and fill factor. Figure 4.8a shows how a decrease in perovskite interface mobility significantly affects the short-circuit current and fill factor of the device. For the devices without a  $C_{60}$  layer, fitting the model to the experimental results suggests an electron mobility of  $5 \times 10^{-13} \text{ m}^2/\text{Vs}$ . An increased trap density at the interface (Figure 4.8b) does not result in the drastic short-circuit current loss that is experimentally observed; therefore, the dominant factor is a low interface mobility.

These results support the fluorescence microscopy experiments of Liu et al. which showed

that while adding thin  $C_{60}$  layers to perovskite cause a significant decrease in photoluminescence (PL), placing BCP alone onto perovskite does not significantly change the PL efficiency (neat perovskite films are as bright or brighter with BCP) [53]. A quenched PL intensity indicates a smaller accumulation of electrons. If the improvement in performance due to  $C_{60}$  was due to small molecules passivating defect states, we would expect the PL quenching with BCP to be similar to that of  $C_{60}$ . Since this is not the case, it was concluded that  $C_{60}$  acts to greatly improve the efficiency of electron extraction from perovskite. Similar results were reported in the literature for perovskite devices using  $TiO_2$  as the ETL, where the addition of fullerene compounds to the ETL enhanced electron extraction at the perovskite/ETL interface [64, 65].

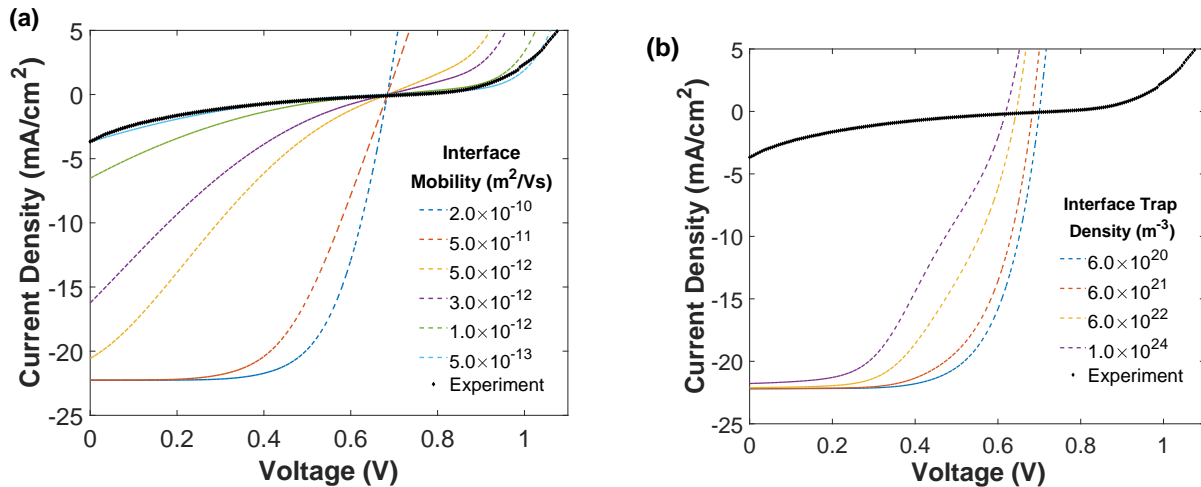


Figure 4.8: JV curves showing the effects of perovskite/BCP interface carrier mobility (a) with ETL trap density set to  $6 \times 10^{20} \text{ m}^{-3}$  and trap density (b) on the 0 nm device with perovskite/BCP interface mobility set to  $2 \times 10^{-9} \text{ m}^2/\text{Vs}$  (the same value as for the 20 nm  $C_{60}$  device). All other parameters were kept the same as in Table 4.1.

We gain more insight into the space-charge effects in these devices by considering the charge density profiles for devices with different  $C_{60}$  thicknesses at zero applied bias (Figure 4.9). In the 0 nm  $C_{60}$  device, due to the low mobility at the perovskite/BCP interface, the electron extraction is poor and results in a lower extraction of electrons than holes from the device, as seen from the low electron density in the BCP layer at the right-hand side of Figure 4.9. This can also be understood as an imbalance in mobilities of the majority charge carrier through their corresponding

transport layer, or equivalently as the addition of an extraction barrier for electrons. The poor electron extraction causes a charge accumulation at the perovskite/BCP interface. In contrast, the devices with  $C_{60}$  have no electron accumulation within the perovskite layer. This supports the fluorescence microscopy measurements done on these devices, which show a much stronger photoluminescence, indicating a larger electron accumulation for the devices without  $C_{60}$  than with  $C_{60}$  [53]. In the devices with  $C_{60}$ , due to the efficient electron extraction from the perovskite, there is a high electron density in the  $C_{60}$  together with a very low hole density and an injection barrier that prevents electrons from moving back into the perovskite. The high electron transfer efficiency also reduces the loss of free carriers due to carrier recombination within the perovskite layer. This means that more electrons can be extracted to the BCP than in the 0 nm  $C_{60}$  device, resulting in a higher current.

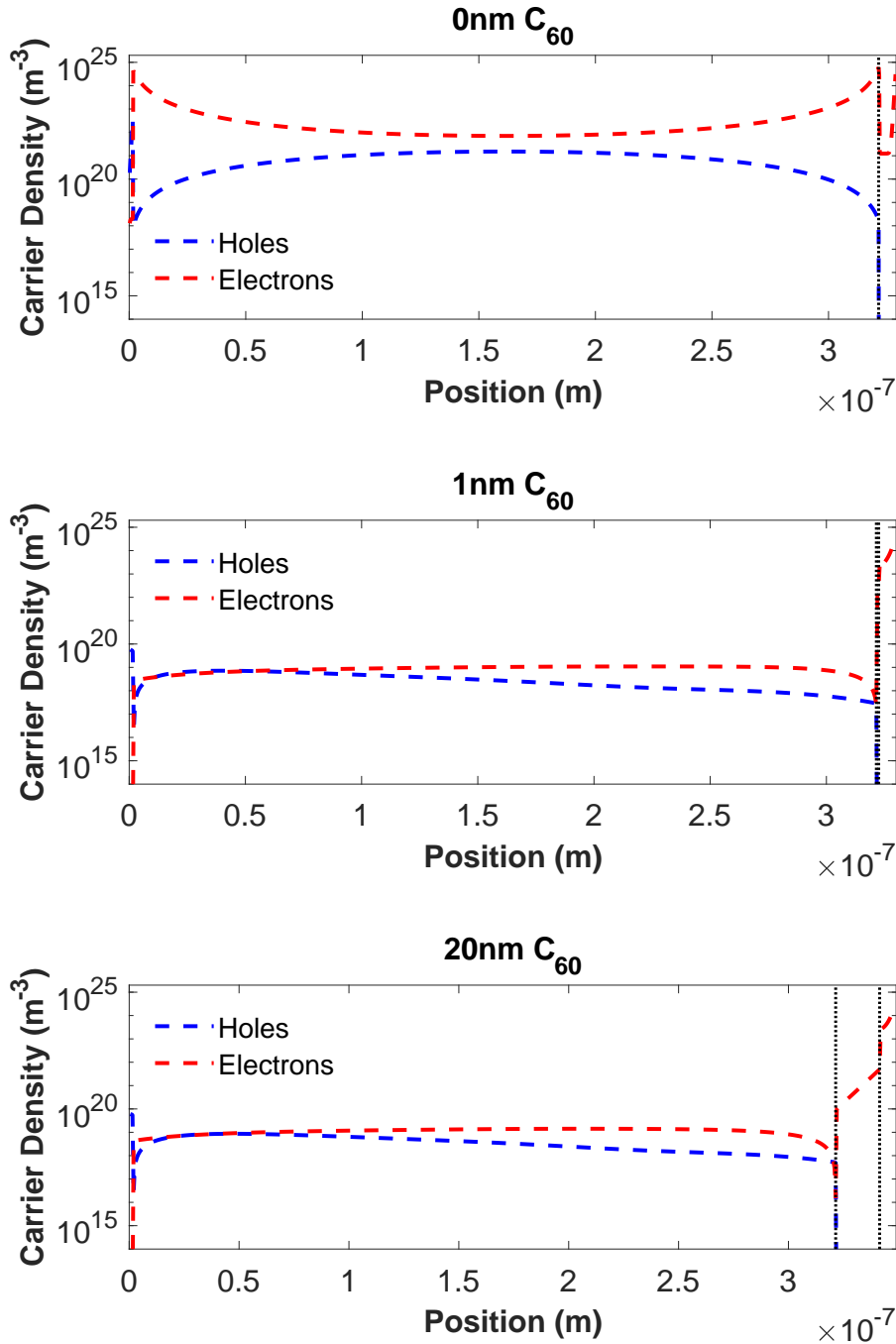


Figure 4.9: Charge carrier densities for the simulated devices with 0 nm, 1 nm, and 20 nm  $\text{C}_{60}$  under illumination at zero applied bias. The perovskite/ $\text{C}_{60}$  and  $\text{C}_{60}$ /BCP interfaces are marked by dotted black lines. The parameters used are listed in Table 4.1.

A possible reason for the reduction of mobility at the perovskite/BCP interface could be the formation of a back-to-back Schottky barrier [66]. The charge transport through this barrier

could be a tunneling process that is exponentially related to the height of the barrier. However, using an energetic barrier for electron extraction instead of a low effective mobility region at the perovskite/BCP interface yields current-voltage curves that are very different from the experimental results (Figure 4.10). Therefore, the energy barrier approach cannot be used to model the poor performance of the 0 nm  $C_{60}$  device. A more likely reason for the less efficient transport could be related to a difference between the two interfaces at the molecular level, causing the perovskite/ $C_{60}$  interface to have a better electron transport pathway.

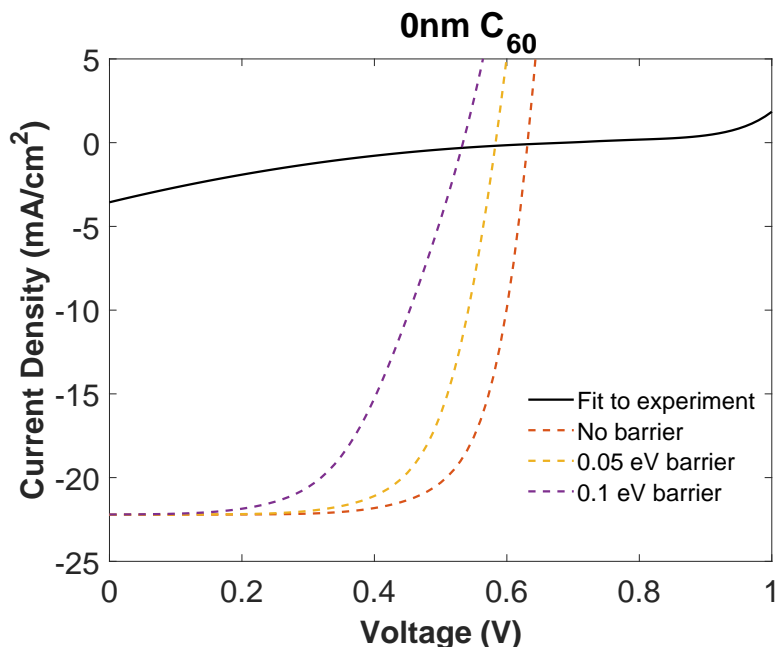


Figure 4.10: The effect of using an energetic barrier for electron extraction instead of a low effective mobility region at the perovskite/BCP interface of devices without  $C_{60}$ . The fit to experiment that was achieved when using a low mobility region is shown for comparison.

Next, we offer an explanation for the origin of the S-shaped JV curve observed in the 0 nm  $C_{60}$  device (Figure 4.7). Several groups have proposed explanations for the appearance of S-shaped JV curves in solar cells. They have been attributed to various factors including interface dipoles [67], charge accumulation [59, 68], injection or extraction barriers [69], imbalanced mobilities [70], and poor extraction of electrons near the cathode due to a mobility drop-off [71]. In the device studied here, the origin is likely a combination of several of the above, namely an injection barrier, mobility



drop-off (equivalently imbalanced mobilities), charge accumulation, and interfacial dipole.

Figure 4.11 shows the 0 nm  $C_{60}$  device under 0.7 V and 0.9 V applied bias, which correspond respectively to points before and after the onset of forward current in the device. At 0.7 V, we see that there is no longer a dip in electron density within the BCP, which indicates that electrons are being injected from the cathode into BCP. However, the electrons are not being injected into the perovskite layer, as seen by the steep difference in electron density on opposite sides of the perovskite/BCP interface. The electron accumulation in BCP is caused by a combination of the 0.42 eV injection barrier for electrons (Figure 4.5) and the low electron mobility at the perovskite/BCP interface. The injection barrier and low interface electron mobility prevent an injection current from flowing. As we further increase the applied voltage from 0.7 V, there is an even larger accumulation of electrons within the BCP near the perovskite/BCP interface and now also an accumulation of holes on the other side of the interface, forming a dipole. The dipole effectively decreases the injection barrier for electrons; however, no injection current will flow as long as an injection barrier is present. Therefore, the net current in the device is near zero until the applied voltage is sufficient to overcome the injection barrier (i.e. about 0.9 V). Notice that the width of the flatter region in the JV curve increases with decreasing interface mobility (Figure 4.8a) since a lower interface mobility requires a stronger net field (and thus a higher applied voltage) to establish an injection current across the interface.

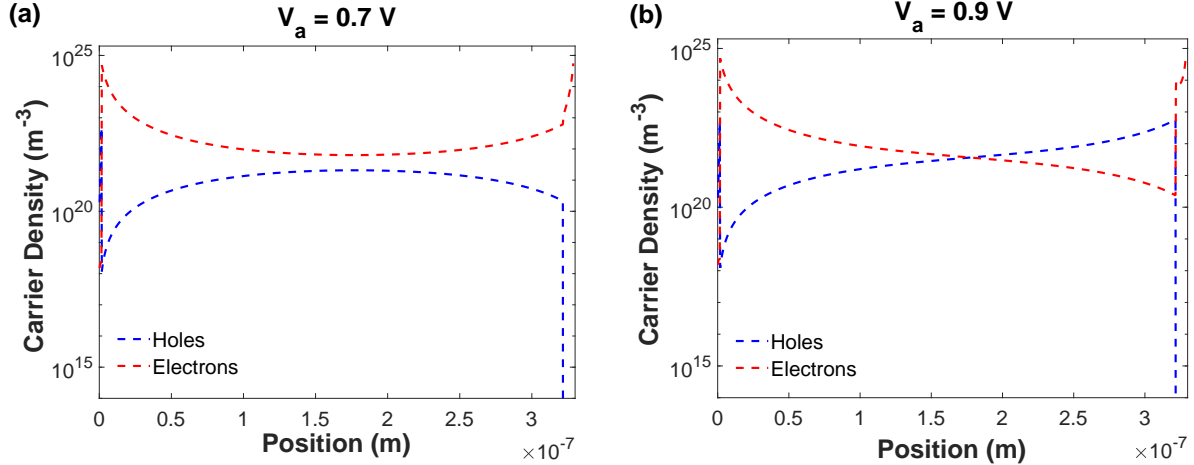


Figure 4.11: Charge carrier densities for device with 0 nm  $C_{60}$  under illumination at 0.7 V (a) and 0.9 V (b) applied bias. The parameters used are listed in Table 4.1.

To ensure the reliability of the simulations, we checked the effects of variation of the HOMO/LUMO levels of the HTL/ETL on the JV curve. In these devices, the most important energy parameters are the relative energy offsets between adjacent layers that are used to compute the gradient of the electric potential at the interfaces. Therefore, we checked the effects of changes of  $\pm 0.1$  eV in the HOMO/LUMO of HTL/ETL, which corresponds to up to a 33% change in the relative offsets between adjacent HOMO/LUMO levels. Even with these changes, which are large relative to the offsets, the simulation is still comparable to the experimental results (Figure 4.12). This demonstrates that even with significant variation of the energy level offsets, our arguments regarding the role of  $C_{60}$  and the reason for the device's poor performance without  $C_{60}$  still hold.

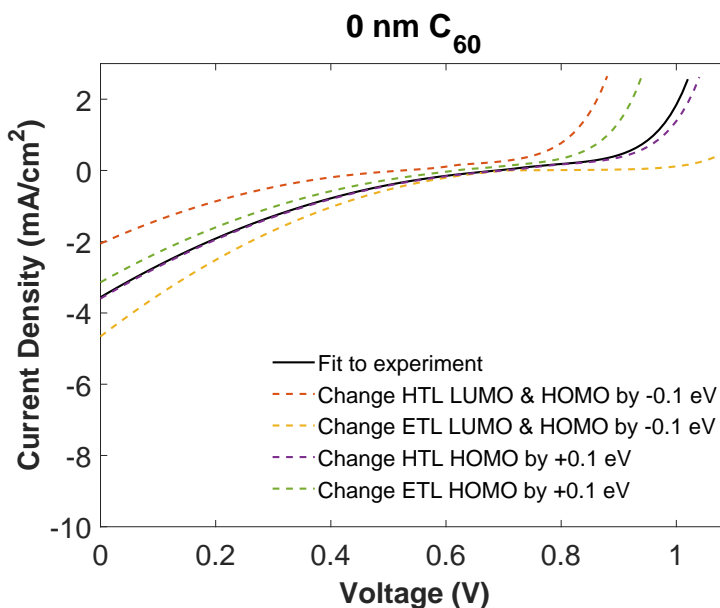


Figure 4.12: The effect of variation of the HOMO/LUMO of the HTL/ETL on the JV curve of the device with 0 nm  $C_{60}$ . The fit to experiment is included for comparison.

#### 4.4 Conclusions

A 1D drift-diffusion model for planar perovskite solar cells has been developed and validated by comparison to reported literature results from an experimentally validated model. The model was then used to describe recent experimental results for inverted planar structure perovskite devices that use fullerene layers for electron transport. By systematically studying the effects of interface mobility and trap density on the JV curves, we find that poor electron extraction at the perovskite interface, modeled by a decreased carrier mobility, is the main cause of the severe decrease in device performance when there is no  $C_{60}$  layer. We demonstrate that the decrease in performance is not due to an increased trap density at the interface. We have also analyzed and provided an explanation for the S-shaped JV curve of the 0 nm  $C_{60}$  device. The main origin of the S-shape is likely due to the non-equal mobilities in the HTL and ETL, which results in charge accumulation and the formation of an interface dipole. The modeling results support the conclusion that very little  $C_{60}$  is needed to enhance carrier extraction. Ultimately, this work helps clarify the role of fullerenes in perovskite solar cells.

## **PART II**

### **Modeling of Photovoltaic Systems**

Increasing energy demand and government-supported goals to transition to renewable energy is accelerating large industrial and utility-level installation of solar power plants. These large plants are generally located in areas with abundant sunlight. Such areas are often in semi-arid and desert climates with high temperatures, causing the plants' energy production to be significantly reduced by two major environmental factors: high ambient temperature, which causes thermal losses, and high concentration of atmospheric dust, which deposits on the panels causing soiling losses [72]. In order to design new systems, improve return-on-investment assessment, and optimize system maintenance, PV system models need to accurately predict energy output including considering losses due to temperature and soiling. The next two chapters analyze existing models and develop improved models to consider these losses when predicting PV system energy production.

## CHAPTER 5

### IMPROVING PV SYSTEM SOILING LOSS PREDICTIONS

Soiling of PV panels is the process in which airborne particles deposit and accumulate on the panel surface, reducing solar irradiance received by the panel by absorbing and reflecting a portion of the incident light [73, 74]. In addition to reversible optical losses, soiling can cause permanent damage to PV modules. In cases of omitted cleaning, cemented dust layers can be very difficult to remove, whereas harsh cleaning with brushes can lead to scratching or abrasion of anti-reflective coatings or panel glass. Non-uniform soiling causes partial shading, which can lead to the formation of hot spots (areas of high temperature that result in localized decrease in efficiency and accelerated material degradation). Even with regular cleaning, mechanical loads during cleaning or thermal shocks when hot panels are cleaned with cold water can break solar cells or cause crack formation. Soiling has been estimated to cause an average loss of 3-4% of the global annual energy yield of photovoltaics [75]. Soiling also introduces additional maintenance costs and increases the uncertainty in the estimation of PV performance, leading to higher financial risks and interest rates charged to plant developers [76]. Improving soiling loss predictions will allow to both more-accurately predict system energy production, which will lower financial risk and interest rates, and form more optimal cleaning maintenance schedules to mitigate some of these losses.

#### 5.1 Background

Soiling has been discussed in the literature for more than 70 years, and yet the fundamental properties of aerosols and their effect on energy transfer are still not fully understood, nor is there a clear solution to the problem [77]. Soiling has been commonly underestimated and overlooked in the PV industry until it came to the forefront recently because of increased deployment of PV systems in parts of the world where soiling is a major issue [78]. For example, in sunny, arid, and dusty regions such as the Middle East, North Africa, and China, power losses due to soiling have been reported to be between 20-70%, while in locations with frequent precipitation or low ambient

particle concentration, the energy loss is typically less than 5% [73, 77]. The vast majority of previous research into soiling has consisted of observations of the reduction in performance due to dust accumulation as a function of exposure time at a particular location. Many researchers use these observations to derive estimates for annual soiling loss (e.g. 5% per year loss) or constant daily soiling rates (e.g. 0.1%/day). These rough estimates are then used in PV performance modeling and for cleaning schedule guidance [78]. A large proportion of research studies use artificial dust particles, which are not representative of natural dust composition [79]. The conclusions from these studies are often contradictory, and much of the information available in the literature applies only to the specific location where the experimental work was conducted due to numerous very localized factors.

Annual PV soiling losses are generally computed by considering the soiling rate (typically the increase in loss per day) for a site combined with rainfall patterns and manual cleaning events. For example, in 2006, Kimber et al. [80] presented a new model for predicting soiling losses in California as a function of rainfall data and the number of manual cleanings. Their empirical model uses typical meteorological year (TMY) data and hourly soiling rates to predict energy production. They suggested a linear model to represent daily system efficiency reduction due to soiling between rainfalls. When daily rainfall exceeds a threshold value, the soiling loss is assumed to drop to a minimum value. After a study of data from many PV plants in California, they found that the soiling rates are between 0.1-0.3% per day during dry periods, which corresponds to annual energy losses between 1.5 and 6.2%, depending on system location. They found that their model is more accurate than using a constant annual soiling loss factor, which is a common approach in the industry. While more advanced approaches have been developed by academic researchers, the Kimber et al. approach appears to be one of the most advanced soiling loss models used commercially. Some of the proposed approaches require too many experimental measurements (e.g. particle accumulation masses, particle diameters, etc.), making them impractical for commercial use at this time. The goal of the work described in this chapter was to analyze some of the more sophisticated approaches proposed by researchers, evaluate the practicality of their implementation

for commercial applications, and encourage some of them to be utilized by the PV industry by implementing more advanced soiling models in a commercial software tool, Enlighten Energy's PV SoilSayer.

In this work, we use Kimber et al.'s approach as a starting point and attempt to improve it by addressing some of its limitations, which are listed below:

- The soiling rates were determined by comparing energy production data to predicted ideal production from solar resource estimates. Any errors in the ideal energy production will contribute to an error in the soiling rate. A better approach to determine soiling rates would be to compare actual energy production data from a soiled module to one that is cleaned regularly.
- They did not consider the effect of angle of incidence (AOI) on soiling losses, even though multiple previous studies have shown a dependency. This dependency means that two PV modules in the same location, but with different tilt angles or a fixed-tilt versus single-axis tracker design, are expected to experience different soiling losses [81, 82].
- Their study monitored 250 PV systems, but all data with an  $R^2$  of less than 0.7 when fitting a line to the dry periods was excluded from the analysis. As pointed out by another study [83], this could have biased the data towards sites with higher soiling where more linear relationships are likely. Sites with smaller losses tend to have smaller  $R^2$  because random errors in solar resource estimates dominate. Another study in California analyzed 186 PV sites and found that soiling losses averaged 0.051%/day, which is significantly less than the 0.2%/day found by Kimber et al. [84]. However, this study also had the flaw where measured energy data was compared with predicted ideal data, so the discrepancy could be caused by different prediction approaches of ideal energy production or different sources for solar resource data. Such discrepancies between studies performed in the same region demonstrate the lack of reliability in existing approaches to model and measure soiling losses.



- Their model requires empirical measurements of soiling at the locations where soiling loss predictions are desired. Often, especially when planning for new solar plant construction, making such measurements over a long duration is not practical, yet an estimate of the soiling losses is still needed. Such estimates could potentially be achieved by studying the impact of environmental conditions such as particulate matter concentration, wind speed, and relative humidity, then developing models that use historical or TMY weather data to predict soiling losses based on these observed relationships.

When considering the approaches to address such soiling model limitations, some studies have proposed that two independent models are required: one to correlate the amount of dust accumulated with locally available weather or environmental conditions, and the second to correlate the amount of dust deposited with energy production loss [79]. Most literature models further separate the prediction of soiling accumulation based on weather into the soiling rate during dry periods and the effects of rain. We take this approach of multiple submodels, with Section 5.2 focused on the soiling rates during dry periods, Section 5.3 considering the effect of rain, and Section 5.4 correlating the dust deposition prediction with energy production loss.

## **5.2 Semi-Physical Modeling of Soiling Accumulation**

Most of the reported soiling research consists of taking field measurements of the energy losses due to soiling on particular PV modules in a particular location and deriving soiling rates (i.e. percent loss per day) based on this data. These regression models typically only apply to the specific location where the experimental work was conducted. It is often not feasible to perform such measurements of soiling losses at each PV site due to lack of necessary equipment, labor costs, or when an energy production prediction is desired for a PV plant that has not yet been built. Therefore, it is desirable in some situations to move beyond site-specific soiling loss studies and have a predictive model for soiling losses in any location in the world that does not require taking new measurements at that location [78]. However, we must note that a generalized model cannot capture all localized effects and therefore can only provide estimates of soiling and is not a replacement

for local experimental measurements. Nevertheless, an estimate based on local environmental parameters is better than assuming a constant annual soiling loss or constant daily soiling rate. This section discusses some of the existing research regarding the physical mechanisms of soiling accumulation, explores existing semi-physical models, and proposes a general model that could be used for such estimates, provided that the empirical parameters are tuned on a region-by-region basis based on soiling observations.

### **5.2.1 Background**

The physics of dust deposition and accumulation are complex due to many influencing factors, ranging from weather, site, and system specifications to surface nano-characteristics as well as their variation in time (Figure 5.1) [79]. Particle size, shape, and constituents, as well as deposition behavior and accumulation rates, can vary dramatically in different localities based on the geography, climate, and urbanization of a region. Airborne dust concentration and rainfall are often considered to be the major determinants of soiling. If sufficiently abundant, rain is effective at cleaning soiled surfaces. However, rain can also increase soiling loss by depositing particles that have been washed out of the atmosphere.

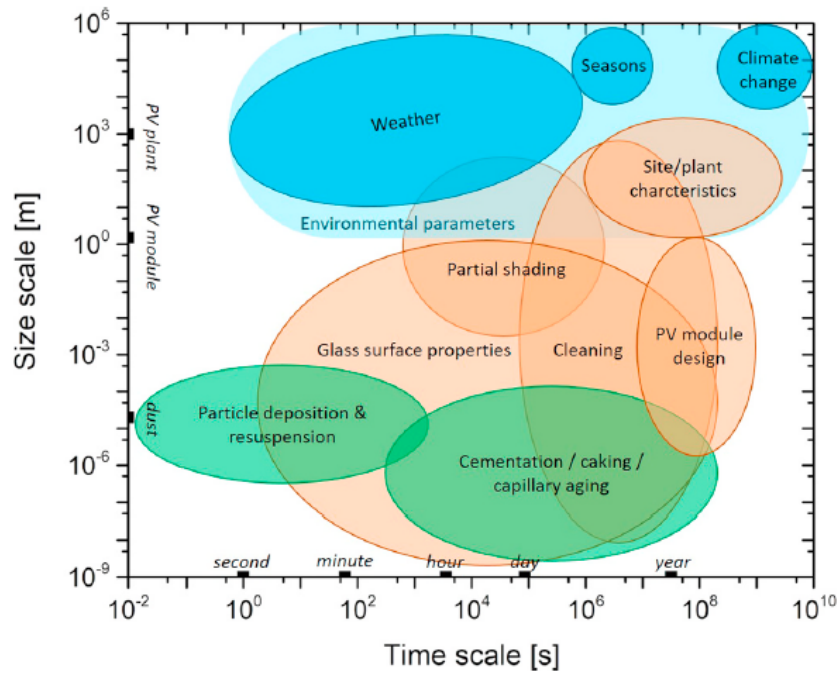


Figure 5.1: Soiling is a complex problem with many influencing factors over a large range of size and time scales. Environmental parameters are shown in blue, microscopic soiling processes are shown in green, and controllable influencing factors related to plant design and maintenance strategies are in orange. Adapted from [85].

Wind speed also may have an important effect because it influences the particle deposition mechanics. Wind speed determines the balance between deposition and resuspension since it can increase both deposition of dust particles and their detachment from the surface. The balance between them is sensitive to many factors, such as the geometry of the PV system, airflow characteristics, dust characteristics (size, shape, composition), and humidity. Multiple previous reports demonstrated both net cleaning (wind-induced resuspension) and net soiling (additional contribution from inertial deposition) effects of wind [86]. Some studies report that for conditions where wind speed is less than 3 m/s, the particle deposition rate can be adequately accounted for by sedimentation alone [74]. It has also been reported that wind is not very effective at removing soiling for particles smaller than 50 microns because smaller particles have a larger adhesive force and resist removal even at wind velocities greater than 50 m/s. Thus, higher wind velocity is generally observed to deposit more dust on a PV module in a dusty environment [72]. Some have

unsuccessfully attempted to enhance dust resuspension during windy periods by increasing the panels' tilt angle to achieve a higher detachment force exerted by the wind [87]. Furthermore, relative humidity, dew, and light rain can strongly enhance dust adhesion to PV surfaces through capillary forces, particle caking, and cementation. These moisture-related adhesion mechanisms can be important even in deserts where while the humidity is low, radiative cooling of glass surfaces at night allows them to cool below ambient air temperature and reach the dew point [75].

One of the most comprehensive studies on the influence of environmental parameters on soiling was performed by Micheli et al. at the U.S. National Renewable Energy Laboratory (NREL), who searched for correlations between soiling and 102 environmental parameters at 20 PV sites [77]. Out of all parameters investigated, they found that the annual average of daily mean particulate matter (PM) and precipitation pattern (quantified by the average length of the dry period) recorded by stations near the PV systems are the best soiling predictors. PM is defined as a mixture of solid particles and liquid droplets suspended in air. There are two types of PM generally reported: PM10 and PM2.5, representing the concentrations of airborne PM less than 10 microns and less than 2.5 microns in diameter in a cubic meter of air, respectively. Note that PM2.5 is a subset of PM10, with these smaller particles typically remaining airborne and traveling longer distances than the larger particles included in PM10 because of their lower mass. PM2.5 is the main cause of haze, which is periodically reduced visibility in urban areas, causing a reduction in solar intensity and alteration of the solar spectrum reaching the ground [88]. The NREL study found no clear conclusion about whether PM10 or PM2.5 was a better predictor of soiling. A separate study performed in the Atacama Desert supports NREL's conclusions, finding that soiling at various sites was strongly correlated with aerosol optical depth, which is known to be correlated to PM [89]. While these works have shown that PM concentration seems to be a good explanation for variation in soiling rates over large distances (geographic location), it has been reported to be inadequate to explain day-to-day variations in soiling rates at a particular location because of other weather conditions [74]. To predict soiling over shorter periods such as weeks, days, or even hours, additional parameters such as wind, RH, and ambient temperatures are thought to be important [90, 91].

The general approach of semi-physical dust accumulation models during the dry period is to consider net dry deposition velocity. Dry deposition is defined as the exchange process of pollutants from the earth's atmosphere to surfaces in the absence of precipitation [73], and dry deposition velocity ( $v_d$ ) is a way to express the rate at which particulate matter from the atmosphere encounter a surface. Models predicting dry deposition are complex and require information that is difficult to obtain; therefore, deposition fluxes are often estimated using PM and assumed dry deposition velocities [92]. The simplest approach uses an empirically-derived net deposition velocity, assumed to be a constant for each location. Then, mass flux accumulation rate (with dimensions mass per area per time) is simply [93]

$$m = v_d PM \quad (5.1)$$

Some studies use a weighted average of PM2.5 and PM10 concentrations [94], while others use only PM10, motivated by the fact that coarse particles are dominant in soiling mass accumulation [93]. Accounting for different particle sizes can improve accuracy, but measuring size distribution requires special equipment, and equipment for measuring particles greater than 10 microns is scarce [85]. More sophisticated approaches describe the dust accumulation as the net sum of competing processes: dry deposition, rebound, and resuspension [74, 95]. Dry deposition, which is defined in this context as the transport of particles to a surface regardless of whether they adhere, is often further broken up into sedimentation (gravitational settling), and deposition due to turbulence and boundary layer (quasi-laminar) effects, and expressed in terms of resistance analogs [73, 74, 85, 94–96, 100, 101]. The total deposition velocity can be expressed as a sedimentation velocity in parallel with two resistors that model the resistance to deposition of the turbulence ( $R_a$ ) and resistance to deposition in the boundary/surface layer ( $R_b$ )

$$v_d = v_d^{turb,bndry} + v_d^{sed} = \frac{1}{R_a + R_b} + v_s \quad (5.2)$$

A diagram of the approach is shown in Figure 5.2. Next, we individually discuss the main mechanisms that contribute to soiling accumulation.

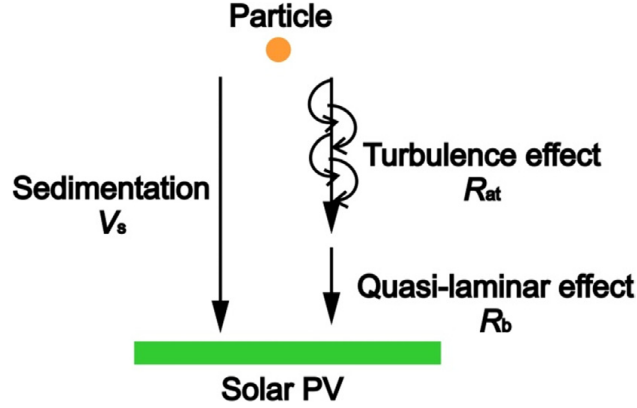


Figure 5.2: Schematic of particle dry deposition model resistance analogy. Adapted from [96].

### Sedimentation

In aerosol physics, sedimentation is described by the Stokes terminal settling velocity which is valid when particle Reynolds number is less than one (true for small particles). Only a very small fraction of soiling particles have Reynolds number greater than one, so Stokes velocity alone can be used to estimate sedimentation. The Stokes terminal settling velocity is the velocity of a particle when the gravitational force  $F_g$ , drag force  $F_D$ , and buoyancy  $F_B$  force experienced by the particle are in equilibrium. To derive the expression for Stokes velocity, a spherical particles with diameter  $d$  is assumed. The balance of forces for terminal velocity dictates [97]

$$F_B + F_D = F_g \quad (5.3)$$

The buoyancy force is the product of air density  $\rho_{air}$ , particle volume  $V$ , and gravitational acceleration  $g$

$$F_B = \rho_{air} V g = \frac{4}{3} \pi \left( \frac{d}{2} \right)^3 \rho_{air} g = \frac{\pi}{6} \rho_{air} g d^3 \quad (5.4)$$

The aerodynamic drag on the particle is given by Stokes law

$$F_D = 3\pi\mu v_g d \quad (5.5)$$

where  $v_g$  is the Stokes velocity that we are solving for and  $\mu$  is the kinematic viscosity of air. The force of gravity on the particle is

$$F_g = \frac{4}{3}\pi\left(\frac{d}{2}\right)^3 \rho_p g = \frac{\pi}{6}\rho_p g d^3 \quad (5.6)$$

where  $\rho_p$  is the particle's density. Substituting Equations 5.4-5.6 into Equation 5.3, we find

$$v_g = \frac{(\rho_p - \rho_{air})gd^3}{18\mu} \approx \frac{(\rho_p)gd^3}{18\mu} \quad (5.7)$$

where we have used the fact that  $\rho_{air} \ll \rho_p$ . To correct for the shape of real non-spherical particles, two correction factors are often added: the Cunningham correction factor  $C$  ( $\approx 1$  for particles larger than one micron), and the dynamic shape factor  $k$  (reported to be between 1.0 and 1.2 for soiling particles). The general equation for sedimentation velocity in the Stokes regime [85, 98] is

$$v_g = \frac{\rho d^2 g C}{18\mu k} \quad (5.8)$$

Many models for soiling set the correction for real particles shape  $C/k$  to one, which means they assume that the spherical assumption is adequate, since often the proper particle shape correction factor for a particular location's soiling is not known. When considering the sedimentation of soiling on PV modules, only those particles that deposit on the optical surface of the module should be considered. Therefore, the tilt angle ( $\theta_t$ ) of the PV panel influences the particle sedimentation velocity as follows [72, 78, 85, 96, 99].

$$v_s = v_g \cos(\theta_t) = \frac{\rho d^2 g C}{18\mu k} \cos(\theta_t) \quad (5.9)$$

### **Turbulence and Boundary Layer effects**

To account for wind turbulence and boundary layer effects, the atmosphere can be separated into two layers: an upper layer where particle transport is described by an atmospheric turbulence, and a quasi-laminar layer (also known as the boundary or surface layer) where particle transport is governed by Brownian diffusion and inertial impaction. The contribution of these effects to the net

deposition velocity can be modeled by two resistors in series

$$v_d^{turb,bndry} = \frac{1}{R_a + R_b} \quad (5.10)$$

where  $R_a = 1/(C_D u_{wind})$  where  $C_D$  is the surface drag coefficient and  $u_{wind}$  is the mean wind velocity. The product  $C_D u_{wind}$  represents the capability of wind to transfer kinetic energy to particles in the air, with  $C_D$  accounting for the turbulence when wind blows over rough surfaces such as land and has a global yearly average value of  $1.2 \times 10^{-2}$  (dimensionless). Numerous expressions exist in the literature for the boundary/surface layer resistance  $R_b$  [94, 96, 100]. The expressions generally have the form

$$R_b = \frac{1}{u_* P_{attach} (E_b + E_{im})} \quad (5.11)$$

where  $E_b$  is the collection efficiency from Brownian deposition,  $E_{im}$  is the collection efficiency from impaction,  $P_{attach}$  is the attachment probability, and  $u_*$  is the friction velocity defined as

$$u_* = u_{wind} \frac{\kappa}{\ln(z_R/z_0)} \quad (5.12)$$

The logarithmic term accounts for the difference in wind speed at different heights, depending on the roughness of the surface.  $z_R$  is the reference height above ground where the wind speed is measured (commonly 10 meters [96]),  $z_0$  is the surface roughness length (a length scale representation of the roughness of a surface), and  $\kappa$  is the Von Karman constant that is widely agreed to have a unitless value of 0.4. When wind hits a solar module, the number of particles that pass by the panel per unit time increases proportionally to the wind speed. Therefore, resistance to wind-induced surface deposition ( $R_b$ ) is inversely proportional to wind speed.

Brownian deposition (quantified by  $E_b$ ) describes the deposition of microscopic particles (less than one micron) that diffuse in space due to random impacts with surrounding air molecules and other aerosol particles and remain entrained in fluid streams [85]. Since such small particles do not significantly contribute to the soiling mass accumulation, Brownian deposition can be neglected. Very large particles only exhibit sedimentation, rapidly depositing from air regardless of flow behavior. Medium-sized particles (about 10 micron in diameter, which is the upper limit



for PM10 measurements) experience viscous forces comparable to their own inertia and thus can exhibit inertial deposition in windy conditions. In calm conditions, medium-sized particles deposit through sedimentation [85]. The dominant size of particles accumulating on outdoor surfaces has been observed to be 10-30 micron. Overall, PV soiling's dominant deposition mechanism is sedimentation, with inertial deposition contributing during windy conditions. The concept that sedimentation is the dominant mechanism is supported by studies that found that the amount of soiling on tilted collectors simply follows the cosine of the tilt angle, which means it simply corresponds to the horizontal component of the collector's surface area as expected by Equation 5.9 [72, 85].

Soiling particles can be carried by an airstream (wind) where impacts from the air molecules keep them traveling with the airstream. If the flow hits an obstacle, like a PV panel, the streamlines deviate from their original path (Figure 5.3). The airflow direction change is transferred to the particles in the airstream by the air molecules impacting them. If the transferred momentum is sufficient to overcome the particles' kinetic inertia, the particles will follow the direction of the airstream. If not, the aerosol particles cannot follow the air and will eventually hit the PV panel's surface, which is referred to as *impaction* or *inertial deposition*. The impaction collection efficiency  $E_{im}$  is a function between 0 and 1, describing the proportion of particles carried past the surface by wind that deposit on the surface due to impaction.

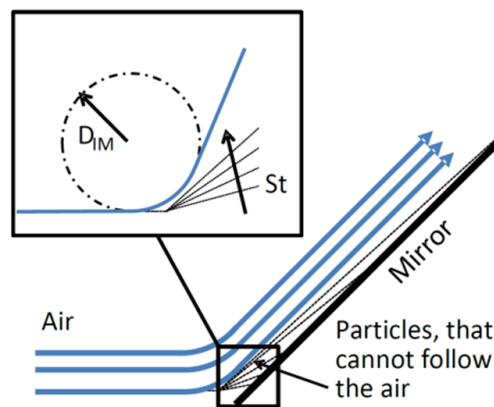


Figure 5.3: Schematic of deposition due to particle impaction. Adapted from [100].

$E_{im}$  increases with increasing particle diameter since more massive particles have larger inertia, which makes them more likely to leave the airstream at a bend in the flow. There are multiple empirical-based step-like functions used for  $E_{im}$  such as

$$E_{im} = \frac{St^2}{(1 + St) * 2} \quad (5.13)$$

was found for vegetative canopies [102], or some (e.g. [99, 100]) use a sigmoidal distribution

$$E_{im} = \frac{1}{1 + \exp(-f_{im}(St - 1))} \quad (5.14)$$

where  $F_{im}$  is an empirical parameter that determines how steeply the function transitions from 0 to 1. Kim and Larson empirically found [103]

$$E_{im} = 10^{-2.8/St} \quad (5.15)$$

All of these  $E_{im}$  equations are expressed in terms of the Stokes number, which characterizes the behavior of particles suspended in a fluid flow and is defined as

$$St = \frac{v_s u_*^2}{g\mu} \quad (5.16)$$

Wolferstetter et al. [100] point out that only the component of the wind vector that points perpendicular towards the panel should be considered, thus impaction velocity is multiplied by the cosine of the difference in angle between the wind direction and the panel azimuth orientation ( $\Delta\theta_{az,w}$ ).

The attachment probability is the probability that a particle that hits a surface will attach to the surface instead of rebounding. Attachment probability decreases with increasing wind speed and particle size since particles will rebound if their kinetic energy is greater than the adhesion force with the panel surface [85]. For example, some field studies reported that impacting particles detached when wind speed reached just 4 m/s [86]. There are no widely adopted models that quantitatively describe rebound in arbitrary conditions. Wolferstetter et al. propose a logistic equation for attachment probability, expressed in terms of a threshold particle diameter for rebound,  $d_{rb}$

$$P_{attach} = 1 - \frac{1}{1 + \exp[-C_{rb}(d_p - d_{rb})]} \quad (5.17)$$

where  $C_{rb}$  describes the steepness of the transition between attachment and rebound and

$$d_{rb} = \frac{\zeta_{rb}}{u_{wind}} + w_{RH}(RH)^2 \quad (5.18)$$

where RH is the relative humidity, and  $\zeta_{rb}$  and  $w_{RH}$  are constants determined during parameterization of the model. This model describes the physical effect of higher humidity causing particles to adhere better to a surface, thus increasing the particle diameter threshold for rebound to larger particles. The rebound threshold diameter decreases with increasing wind speed because particles in higher wind speed have more kinetic energy, therefore reducing the mass required to give them enough kinetic energy to overcome the surface adhesive forces.

## Resuspension

Resuspension describes the process in which soiling that has already been present on the surface of a PV panel for some time detaches from the panel due to wind overcoming the adhesion force. Resuspension is very difficult to model because it varies greatly in natural conditions and is sensitive to adhesion forces, particle and surface chemistry, and particle shapes [86]. One study found that the wind velocity necessary for resuspension of particles from flat surfaces varied from 0.82 m/s to 2219.8 m/s for different particles [104]. Fundamental chemistry studies of soiling adhesion using atomic force microscopy found that particles with higher organic surface content have higher adhesive force than particles with no organic surface content. They also found that cementation occurs when high-organic particles are exposed to dew, high humidity, or light rain. They found that soiling particles close to highways are contaminated with hydrocarbons from diesel fuel, which tend to bind particles together and form cement-like films adhering to glass [105]. Such localized effects make adhesion forces nearly impossible to predict in a generalized way, and thus a generic resuspension equation that is empirically fitted to the observed resuspension may be the best approach. A desert study in Qatar observed that resuspension strongly increases for wind speeds above 4 m/s. They also observed a decrease in resuspension with increasing RH, with a threshold of about 60%, above which almost no resuspension occurs [74].

## 5.2.2 Limitations of Existing Models

When Enlighten Energy Ltd., as part of our research collaboration, came up with the idea of implementing a model that considers soiling based on environmental variables, the natural approach was to start with a model from the literature. Guo et al.'s model [106] was chosen as one of the only clearly explained and validated semi-physical soiling models in the literature. Here, we describe the limitations which were found when trying to predict soiling using Guo et al.'s model.

For completeness, we will first outline the derivation of their model, which predicts soiling losses due to particulate matter concentration (PM10), wind speed, and relative humidity. It considers the non-linear effects of dust deposition, resuspension of deposited dust, and the effect of relative humidity on resuspension. Guo et al. define a *cleanness index*, which is simply a measure of the relative performance in terms of the DC power output of a soiled PV array relative to a clean array operating under the same solar irradiance. This is similar to what other researchers call the *soiling ratio*. The semi-physical model assumes that the daily change in a PV panel's cleanness index is proportional to the difference between the daily average deposition and resuspension flux. Dust deposition flux is proportional to the ambient dust concentration (PM10), while resuspension flux is a function of wind speed and relative humidity. The dry deposition model by Kim and Larson [103] has been adopted. Dry deposition velocity is expressed as a combination of gravitational settling  $V_g$  and turbulent deposition  $V_t$

$$V_d = V_t + V_g = u\eta_{dI} + \frac{\rho_p g d_p}{18\mu} \quad (5.19)$$

where  $\mu$  is the dynamic viscosity of air,  $\rho_p$  is the density of an aerosol particle, and  $d_p$  is particle diameter. The friction velocity,  $u$ , is assumed to be directly proportional to the scalar wind speed,  $u_{sc}$ , with the proportionality coefficient  $\alpha_1$  determined by empirical fitting

$$u = \alpha_1 u_{sc} \quad (5.20)$$

The term  $\eta_{dI}$  is defined by

$$\eta_{dI} = \exp\left(\frac{-\alpha_0 g v}{V_g u^2}\right) \quad (5.21)$$

where  $\alpha_0$  is an empirical parameter which controls the effect of turbulence on dust deposition velocity,  $g$  is gravitational acceleration ( $9.81 \text{ m/s}^2$ ), and  $\nu$  is kinematic viscosity of air ( $1.5 \times 10^{-5} \text{ m}^2/\text{s}$ ).

Therefore, the full expression for deposition velocity in terms of scalar wind speed is

$$V_d = \alpha_1 u_{sc} \exp\left(\frac{-\alpha_0 g \nu}{V_g \alpha_1^2 u_{sc}^2}\right) + V_g \quad (5.22)$$

Next, the dust deposition flux may be expressed as the product of deposition velocity and the particulate matter concentration (PM10, which we label as  $P_{10}$  in the equations)

$$F_d = P_{10} \left[ \alpha_1 u_{sc} \exp\left(\frac{-\alpha_0 g \nu}{V_g \alpha_1^2 u_{sc}^2}\right) + V_g \right] \quad (5.23)$$

Guo et al. use the following equation to model dust resuspension flux, taking into consideration relative humidity ( $H$ ), which has been reported to affect the threshold friction velocity for dust resuspension.

$$F_r = \frac{\beta_2 [\alpha_1 u_{sc} - (u_{th,0} + \beta_1 H)] \alpha_1^2 u_{sc}^2}{1 + \exp[-100 [\alpha_1 u_{sc} - (u_{th,0} + \beta_1 H)]]} \quad (5.24)$$

where the parameters  $\beta_1$  and  $u_{th,0}$  control the effect of relative humidity on dust resuspension. Note that this is a logistic function (smoothed step-function). Due to the exponential in the denominator,  $F_r$  approaches 0 when the friction velocity is less than the resuspension threshold, or mathematically  $\alpha_1 u_{sc} < (u_{th,0} + \beta_1 H)$ . When the friction velocity is significantly larger than the threshold, the denominator goes to 1. When the friction velocity is near the threshold, the exponential ensures a continuous, smooth transition.

The net deposition flux is the difference between dust deposition and dust resuspension flux. Therefore, the change in cleanness index for a 24 hour period is

$$\Delta CI = \gamma(F_r - F_d) \quad (5.25)$$

Table 5.1 lists the empirical parameters of the model.

Table 5.1: Empirical parameters of the Guo et al. model.

Parameter	Value
$\gamma$	$2.64384 \times 10^6 \text{ m}^2\text{s/kg}$
$\alpha_0$	$1.71 \times 10^3$ (unitless)
$\alpha_1$	0.375 (unitless)
$\beta_1$	$1.95 \times 10^{-2} \text{ m/s/\%RH}$
$\beta_2$	$3.00 \times 10^{-9} \text{ kgs}^2/\text{m}^5$
$u_{th,0}$	0 m/s
$V_g$	0.0199 m/s

An attempt to run the as-is Guo et al. model using weather and PM data for Riverside, California, was unsuccessful. The model predicted very low levels of soiling deposition and high resuspension flux such that almost no net soiling accumulation was predicted to occur (Figure 5.4a). The cause of this seems to be the highly empirical nature of the model, which was developed for a site in Doha, Qatar, with a high PM of  $120 \mu\text{g}/\text{m}^3$ . Guo et al. tuned the resuspension flux equation's coefficients to be appropriate for this high PM, but the resuspension equation is independent of PM. Therefore, when the model is used for Riverside, which has a much lower PM of  $20 \mu\text{g}/\text{m}^3$  (typical of California), the resuspension flux overwhelms the deposition flux. In order to avoid this issue, we tried simply setting the resuspension term to zero. However, without the resuspension term to account for the fact that much of the wind-blown dust hitting a solar panel does not adhere, the model overestimates wind-induced deposition, leading to unphysical spikes of several orders of magnitude in the hourly soiling rate (Figure 5.4b).

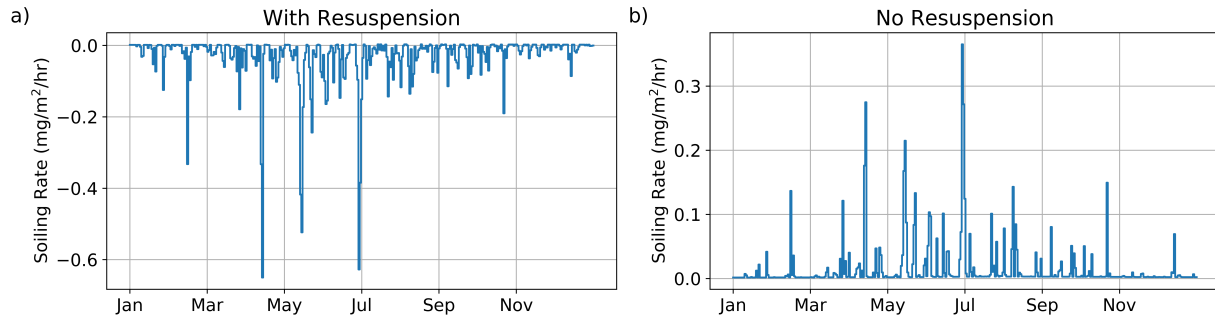


Figure 5.4: One year of hourly soiling rates predicted by the Guo et al. model with (a) and without (b) the resuspension term.

A third limitation is that the model does not consider the effect of the tilt angle. As we described in the literature review above, numerous studies have found that soiling accumulation decreases with increasing tilt angle and follows approximately a cosine law. The development of a model that addresses these limitations is described in the next section.

### 5.2.3 Developing a General Soiling Accumulation Model

This section describes the development of a general semi-physical model for soiling estimation that yields correct trends for locations worldwide. Note that this model is only intended to be used for rough estimates of the possible soiling that a location may experience when soiling measurements are not available (e.g. for pre-construction site planning). We propose data-driven models that would use soiling measurements to provide more accurate soiling predictions in Section 5.8. Our soiling model is based on many of the same principles as in Guo et al. and other literature models discussed in Section 5.2.1. Ideas from several models were combined in an attempt to develop a more general model that does not include too many site-specific features or require too much detailed information about the soiling (e.g. particle sizes and chemistry) that is not practical to obtain. The model describes soiling accumulation as the net of three contributing mechanisms: sedimentation, wind-induced deposition, and resuspension. The equations for the three mechanisms are presented below.

## Sedimentation

Here we take the standard approach as described in Section 5.2.1 with the Cunningham and dynamic shape correction factors set equal to one since it is impractical to determine these in many situations. In contrast with the Guo et al. model, we include the influence of panel tilt angle ( $\theta_t$ ) on sedimentation velocity. The velocity of sedimentation onto the tilted panel surface is

$$v_s = v_g \cos(\theta_t) = \frac{\rho d^2 g}{18\mu} \cos(\theta_t) \quad (5.26)$$

where  $v_g$  is the sedimentation velocity on a horizontal surface. In the initial implementation, the particle density was assumed to be that of sand ( $1631 \text{ kg/m}^3$ ) [107], and the particle diameter was assumed to be  $13 \mu\text{m}$ . The kinematic viscosity of air ( $\mu$ ) was taken at  $25^\circ\text{C}$ , which is a reasonable approximation of the average air temperature for a large portion of solar power stations and has a value of  $15.52 \times 10^6 \text{ m}^2/\text{s}$  [108]. Kinematic viscosity varies by only about 0.6% per degree, so using the constant temperature assumption is not expected to cause much error.

## Wind-Induced Deposition

For considering additional deposition due to wind, we describe particle transport in terms of the sum of an aerodynamic and surface resistance. Brownian diffusion is ignored since it is only significant for very small particles. We use the expression for impaction collection efficiency from Kim et al. [103], combined with the probability of attachment and azimuth orientation effect from Wolfertstetter [100].

$$v_{d,wind} = \frac{\cos(\Delta\theta_{az,w})}{R_a + R_b} = \frac{\cos(\Delta\theta_{az,w})}{\frac{1}{C_D u_{wind}^2} + \frac{1}{u_* E_{im} P_{attach}}} \quad (5.27)$$

where  $\Delta\theta_{az,w}$  is the difference between panel azimuth orientation and wind direction, and impaction efficiency is given by

$$E_{im} = 10^{-2.8/St} \quad (5.28)$$

with

$$St = \frac{v_s u_*^2}{g\mu} \quad (5.29)$$



For the surface drag coefficient,  $C_D$ , the global yearly average value of 0.012 (dimensionless) is used [96].

The attachment probability is described by

$$P_{attach} = 1 - \frac{1}{1 + \exp[-C_{rb}(d_p - d_{rb})]} \quad (5.30)$$

where the parameterization constant  $C_{rb} = 8 \times 10^4$  describes the steepness of the transition between attachment and rebound and

$$d_{rb} = \frac{\zeta_{rb}}{u_{wind}} + w_{RH}(RH)^2 \quad (5.31)$$

where  $\zeta_{rb} = 1 \times 10^{-5}$  and  $w_{RH} = 4 \times 10^{-4}$  are parameterization constants.

Figure 5.5 shows the attachment probability as a function of particle diameter and wind speed. As expected, we see that the attachment probability is nearly one for small particles and zero for large particles, which have higher kinetic energy that overcomes the surface adhesion energy.

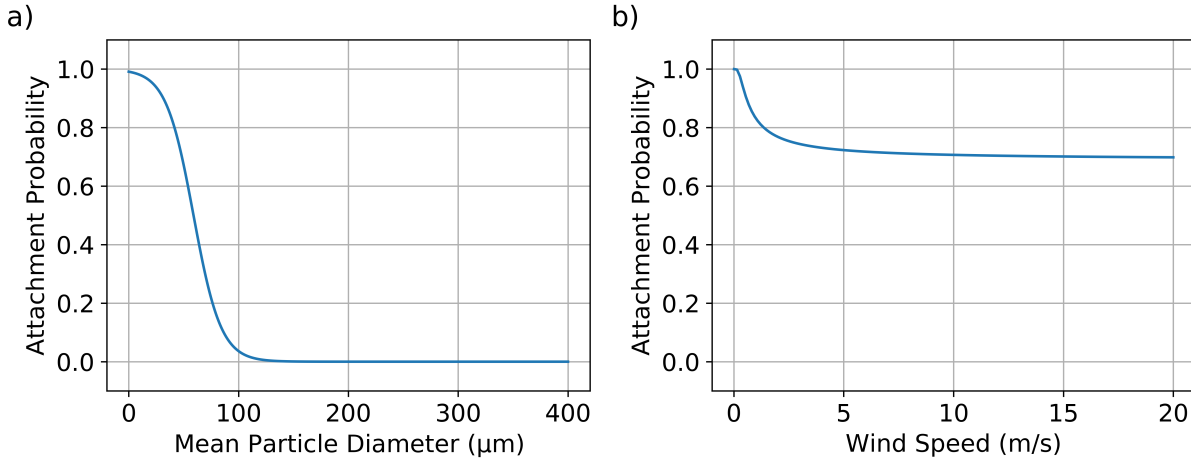


Figure 5.5: Attachment probability as a function of a) particle diameter (with wind speed of 1 m/s and relative humidity of 70%) and b) wind speed (with particle diameter of 15  $\mu\text{m}$  and relative humidity of 50%).

Overall, the aerodynamic contribution is linear with wind speed, and the surface contribution rises to a step-like behavior, where a minimum wind speed and diameter are needed for particles to have enough inertia to exit the fluid flow and deposit by impaction (Figure 5.6a). The relationship between the wind-induced deposition and relative humidity is almost linear for typical soiling

particle diameters of 10-20  $\mu\text{m}$ . For larger particles (e.g. 50  $\mu\text{m}$ ), the effect of rebound (described by  $P_{attach}$ ) begins to have a non-linear effect (Figure 5.6b), with wind-induced deposition staying close to zero for low RH and rising more rapidly for higher RH.

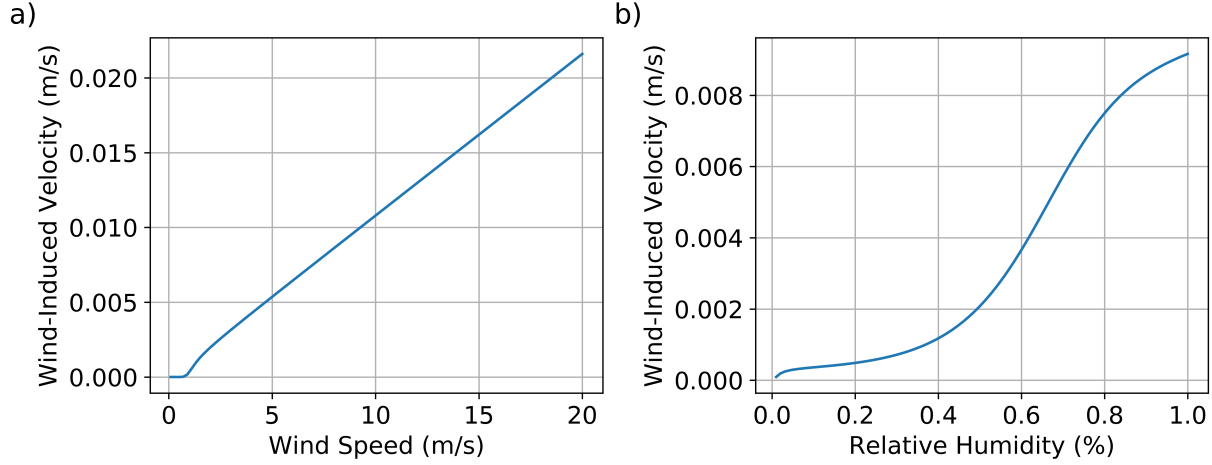


Figure 5.6: Wind-induced velocity as a function of a) wind speed (for 10  $\mu\text{m}$  particles in 40% relative humidity) and b) relative humidity (for 50  $\mu\text{m}$  particles at 2 m/s wind speed).

### Resuspension

Resuspension is modeled based on Guo et al.’s model and assumed to occur only when the friction velocity is larger than a threshold friction velocity. The resuspension flux ( $\text{kg}/\text{m}^2/\text{s}$ ) of soiling is given by

$$F_{resusp} = \beta_2 u_*^2 (u_* - u_{*,th}) \tag{5.32}$$

with the threshold friction velocity for resuspension linearly increasing with RH. The slope of increase is based on the report by Neuman et al. [109], who found that the threshold wind velocity ( $u_{th}$ ) needed for resuspension is 0.24 m/s at 0% RH and 0.31 m/s at 90% RH. The threshold friction velocity is given by

$$u_{*,th} = \frac{\kappa(u_{th,RH=0} + \beta_1 RH)}{\ln(z/z_0)} \tag{5.33}$$

where  $\beta_1 = 1.95$  and  $\beta_2 = 3.0 \times 10^{-10} \text{ kgs}^2/\text{m}^2$ . Note that RH is defined as a decimal value (i.e. 60% is entered as 0.6 in the equation). Resuspension flux is zero for wind speeds less

than the threshold velocity and increases rapidly for wind speeds above the threshold (Figure 5.7). It decreases linearly with increasing relative humidity. Unlike wind-induced deposition, the resuspension equation here does not consider wind direction, mainly because this effect is not yet understood [104]. Carefully designed experiments will be needed to improve our understanding of resuspension.

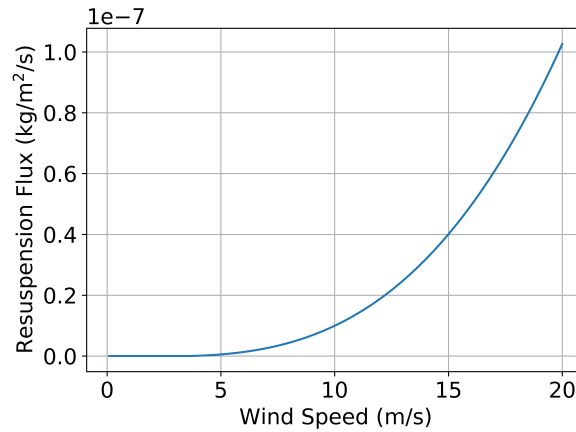


Figure 5.7: Resuspension flux versus wind speed for RH 40%.

### Net Accumulation

The net soiling accumulation rate is found by multiplying the total deposition velocity by PM10 and subtracting the resuspension flux

$$\dot{m}_{accum} = P_{10}(v_s + wv_{d,wind}) - F_{resusp} \quad (5.34)$$

where  $w = 0.1$  is a dimensionless fitting parameter controlling the relative effect of wind-induced deposition and sedimentation.

Figure 5.8 shows the dependence of net soiling accumulation flux on wind speed. At low wind speed below the threshold for deposition due to impaction, the flux is only due to sedimentation and, therefore, independent of wind speed. At moderate wind speeds, the flux increases linearly with wind as more deposition due to impaction occurs. At high wind speeds, resuspension flux can

be (depending on the RH) higher than deposition flux, resulting in a net cleaning effect. The curve shifts to the right with increasing RH

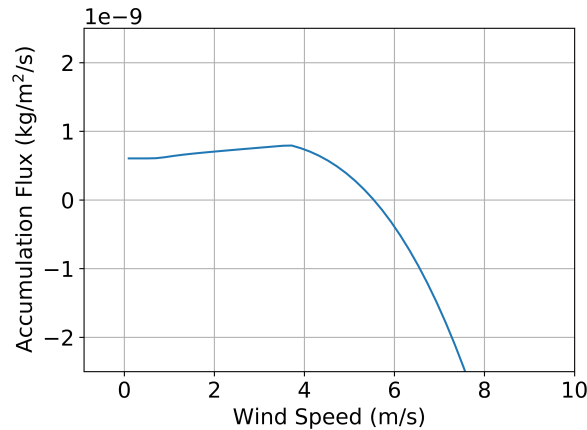


Figure 5.8: Net soiling mass accumulation flux at 40% RH,  $50 \mu\text{g}/\text{m}^3$  PM10 concentration, and  $20^\circ$  tilt angle.

### Comparison with Guo et al. Model

Figure 5.9 shows a comparison of the hourly soiling rates over one year for a fictional PV plant in Riverside, California. We see that our model gives a more physically realistic result, showing significant positive soiling rates with occasional negative soiling rates due to resuspension during high-wind events. The basic shape of the curve is determined by the average PM values, with additional wind-induced soiling appearing as the smaller noisy spikes on top.

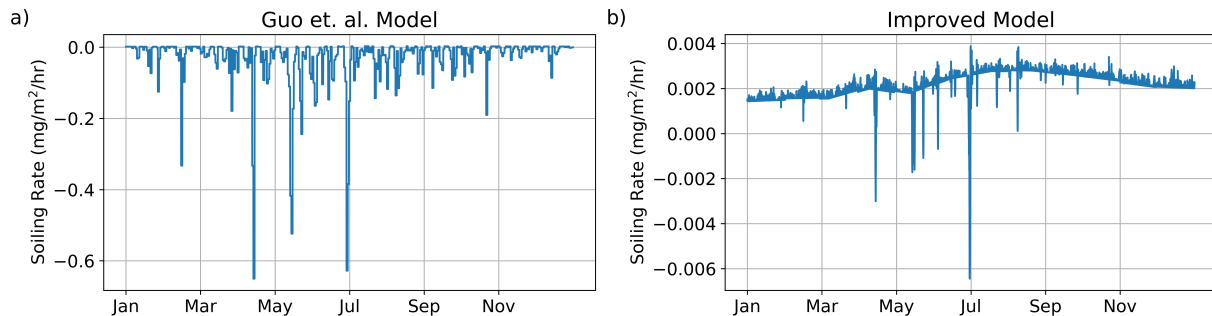


Figure 5.9: Comparison of hourly soiling mass accumulation rates for Riverside, CA as predicted by the Guo et al. model (a) and the improved model proposed in this thesis (b).

This model was developed with very limited soiling data from only several sites and therefore is mostly intended as a proof-of-concept and to provide rough estimates and trends. All parameters of the model are expected to be needing region-specific tuning once reliable soiling data for a diverse range of locations becomes available. The initial implementation of the model was tuned to be consistent with soiling observed in California. With the development and industry adaption of fully autonomous, low-maintenance soiling measurement stations (e.g. [110–113]), the availability of reliable soiling data is expected to increase significantly in the near future, which would allow region-specific tuning of such a semi-physical model.

### **5.3 Effect of Rainfall**

The net effect of soiling losses is strongly dependent on rainfall. There is a consensus in the literature that rain often effectively cleans solar panels; however, a minimum amount of precipitation is needed for effective cleaning. Reports vary regarding the rain threshold. Also, rain can hurt the soiling problem if the duration is brief and the intensity is light by depositing high concentrations of residue onto a PV (e.g. water spots induced by soluble salt contained in the rainwater) or providing water for a cementation process where soiling strongly adheres to the PV surface [72, 78]. Cementation is reported to occur in regions with high dust and humidity (possibly leading to heavy morning dews). At high humidity, water-soluble particles form microscopic droplets of salt solutions, which also retain some insoluble particles. When dried by evaporation, the precipitated salt acts as a cement to anchor insoluble particles to the surface [89]. Soiling that has cemented to the surface often cannot be removed without mechanical detergent scrubbing, thus increasing the cost of manual cleaning [72]. Some examples of empirical observations of rainfall effects at different locations are listed below (this list is not intended to be comprehensive)

- Rain events were found to clean soiling on panels (with the exception of bird droppings) panels to within 1% of the manually cleaned ones. Losses due to bird droppings were recovered to only 3% loss after heavy rain (9 mm) (Phoenix, Arizona) [81].
- Rain effectively cleaned modules as long as daily rainfall surpassed about 4-5 mm (Southern

Spain) [82].

- Cleaning action of rain generally only occurs when rainfall is more than 4-5 mm/day (Arizona) [99].
- Relatively modest rainfall events of as low as 2.8 mm were sufficient to clean panel to a level that restored power output to within 1% of the manually cleaned panel. (Portland, Oregon) [114].
- Even light rain below 1 mm is enough to clean cover glass, reducing losses to below 5%. Note that this study defines the soiling loss of a "clean" panel at a higher value (5%) than most other studies [115].
- When comparing locations, some sets of locations had the same soiling rates but different soiling losses, mainly due to different rainfall amounts. Precipitation of 0.5 mm was enough to clean systems that had less than 10% soiling loss. For systems with higher soiling losses, higher precipitation amounts were needed. (Atacama desert) [89].
- Precipitation amounts of 5 mm or less have the effect of promoting soiling, but amounts of > 15 mm have a cleaning effect (Zimbabwe) [116].
- The rainfall threshold needed for effective cleaning varies from 0.3 mm to 20 mm. Variation in values can be attributed to the complexity of surface cleaning by falling droplets, where surface wettability, dust type, impact velocity of the droplet, surface incline angle, dust adhesion state (cemented, caked, aged) all affect the cleaning effectiveness. Dew could also clean the surface but has been observed to do so rarely (Review paper describing multiple locations) [74].
- Soiling loss was reduced by 0.5-1%/mm of rainfall when daily rainfall was > 2 mm. Some increases in soiling loss were observed when daily rainfall was <2 mm (Arizona) [117].

Given the wide variability in the observed effectiveness of panel cleaning by rainfall, our model requires a user input (named *Rainfall Clean Amount*) that specifies the amount of rainfall that

results in a perfect or near-perfect clean. The quality of the cleaning effect of rainfall is specified in terms of the soiling loss remaining after a rainfall event with precipitation amount reaching the Rainfall Clean Amount. We assume that any rainfall less than the Rainfall Clean Amount results in a partial cleaning that is proportional to the rainfall divided by the Rainfall Clean Amount. For example, if 6 mm of rainfall is needed for a clean which leaves 5% soiling loss (Rainfall Clean Quality = 5%), then 2 mm will result in a  $0.33 \cdot 0.95 = 31.35\%$  reduction in the soiling amount. Users can also specify a minimum hourly rainfall rate threshold needed to result in a cleaning effect. Further details about the rainfall cleaning model parameters are described in Appendix A. Figure 5.10 shows an example of the reduction in soiling losses due to rain. Note that in contrast to the soiling amount, the soiling losses, which are defined as an energy loss, are zero when there is no sunlight.

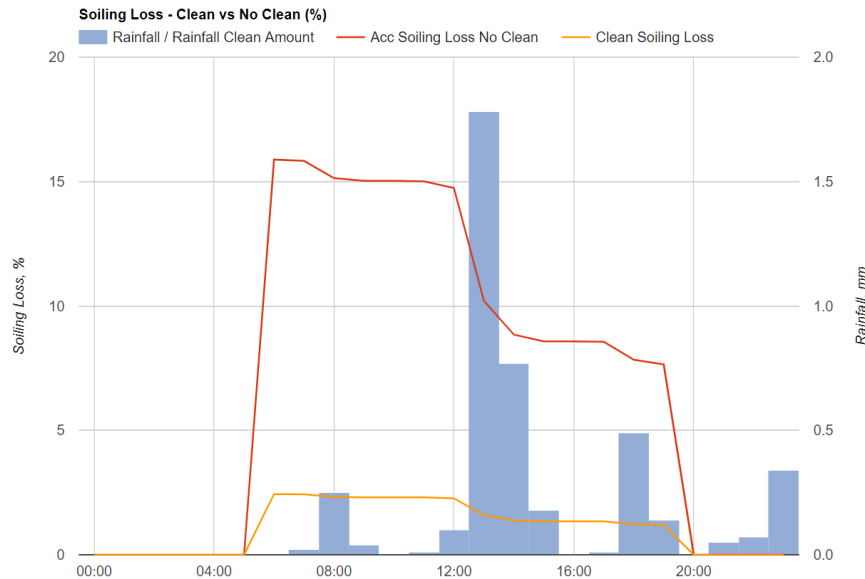


Figure 5.10: Reduction in soiling losses due to rainfall. This plot is from Enlighten Energy’s PV SoilSayer software, which contains an implementation of the soiling model described here.

The wetting of the ground due to rainfall has been observed in some studies to result in a slowing or even temporary stopping of soiling accumulation for some time after the rainfall event. This can be highly location-dependent and also dependent on the dominant source of soiling. For example, if the source of soiling is dust from the ground, then it is likely that a wet ground will not result

in any significant soiling. However, if the source of soiling is pollution from a nearby factory or pollen from nearby trees, this concept may not apply. Some models assume a *Grace Period*, which is the period of time after a rainfall event where there is no soiling accumulation [80, 84, 89]. The length of the Grace Period varies depending on the model, with typical values ranging from 5 to 21 days. Due to this effect's location-dependence, if the Grace Period due to precipitation was used in our model, it would have to be provided by the user based on local measurements. Since the Grace Period phenomenon was only observed in a few studies (and even these studies observed it on only some of their sites) and none of our measured soiling data supports the concept of a Grace Period, we have not incorporated this into the model.

#### **5.4 Incidence Angle Modifier due to Soiling**

The losses due to soiling are also influenced by the angle of incidence (AOI) of the incoming solar radiation. Multiple studies [81, 82, 89, 99, 115, 118] have found that the losses due to soiling are significantly increased at larger AOIs. The AOI of direct solar radiation depends on the sun's position in the sky and the solar panel tilt angle, which is variable for panels that track the sun (single-axis trackers). It may not be cost-effective to clean modules that track the sun due to the lower impact of soiling in these modules due to the lower AOIs that they experience [81]. On sunny days, losses have been found to be symmetric about solar noon, where they reach a minimum [89, 115]. Changes in angular response are likely due to changes in the optical path length (OPL) of the direct radiation through absorbers and scatterers in the dust layers over the PV module; a shorter OPL (e.g. at noon) leads to less attenuation of direct irradiance that reaches the module surface, while longer OPL leads to more attenuation, enhancing soiling effects [89]. On cloudy days, where global irradiance is mostly composed of diffuse radiation, losses appear to be mostly independent of AOI, probably due to the isotropic nature of diffuse radiation [115]. Since the proportion of diffuse to direct solar irradiance varies from day-to-day, models that attempt to describe the IAM due to soiling need to consider separately diffuse and direct irradiance.

Martin and Ruiz developed an experimentally-validated analytic model (we will call this the



MR model) that describes soiling-dependent losses due to incident light that is not perpendicular to the solar panel surface [119–121]. These losses include angle of incidence effects and effects due to the relative proportions of direct, diffuse, and ground-reflected solar irradiation. In this section, we will describe this model, and in the next section, we will combine the MR model with the soiling accumulation model to achieve a more comprehensive model for soiling losses.

The MR model was obtained from the optical analysis of commercial PV modules of different technologies. In order to accurately describe the angular losses, the MR model considers the following four solar radiation contributions: direct normal, diffuse horizontal-circumsolar, diffuse horizontal-isotropic, and ground-reflected. Direct normal irradiance (DNI) is measured at the Earth’s surface with a surface element perpendicular to the Sun and is equal to the extraterrestrial irradiance above the atmosphere minus the atmospheric losses due to absorption and scattering. Diffuse horizontal irradiance (DHI) is the radiation at the Earth’s surface from light scattered by the atmosphere. Under the Hay and Davies diffuse model, DHI is divided into circumsolar and isotropic components with *circumsolar* referring to the light that has the apparent origin in the region of the sky around the sun, and *isotropic* referring to the remaining portion of diffuse that is approximately isotropic across the sky. Ground-reflected irradiation is the irradiation received from above a horizontal surface after it is reflected from the ground. It depends on the reflectivity of the ground surface, known as albedo. Each of these irradiances can be further transposed to calculate the plane-of-array (POA) irradiance, which is the portion of the radiation that hits a tilted surface (in our case, the solar panel).

The short circuit current of a solar cell can be expressed in terms of the plane-of-array irradiance from the four solar radiation contributions described above as

$$I_{sc} = \frac{\tilde{I}_{sc}}{\tilde{G}} \left[ E_{dir}^{POA}(1 - F_B) + E_{dif,circ}^{POA}(1 - F_B) + E_{dif,iso}^{POA}(1 - F_D) + E_{alb}^{POA}(1 - F_A) \right] \quad (5.35)$$

where  $E_{dir}^{POA}$ ,  $E_{dif,circ}^{POA}$ ,  $E_{dif,iso}^{POA}$ , and  $E_{alb}^{POA}$  denotes POA direct, POA diffuse-circumsolar, POA diffuse-isotropic, and POA ground-reflected irradiance, respectively.  $\tilde{I}_{sc}$  is the short-circuit current under a direct irradiance of  $\tilde{G}$ , and the  $F_B$ ,  $F_D$ , and  $F_A$  are empirical angular loss factors that account for soiling losses due to non-perpendicular incident light. To calculate the POA diffuse irradiance,

the MR model uses the Hay-Davies transposition model [122]

$$E_{dif}^{POA} = E_{dif,circ}^{POA} + E_{dif,iso}^{POA} = E_{dif} \left[ \frac{E_{dir} \cos(\alpha)}{E_{etr} \cos(\theta_z)} + \left( 1 - \frac{E_{dir}}{E_{etr}} \right) \frac{1 + \cos(\theta_T)}{2} \right] \quad (5.36)$$

where  $\theta_z$  is the solar zenith,  $\theta_T$  is the tilt angle of the solar panel,  $E_{etr}$  is extraterrestrial irradiance, and  $\alpha$  is the angle of incidence. Transposition of direct normal irradiance to POA irradiance is given simply by

$$E_{direct}^{POA} = E_{dir} \cos(\alpha) \quad (5.37)$$

Ground-reflected irradiance can be expressed as

$$E_{alb}^{POA} = aG \frac{1 - \cos(\theta_T)}{2} \quad (5.38)$$

where  $G$  is ground horizontal irradiance, which is the total amount of radiation received from above by a surface horizontal on the ground, and  $a$  is the albedo coefficient.

Substituting Equations 5.36-5.38 into 5.35, we get the main equation of the MR model

$$I_{sc} = \frac{\tilde{I}_{sc}}{\tilde{G}} \left[ E_{dir} \cos(\alpha) [1 - F_B] + E_{dif} \frac{E_{dir} \cos(\alpha)}{E_{etr} \cos(\theta_z)} [1 - F_B] + \right. \quad (5.39)$$

$$\left. + E_{dif} \left( 1 - \frac{E_{dir}}{E_{etr}} \right) \frac{1 + \cos(\theta_T)}{2} [1 - F_D] + aG \frac{1 - \cos(\theta_T)}{2} [1 - F_A] \right] \quad (5.40)$$

The angular loss factors are defined by

$$F_B(\alpha) = \frac{\exp(-\cos(\alpha)/a_r) - \exp(-1/a_r)}{1 - \exp(-1/a_r)} \quad (5.41)$$

$$F_A(\theta_T) \approx \exp \left[ -\frac{1}{a_r} \left( c_1 \left( \sin\theta_T + \frac{\theta_T - \sin\theta_T}{1 - \cos\theta_T} \right) + c_2 \left( \sin\theta_T + \frac{\theta_T - \sin\theta_T}{1 - \cos\theta_T} \right)^2 \right) \right] \quad (5.42)$$

$$F_D(\theta_T) \approx \exp \left[ -\frac{1}{a_r} \left( c_1 \left( \sin\theta_T + \frac{\pi - \theta_T - \sin\theta_T}{1 + \cos\theta_T} \right) + c_2 \left( \sin\theta_T + \frac{\pi - \theta_T - \sin\theta_T}{1 + \cos\theta_T} \right)^2 \right) \right] \quad (5.43)$$

where  $F_A$  and  $F_D$  are approximations to the solutions of integrals that consider the contribution of each solid angle from which light is incident on the PV module.

The parameter  $a_r$  is the angular losses empirical coefficient. The MR model was developed such that a perfectly clean panel has  $a_r = 0.16 - 0.17$ . A panel with "moderate dust quantity" which is described as a 2% loss in short-circuit current, has  $a_r = 0.20$ , and a panel with a "high" amount of dust (8% loss in short-circuit current) has  $a_r = 0.27$ . On clear days, angular losses are dominated by the direct irradiance loss factor  $F_B$ . Perfectly clean panels still have optical losses at higher AOI due to the reflection of light by the panel surface. The losses significantly increase with soiling. The diffuse and albedo angular loss factors only depend on  $a_r$  and the panel tilt angle. Since these describe losses due to scattered/reflected light, they are independent of the AOI. Figure 5.11 show these loss factors as a function of tilt angle for a clean and dirty panel. The albedo angular loss function goes to one at zero tilt angles since there is no contribution to short-circuit current from ground-reflected light when a panel is perfectly horizontal.

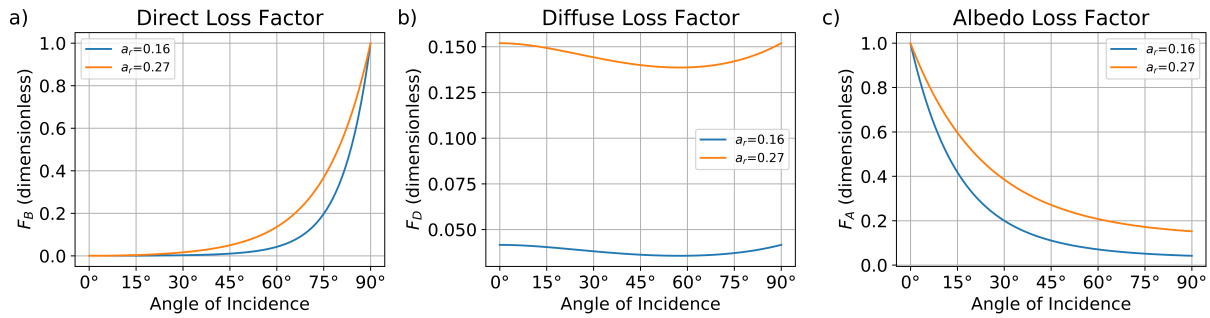


Figure 5.11: Empirical angular loss factors for direct (a), diffuse (b), and albedo (c) irradiance as functions of angle of incidence for two angular loss coefficients ( $a_r$ ).

## 5.5 Combining Incidence Angle Modifier with Soiling Accumulation Models

The soiling accumulation models and MR soiling loss model can be combined to allow for a predictive model of both soiling accumulation and its resulting energy production losses. We realize that Martin and Ruiz's soiling coefficient is approximately proportional to the amount of soiling on the panel. Thus, while Martin and Ruiz use the soiling coefficient only to describe angular reflection losses, we can also use it to describe the transmission losses due to surface area coverage of soiling. We model the total hourly soiling losses ( $L_{tot}^{soiling}$ ) in terms of a transmission

loss ( $L_{trans}^{soiling}$ ) and additional angular reflection losses due to soiling ( $L_{ang}^{soiling}$ ). Percentage losses are multiplicative, with the overall loss being

$$L_{tot}^{soiling} = 1 - (1 - L_{trans}^{soiling})(1 - L_{ang}^{soiling}) \quad (5.44)$$

For the angular losses, we want to isolate the additional losses due to soiling from the total angular losses to properly calculate the impact of soiling on PV power production. Therefore, angular losses that exist on perfectly clean panels are excluded from the calculation of the soiling loss. The overall contribution to soiling losses due to increased angular losses is expressed as the product of the relative percent increase in angular losses due to soiling and the percent angular losses of a clean panel.

$$L_{ang}^{soiling} = \left( \frac{I_{sc}^{clean}(\alpha)/\tilde{I}_{sc} - I_{sc}^{dirty}(\alpha)/\tilde{I}_{sc}}{I_{sc}^{clean}(\alpha)/\tilde{I}_{sc}} \right) \quad (5.45)$$

where  $I_{sc}(\alpha)/\tilde{I}_{sc}$  is found using the MR Equation 5.39. Note that by expressing the loss in terms of the ratios of short-circuit current at an AOI to the nominal short-circuit current ( $\tilde{I}_{sc}$ ), the loss can be calculated in terms of the irradiance components and angular loss factors, without knowledge of the nominal short-circuit current. A value of 0.16 is used for the angular loss coefficient for the clean panel's  $I_{sc}$  ratio. The dirty panel's  $I_{sc}$  ratio is calculated using an angular loss coefficient estimated from the soiling mass accumulation model as described below.

We adapt our soiling accumulation model to calculate the daily accumulated soiling in terms of an MR angular loss coefficient (we refer to this as the *soiling coefficient*) by scaling the accumulated soiling mass to produce soiling coefficients that match with experimental angular soiling loss data. The scaling coefficient is similar in concept to the  $\gamma$  parameter which is used to convert soiling mass to clearness index change in Guo et al.'s model (see Section 5.2.2). A multiplicative scaling of the soiling mass (in kg) by 28.5 was chosen. The scaling will likely need to be adjusted for some geographic regions, due to different compositions of soiling. This adaptation can also be done with other soiling mass accumulation models.

The hourly transmission loss is empirically related to the difference between dirty and clean panel soiling coefficients. According to Martin and Ruiz, an angular loss coefficient of 0.27

corresponds to a panel with 8% soiling loss at zero AOI, and a coefficient of 0.16 corresponds to a perfectly clean panel. Therefore, an approximation can be made that for each 1% soiling loss at zero AOI (this isolates the transmission portion of the soiling loss), the angular loss coefficient must increase by  $c = (0.27 - 0.16)/8 = 0.01375$ . The transmission loss due to soiling is defined as

$$L_{trans}^{soiling} = c(a_r^{dirty} - a_r^{clean})/100 \quad (5.46)$$

For soiling accumulation models that express soiling in terms of a percentage energy loss, the percentage is approximately converted to a soiling coefficient, based on the soiling loss at solar noon (equivalent to the transmission loss) using Equation 5.46. In this way, we can use hourly or daily weather data (rainfall, wind speed, PM10, and relative humidity) to calculate the hourly soiling coefficients for use in the MR equations that compute angular soiling losses.

Figure 5.12 shows the soiling loss profile on a clear day as predicted by our combined model. We can see the characteristic shape of the curve as reported in experimental studies where losses are highest close to the beginning and end of each day due to the higher angle of incidences at these times [123].

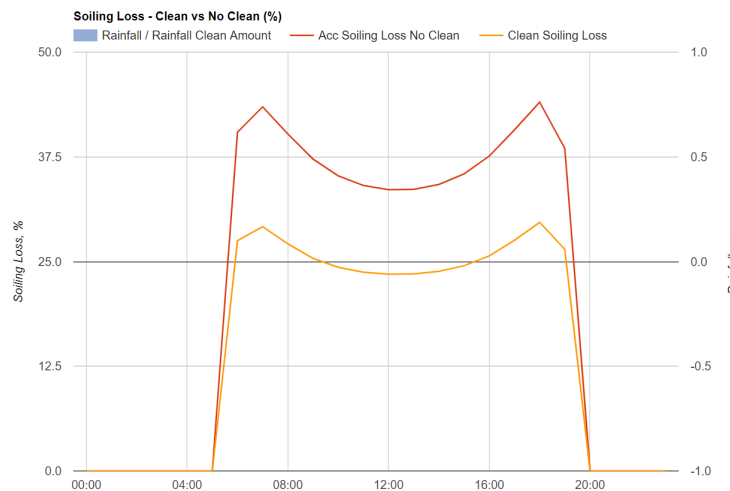


Figure 5.12: Hourly soiling loss profile over a single day for two different panels: a "no clean" panel that was never cleaned and a "clean" panel that is periodically cleaned according to a cleaning cycle. This plot is from Enlighten Energy's PV SoilSayer software, which contains an implementation of the soiling model described here.

## 5.6 Model Validation

The semi-physical soiling accumulation model was validated by comparing its predictions with a soiling study published by NREL [124]. In this study, NREL monitored the soiling rate and precipitation for 20 sites. For verification, we selected Site 3 (Calipatria, CA) and 11 (Lamont, CA) from the study, which had less noisy data and more significant observed soiling (many of the sites had yearly average soiling ratios that were greater than 99%). Site 3 is a single-axis tracker, while Site 11 is a fixed tilt ( $20^\circ$ ) system, so this site selection allowed testing the soiling models for both types of systems. Inputs to the soiling model were daily precipitation data provided in NREL's publication, hourly weather data for the year when the soiling measurements were taken downloaded from NSRDB [125], and monthly average particulate matter data taken from the US Environmental Protection Agency's (EPA) database [126]. The daily precipitation data was converted to an hourly format by dividing by 24. We compared the yearly average soiling rates, which are computed by taking the average of the soiling rates during the dry periods. For both sites, the model's soiling rates matched with NREL's measured values to within 0.01%/day (Site 3 had 0.1%/day and Site 11 had 0.13%/day).

Additionally, we compared the soiling accumulation time-series. Figure 5.13a shows the comparison for NREL Site 3 when using unmodified input data, as described above. The predicted soiling rate during the dry period matches the measurements, but there are discrepancies in the effect of rainfall. One possible reason for these discrepancies are that the daily rainfall data lacks information about rain intensity (mm/hr), while the same amount of daily rain can be more or less effective in cleaning depending on its intensity. Secondly, NREL's publication provides rainfall data from an online database (PRISM [127]), instead of measuring it directly at the sites. This could mean that the off-site PRISM data measured a different amount of rain than occurred at the site. For a proof of concept, we adjusted the rainfall amounts of a few rain events where the measured effect of rain was different than predicted (Table 5.2). Note that we did not change the main rainfall pattern (dates when significant rain of more than 1 mm occurred).

Table 5.2: Daily rainfall adjustments needed to account for measured soiling ratio time-series for NREL Site 3.

Date	Original Rainfall (mm)	Adjusted Rainfall (mm)
Apr 24	1.04	0.13
Jun 8	0.354	1
Jul 18	3.64	4.64
Sep 7	0.4	0
Oct 15	3.1	7

Figure 5.13 shows the forecast with these adjustments to the rainfall input data. Changes to decrease rainfall can be justified as follows. The rainfall could have been very light and distributed throughout the day, leading to almost no cleaning effect. For example, often rainfall of less than 0.5 mm/hr does not result in a cleaning effect [117]. However, the dataset does not contain information about rainfall intensity. Changes to increase rainfall can be justified by the chance that the rainfall could have been higher at the site than the PRISM database value or more effective at cleaning than predicted.

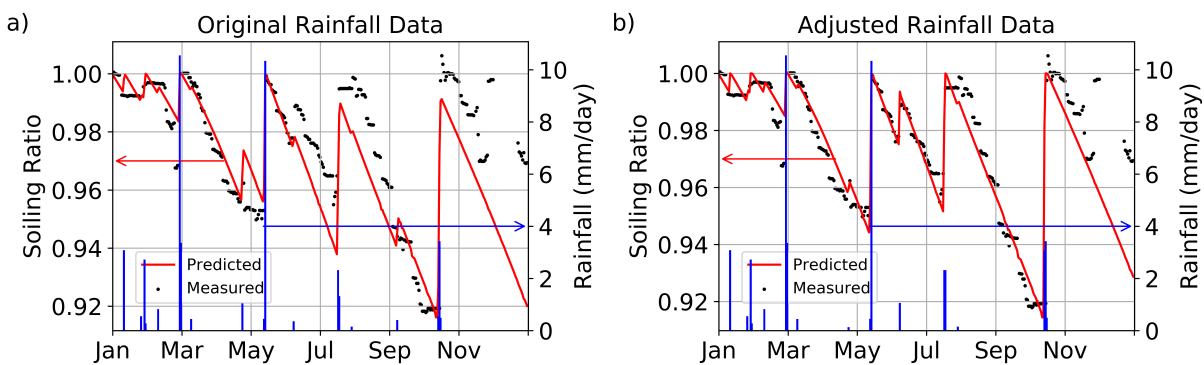


Figure 5.13: Comparison of model predictions with NREL Site 3 (Calipatria, California) when using precipitation data provided by NREL (a) and when using modified rainfall data (b).

We repeated the same validation approach for NREL Site 11 (Lamont, CA) with the results without and with adjustment to the rainfall shown in Figure 5.14. With this site, we had to add a

few partial rainfall clean events to account for the measured increases in the soiling ratio that did not correspond to any recorded rainfall. The changes to rainfall are listed in Table 5.3.

Table 5.3: Daily rainfall adjustments needed to account for measured soiling ratio time-series for NREL Site 11.

Date	Original Rainfall (mm)	Adjusted Rainfall (mm)
Apr 29	0	0.25
May 24	0	0.75
Aug 15	0	0.2
Oct 8	0.65	2.3

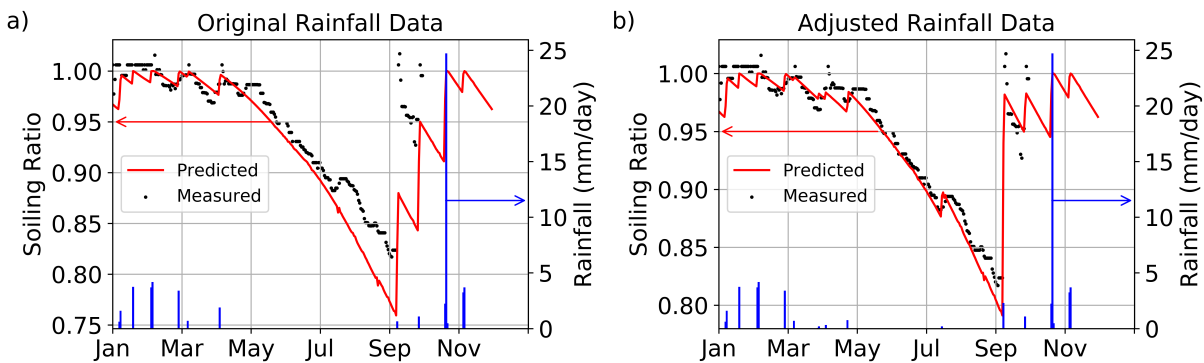


Figure 5.14: Comparison of model predictions with NREL Site 11 (Lamont, California) measured data when using precipitation data provided by NREL (a) and when using modified rainfall data (b).

In conclusion, model validation showed an excellent agreement between measured and predicted dry period soiling rates but a difficulty in predicting the effectiveness of rainfall in cleaning the panels. Modifying the rainfall to change its effectiveness in cleaning allowed to account for most of the discrepancies between measured and predicted data. This demonstrates the need for reliable hourly rainfall data measured on-site and further research into understanding rainfall’s effectiveness in cleaning panels as a function of the rain intensity and amount.



## 5.7 Integration into Commercial Software

The ultimate goal of PV soiling modeling is to evaluate the impact of soiling on a PV system's energy production and optimize panel cleaning schedules. Here we briefly describe the integration of the soiling loss prediction models into a brand new commercial software, Enlighten Energy's PV SoilSayer. PV SoilSayer is a web application that provides users with soiling loss estimates and optimal cleaning cycle forecasts in order to improve the accuracy of PV energy production models, minimize operational costs, and maximize PV system performance [128]. It consists of models from the open-source PV modeling Python package PVLIB (version 0.7.2) [129], soiling models developed in this dissertation, and Enlighten Energy's proprietary optimal cleaning cycle algorithms, which find an optimal cleaning schedule for the power plant that will minimize financial losses due to soiling, taking into account the cost of cleaning. PVLIB only has two soiling models: the industry-standard Kimber model, which assumes a constant daily soiling rate and rainfall cleaning threshold, and the newer HSU (Humboldt State University) model, which uses particulate matter data and user-specified deposition velocity (or an assumed default value) to estimate the effect of deposited mass on the soiling ratio through an empirical equation. Both of these models have limitations. The Kimber model requires knowledge of the soiling rate, is not able to capture seasonal changes in the soiling rate, and uses over-simplified assumptions about rainfall cleaning. The HSU model does allow capturing local changes in soiling rates through the particulate matter data, but requires knowledge of the deposition velocity (which can vary by location), does not consider any effects of wind speed or humidity, and makes the over-simplified assumption that panels are perfectly cleaned with each rainfall greater than 1 mm [94]. In an attempt to overcome some of these limitations and gain better accuracy in predicting soiling losses and optimal cleaning cycles on the daily resolution, the soiling loss models described in this chapter were integrated into PV SoilSayer.

Figure 5.15 shows a flow-chart of the approach used to incorporate the soiling loss models that were developed in this work into PV SoilSayer. The work-flow of using PV SoilSayer is as follows. First, users select weather data (typical meteorological year, historical, or next year forecast) from

one of several sources by entering the PV system’s location. Users then specify system design parameters such as power ratings, tilt angle, module type, cell type, array type, and ground-reflection coefficient (albedo). Users also specify the DC-to-AC inverter efficiency and other fixed losses such as those due to wiring, age, light-induced degradation, shading, and snow. Next, users select one of several soiling loss models with options including using the semi-physical model described in this chapter, specifying constant daily soiling rates for each month, and uploading measured weather and soiling data. Users also have control over the effects of rain, such as the amount of rain necessary to significantly clean a panel, the minimum amount of rain needed to achieve a partial reduction of soiling, and the amount of soiling left after non-perfect rain cleanings. These inputs are expected to be determined from empirical observation. Finally, users can select one of several cleaning cycle optimization algorithms. The soiling loss and cleaning cycle algorithms predict a one year PV system performance forecast and an optimal cleaning schedule. The results include a comparison (both through yearly values and dynamic yearly, monthly, and daily plots) of the predicted losses when no panel cleaning is performed ("No Clean" case) and losses when panel cleaning is performed according to the calculated cleaning schedule ("Clean" case). The recommended calendar dates for cleaning are reported. Appendix A describes PV SoilSayer in more detail.

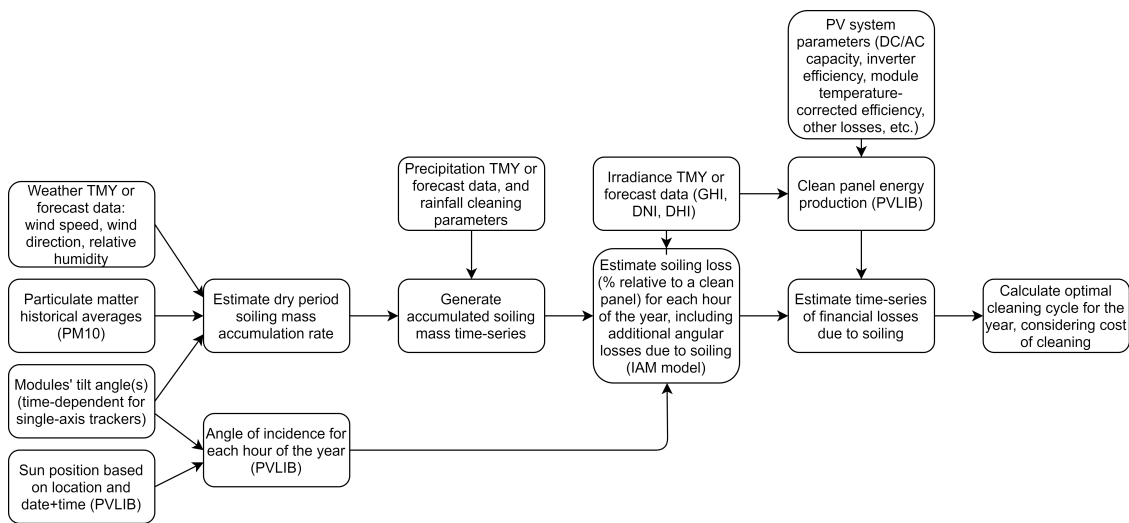


Figure 5.15: Flow-chart of the approach used to incorporate the soiling loss models that were developed in this work into PV SoilSayer.

Figures 5.16-5.18 show an example results report from PV SoilSayer for a fictional 300 megawatt solar power plant in Calexico, CA. In this sample forecast, the cleaning optimization predicts that two manual clean events, on April 25 and June 13, results in the highest net revenue. We see from the *Total Value of Energy Gain* that the first clean event is expected to save approximately \$0.6 million and the second saves \$1.1 million in soiling losses, before considering the cleaning cost of \$250,000 per clean. The *Payoff Date* shows the estimated date after which the gain in energy due to cleaning will become greater than the cost of cleaning. The average daily and hourly soiling rates during dry periods for each month are also shown. The daily soiling rates range from 0.16% to 0.33%, which is consistent with Kimber's findings of daily dry period soiling rates of 0.1% – 0.3% for California [80]. The average monthly soiling ratios for the plant if it is cleaned according to the optimal cleaning schedule versus not cleaned are also shown.

Sites Weather Resources PV System Info Soiling Profile Cleaning Configuration **Report**

### System Inputs

Project Name	Location	Weather Resource	DC System Size	AC System Size	Module Type	Mounting System
Calexico Test	calexico, CA	MeteoNorm 7.2	300000 kWp DC	270000 kWp AC	Glass Backsheet	Mounting: 1 Axis Backtracking

Max Tracker Angle	Elevation Angle	Azimuth Angle	Inverter Efficiency	Ground Coverage Ratio	System Loss Factor
55	0	180	98	0.4	4.43%

Soiling Profile	Rainfall Clean Amount	Value of Energy	Cost of Cleaning	Angular Soiling Losses
Soiling Calculator	Minimum: 2 mm/m <sup>2</sup> /hr Maximum: 5 mm/m <sup>2</sup> /hr Rainfall Clean Quality: 1%	\$ 0.065 / AC kWh	\$ 250000 / Clean	Calculate Soiling Losses due to Sun Angle

Clean Cycle Configuration	Number of Days to Clean	Manual Clean Quality
Optimal Clean Cycle Resolution: Daily Start Date: 2020-01-01 Starting DC Soiling Ratio: 0%	10	0 %

### Total Annual Events

Total Rainfall Clean Events	Total Muddy Rain Events	Total Sandstorm Events	Total Manual Clean Events
8	0	0	2

### Total Annual No Clean Losses

Total Amount of AC Energy Produced No Clean	Avg AC Annual Soiling Loss % No Clean	Total Amount of AC Energy Lost No Clean	Total Cost of AC Energy Lost No Clean
596,653,261.64 kWh	8.79%	57,509,092.24 kWh	\$3,738,091.00

### Total Annual Clean Losses

Total Amount of AC Energy Produced Clean	Avg AC Annual Soiling Loss % Clean	Total Amount of AC Energy Lost Clean	Total Cost of AC Energy Lost Clean
623,959,479.69 kWh	4.62%	30,202,874.18 kWh	\$1,963,186.82

### Total Annual Cost Savings - No Clean vs. Clean

Total Amount of AC Energy Gain Clean vs. No Clean	Total Value of AC Energy Gain Clean vs No Clean	Total Cost of Cleaning	Total Net Annual Revenue Gain Clean vs No Clean
27,306,218.05 kWh	\$ 1,774,904.17	\$ 500,000.00	\$ 1,274,904.17

Figure 5.16: Beginning of PV SoilSayer results report, showing the forecast inputs and comparison of the predicted annual energy production and soiling losses for a system that is never cleaned ("No Clean" case) versus a system that is cleaned according to an optimized cleaning schedule ("Clean" case).

### Manual Clean Events

Manual Clean Date	Payoff Date	Total AC Energy Gain	Total Value of Energy Gain
Apr 25, 2020	May 18, 2020	9,838,361.79 kWh	\$ 639,493.52
Jun 13, 2020	Jun 27, 2020	17,467,856.26 kWh	\$ 1,135,410.66

### Average Soiling Rates

Units	Jan	Feb	Mar	Apr	May	Jun	Jul	Aug	Sep	Oct	Nov	Dec
Avg. Daily Soiling Rates, %	0.2370	0.2107	0.1851	0.1749	0.1615	0.1916	0.3029	0.2461	0.2081	0.2583	0.3251	0.3348
Avg. Hourly Soiling Rates, %	0.0099	0.0088	0.0077	0.0073	0.0067	0.0080	0.0126	0.0103	0.0087	0.0108	0.0135	0.0140

### Average Soiling Ratios - Clean

Units	Jan	Feb	Mar	Apr	May	Jun	Jul	Aug	Sep	Oct	Nov	Dec
Avg. DC Soiling Ratios, %	2.3105	3.8630	5.2220	5.5025	2.9689	4.3598	4.0087	6.9562	4.0098	4.8698	6.8194	4.7848
Avg. AC Soiling Ratios, %	2.3224	3.8809	5.2190	5.4929	2.9640	4.3500	3.9959	6.9770	4.0124	4.8871	6.8629	4.8198

### Average Soiling Ratios - No Clean

Units	Jan	Feb	Mar	Apr	May	Jun	Jul	Aug	Sep	Oct	Nov	Dec
Avg. DC Soiling Ratios, %	2.3105	3.8630	5.2220	6.1003	11.0978	16.6616	16.9113	12.3313	4.0098	4.8698	6.8194	4.7848
Avg. AC Soiling Ratios, %	2.3224	3.8809	5.2190	6.0897	11.0889	16.6596	16.9253	12.3753	4.0124	4.8871	6.8629	4.8198

### Annual PV Clean Cycle Calendar

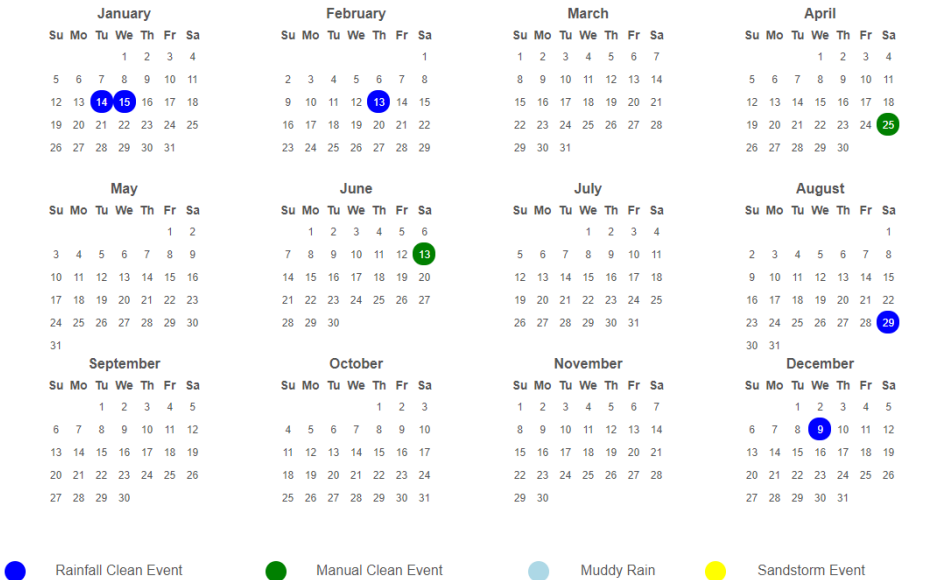


Figure 5.17: Optimal manual cleaning dates and soiling rates results page from a sample PV SoilSayer forecast.

The last portion of the report contains interactive plots for visually comparing the predicted soiling losses, energy production, and energy losses for the plant with and without manual cleanings. Figure 5.18 shows two of these plots.

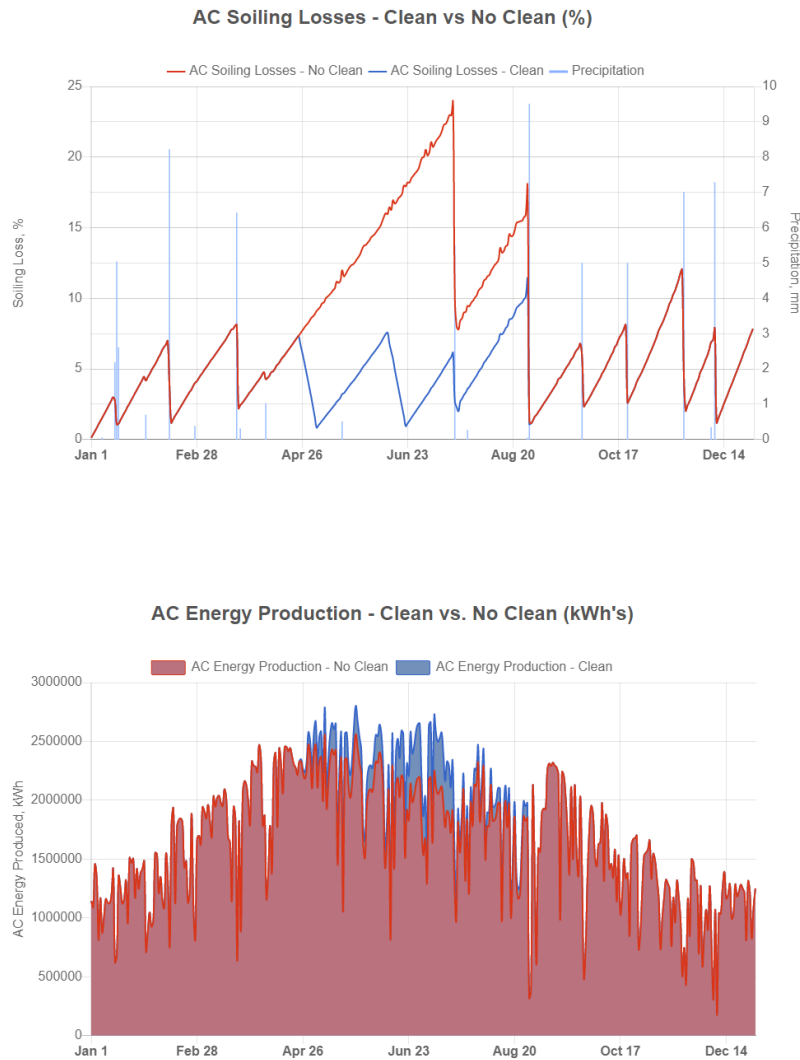


Figure 5.18: Visualization of soiling losses and energy production from a sample PV SoilSayer forecast. The sharp reductions in soiling loss correspond to manual and rainfall cleanings of the panels.

One can also view plots that show the energy production and soiling losses for any month or day in the year. Figure 5.19 visualizes the clean versus no clean system comparison for June. We see the drop in soiling loss of the "Clean" panel starting on June 13, which is the recommended cleaning date. The soiling loss drops over the course of ten days, since that is the user-specified

time required to clean the entire power plant. Note that the clean panel soiling loss never drops to zero because portions of the plant start accumulating soiling, while other portions of the plant are still undergoing cleaning. This demonstrates the importance of considering the time required to clean. After the cleaning event, we see a larger difference between the no-clean versus clean panel's energy production.

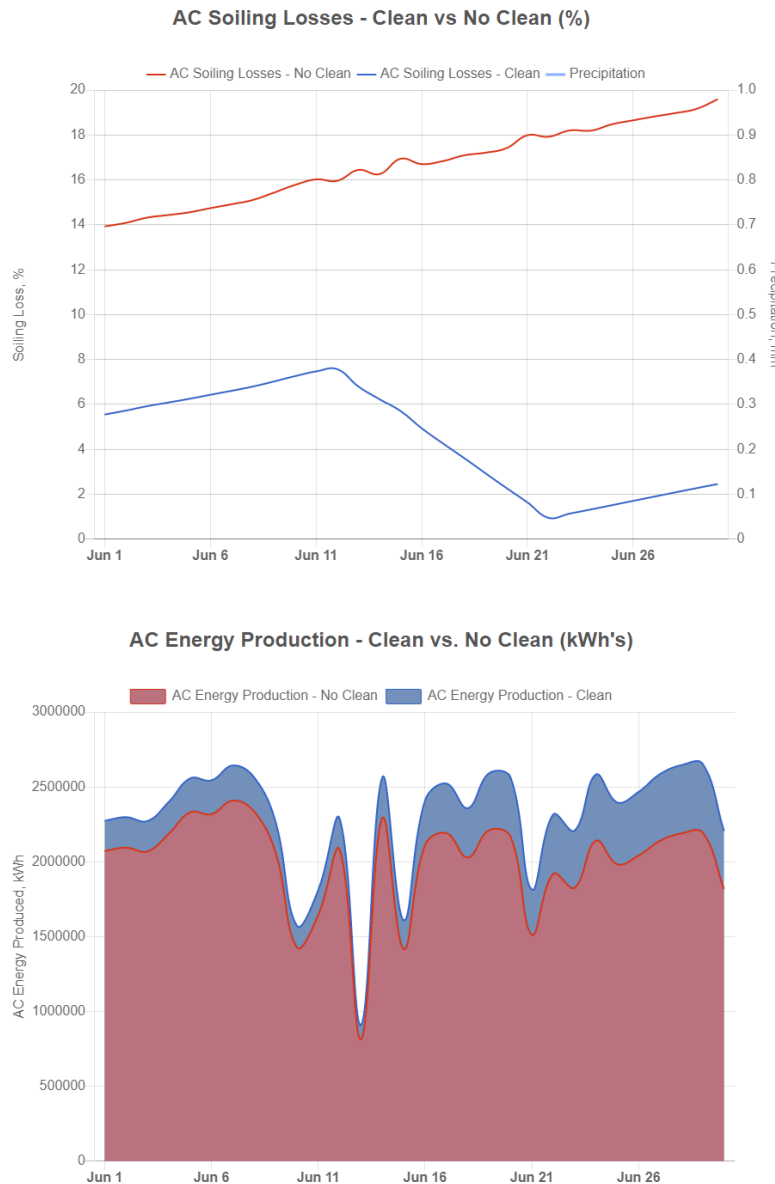


Figure 5.19: Visualization of soiling and energy production for a single month from a sample PV SoilSayer forecast. A manual cleaning event occurs from June 13 to June 22, reducing the soiling loss on the "Clean" panel and increasing the difference between "Clean" and "No Clean" panel energy production.

## Effect of Inverter Clipping

Our model considers the reduction of absorbed irradiance due to soiling, instead of applying an assumed soiling loss directly to the AC power output. Therefore, the model captures the impact of inverter clipping (the situation where the DC power production is greater than the AC inverter rating) on the AC power loss due to soiling. During times when inverter clipping occurs, meaning that part of the DC power is not converted to AC power, any DC soiling loss that is lower than the power loss due to clipping will not translate to an observable AC soiling loss. Thus on high irradiance days when inverter clipping occurs, the daily total soiling loss will be lower than on lower irradiance days. With alternating higher and lower irradiance days, the AC soiling losses will oscillate, as seen in Figure 5.20.

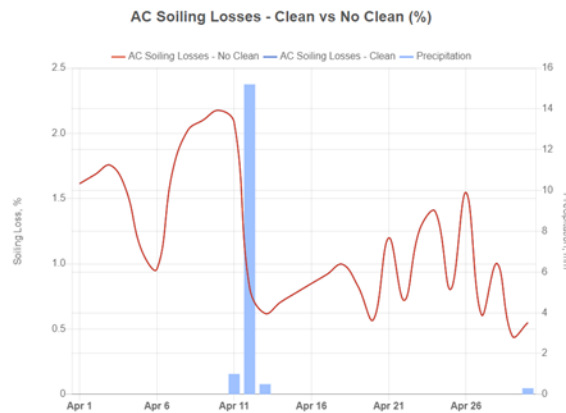


Figure 5.20: AC soiling loss with oscillations caused by inverter clipping.

To confirm that these oscillations are, in fact, due to inverter clipping, we can rerun the same forecast with the DC and AC system sizes set to be equal, thus removing the possibility of clipping. We now see an approximately linear increase in soiling since now the AC soiling loss is equal to the DC soiling loss (Figure 5.21).



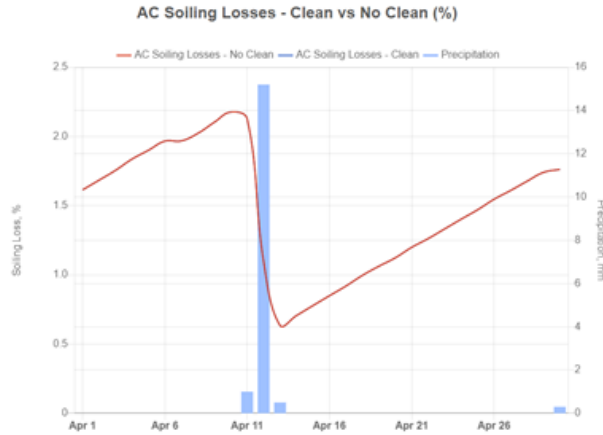


Figure 5.21: AC soiling loss for same forecast as Figure 5.20, but without inverter clipping.

### Sensitivity to Weather Parameters

PV soiling is highly dependent on the weather; therefore, it is important to consider the variation in soiling and optimized cleaning cycle predictions when weather predictions from different sources are used. As an example, Table 5.4 compares the one-year soiling and optimal cleaning forecast for a site in Lamont, California, when using four different weather resources available to users of PV SoilSayer: Meteonorm 30 year TMY, AccuWeather last year, AccuWeather next year prediction, and 10-year precipitation-based TMY generated from AccuWeather historical data.

Weather Resource	Annual Total Irradiance (W/m <sup>2</sup> )	Annual Precipitation (mm)	Longest Dry Period	Average Daily Soiling Rate (%/day)	# of Rainfall Cleans	Optimal # of Manual Cleans	Annual AC Soiling Loss of Never Cleaned PV	Annual AC Soiling Loss of Cleaned PV	Percent Increase in Revenue due to Cleaning
Meteonorm 30 Year TMY	1930	147	June-Sept	0.132%	17	3	5.4%	2.1%	2.1%
Precipitation P50 TMY	2129	70	April-Oct	0.129%	12	4	7.7%	2.1%	4.4%
AccuWeather Last Year	1988	235	July-Oct	0.131%	19	3	6.2%	2.1%	3.1%
AccuWeather Next Year	1925	161	June-Sept	0.131%	21	3	5.5%	1.7%	2.7%
Average	1993	153.25		0.131%	17.3	3.3	6.2%	2.0%	3.1%
Standard Deviation	95	68		0.001%	4	0.5	1.1%	0.2%	1.0%
Coefficient of Variation	5%	44%		1%	22%	15%	17%	10%	31.5%

Table 5.4: Variability of forecast for a site in Lamont, CA (NREL Site 11 from [124]) when using different weather prediction resources.

The different weather resources available for predicting next year’s weather vary significantly (coefficient of variability 44%) in their precipitation prediction, which impacts the soiling forecasts. For California, historical data suggests that the past ten years have on-average been drier than the past 30 years, which explains the low precipitation value in the precipitation-based 10-year TMY compared with the 30-year TMY. However, it seems like last year (2019) had significantly more precipitation than the 10-year median. AccuWeather’s prediction for next year shows precipitation that is more similar to last year than the 10-year TMY. The different weather resources also find different lengths of the summer dry period, ranging from 4-7 months and differing in the start and end month. As a result of these differences, the predicted soiling losses of a never cleaned panel are 5.5%-7.7%, and the expected revenue gain due to cleaning is 2.1%-4.4%. The average daily soiling rate is nearly identical for all weather resources since it is defined during dry periods only and most strongly dependent on particulate matter data that was taken from the same EPA data source for all four forecasts. Figure 5.22 compares the one-year soiling loss time-series prediction when using the four different weather resources. We see that the overall soiling pattern is consistent, but the soiling loss amounts and start and end of the summer dry period vary.

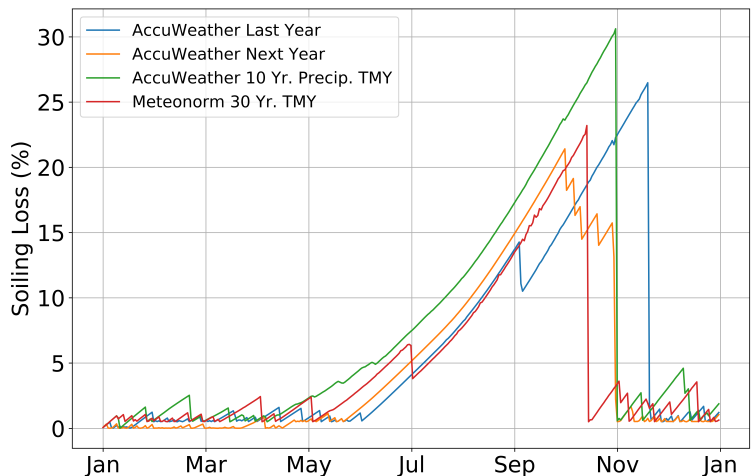


Figure 5.22: Comparison of soiling time-series predictions for a site in Lamont, CA (NREL Site 11 from [124]) when using different weather prediction resources.

While long-term weather prediction is outside the scope of this thesis, these results show that soiling loss prediction accuracy is limited by the accuracy of the weather prediction (especially of precipitation patterns). Even with a perfect soiling model, soiling forecasts may be very inaccurate if the year's precipitation pattern prediction is inaccurate. Therefore, future soiling models need to be combined with advanced long-term weather forecasting. (AccuWeather claims to provide this with their Next Year forecasts, but we could not find any peer-reviewed validation of their predictions). Additionally, it is important to consider the potential error due to weather predictions when interpreting soiling forecast results. Knowing the forecast's uncertainty can be just as important as the forecast itself since it allows investors, PV developers, and maintainers to make decisions based on the relationships between probability, risk, or reward. For example, we cannot be sure that a certain manual clean will save revenue (e.g. there could be a strong rainfall that cleans the panels right after investing in the manual cleaning). However, if the probability that a cleaning rainfall occurs during a traditionally dry period is very low and the soiling loss during this period is high, the risk to reward comparison would suggest that the plant be cleaned. In future soiling and cleaning optimization software, the forecasts should be rerun with 10th and 90th percentile precipitation predictions to bound the soiling prediction and show the possible variations in the optimal cleaning cycle.

## **5.8 Predicting Soiling with Machine Learning**

Even with reliable soiling data, semi-physical models will likely need to be custom-tuned to each region, and the equations that describe soiling in one region may not be fully applicable to another region. While optimization packages for deriving equation parameters are readily available, attempting to explain a very complicated process with a particular set of equations may over-constrain the problem and limit the ability of the model to predict soiling at some locations where non-typical processes may be occurring (e.g. additional soiling from a nearby factory, farm, or highway). Additionally, it is difficult, costly, and time-consuming to conduct experiments that isolate the coupled effects of particulate matter, wind speed, humidity, rainfall, and tilt angle, which

would be needed for a careful empirical fit of the equations. Therefore, once soiling data becomes widely available, data-driven machine learning (ML) approaches such as multiple linear regression (MLR) and artificial neural networks (ANN), where the predictive models are trained on site-specific historical data, will likely be preferable. Previous studies have employed MLR and ANN for soiling modeling and were able to achieve good prediction accuracy [90, 106, 116, 130–133]. In this section, we explore two ideas for using ML for soiling modeling. The first approach is to use ML for predicting a soiling mass accumulation rate from environmental variables, and then use a semi-physical model (based on known/measured optical properties of soiling) to predict the soiling loss based on the accumulated soiling mass. This approach could allow for the development of ML-based soiling accumulation models on a regional level that can be used to calculate a soiling loss based on each PV site’s configuration (considering properties such as PV panel type, orientation, inverter efficiency). In the second approach, one would use ML to directly predict the power production loss due to soiling based on environmental variables. This approach would likely be site-specific since both environmental variables and site configuration influence the soiling loss. In this section, we discuss the development of proof-of-concept MLR and ANN models using the above two approaches.

### 5.8.1 Introduction to MLR and ANN

The multi-variable linear regression approach aims to build a simple linear equation that relates a set of independent variables (i.e. predictors) to the dependent variable (i.e. response variable). The response variable  $y$  is expressed as a linear function of environmental variables ( $x_1, \dots, x_i$ )

$$y = a_0 + a_1x_1 + a_2x_2 + \dots + a_ix_i \quad (5.47)$$

The values of coefficients resulting in the smallest least-squares difference between modeled and measured results are found. A disadvantage of the MLR approach is that it assumes linear relationships between the independent variables and the response, which is not necessarily true for soiling.

An artificial neural network model is a mathematical representation of an interconnected system of neurons that interchange communication among themselves [131]. For curve fitting, ANNs are used to capture the relationships between a set of numerical input data and a set of numerical target data. An ANN consists of multiple layers of neurons: an input layer, one or more hidden layers, and an output layer (Figure 5.23). The input layer receives the input data points. A hidden layer manipulates the incoming data using an activation function,  $G$ , to define the output of each  $i$ th hidden neuron based on the received inputs. Finally, the output layer receives the processed information from the last hidden layer and computes the final prediction using

$$y = \sum_{i=1}^{N_{hidden}} \vec{\beta}_i G(\vec{w}_i \vec{x}_i + b_i) \quad (5.48)$$

where  $\vec{w}_i$  is the input weights vector that connects inputs to each  $i$ th hidden neuron,  $b_i$  is the input bias of each hidden neuron, and  $\vec{\beta}_i$  is the output weights vector that connects the outcomes of each hidden neuron to the output neuron.

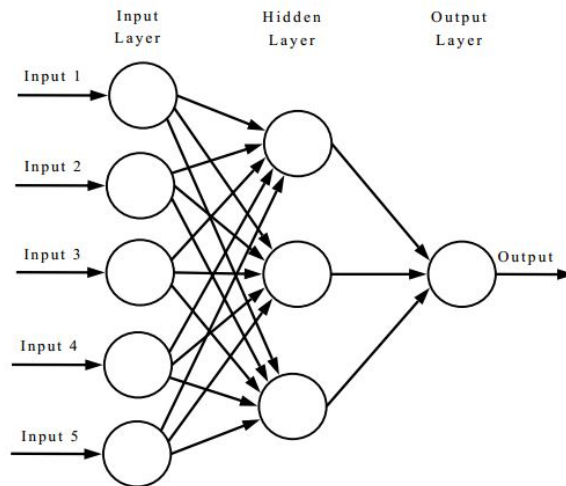


Figure 5.23: Diagram of an ANN. From [134].

For evaluation of machine learning model predictions, three metrics are often used: coefficient of determination ( $R^2$ ), mean squared error (MSE), and accuracy defined by mean absolute percent

error (MAPE). The  $R^2$  value describes the variability in the output based on the input variables as

$$R^2 = 1 - \frac{\sum_{i=1}^n (y_{measured,i} - y_{predicted,i})^2}{\sum_{i=1}^n (y_{measured,i} - \bar{y}_{measured})^2} \quad (5.49)$$

where the  $\bar{y}_{measured}$  is the average of all the measured values. A value of  $R^2 = 100\%$  means that all variability of the data is explained by the input variables, while a value of  $R^2 < 100\%$  means that other unaccounted factors are affecting the target data. The MSE is

$$MSE = \frac{1}{n} \sum_{i=1}^n (y_{measured,i} - y_{predicted,i})^2 \quad (5.50)$$

The accuracy is defined as

$$\text{Accuracy} = MAPE = \frac{1}{n} \sum_{i=1}^n \left( 1 - \left| \frac{y_{measured,i} - y_{predicted,i}}{y_{measured,i}} \right| \right) \times 100\% \quad (5.51)$$

## 5.8.2 Soiling Mass Accumulation

Due to a lack of reliable experimental data of soiling mass accumulation, this approach was tested on data generated from the semi-physical soiling model. Since the soiling model represents realistic soiling patterns, if the data-driven approaches (which receive no knowledge of the physical equations) are able to replicate the results of the soiling model, there is a reasonable chance that they will also be able to replicate measured soiling data. To develop the machine learning approach work-flow, we treat the soiling model's results (from a forecast for Riverside, California) as real measured data. The first step in developing a machine learning model is to analyze the correlations between the dataset's features. Here, we looked at both the Pearson Product-Moment and Spearman Rank-Order correlation coefficients by using the open-source Python packages Pandas and Seaborn. The Pearson correlation coefficient evaluates the linear correlation between two variables. Figure 5.24 visualizes the Pearson correlations between all of the input environmental variables used for the soiling model and the predicted soiling rate.

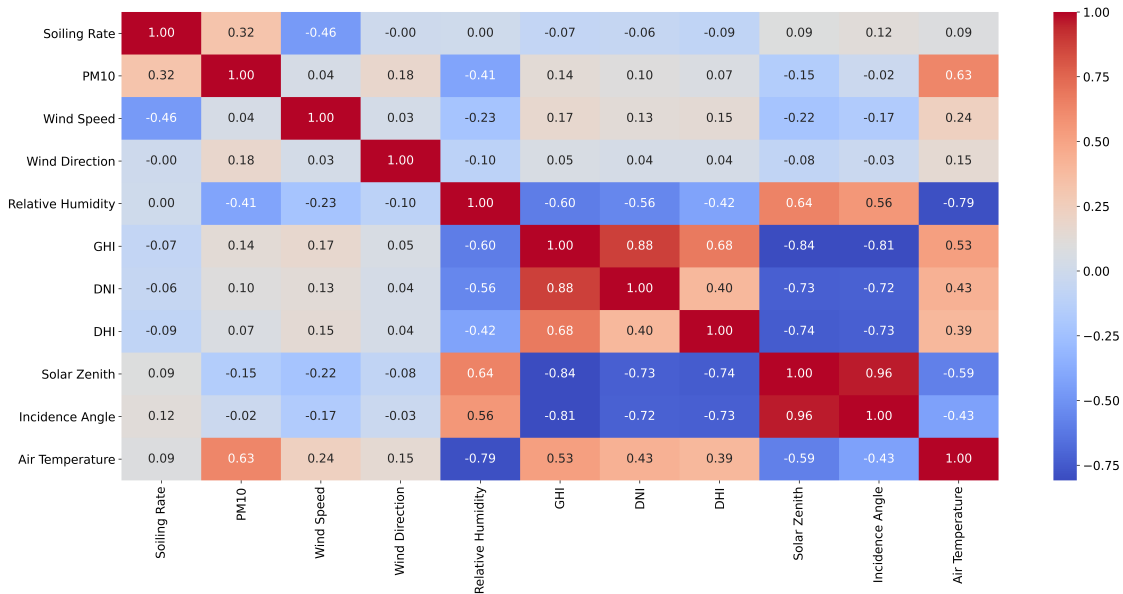


Figure 5.24: Heatmap of Pearson correlation coefficients between environmental variables and predicted soiling rate.

This heat map can elucidate the interactions between variables in a dataset. For example, we see a strong positive correlation between PM10 and air temperature. This could make sense since California (where the weather data is from) has less rainfall in the summers, which results in higher PM10 levels. Relative humidity is negatively correlated with air temperature and irradiance (GHI, DNI, DHI), which can again be explained by the drier summers. It is important to remember that the existence of a correlation between two variables does not necessarily mean there is a causality relationship. For example, while air temperature could be causing lower humidity, it likely does not directly cause a rise in PM10. Since our goal here is to develop an ML work-flow for predicting the soiling rate, we treat the predicted soiling rate as if it was a measured quantity and observe the correlations with other environmental variables. Looking at the correlation heat map, we see that soiling has a significant positive correlation with PM10 and a negative correlation with wind speed. Wind direction and relative humidity are found to have no linear correlation with the soiling rate. However, we cannot assume that there is no relationship between soiling and environmental parameters with near-zero Pearson correlations because the relationships may be non-linear. We

should also evaluate the Spearman Rank-Order correlation coefficients, which measure how well a relationship between two variables can be described by a monotonic function. Figure 5.25 visualizes the Spearman correlations in our dataset.

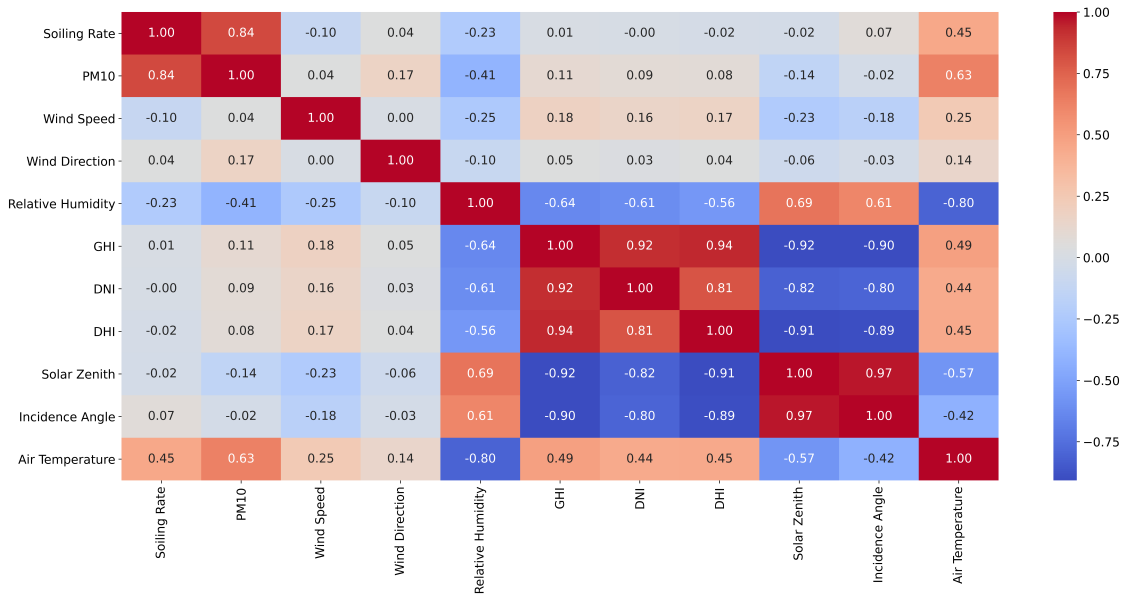


Figure 5.25: Heatmap of Spearman correlation coefficients between environmental variables and predicted soiling rate.

As expected, the variables with strong Pearson correlations also have strong Spearman correlations since a line is a simple form of a monotonic function. We also now see a significant negative correlation between the soiling rate, relative humidity, and air temperature. Since the Pearson correlation between RH and soiling is zero, but the Spearman coefficient is significant, we can conclude that these two variables are non-linearly related. This is expected since the soiling model that this data was generated with includes RH in non-linear terms only. Since air temperature and humidity are also strongly correlated, we chose to use only humidity for training our models (it is generally desirable to use independent variables for training an ML model).

The following approach was used for creating the MLR and ANN models. First, the soiling data (generated from the semi-physical model) was normalized by dividing each variable by the mean of that variable. ANN requires normalization to achieve good results. The same normalization



was also done on MLR for consistency in data preprocessing, although it was found that using normalization did not have any effect on the MLR prediction. Then, the data was split 80%:20% into training and testing data. Four independent variables that are believed to be the dominant predictors of soiling were chosen for the models: PM10, wind speed, RH, and the difference in angle between panel azimuth and wind direction. The quantity to predict was the hourly soiling accumulation rate. The MLR and ANN models were run using the `LinearRegression` and `MLPRegressor` (Multi-Layer Perceptron) methods from the Python package `Scikit-Learn`. The MLP Regressor used the default parameters except for changing to the L-BFGS solver (documented to work better than the default for smaller datasets) and using three hidden layers of ten neurons each. The numbers of hidden layers and neurons to use were determined through a series of 5-fold cross-validation trials performed on the training data (80% of the dataset), searching for the values that gave the best prediction metrics ( $R^2$ , MSE, and MAPE). K-fold cross-validation is the procedure of further splitting up a training dataset into  $k$  groups, and repeating model training  $k$  times, where each time a different group is used for testing and the rest of the groups are used for training. By changing the parts of the dataset that are used for training and testing, cross-validation calculates more representative model accuracy metrics than if only a single test:train split was used.

To evaluate the importance of PM10, wind speed, wind direction relative to the panel, and relative humidity variables for the MLR and ANN predictions, the prediction accuracy was compared when the models were trained with one, two, three, and all four of these variables. For the single variable training, PM10 was chosen since it has the highest positive Pearson and Spearman correlations to the soiling rate. Wind speed was added as the second variable since it is the only other variable that has a strong linear correlation with the soiling rate. The Spearman correlations show that relative humidity has a significant correlation with soiling, so it was added as the third variable. While showing only small correlation coefficients, we added wind direction as the fourth feature because we know that the soiling model attempts to include its effect.

Table 5.5: Comparison of ANN and MLR performance when different numbers of features (environmental variables) are used for model training.

Features	Model	$R^2$	MSE	MAPE
PM10	MLR	0.119	$1.03 \times 10^{-6}$	59.5%
	ANN	0.119	$1.03 \times 10^{-6}$	59.6%
PM10, wind speed,	MLR	0.379	$7.24 \times 10^{-7}$	69.3%
	ANN	0.851	$1.73 \times 10^{-7}$	86.9%
PM10, wind speed, RH	MLR	0.379	$7.23 \times 10^{-7}$	69.1%
	ANN	0.986	$1.63 \times 10^{-8}$	93.7 %
PM10, wind speed, RH, wind direction	MLR	0.381	$7.22 \times 10^{-7}$	69.6%
	ANN	0.989	$1.25 \times 10^{-8}$	94.6 %

When just using PM10, the ANN does not perform any better than MLR. The accuracy of MLR and ANN predictions both increase when including both PM10 and wind speed. As could be expected, adding variables that have non-linear correlations with soiling (relative humidity and wind direction) result in no improvement for the MLR model, but do improve the ANN model, which is capable of capturing non-linear relationships. The prediction accuracy had almost no significant improvement when adding wind direction, which showed only a small Spearman correlation with soiling. The lack of dependence of soiling on wind direction, even when the model which was used to generate this data includes wind direction, can be understood by the fact that wind’s contribution to resuspension is dominating over its contribution to deposition. We know this from the negative Pearson correlation between soiling and wind speed. Since the model only includes wind direction for wind-induced deposition, we do not see its effects. This exercise demonstrates that looking at significant Spearman correlations allows choosing a set of features for an ANN model that results in high prediction accuracy.

Figure 5.26 shows comparisons of predicted hourly soiling rates for Riverside, California when all four environmental variables were used. With all four variables, the ANN model achieved a much higher prediction accuracy, higher  $R^2$ , and lower MSE than the MLR model. We see that the MLR model struggles to predict many of the values because it attempts to find linear relationships

between soiling and environmental variables when the real relationships are non-linear. MLR is unable to capture the periodic spikes of large negative soiling rates due to resuspension at high wind conditions. In attempting to capture these spikes, the MLR model found a negative linear coefficient between wind speed and soiling, incorrectly implying that wind speed always gives rise to a reduction in soiling. MLR also has a wide scattering of points missing the actual data when trying to predict soiling at lower wind speeds. In contrast, ANN can reasonably capture the negative soiling rate spikes and achieve a very good agreement with actual values at low wind speeds, as seen by the thinner band of points that better match the actual values.

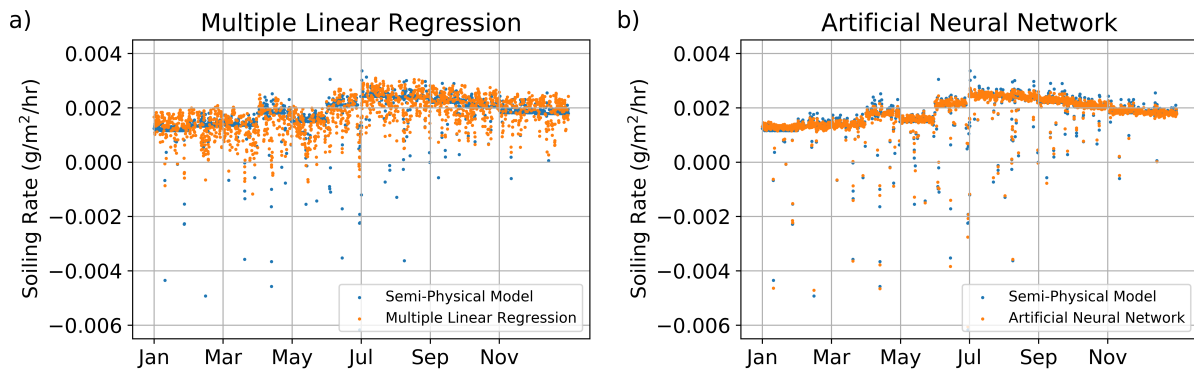


Figure 5.26: Comparison of hourly soiling rates predicted by MLR and ANN models to rates predicted by the semi-physical model (with resuspension) that they were trained on. Only data points from the testing set are shown.

The soiling data generated for the above ML exploration assumed that a strong resuspension occurred at high wind speeds, resulting in a strong cleaning effect and spikes of negative hourly soiling rates. The actual resuspension depends strongly on RH, particle chemistry and size, and PV surface properties. It is possible that no significant resuspension occurs at many PV sites and many soiling models neglect resuspension. Therefore, we retrained the ML models using simulated data from a version of the semi-physical model without the resuspension term. Generating data without resuspension allows us to test MLR and ANN on a different dataset that exhibits different trends. The main difference is the lack of spikes, resulting in a smoother curve. In contrast with the last test, we find that both MLR and ANN achieve similar prediction accuracies of about 98%.

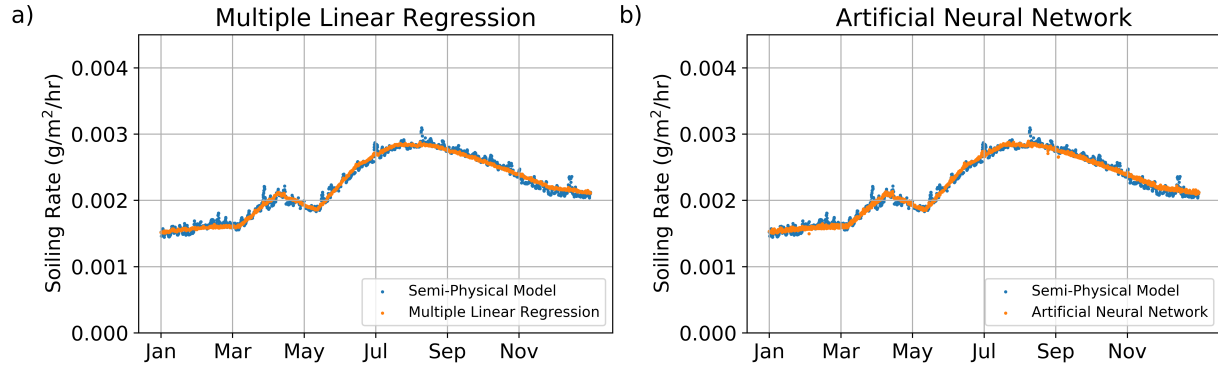


Figure 5.27: Comparison of hourly soiling rates predicted by MLR and ANN models to rates predicted by the semi-physical model (without resuspension) that they were trained on. Only the test data points are shown.

Table 5.6: Statistical metrics comparing MLR and ANN model performance when using a dataset generated with the semi-physical soiling model without the resuspension term.

Model	$R^2$	MSE	MAPE
MLR	0.983	$3.47 \times 10^{-9}$	97.8%
ANN	0.982	$3.49 \times 10^{-9}$	97.8%

These results confirm that both ANN and MLR are promising approaches for predicting soiling mass accumulation as a function of environmental variables. For sites where soiling phenomena are highly non-linear (e.g. those experiencing non-linear resuspension due to wind), the ANN approach is expected to achieve more accurate predictions than MLR. Additionally, we have shown that analyzing statistical correlations of results from physical or semi-physical models can be a method for verifying their qualitative behavior.

### 5.8.3 Soiling Loss

To investigate the possibility of using machine learning to directly predict future soiling loss from historical soiling and environmental data, the approach was tested on approximately 1.5 years (February 2019 to June 2020) of measured data from a PV power plant in California. Data from 2019 was used to predict soiling in 2020. The following environmental parameters were measured

with an hourly resolution at the plant: PM10, relative humidity, wind speed, wind direction, rainfall, and air temperature. Soiling loss was measured using a standard soiling measurement station comprised of two panels, one of which is regularly manually cleaned, while the other is allowed to accumulate soiling. The ratio of the short-circuit current of the cleaned and dirty panels was measured every minute. Soiling loss measurement is most reliable when there is high irradiance; therefore, only soiling measurements taken between 9 am and 3 pm (local time) were used for the analysis. Additionally, unphysical outliers in the soiling and weather data were removed. Following previous literature studies of soiling data [77], rainfall data was used to generate a *dry period length* time-series variable, which is simply equal to the number of days that have passed since the last rainfall.

First, the Spearman Rank-Order correlation coefficients between the variables in the dataset were calculated. The correlations between a ten-day moving average of all variables are stronger than between hourly or daily values. This is likely because the daily fluctuations in the variables make it more difficult to capture relationships between them. Since we are mostly interested in long-term soiling loss trends (e.g. the soiling loss after a few weeks of exposure), ten-day moving averages were used for the rest of the ML model development. Figure 5.28 shows a heat map of Spearman correlation coefficients between ten-day moving averages of the variables.

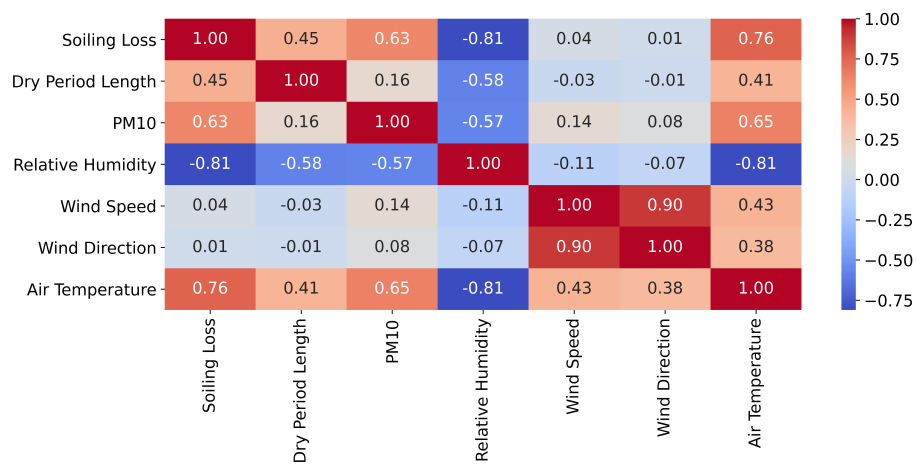


Figure 5.28: Heatmap of Spearman correlation coefficients between ten-day moving averages of soiling and environmental variables measured at a PV power plant in California.

Next, the MLR and ANN models (from the previous section) were trained on measured data from 2019 using dry period length, PM10, and relative humidity as the input variables. Wind speed and wind direction were excluded since the correlations analysis above showed almost no correlations of these variables to soiling loss in this dataset. The air temperature was also excluded since a large period of missing temperature data in 2020 prevents using this variable to predict soiling. Also, the correlation between air temperature and soiling is likely a side effect of more soiling in the summer, and this effect is already captured by the dry period length and relative humidity variables. As a baseline comparison, we also attempted to fit the soiling data using the industry-standard model from Kimber et al. [80] (see Section 5.1), which uses a constant soiling rate and assumes that the soiling drops to some minimum value at each significant rainfall event. Figure 5.29 compares the attempt to fit the training data with the three different models. The MLR and ANN models were able to fit the training data significantly better than the Kimber model.

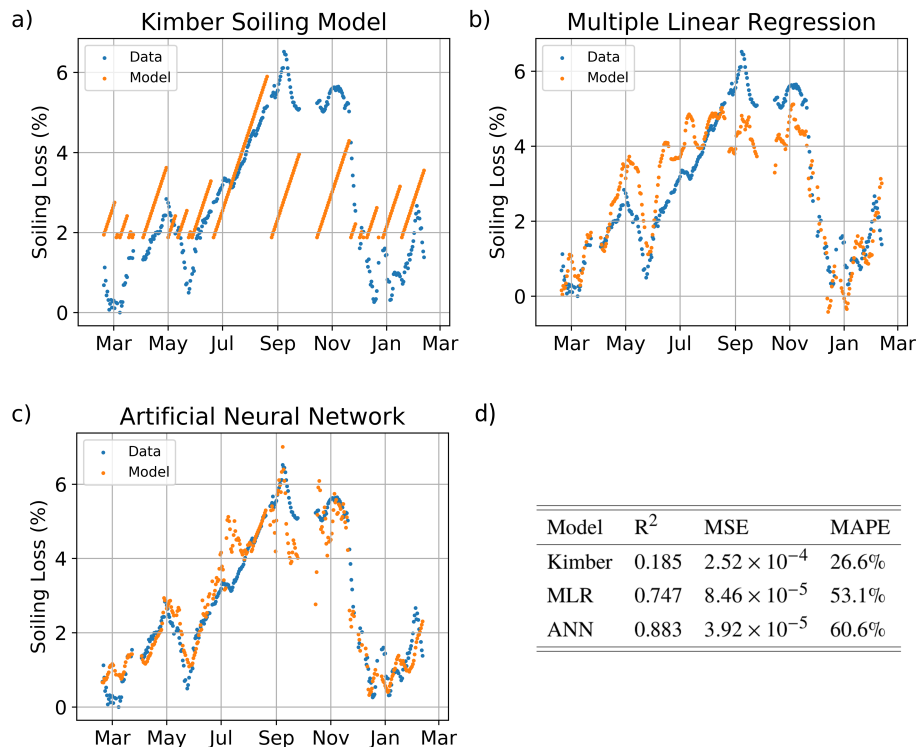


Figure 5.29: Comparison of Kimber, MLR, and ANN models' ability to fit the training data (measured soiling and environmental parameters for 2019).

Since the ability to fit existing data does not necessarily indicate any predictive ability, we tested the models' performance when predicting soiling in 2020 based on the measured environmental parameters (Figure 5.30). Note that the models were trained solely on 2019 data; therefore, they predict soiling in 2020 based only on the learned relationships from the previous year. The models have trouble predicting soiling when it is low (e.g. in February and March), possibly due to the low signal-to-noise ratio in those measurements. In practice, the PV industry is interested in predicting significant soiling losses (those which will require manual cleaning). Therefore, we computed two sets of prediction accuracy metrics: one for the entire 2020 region for which there was measured data (February 25 through June 16) and one for the portion of the region where there is more significant soiling loss (April 23 through June 16). The artificial neural network was found to have the highest prediction accuracy.

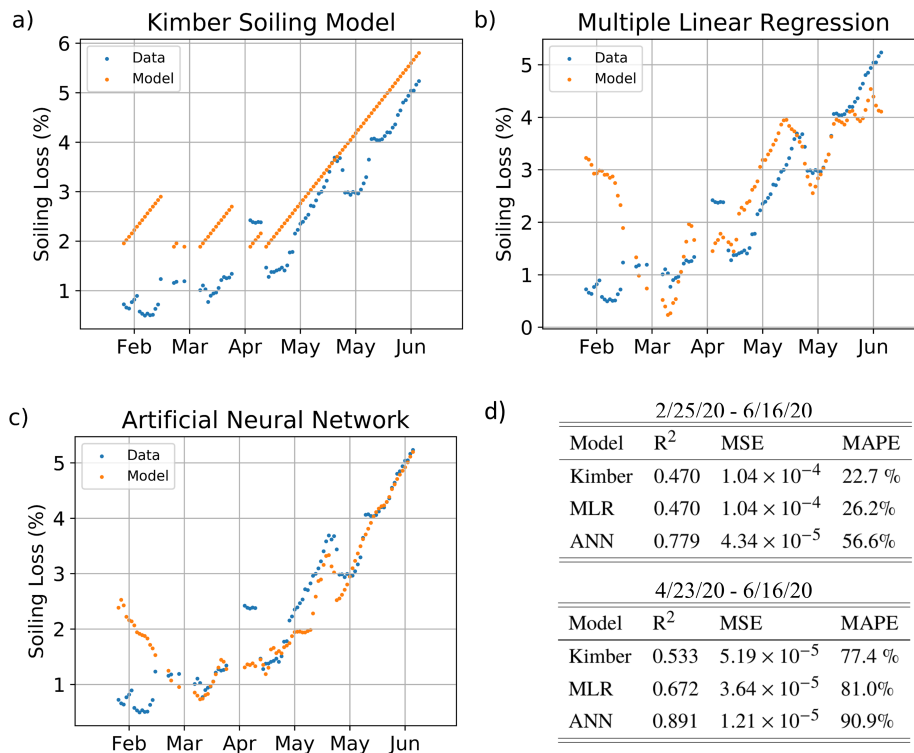


Figure 5.30: Comparison of Kimber, MLR, and ANN models' ability to predict soiling in 2020, when trained on data from 2019. Statistical metrics for two different prediction periods are shown: February 25 through June 16, and April 23 through June 16.

These results suggest that it may be possible to predict future soiling loss at a given site based on measurements of soiling and environmental parameters. However, we must remember that the prediction of future soiling depends on our ability to predict future environmental parameters, which can be challenging. While we may not know the exact values of next year's environmental parameters, we may be able to make reasonable estimates based on typical weather patterns or anomalies (e.g. we may know that next year is expected to be wetter/drier than normal). Reliable historical weather data and medium/long-term weather forecasting will be important to enable such soiling predictions.

## **5.9 Conclusions**

In this chapter, we explored both semi-physical and machine learning approaches to modeling the soiling of PV panels. After reviewing the main physical mechanisms of soiling and limitations of existing semi-physical soiling accumulation models, we developed a general model that is expected to be reasonably applicable globally, provided that the empirical coefficients are fitted on a region-by-region basis. Additionally, we developed a novel practical approach of integrating a soiling accumulation prediction with an existing validated model for optical losses due to soiling (the Martin and Ruiz model). The overall photovoltaic system soiling model was validated by comparing with published soiling loss studies performed by NREL. We helped integrate the semi-physical soiling models with a Python package for PV energy production prediction (PVLIB) and cleaning cycle optimization algorithms, which resulted in the release of a brand new commercial software (described further in [Appendix A](#)). Finally, considering the inherent limitations of semi-physical modeling of highly coupled and complex environmental processes, we explored machine learning approaches to soiling modeling. The feasibility of these approaches was demonstrated by showing that MLR and ANN can replicate the results of semi-physical soiling models and predict future soiling loss based on historical measurements of soiling and environmental parameters. This motivates the need to install soiling, weather, and PM10 sensors at PV system sites where soiling is a significant issue. The models and software that we developed are expected to help PV system



developers, maintainers, engineers, and researchers have a better understanding of soiling losses at their current and potential future sites, as well as have access to easier-to-use and more-accurate soiling analysis tools.

## CHAPTER 6

### COUPLED THERMAL-ELECTRICAL MODELING OF INTEGRATED PV SYSTEMS

When measuring and predicting solar cell performance, a standard value for cell temperature is often used (e.g. 20°C or 25°C). However, the temperature of a solar cell in operation can be significantly different from the standard value. A solar cell's efficiency generally decreases as the operating temperature increases, primarily due to increased internal carrier recombination rates caused by increased carrier concentrations [135]. Electrical PV models, which are often developed and fitted to experimental data under standard test conditions, need to be corrected to consider the impact of temperature on electrical performance. Therefore, to predict a PV system's power generation in realistic conditions, the cell temperature must be estimated. In this chapter, we compare empirical and physical approaches for cell temperature predictions and describe the development of a PV thermal-electrical modeling approach that makes use of a commercial general heat transfer solver. Finally, we demonstrate example applications of the model to simulation of residential PV and vehicle-integrated PV, as well as, coupling of the PV model to a thermal-electrical model for batteries.

#### 6.1 Empirical Models

A common approach to considering temperature-induced losses when calculating PV performance is to first predict cell temperatures with empirical models, and then use these predicted temperatures in equivalent circuit models. In this work, we tested six empirical models for cell temperature, three of which (Faiman, PVsyst, and SAPM) are implemented in the open-source PV simulation package PVLIB. These models are briefly introduced below.

##### Basic NOCT Model

Most empirical cell temperature models use a PV characteristic called *Normal Operating Cell Temperature* (NOCT). NOCT is the temperature of a free-standing cell under open-circuit condition

under plane-of-array (POA) irradiance of  $800 \text{ W/m}^2$ , ambient air temperature of  $20^\circ\text{C}$ , and  $1 \text{ m/s}$  wind speed [136]. The most basic empirical model assumes that the cell temperature is simply the ambient air temperature plus the difference between NOCT and  $20^\circ\text{C}$  (reference temperature for NOCT measurement) multiplied by the ratio of POA irradiance ( $E$ ) to the NOCT irradiance of  $800 \text{ W/m}^2$  [137].

$$T_C = T_{air} + (NOCT - 20) \frac{E}{800} \quad (6.1)$$

### **Bizzarri et al.**

Bizzari et al. proposed a model that takes into account any additional convection due to wind speeds ( $WS$ ) that are greater than the NOCT-specified  $1 \text{ m/s}$  [137]. The relationship between wind speed and convection is controlled by a convection coefficient  $h$ .

$$T_C = T_{air} + \frac{(NOCT - 20)}{800 + h(WS - 1)(NOCT - 20)} E \quad (6.2)$$

### **Faiman**

The Faiman model accounts for convection by assuming a simple two-coefficient ( $u_c$  and  $u_v$ ) linear convection expression [138].

$$T_C = T_{air} + \frac{E}{u_c + u_v \times WS} \quad (6.3)$$

### **PVsyst**

The model implemented in the software PVsyst is the Faiman model with an additional explicit consideration of absorption  $\alpha$  and panel efficiency  $\eta$  [129].

$$T_C = T_{air} + \frac{\alpha E(1 - \eta)}{u_c + u_v \times WS} \quad (6.4)$$

The implemented model uses a default value of  $u_v = 0$ .

## Sandia Array Performance Model

This model accounts for potential differences between module and cell temperature. The module temperature is expressed as the sum of the air temperature and an exponential term [129].

$$T_m = E e^{(a+b \times WS)} + T_{air} \quad (6.5)$$

The cell temperature is calculated from the module temperature by

$$T_C = T_m + \frac{E}{E_0} \Delta T \quad (6.6)$$

where  $\Delta T$  is the empirically-estimated difference between module back surface temperature and cell temperature. Table 6.1 shows the empirical parameters used in the SAPM model.

Table 6.1: SAPM temperature model coefficients.

Module Type	a	b	$\Delta T$
Open-Rack Glass-Glass	-3.47	-0.0594	3
Open-Rack Glass-Backsheet	-3.56	-0.075	3
Rooftop Glass-Glass	-2.98	-0.0471	1
Rooftop Glass-Backsheet	-2.81	-0.0455	0

## Duffie and Beckman

The Duffie and Beckman model attempts to account for both wind convection and module efficiency [139].

$$T_C = T_{air} + \frac{E}{800} \frac{a}{(u_c + u_v WS)} (NOCT - 20)(1 - \eta) \quad (6.7)$$

## Model Comparison

In order to evaluate the accuracy of the empirical models, we compared their temperature predictions with measured module temperatures from a solar power plant in California. This comparison was first made using the original (default) coefficients that are specified by the empirical models, which is a common way the models might be used by engineers who are looking for a quick estimate

of PV energy production. One exception to the use of default coefficients is that the NOCT and efficiency values were taken from the manufacturer datasheet. Note that other model coefficients are not generally available on manufacturer datasheets. The comparison of modeled versus measured results for three days is shown in Figure 6.1 and Table 6.2.

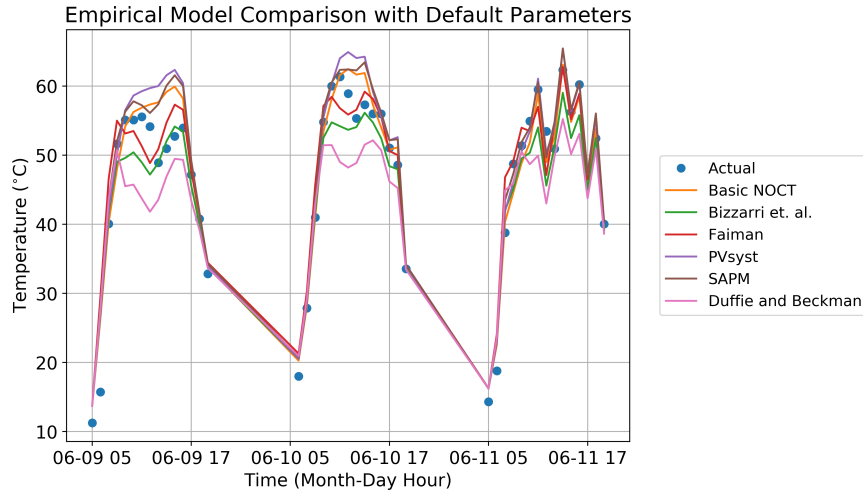


Figure 6.1: Comparison of empirical models using default parameters.

Table 6.2: Errors of empirical models for results shown in Figure 6.1.

Model	$R^2$	RMSE	MAE
Basic NOCT	0.782	6.33	5.02
Bizzarri et al.	0.926	3.69	2.78
Faiman	0.923	3.75	2.82
PVsyst	0.93	3.58	2.56
SAPM	0.912	4.03	2.94
Duffie and Beckman	0.852	5.22	4.03

For a better statistical comparison, the module temperatures were predicted for an entire year and compared with measured data in Table 6.3. (The results plot is not shown because there are too many data points to plot the data effectively).

Table 6.3: Errors of empirical models for entire year using default parameters.

Model	$R^2$	RMSE	MAE
Basic NOCT	0.908	5.18	3.97
Bizzarri et al.	0.953	3.70	2.38
Faiman	0.952	3.75	2.42
PVsys	0.959	3.44	2.68
SAPM	0.955	3.63	2.60
Duffie and Beckman	0.915	5.00	3.60

Seeing that some of the model predictions appear to be simply shifted from the measured data, for the second comparison, multivariable optimization was used to find empirical model coefficients (including NOCT) that best fit the data. The optimization was done using the Python SciPy package’s `optimize.least_squares()` function with bounds specified on parameters to maintain physically realistic values. The comparison of modeled versus measured results for three days is shown in Figure 6.2 and Table 6.4.

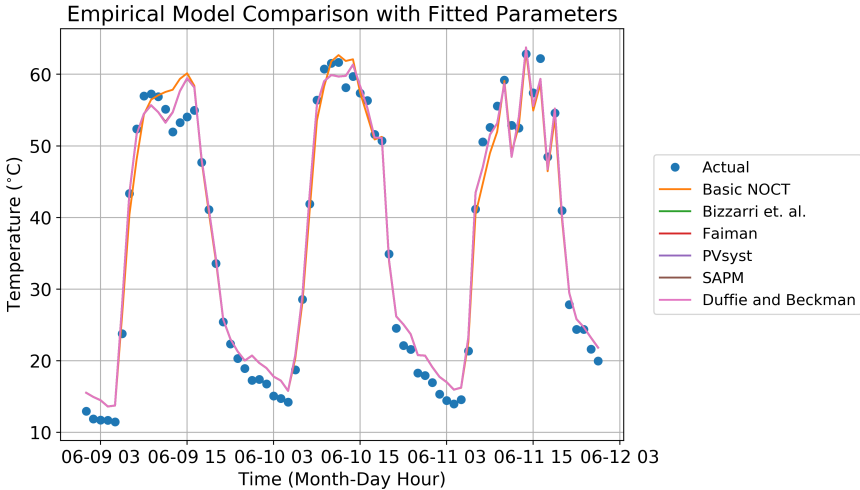


Figure 6.2: Comparison of empirical models with parameters fitted using least-squares optimization.

Table 6.4: Errors of empirical models' results shown in Figure 6.2.

Model	$R^2$	RMSE	MAE
Basic NOCT	0.981	2.51	2.06
Bizzarri et al.	0.986	2.15	1.86
Faiman	0.986	2.15	1.86
PVsyst	0.986	2.15	1.86
SAPM	0.986	2.15	1.86
Duffie and Beckman	0.986	2.15	1.86

The error between one-year module temperatures predictions from the fitted model are compared with measured values in Table 6.5.

Table 6.5: Errors for one year of module temperatures predicted by empirical models using fitted parameters.

Model	$R^2$	RMSE	MAE
Basic NOCT	0.977	2.80	2.16
Bizzarri et al.	0.980	2.62	1.93
Faiman	0.980	2.62	1.93
PVsyst	0.980	2.62	1.93
SAPM	0.980	2.61	1.92
Duffie and Beckman	0.980	2.62	1.93

When using optimization to fit the empirical coefficients to the data, all models except Basic NOCT result in cell temperature predictions that are almost identical. In conclusion, multiple empirical models can accurately predict free-standing solar module temperatures if their coefficients are fitted to measured data.

## 6.2 Physical Thermal-Electrical Model

### 6.2.1 Introduction and Motivation

In the last section, we have shown that empirical models can accurately predict free-standing solar module temperatures, provided they are fitted to measured data. In cases where measured data

is unavailable, the default values provided in PV modeling libraries/software are typically used. However, using default empirical model coefficients can lead to significant errors in temperature predictions. A validated physical model can allow to more-accurately estimate cell temperatures for use in temperature-dependent solar cell performance models, such as those used within mainstream PV modeling software. A physics-based approach to cell temperature and electrical performance prediction is to couple an electrical PV model with a first-principles heat transfer solver.

Another application of a heat transfer solver could be to predict NOCT for modules, given the module's known thermal properties. This application is motivated by several limitations of NOCT measurements listed below:

- Normal "operating temperature" is defined at open-circuit condition at which the device is not producing any current. A device that produces current has an associated efficiency (e.g. 10-25%), which means that some of the solar energy is converted into electricity instead of being absorbed as heat. Therefore, the NOCT temperature is expected to be higher than a device which is producing power [136].
- NOCT does not apply to non-freestanding modules (e.g. roof mounted), where there is generally less convective cooling, resulting in higher temperatures.
- NOCT measurement typically requires waiting for very specific outdoor conditions, which in some locations may only occur on several days a year. An NREL study found that many manufacturers may not be reliably measuring NOCT when performing a side-by-side test of three modules of the same type with manufacturer-reported NOCT values that differ by 10°C. NREL found that the true NOCT of these modules varies by less than 0.2°C, as would be expected for modules of the same type. Running a heat transfer simulation, they concluded that the variation in manufacturer reported values could be due to changing sky, ground, and ambient temperatures during the measurements [140].
- NOCT provides no information about how temperature varies with wind or irradiance.



Finally, a physical model based on heat transfer can be used to predict transient temperatures of modules when they are integrated into various structures (e.g. on buildings, vehicles, or combined with a heat exchanger as part of a PV-thermal system). Using an empirical approach would likely require fitting the empirical model for each specific structure, with coefficients changing depending on the design's thermal properties. This approach requires many experiments to gather cell temperature data. Utilizing a physical model can avoid the need for these experiments and allow for rapid computational testing of PV system designs. Additionally, the heat transfer approach allows one to predict not only the module temperature but also any effects of the solar panel on the temperatures of the building or vehicle on which it is mounted. Such a model can allow for computer-aided engineering of solar applications without the need to test every design idea experimentally.

### **6.2.2 Methods**

In this work, a coupled physical thermal-electrical model of a PV was developed using the commercial heat transfer software TAITherm (ThermoAnalytics, Inc.) [141], which uses a numerical, finite volume approach based on first principles physics. The PV model is based on the works of Sommerfeldt and Schon [142, 143], who used TAITherm for modeling photovoltaic-thermal (PVT) systems, with several significant differences. Sommerfeldt's work was focused on reverse engineering heat transfer coefficients for the PVT system based on measured data, so the electrical portion of the PV was not modeled, but instead, the measured power was used to set a negative imposed heat on the PV layer. In Schon's work, the electrical portion was modeled with a five-parameter equivalent circuit, but the non-linear equation for current was solved in a brute force inefficient way using two nested "while" loops. Schon reports that the simulation took 10-20 minutes per time-step, and it is likely that the inefficient electrical solution implementation contributed to this unsatisfactory performance. This performance limitation would make simulating a PV module over the course of a 12 hour day with a time-step of 1 minute (typical for transient heat transfer simulations) take 120 hours. Most users would desire a faster simulation time.

This work developed a proof-of-concept extension to TAItherm for PV modeling. Improvements over Schon’s work include a more efficient implementation for solving the equivalent circuit equations, accounting for the dependence of power generation on the AOI of solar radiation, and allowing to consider the effects of soiling. In some use-cases, one is only interested in approximating the potential power generation of a generic PV system, and the electrical parameters are unknown (e.g. evaluating the potentials of future PV technologies). For these cases, an option was implemented to estimate the power generation using the efficiency, incident solar radiation, and AOI dependence. The following sections detail the calculations used to compute power, angular dependence, and the effect of soiling losses.

### Computing Power Using Equivalent Circuit Model

The five-parameter equivalent circuit describes a simple current balance where the current reaching the module contacts (usable current) is the difference between photogenerated current,  $I_L$ , and the current lost inside the cells [144]

$$I = I_L - I_D - I_{sh} \quad (6.8)$$

where the current losses are referred to as the shunt current,  $I_D$ , and the leakage current,  $I_{sh}$ . The current through the shunt diode ( $I_D$ ) describes the current lost due to radiative recombination of minority carriers at the semiconductor junction under forward-bias voltage. The leakage current describes current that is lost for reasons other than radiative recombination at the semiconductor interface. This can be due to pinholes between the layers in the cell, allowing an alternate path for the current. A series resistance,  $R_s$ , is used to describe the resistance related to finite carrier mobilities and imperfect contacts between the active layer and electrodes. Figure 6.3 shows the five-parameter equivalent circuit representation of a solar cell.

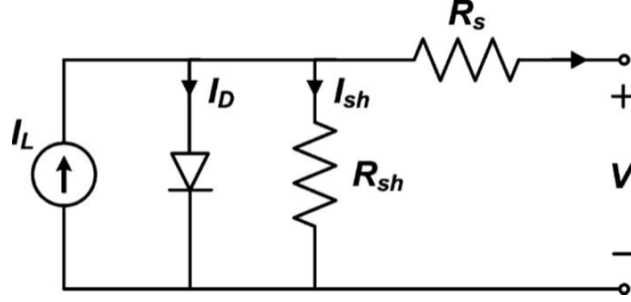


Figure 6.3: Five-parameter equivalent circuit representation of a solar cell. Adapted from [145].

The current through the shunt diode is modeled by the Shockley diode equation

$$I_D = I_0 e^{(V+IR_s)/a} - 1 \quad (6.9)$$

where  $I_0$  is the reverse-bias saturation current and  $a$  is the modified diode ideality factor, which is given by

$$a = N_s n V_t \quad (6.10)$$

where  $n$  is the diode ideality factor, which takes into account the deviation of the diode from the Shockley diffusion theory,  $N_s$  is the number of cells in series, and  $V_t = k_B T/q$  is the thermal voltage. Using Kirchoff's loop law on the equivalent circuit in Figure 6.3, we see that

$$V + IR_s - I_{sh} R_{sh} = 0 \quad (6.11)$$

so

$$I_{sh} = \frac{V + IR_s}{R_{sh}} \quad (6.12)$$

Combining the above equations, the current-voltage relationship is

$$I(V) = I_L - I_0 (e^{(V+IR_s)/a} - 1) - \frac{V + IR_s}{R_{sh}} \quad (6.13)$$

where the five empirical circuit parameters are  $I_L$ ,  $I_0$ ,  $a$ ,  $R_s$ , and  $R_{sh}$ . The temperature-dependence of these parameters in terms of the reference values (denoted by the subscript *ref*) is described by

the equations below

$$a = a_{ref} \frac{T}{T_{ref}} \quad (6.14)$$

$$I_L = \frac{S}{S_{ref}} \frac{M}{M_{ref}} [I_{L,ref} + \alpha_{Isc}(T - T_{ref})] \quad (6.15)$$

$$I_0 = I_{0,ref} \left( \frac{T}{T_{ref}} \right)^3 \exp \left[ \frac{1}{k} \left( \frac{E_g}{T} \Big|_{T_{ref}} - \frac{E_g}{T} \Big|_T \right) \right] \quad (6.16)$$

$$R_s = R_{s,ref} \quad (6.17)$$

$$R_{sh} = \frac{S_{ref}}{S} R_{sh,ref} \quad (6.18)$$

where  $S$  is the plane-of-array irradiance,  $\alpha_{Isc}$  is the temperature coefficient of  $I_{sc}$  (available on manufacturer datasheets),  $\frac{M}{M_{ref}}$  is the air mass modifier (taking into account deviations from standard AM1.5 solar spectrum),  $E_g$  is the semiconductor bandgap, and  $k_B$  is Boltzmann's constant. Note that the bandgap is also temperature-dependent with the relationship typically described empirically. For example, the temperature-dependence of silicon's bandgap can be described by

$$\frac{E_g}{E_{g,ref}} = 1 - 0.0002677(T - T_{ref}) \quad (6.19)$$

The non-linear equation for current (6.13) can be solved efficiently by using the `fsolve` function from SciPy. `fsolve` is a wrapper around the highly-optimized Fortran library MINPACK's hybrid and hybrj non-linear equation root-finding routines. The current, voltage, and power at the maximum power point ( $P'_{mp}$ ) are determined by simply finding the current and voltage in the IV curve whose product is maximum. This power is scaled by area to account for any discrepancy between the solar cell area that was used by the manufacturer to determine the empirical electrical parameters ( $A_{manuf}$ ) and the area used in the TAItherm model ( $A_{TAI}$ ).

$$P_{mp} = P'_{mp} \frac{A_{TAI}}{A_{manuf}} \quad (6.20)$$

Since equivalent circuit parameters are measured for a perfectly clean module under normal (perpendicular to the surface) incidence of solar radiation, the power calculated here is also assuming normal incidence and no soiling losses. Corrections for AOI-related losses and soiling losses can be applied as described in Section 6.2.2.

## Equivalent Circuit Parameter Extraction

One potentially challenging aspect of using the five-parameter equivalent circuit approach is finding the values of the five parameters. These parameters are not readily available from manufacturer datasheets and are generally found with a combination of numerical solutions and fitting of IV curves [146]. We did not have access to IV curve data for this work and therefore needed a solution that could rely solely on the manufacturer datasheet. We used the method developed by Cubas et al. [14], which is a mostly analytical approach, leaving just a single equation that needs to be solved numerically.

This approach starts by evaluating the IV equation (6.13) at short-circuit current, open-circuit voltage, and maximum power point conditions. At short-circuit current, we get

$$I_{sc} = I_L - I_0(e^{I_{sc}R_s/a} - 1) - \frac{I_{sc}R_s}{R_{sh}} \quad (6.21)$$

Cubas et al. neglects the second term (diode term) in this equation since at short-circuit condition, it is much smaller than the other two terms. This allows to rewrite the expression as

$$I_L = \frac{R_{sh} + R_s}{R_{sh}} I_{sc} \quad (6.22)$$

Evaluating Equation 6.13 at the open-circuit condition, we get

$$0 = I_L - I_0(e^{V_{oc}/a} - 1) - \frac{V_{oc}}{R_{sh}} \quad (6.23)$$

Combining Equations 6.22 and 6.23, we can write the saturation current as

$$I_0 = \frac{(R_{sh} + R_s)I_{sc} - V_{oc}}{R_{sh}e^{V_{oc}/aV_t}} \quad (6.24)$$

Evaluating Equation 6.13 at the maximum power point gives

$$I_{mp} = I_L - I_0(e^{(V_{mp}+I_{mp}R_s)/a} - 1) - \frac{V_{mp} + I_{mp}R_s}{R_{sh}} \quad (6.25)$$

where Cubas et al. approximated  $e^{(V_{mp}+I_{mp}R_s)/a} - 1 \approx e^{(V_{mp}+I_{mp}R_s)/a}$  because of the relative magnitudes of the terms. Combining Equations 6.22, 6.24, and 6.25, an expression that does not depend on  $I_L$  or  $I_0$  can be derived

$$I_{mp} = I_{sc} - \left( I_{sc} - \frac{V_{oc} - R_s I_{sc}}{R_{sh}} \right) \left[ \exp\left( \frac{V_{mp} + I_{mp}R_s - V_{oc}}{aV_T} \right) \right] - \frac{V_{mp} + I_{mp}R_s - I_{sc}R_s}{R_{sh}} \quad (6.26)$$

Another equation can be generated by applying that fact that the derivative of the power  $P = IV$  is zero at the maximum power point. Differentiating by parts, we have

$$\left. \frac{\partial P}{\partial V} \right|_{mp} = V \left. \frac{\partial I}{\partial V} \right|_{mp} + I_{mp} = 0 \quad (6.27)$$

$$\left. \frac{\partial I}{\partial V} \right|_{mp} = -\frac{I_{mp}}{V_{mp}} \quad (6.28)$$

Next, we differentiate Equation 6.13 with respect to V and combine with the above equation to get

$$\frac{dI}{dV} = -\frac{I_0}{aV_T} \left( 1 + \frac{dI}{dV} R_s \right) \left[ \exp\left(\frac{V + IR_s}{aV_T}\right) \right] - \frac{1}{R_{sh}} \left( 1 + \frac{dI}{dV} R_s \right) \quad (6.29)$$

Combining this with Equations 6.22, 6.24, and 6.26, an implicit expression for the series resistance  $R_s$  can be derived

$$\begin{aligned} & \frac{aV_T V_{mp} (2I_{mp} - I_{sc})}{(V_{mp} I_{sc} + V_{oc} (I_{mp} - I_{sc})) (V_{mp} - I_{mp} R_s) - aV_T (V_{mp} I_{sc} - V_{oc} I_{mp})} \\ & = \exp\left(\frac{V_{mp} + I_{mp} R_s - V_{oc}}{aV_T}\right) \end{aligned} \quad (6.30)$$

This expression is solved numerically for  $R_s$  using an iterative solver (in this work we used Matlab's `fsolve` function). Next, Equations 6.26 and 6.30 are combined to find an expression for  $R_{sh}$  in terms of known datasheet parameters and  $R_s$

$$R_{sh} = \frac{(V_{mp} - I_{mp} R_s)(V_{mp} - R_s(I_{sc} - I_{mp}) - aV_T)}{(V_{mp} - I_{mp} R_s)(I_{sc} - I_{mp}) - aV_T I_{mp}} \quad (6.31)$$

Now that the two equivalent circuit resistances are known, the photocurrent and saturation current are calculated using Equations 6.22 and 6.24. Figure 6.4 summarizes the procedure.

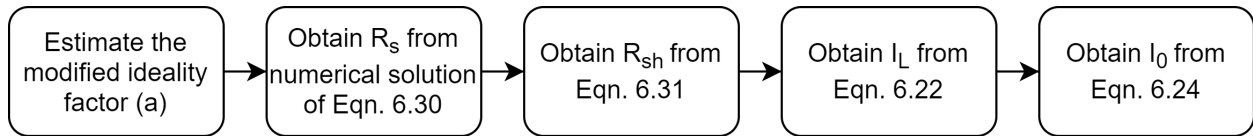


Figure 6.4: Flow chart of the Cubas et al. procedure to find the equivalent circuit parameters.

Two limitations of this procedure are that it relies on an estimate for the modified ideality factor and only uses the manufacturer values at STC from the datasheet. Since the goal of the equivalent circuit model is to model the electrical performance of the solar cells at various operating temperatures, we should use the data for both STC and NOCT conditions (which is almost always available) when extracting the model parameters to ensure that the model can capture temperature-dependent effects. In order to improve the fit of the equivalent circuit parameters to the datasheet, we ran the Cubas et al. method iteratively through a sweep of estimates for the modified ideality factor ( $a$ ), finding the value of  $a$  that results in the least sum of relative errors between the calculated values and measured values of eight parameters that are available on datasheets ( $V_{mp}$ ,  $I_{mp}$ ,  $V_{oc}$ , and  $I_{sc}$  for both STC and NOCT conditions). Figure 6.5 shows our modified method. The algorithm was implemented in Matlab with all non-linear equations solved using the `fsolve` function.

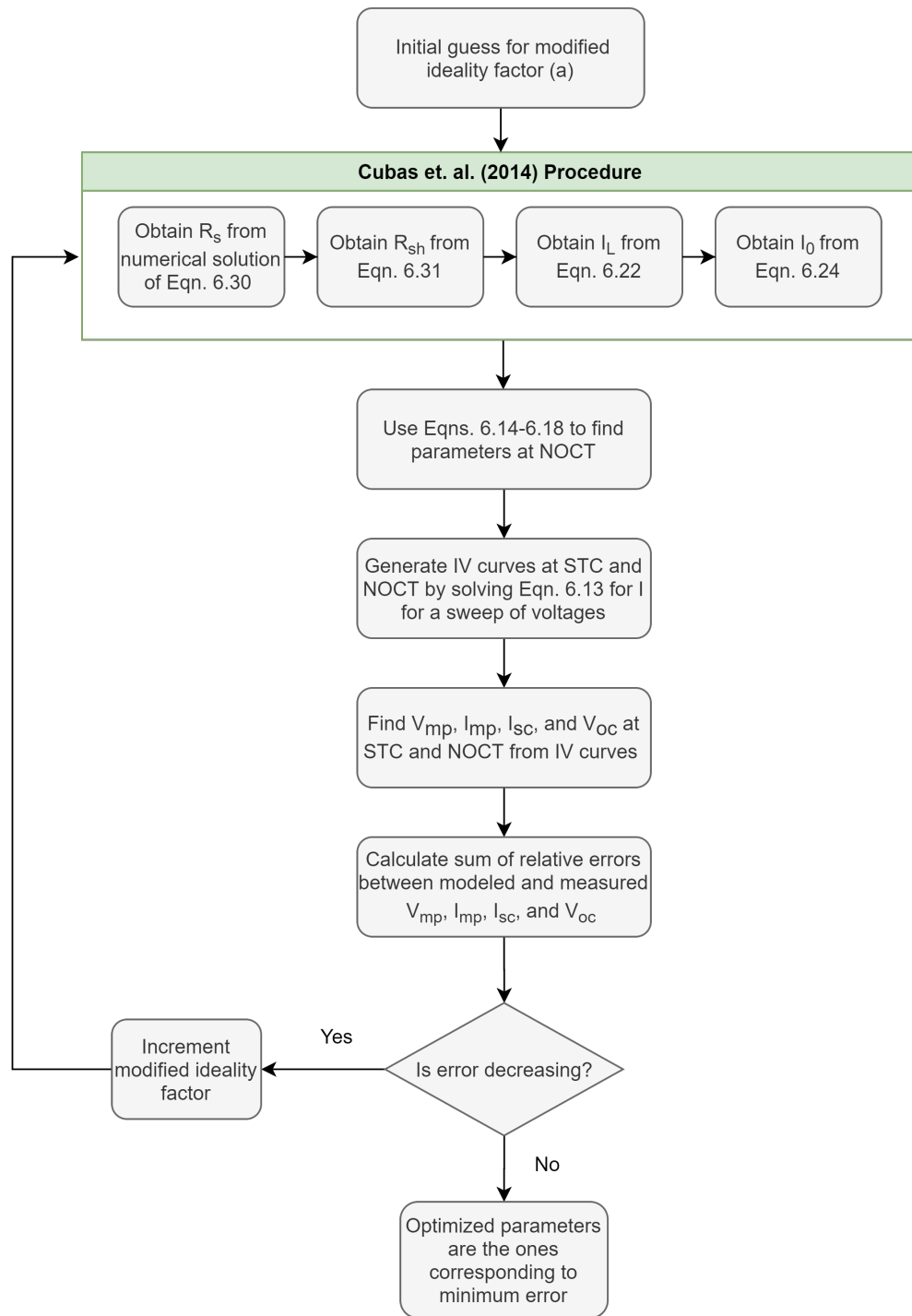


Figure 6.5: Flow chart of the improved equivalent circuit parameters extraction method.

Figure 6.6 shows sample results from the Matlab parameter extraction code. We see that the IV curves at STC and NOCT change significantly during the iterative optimization process, with the fill factor decreasing with increasing ideality factor.



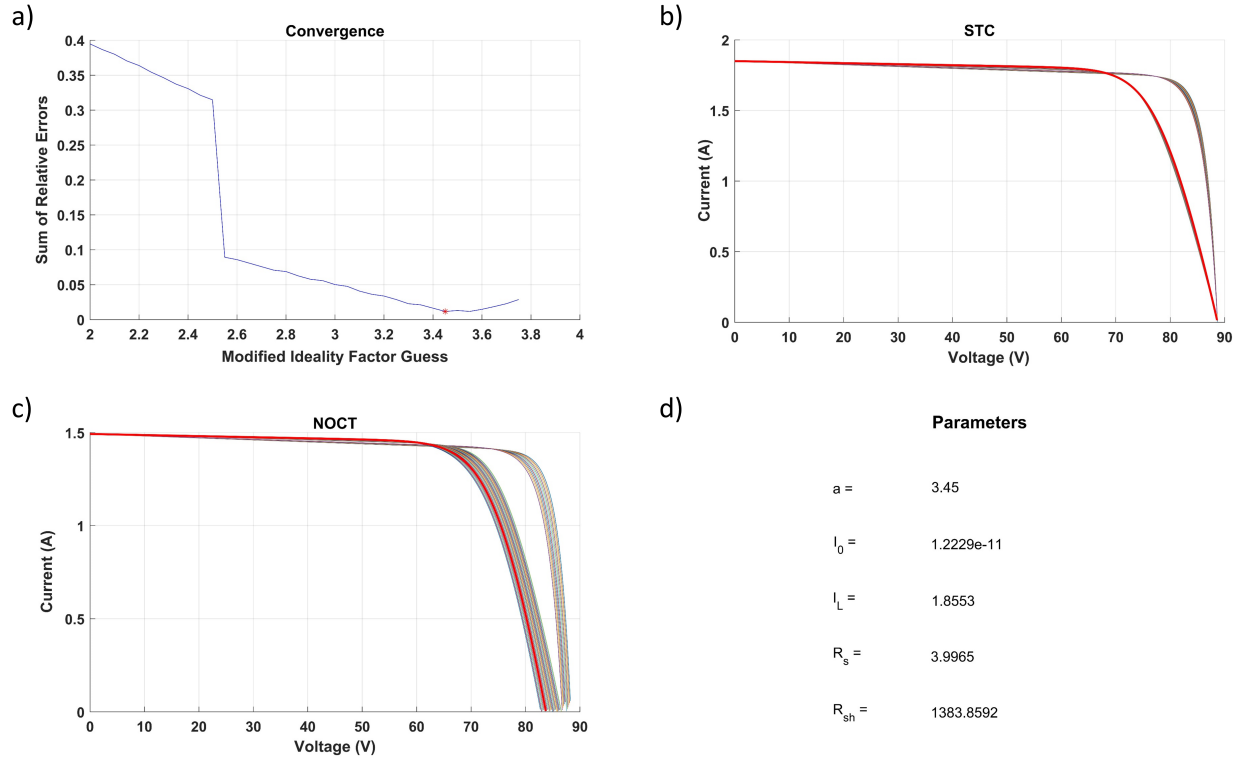


Figure 6.6: Example of results from our modified parameter extraction tool. a) Convergence behavior as the ideality factor guess is incremented. b, c) IV curves generated during the iterative process, with the optimized ones plotted in red. Fill factor decreases as ideality factor increases. d) Values of optimal parameters for this run.

### Estimating Power from a Nominal Efficiency

In some cases, the user may not have measured electrical parameters or simply is not interested in that level of detail for their model. Therefore, we also allow the user to use a simplified option of estimating power production from a nominal power conversion efficiency ( $\eta$  in %) and a temperature coefficient ( $\beta_\eta = \Delta\eta/^\circ C$ ). Power production of a perfectly clean module under normal irradiance is estimated as

$$P_{mp} = (\eta + \beta_\eta(T - T_{ref}))P_{inc} \quad (6.32)$$

As with the equivalent circuit approach, the estimated power production can be corrected to account for angular dependence and soiling losses as described in the following sections.

## Correction due to Angular Dependence

Angular losses are described in terms of an incidence angle modifier (IAM), which is the ratio of transmission of light into a PV module when the light is incident at an angle to the transmission of light at normal incidence. We account for angular losses by using the empirical model for IAM developed by Martin and Ruiz [119–121] (introduced in Section 5.4). We chose this model because it can also consider the angular losses on soiled PV modules. The full MR model requires knowledge of the diffuse, direct, and albedo components of solar irradiation. TAItherm's API currently does not allow retrieving the albedo (ground-reflected) component of radiation since TAItherm combines ground-reflected radiation and diffuse radiation into one quantity. Therefore, we use a simplification, following the approach from a previous study of PV angle-dependence [147], where we estimate the incidence angle modifier for diffuse radiation as the average of the IAMs for direct radiation for all angles of incidence.

The MR model defines the IAM for direct irradiance as

$$K_{\alpha}^{dir} = 1 - F_B(\alpha) = 1 - \left[ \frac{\exp(-\cos(\alpha)/a_r) - \exp(-1/a_r)}{1 - \exp(-1/a_r)} \right] \quad (6.33)$$

where  $F_B$  is called the angular loss factor,  $\alpha$  is the irradiance angle of incidence, and  $a_r$  is the empirical angular loss coefficient. Increasing the value of  $a_r$  allows modeling larger angular losses, like those occurring on soiled modules. For greater flexibility, we also implemented support for a user-specified direct irradiance IAM vs. AOI curve that is spline-interpolated to find the IAM for direct irradiance at any AOI. For both the empirical model and the user-defined direct irradiance IAM curve, the overall IAM ( $K_{\alpha}$ ) is calculated by

$$K_{\alpha} = \left[ E_{dir}^{POA} K_{\alpha}^{dir} + (E_{dif}^{POA} + E_{alb}^{POA}) \overline{K_{\alpha}^{dir}} \right] / E_{total}^{POA} \quad (6.34)$$

$$= \left[ E_{dir}^{POA} K_{\alpha}^{dir} + E_{dif,TAI}^{POA} \overline{K_{\alpha}^{dir}} \right] / E_{total}^{POA} \quad (6.35)$$

where  $E_{dir}^{POA}$ ,  $E_{dif}^{POA}$ ,  $E_{alb}^{POA}$  and are the plane-of-array (POA) direct, diffuse, and albedo irradiance, respectively. The average of  $K_{\alpha}$  over all angles of incidence is denoted by  $\overline{K_{\alpha}}$ . Note that the "diffuse irradiance" in TAItherm ( $E_{dif,TAI}$ ) is defined as the sum of diffuse-sky and albedo irradiance.

The IAM is always a value between zero and one and can be considered as an efficiency due to incident angle. The power is scaled by the IAM at each time-step to account for the angular dependence.

$$P_{actual} = P_{mp}K_{\alpha} \quad (6.36)$$

where  $P_{mp}$  is the PV power computed through Equation 6.20 or 6.32. Equivalently, the PV can be thought of as having an effective efficiency

$$\eta_{eff} = \eta K_{\alpha} \quad (6.37)$$

### Correction due to Soiling

Soiling both blocks plane-of-array solar irradiation (transmission loss) and results in more severe angular reflection losses. The Martin and Ruiz model (MR) accounts for the angular reflection losses, including the influence of soiling, through an empirical angular loss coefficient. In our thermal-electrical model, a correction for soiling losses can be applied by providing a set of MR angular loss coefficients or soiling losses (in percents) for each time-step in the simulation. If percent soiling losses are supplied, the model expects that these losses already include the additional angular losses due to soiling and applies the soiling losses directly to the power calculations, leaving the angular loss coefficient at the clean panel value. If soiling is specified through angular loss coefficients, the model estimates both the transmission losses due to soiling and the angular reflection losses. The angular losses are calculated by the IAM equations described above. To estimate a transmission loss due to soiling, the model uses an empirical correlation based on the MR model. As discussed in Section 5.5, an approximation can be made that for each 1% soiling loss at zero AOI (this corresponds to the transmission portion of the soiling loss), the angular loss coefficient must increase by 0.01375. The transmission loss due to soiling is defined as

$$L_{trans}^{soiling} = c(a_r^{dirty} - a_r^{clean})/100 \quad (6.38)$$

where the loss is a percentage expressed as a decimal,  $a_r^{dirty}$  and  $a_r^{clean}$  are the angular loss coefficients of a dirty and clean panel, respectively, and  $c$  is an empirical relationship relating the

coefficients to transmission loss (with a default value of  $0.01375^{-1} = 72.7$  based on the empirical relationships mentioned above).

The overall losses due to soiling and incident angle dependence can be expressed as a multiplicative combination of the transmission loss and angular loss.

$$L_{tot} = L_{trans}^{soiling} (1 - K_{\alpha}) \quad (6.39)$$

The PV power when accounting for angular and soiling effects becomes

$$P_{actual} = P_{mp} K_{\alpha} (1 - L_{trans}^{soiling}) \quad (6.40)$$

Equivalently, the PV can be thought of as having an effective efficiency

$$\eta_{eff} = \eta K_{\alpha} (1 - L_{trans}^{soiling}) \quad (6.41)$$

## Implementation

The thermal portion of the modeling simply involves creating the PV system geometry and specifying the material properties and boundary conditions in TAItherm. The calculations for power production, angular dependence correction, and soiling loss correction were implemented in Python and coupled with the thermal model through a TAItherm user routine. User routines allow the user to interact with the heat transfer solver through an Application Programming Interface (API) to enforce custom boundary conditions or implement custom calculations. User routines can be coupled with the solver at various points in the solution (beginning or end of the solution, each time-step, or each iteration within each time-step of the thermal simulation). The PV calculations user routine is called at the end of each time-step of the transient thermal simulation. This user routine computes the power production (either through solving equivalent circuit equations or from nominal efficiency) at the current time-step, using the newly computed module temperature while accounting for AOI dependence and any soiling losses. Then a negative heat is imposed on the PV module(s) to account for the portion of solar radiation that is converted to electricity instead of heat. The results of the power production calculations are appended to an output file at each time step. A flow chart of the modeling approach is shown in Figure 6.7.

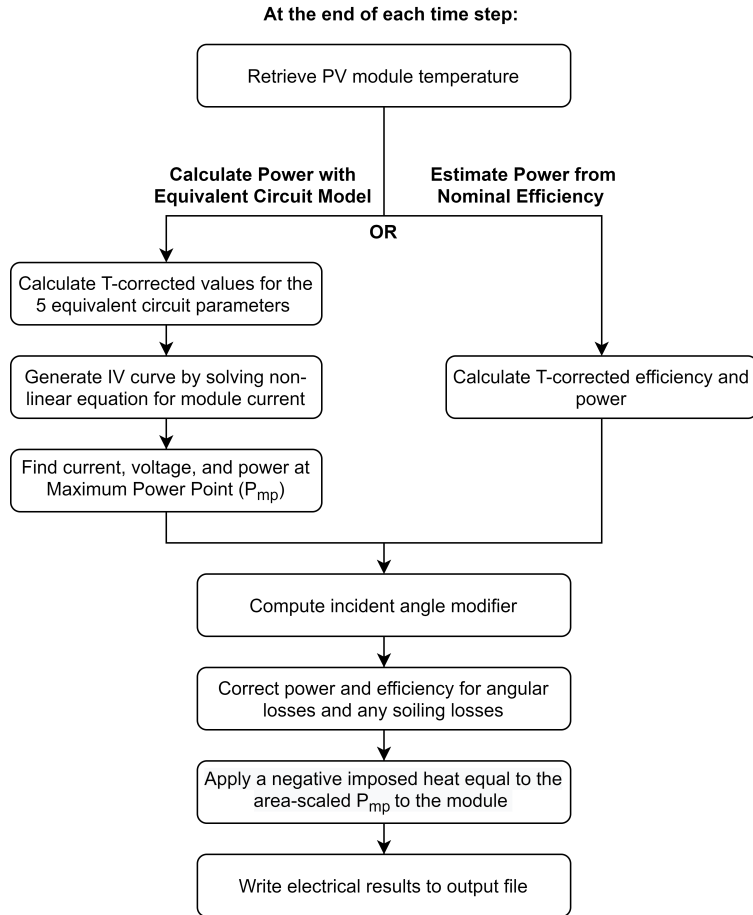


Figure 6.7: Flow chart of the calculations at each time step of the coupled thermal-electric PV model.

Using the equivalent circuit approach allowed a 5572 element TAITherm (2020.1.0) model of a vehicle with a solar roof to solve (without parallel processing) both the heat transfer and electrical models in under one second per time-step (on a Linux machine with a 3.7 GHz Intel i7-8700K CPU). Running the simulation under natural weather conditions over a 12 hour day with one hour time-steps took under two minutes.

### 6.2.3 Model Validation

#### Thermal Model

The thermal PV model was first validated by comparing the temperature prediction of a free-standing PLM260M-60-DG series monocrystalline silicon module under NOCT conditions to the value reported by the manufacturer (see Appendix B for the datasheet). The thermal model was made in TAITherm, following the approach from Sommerfeldt and Schon's previous works [142, 143]. These works represented the PV module by a flat plate with three layers: the PV cells, plastic EVA encapsulate, and the rear glass. The front glass was omitted due to TAITherm's inability to model transparent and opaque layers together in a single part. Since the density of glass and silicon are similar, a combined PV and glass layer was modeled by increasing the layer thickness and adjusting the surface properties to account for the reflectivity, absorptivity, and emissivity of the glass. McAdams linear wind convection [148] was used on the front and back of the free-standing PV model. The layer properties are given in Table 6.6. Note that NOCT is defined under open-circuit conditions; therefore, no electrical model was used for this validation since no current is produced. TAITherm predicted a temperature of 43.9°C, which is consistent with the manufacturer-reported value of  $44 \pm 2^\circ\text{C}$ .

Table 6.6: Physical properties of the solar module.

Layer	Thickness mm	Density kg/m <sup>3</sup>	Conductivity W/m – k	Specific Heat J/kg – K
PV Front Glass and Silicon	0.225+2.5	2330	148	677
EVA	0.5	960	0.7	2090
Rear Glass	2.5	6000	1.8	500

Next, the qualitative relationships between cell temperature and irradiance, air temperature, and wind speed were confirmed (Figure 6.8). TAITherm predicts that cell temperature varies linearly with irradiance and air temperature, and inversely with wind speed, which is consistent with the empirical models.

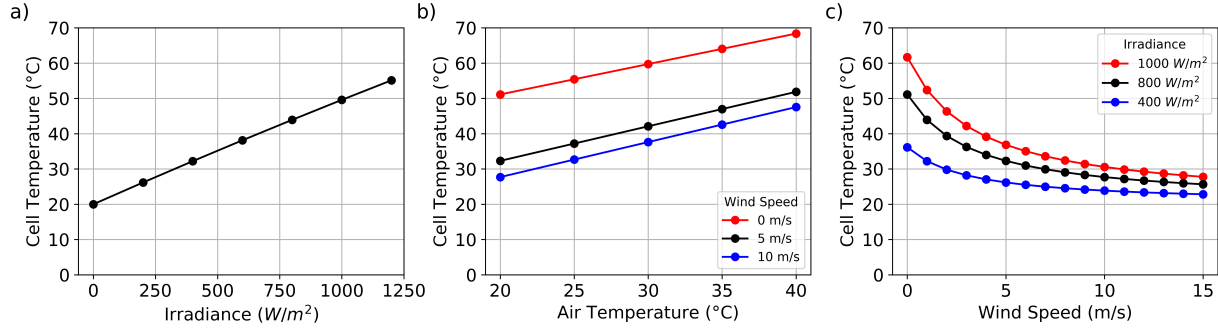


Figure 6.8: TAITherm prediction of cell temperature variation with a) irradiance, b) air temperature, and c) wind speed.

### Equivalent Circuit Electrical Model

For initial verification of the electrical model, equivalent circuit parameters for the PLM260M-60-DG series solar module were taken from Schon's work (Table 6.7). (Note that these parameters were derived in Schon's work at the cell level and therefore  $R_{s,ref}$  and  $R_{sh,ref}$  are smaller than what would be expected for the overall module value since the module is made up of 60 cells).

Table 6.7: Electrical parameters of the solar module.

Parameter	Value
$I_{0,ref}$	$1.0888 \times 10^{-8}$
$I_{L,ref}$	9.0507
$R_{s,ref}$	0.004255
$R_{sh,ref}$	56.052
$n_I$	1.2
$\alpha_{Isc}$	-0.06 %/°C

While measured data of the temperature-dependent electrical properties were not available, the temperature-dependent effects were verified qualitatively. Figure 6.9 shows the simulation results for the solar module under weather conditions representing a sunny day in Phoenix, Arizona. As expected, the photocurrent plot shows a Gaussian-like shape, with the highest current production occurring during the highest irradiance. Transient cell temperature lags behind the peak irradiance

(and current) since it takes some time for the cell to heat up after peak solar loading is reached. We see the efficiency of the cell decrease by several percent when its temperature increases. The silicon bandgap decreases with increasing temperature, while the ideality factor and diode saturation current increase.

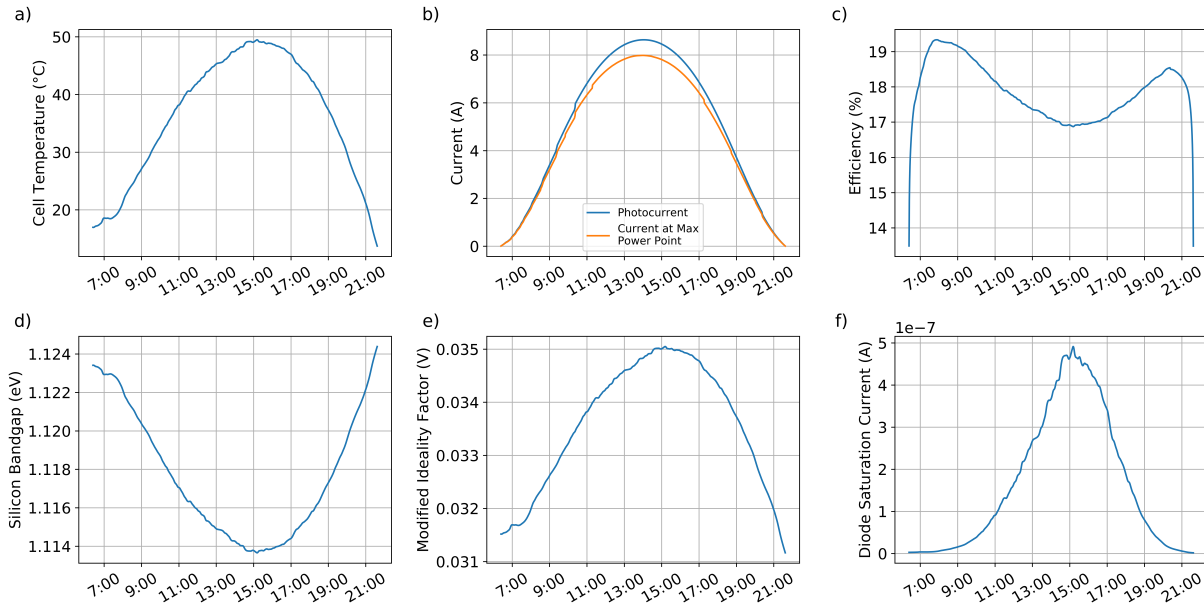


Figure 6.9: One day simulation results for a) cell temperature, b) current, c) efficiency, d) silicon bandgap, e) modified ideality factor, and f) diode saturation current.

Figure 6.10 shows the impact of cell temperature on the IV curve when using the equivalent circuit parameters from Table 6.7. As expected, we see a lower  $V_{oc}$  and fill factor with increasing temperature, resulting in lower power conversion efficiency. In this example, maximum power at  $65^{\circ}\text{C}$  is 29% lower than at  $15^{\circ}\text{C}$ .



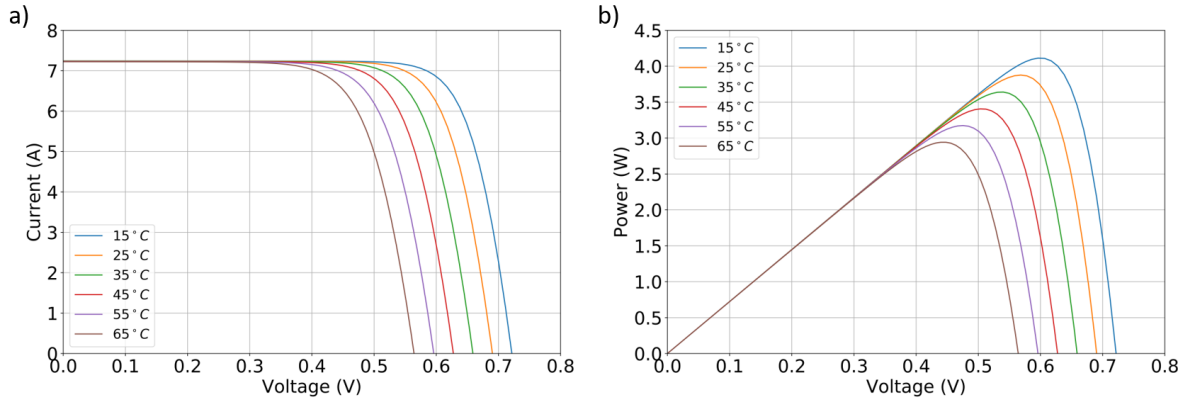


Figure 6.10: Example of the effect of cell temperature on a) IV curve and b) power production.

### Coupled Thermal-Electrical Model

Finally, the coupled PV thermal-electrical model was validated against measured data (provided by Enlighten Energy, Ltd.) of First Solar Series 4 CdTe single-axis tracker module temperatures and short-circuit currents. Since measured values of the components of solar radiation, tracking axis orientation, and the precise sun-tracking path for these modules were not disclosed, the angular dependence of power production was not modeled. However, the angular effects of clean modules that track the sun are small ( $< 2\%$ ) [149] and, therefore, would only slightly affect the results. Since we are interested in the overall module temperatures, and temperature gradients across such a thin material are small, the module was modeled in TAITherm as a single element plate with thermal properties shown in Table 6.8.

Table 6.8: Physical properties of the CdTe solar module.

Thickness mm	Density $\text{kg/m}^3$	Conductivity $\text{W/m} - \text{k}$	Specific Heat $\text{J/kg} - \text{K}$	Emissivity <i>dimensionless</i>
6.8	2451	6.2	718	0.9

The density was calculated from the module area and thickness provided in the datasheet (see Appendix B). The specific heat was estimated using a volume-weighted average of specific heat of glass (750 J/kg-K [150]) and specific heat of CdTe (210 J/kg-K [151]). The thermal conductivity

of CdTe (from [151]) was used. A sensitivity study showed that varying the specific heat between 500-2000 J/kg-K and conductivity between 3-150 W/m-k had a negligible impact on the results. The specific heat affects only the relatively fast transient thermal behavior of a material, while here, we are interested in panel temperatures on the hourly time-scale. Conductivity likely did not have a significant effect because a free-standing panel’s thermal behavior is dominated by the convection and radiation modes of heat transfer.

The measured dataset includes hourly measurements of POA total irradiance, GHI irradiance, wind speed, ambient air temperature, module temperature, and short-circuit currents for four nominally identical CdTe modules. The averages of the four modules’ POA irradiance, GHI irradiance, wind speed, ambient air temperature were specified as boundary condition curves for the following TAItherm user-inputs: imposed solar flux, fluid velocity for convection, fluid temperature for convection, and environmental bounding box temperature. The equivalent circuit parameters were derived using the parameter extraction method described in Section 6.2.2 with the manufacturer nominal values for  $V_{mpp}$ ,  $I_{mpp}$ ,  $V_{oc}$ ,  $I_{sc}$ , and temperature coefficient of  $I_{sc}$  for the FS-4122-3 module as inputs (see Appendix B for the datasheet). Table 6.9 shows the derived equivalent circuit parameters.

Table 6.9: Derived equivalent circuit parameters of the First Solar 4 Series FS-4122-3 solar module.

Parameter	Value	Units
$a_{ref}$	3.46	dimensionless
$I_{L,ref}$	1.855	A
$I_{0,ref}$	$1.317 \times 10^{-11}$	A
$R_s$	3.984	$\Omega$
$R_{sh,ref}$	$1.390 \times 10^3$	$\Omega$
$\alpha_{I_{sc}}$	+0.04	$\%/^{\circ}\text{C}$

The coupled thermal-electrical TAItherm simulation (as shown in Figure 6.7) was run using 0.1 hour time steps for a 15 hour summer day (June 27, 2019, was chosen arbitrarily). Figure 6.11 shows a comparison of the calculated and measured results for module temperature and short-circuit

current. The error bars show one standard deviation of the measured values for the four modules. (Note that module currents for the four cells were nearly identical for most of the day, causing very small error bars). This validation shows that the approach of coupling a heat transfer solver with an equivalent circuit model developed in this chapter can allow to accurately calculate module temperatures and currents.

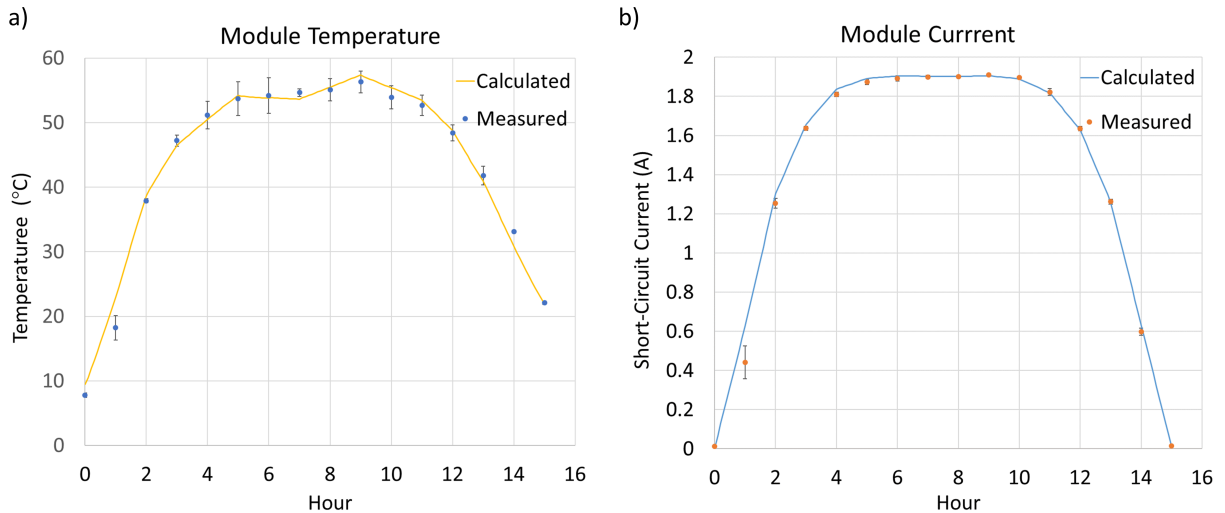


Figure 6.11: Comparison of one day of modeled and measured First Solar Series 4 CdTe module temperature and short-circuit current.

## 6.2.4 Comparison with Empirical Models

Next, we present a comparison of cell temperature predictions from the popular empirical models (described in Section 6.1) with those from the heat transfer physical model. For the empirical models, we use the default coefficients that were derived by the developers of each model since this is how PV engineers and technicians often use the models. Figure 6.12 shows the comparison of cell temperature versus irradiance predictions under 1 m/s and 5 m/s wind. All models yield similar temperature predictions under 1 m/s wind (NOCT conditions at which empirical models are typically fitted), but diverge drastically under 5 m/s wind. As expected, the models that do not include wind as an independent variable (basic NOCT and PVsyst) result in the highest temperature predictions, showing the importance of considering variable wind convection if panels

are installed at a location with varying wind speeds. Clearly, all of the empirical models cannot be simultaneously accurate (at least when using default coefficients).

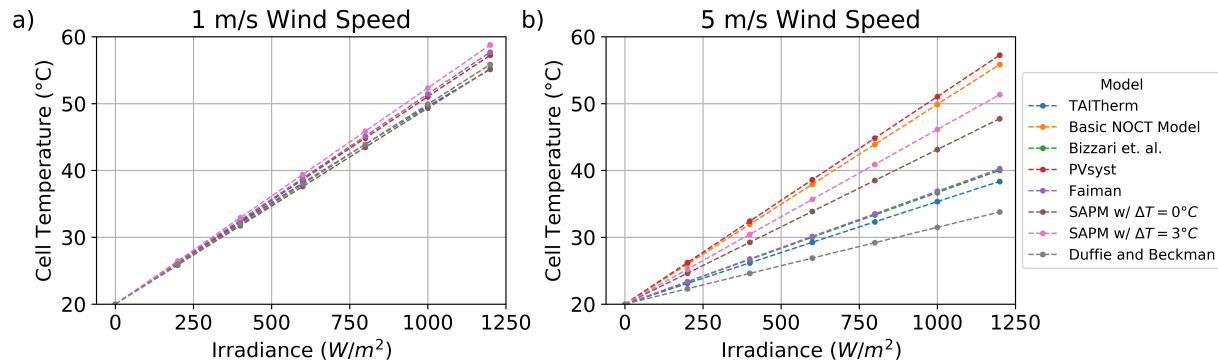


Figure 6.12: Comparison of cell temperature versus irradiance predictions under 1 m/s and 5 m/s wind.

Figure 6.13 compares the cell temperature predictions as functions of air temperature and wind speed (only the models that include wind speed as an independent variable were compared). Again, we see a wide discrepancy between empirical models.

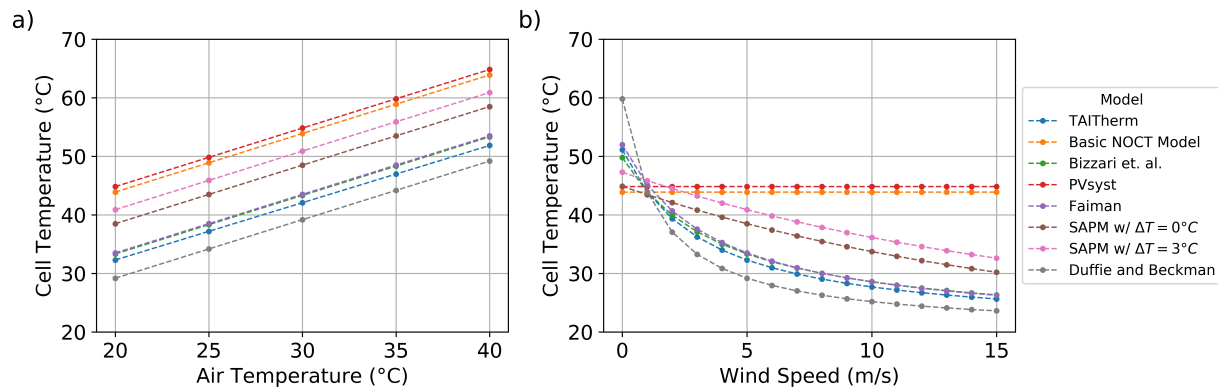


Figure 6.13: Comparison of cell temperature versus air temperature and wind speed predictions.

In order to check whether an empirical model can be fitted to match a heat transfer solver’s results for a free-standing solar cell in operation, we modified coefficients in the PVsyst model and compared predictions of cell temperature versus wind speed and irradiance to TAItherm results. We see that excellent agreement between the heat transfer solver and the empirical model can

be achieved, showing that it may not always be necessary to use a heat transfer solver. However, benefits of the heat transfer approach remain for situations where measured data for empirical model fitting may not be available and for rapid computational testing of different engineering designs and panel integrations into structures.

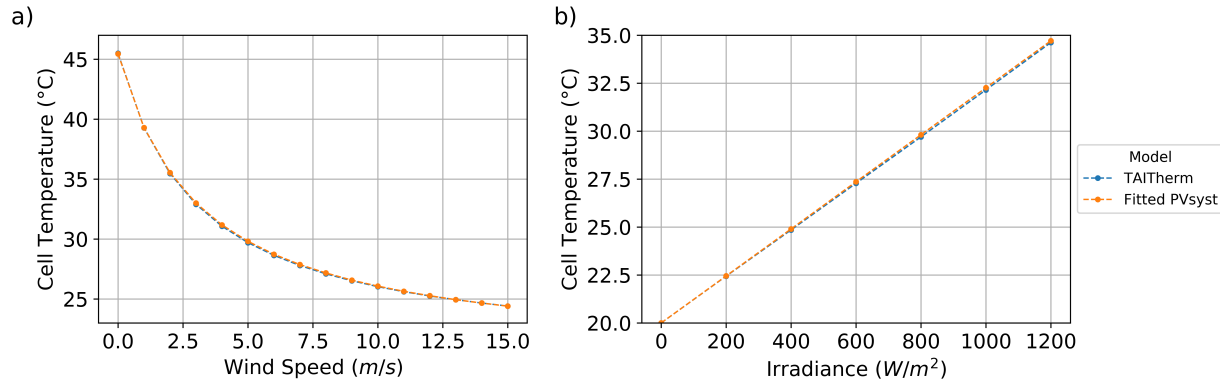


Figure 6.14: Comparison of cell temperature predictions versus wind speed and irradiance made with a fitted PVsyst model ( $\eta_m=18\%$ ,  $\alpha = 0.9$ ,  $u_c = 23.2$ ,  $u_v = 7.4$ ) and TAItherm.

## 6.3 Example Applications

Here, we present three proof-of-concept example applications of the thermal-electric PV model.

### 6.3.1 Building Rooftop PV Systems

The coupled thermal-electric model was used to predict the temperature-corrected power production of a  $64.8 \text{ m}^2$  residential rooftop PV system in Phoenix, Arizona. The starting point for this model was a TAItherm tutorial model of a house (Figure 6.15). PV panels were added to the geometry by adding three PV material layers, with properties described in Table 6.6, to a portion of the roof. For this proof-of-concept model, the PV system is assumed to be made of the same monocrystalline silicon modules (PLM260M-60-DG series) as in Section 6.2.3.

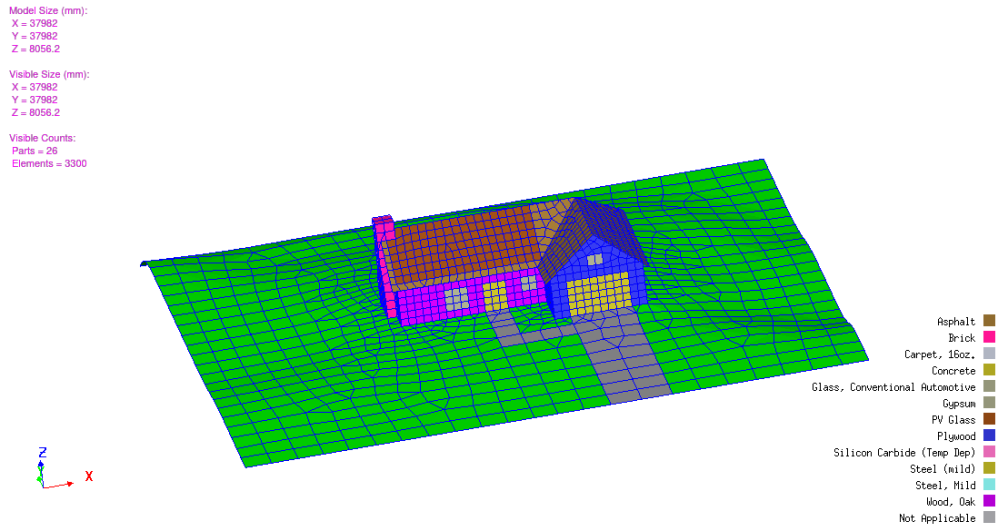


Figure 6.15: TAItherm house model with roof-mounted solar panel.

We first ran the model for one typical hot and sunny summer day in Phoenix (high temperature of 41°C). Weather data for Phoenix was taken from July 15 in the typical meteorological year (TMY) dataset from the National Solar Radiation Database (NSRDB). To evaluate the impact of temperature on the system’s energy production, we compared the model’s results when module temperatures are computed versus when a constant temperature of 25°C (standard test conditions) is assumed (Figure 6.16).

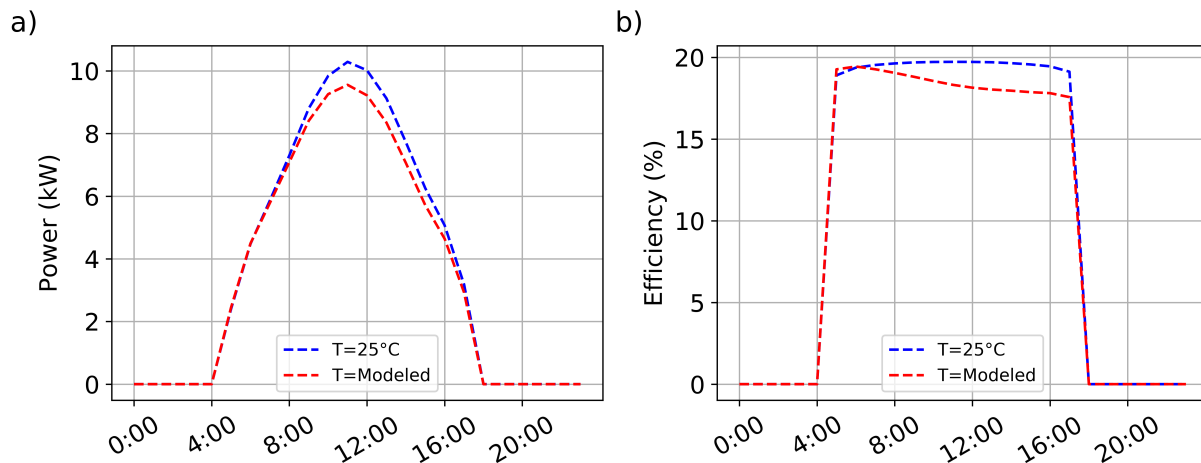


Figure 6.16: PV rooftop system simulation results for a typical day in July in Phoenix, Arizona. Predicted power (a) and efficiency (b) with and without considering temperature-induced losses.

Summing the power over one day, the total energy production with and without temperature correction is predicted to be 99 kWh versus 107 kWh, showing that if panel temperature is not considered, the power production would be overestimated by 8%. The average household electricity usage in the U.S. is 900 kWh per month or about 30 kWh per day [152]. Such a PV system producing 100 kWh on summer days would satisfy the household electricity needs, partially charge electric vehicles that the residents may own (for example, a Tesla Model 3 uses about 26 kWh per 100 miles [153]), and even have some energy remaining to sell back to the grid.

Additionally, the annual energy production was modeled using TMY weather data from the NSRDB. TAITherm also needs cloud cover in order to estimate the sky temperature for the infrared radiation exchange calculations. Cloud cover, which is not available in NSRDB TMY datasets, was estimated as the ratio of DNI under realistic sky conditions to DNI under clear sky conditions (provided in the NSRDB as part of its clear-sky model). Soiling loss coefficients for a typical year in Phoenix for fixed tilt roof panels, with tilt angle equal to the roof's tilt in the TAITherm house model ( $40^\circ$ ) were estimated by running the physical soiling model developed in Chapter 5 using TMY data from Meteonorm [154]. (The NSRDB TMY data could not be used because it does not include rainfall, which is essential for soiling prediction). The predicted DC energy production for the rooftop PV system with and without a correction for soiling losses is shown in Figure 6.17.

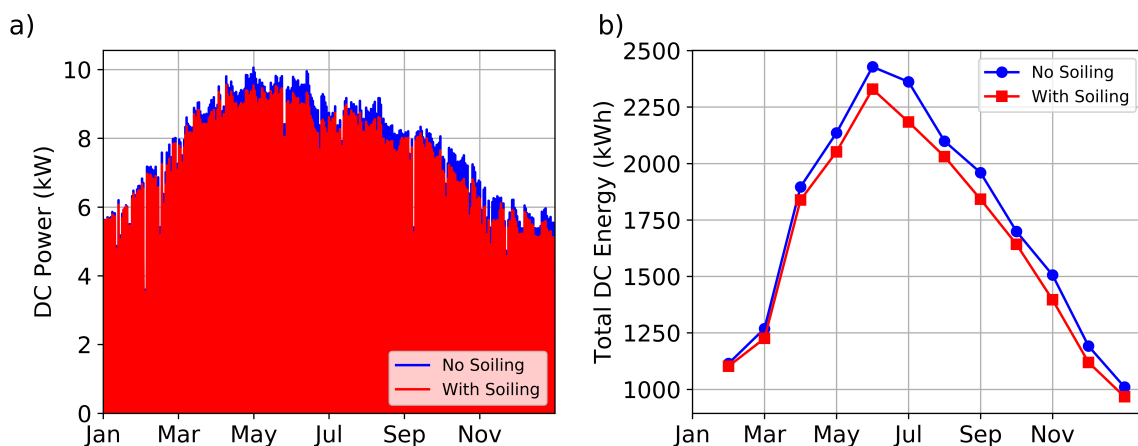


Figure 6.17: Predicted PV energy production with and without including soiling losses. a) Daily DC power. b) Monthly DC energy production.

Figure 6.18 shows the soiling coefficients and the corresponding DC power production losses due to soiling.

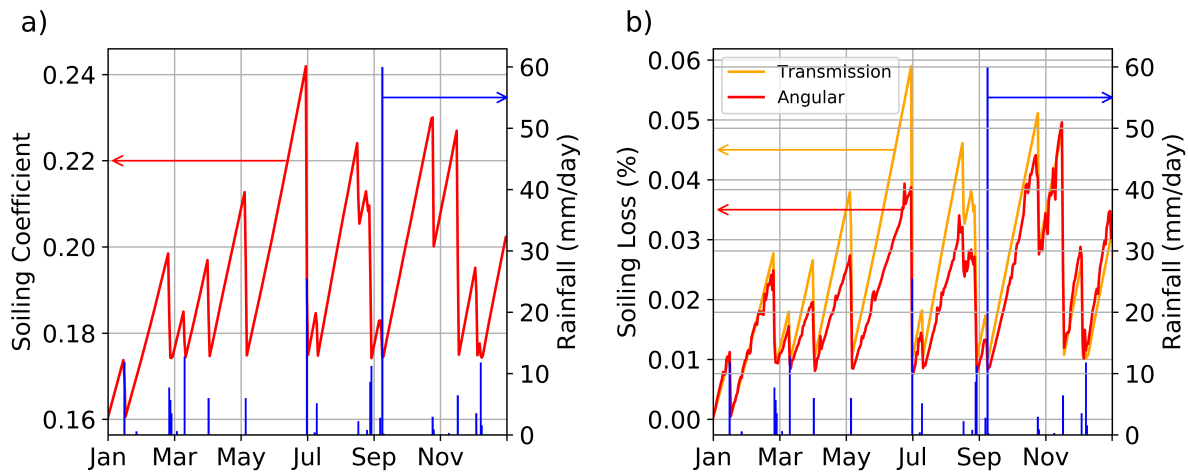


Figure 6.18: a) Soiling coefficients used as input. b) Transmission and angular losses due to soiling calculated by the thermal-electrical model. Daily rainfall totals are shown with blue bars.

One could argue that similar results can be achieved with empirical-based temperature corrections such as those in PVLIB. For simple energy production prediction of a typical rooftop PV system, a heat and radiation transfer solver is not necessary. However, such an approach may be useful for PV system engineering related to heat transfer, such as designing passive or active cooling solutions to improve PV efficiency, designing PVT systems, or studying the rooftop system’s impact on the temperature inside the house. Additionally, more complex integrations of solar panels on irregular surfaces (e.g. vehicle-integrated solar panels, wearables, or solar-powered clothing) cannot be modeled by standard PV modeling approaches such as those implemented in PVLIB. To predict the energy production of such systems, a radiation transfer solver such as TAItherm is almost essential.

### 6.3.2 Vehicle-Integrated Solar Panels

The inspiration for exploring this application was recent news on the development of prototypes of electric vehicles with rooftop solar panels, which may extend the driving range or recharge the car’s



auxiliary battery that powers secondary systems such as screens and climate control [155–158]. Currently, the amount of range extension is limited, but it still provides some benefits, and therefore, there is active research in this area. Hyundai is also researching incorporating semi-transparent solar panels into the panoramic sunroofs of internal combustion engine vehicles to directly charge batteries and reduce the engine’s workload, which is claimed to be the first technology of this type [156]. Vehicle-integrated solar panels (VISPs) could potentially provide a larger benefit on commercial vehicles (e.g. trucks, buses, and trains) where there is more surface area available for installing solar panels. Several variations of VISP systems were explored in this work. All of the models were based on TAItherm’s tutorial model of a Jeep Grand Cherokee.

### Conventional Rooftop PV

In the first version of the model, the entire surface area of the Jeep’s roof was covered by conventional monocrystalline silicon solar panels (PLM260M-60-DG series) by adding the same three PV material layers as in Section 6.2.3. Figure 6.19 shows the TAItherm model geometry.

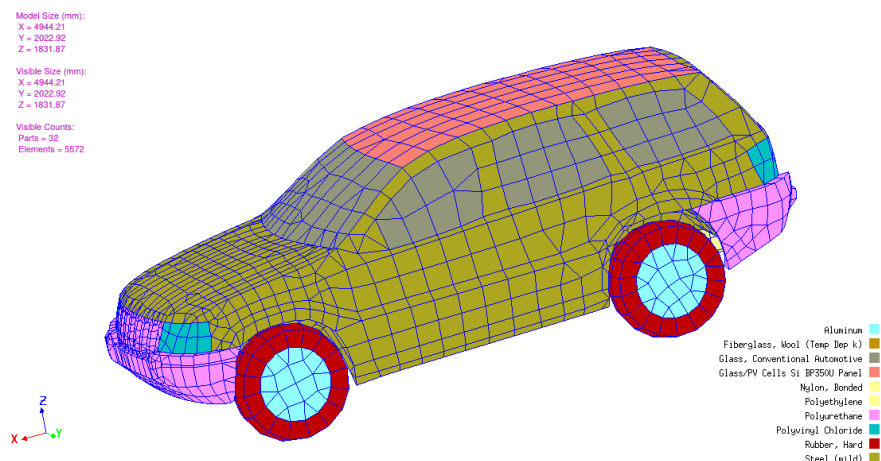


Figure 6.19: TAItherm Jeep model with roof-mounted solar panel.

Like in the building rooftop PV modeling example, we first ran the model for one day (July 15 in the NSRDB TMY dataset for Phoenix). Figure 6.20 compares the results when different factors affecting PV performance are included: irradiance-only, irradiance with angular dependency, and

irradiance with both angular and temperature dependency. The AOI dependence in these results, while having a significant impact on the efficiency near sunrise and sunset, decreases the day's total energy production by only 3%. This is because the sun stays high in the sky for most of the day in the summer in Phoenix, and the PV panel is horizontal, leading to low AOIs that correspond to almost no angular losses. The reduced efficiency due to angular dependence occurs when there is low irradiance, so it has a low impact on overall energy production. Angular effects will be more important in winter months, in Northern latitudes, and for PV installations where the PVs cannot be mounted to minimize the AOI (e.g. building facades and pitched roofs that do not correspond to an optimal panel tilt for that latitude). The effect of temperature dependence was explored by comparing results when module temperatures are computed versus when a constant temperature of 25°C is used. Like in the residential roof example, we again see a significant reduction in power production due to temperature-induced losses during the peak sunlight hours. Summing the power over an 8 hour period (9 am to 5 pm), the total energy production with and without temperature correction is predicted to be 3.8 kWh versus 4.4 kWh, showing that if panel temperature was not considered, the power production would have been overestimated by 17%.

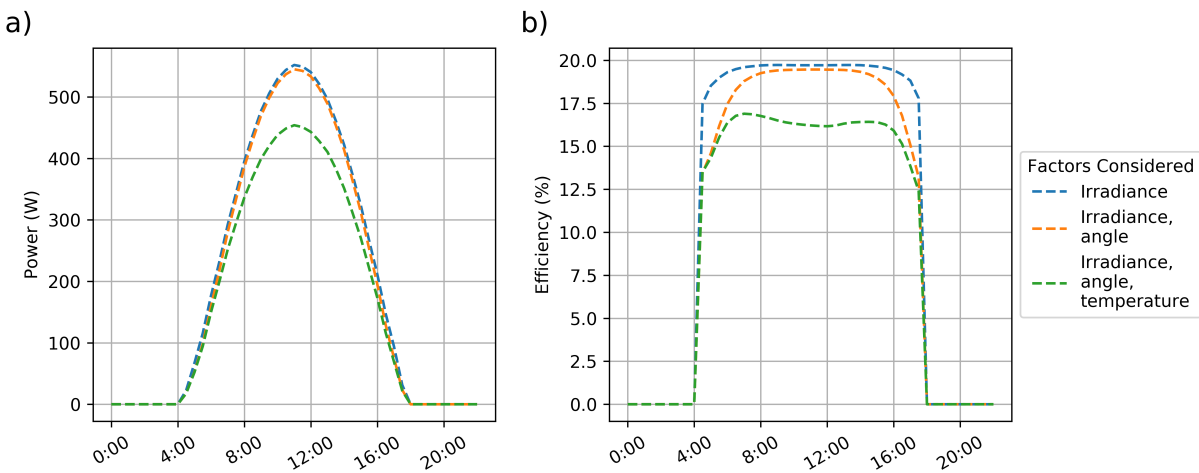


Figure 6.20: Comparison of a single day of modeled vehicle-integrated solar panel power (a) and efficiency (b) when different factors affecting PV performance are considered (irradiance dependence only, irradiance and angle dependence, and irradiance, angle, and temperature dependence).

The VISP's predicted energy production of 3.8 kWh during eight hours (e.g. a workday during which the car is parked outside) could be used in several ways. A ventilation system could be run while the car is parked in the sun to lower the cabin temperature and thus reduce AC use when the occupants return to their car. Alternatively, the power could be used to charge an auxiliary battery that powers secondary vehicle electronic systems (e.g. infotainment, interior lights, electrical plugs) or to power the vehicle owner's electronics. Such a PV battery could be especially useful if one uses the Jeep for rustic camping, allowing campers to charge electronics without running the engine and without potentially discharging the main battery. On a potential future electric-SUV with a similar roof surface area, the panels could even be used to slightly supplement the charge in the main battery. Assuming an EV energy efficiency of 26 kWh/100 miles [153], such a PV system could give an additional 15 miles of range after the car is parked for 8 hours in the sun. This could be enough to use the EV for short-distance commuting without ever having to plug it into a charging station.

Assuming an idealized scenario where the Jeep is always located in an unshaded area and the PV panel is kept perfectly clean, a total annual energy production of 963 kWh could be achieved in a typical meteorological year in Phoenix, Arizona (weather data from NSRDB). Assuming 26 kWh/100 miles EV efficiency, this would provide 3700 miles of solar-powered range a year, which is about 1/4 of the average driver's annual mileage in the U.S. [159]. Of course, the actual amount will likely be lower due to shading and soiling, but this simulation provides us an upper-bound estimate of what is possible. The simulation shows that integrating a conventional PV in an SUV's roof is not sufficient for a fully solar-powered car for the average driver. A PV technology that could allow using a greater surface area of the vehicle is explored in the next section.

## **Transparent PV**

Transparent photovoltaics (TPVs), which selectively absorb ultraviolet and near-infrared light while allowing high transmittance of visible light, could allow harvesting solar energy from the surfaces of buildings, automobiles, and electronic device displays without impacting function or aesthetics.

TPVs have caught the attention of the automotive industry, with some automakers looking at incorporating TPVs, for example, for sunroofs where the energy could be used to power fans to cool a car parked in the sun [160]. Transparent windows with TPVs with nearly 10% PCE are already being commercialized [161]. In the future, TPVs could be incorporated into automobile windows or even cover the entire surface area of vehicles for maximal energy production. Here we use our thermal-electrical PV model to predict the potential energy production of a Jeep Grand Cherokee for a windows-only (including a large sunroof) and entire surface area TPV system in five U.S. cities: New York NY, Lansing MI, Honolulu HI, Los Angeles CA, and Phoenix AZ.

Since we are modeling an emerging technology, electrical parameters were not available. Therefore, we used an estimated realistically achievable efficiency of 15% [162]. Angular effects were considered by specifying measured IAM curves from a TPV angular effects study [147]. The capability of TAItherm to model transparent materials was used for the Jeep's windows with measured values of TPV spectral transmittance and reflectance [163] specified as curves. TAItherm integrates the spectral values to determine overall transmissivity and reflectivity for use in the transparent materials solver. To model the TPVs on the Jeep's body panels, regular solid materials were used due to TAItherm's inability to model a transparent material on top of a non-transparent one. Much of the light transmitted through the TPV film will be absorbed by the body panel underneath, so the effect of neglecting to explicitly model the optics is likely small. However, note that this neglects the potential additional energy production from light that is reflected from the vehicle body panel surface back through the film. Figure 6.21 shows the spectral optical properties and angular dependence used in the model.

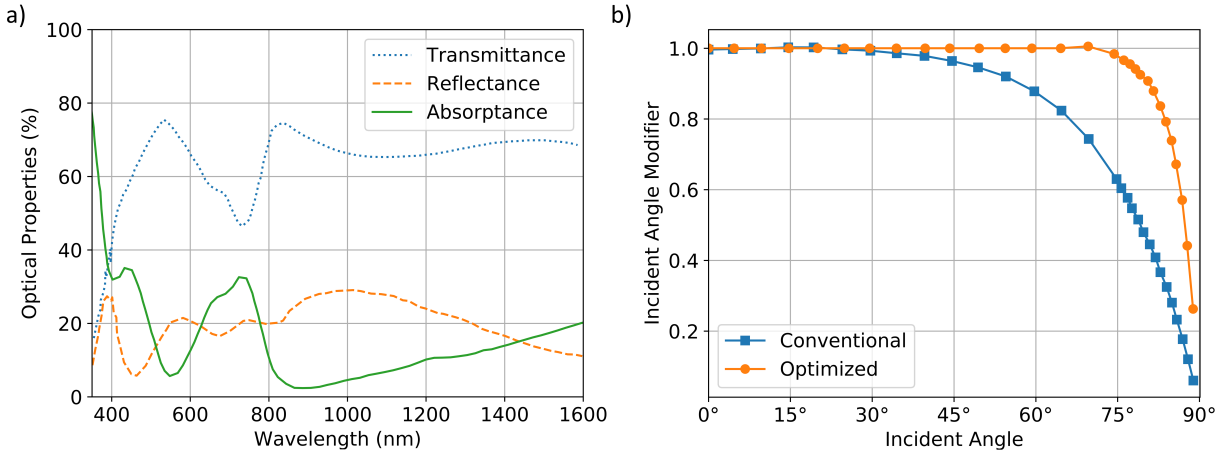


Figure 6.21: a) TPV UV-vis spectrum for front illumination. Data from [163]. b) Incident angle modifier for a conventional thin film PV and one that is optimized for improved angle-dependence. Data from [147].

TMY weather data for the five cities was obtained from the NSRDB. The Jeep was assumed to be outside in an unshaded area (but under realistic weather patterns, including cloud cover) for the entire year. The TAItherm built-in ground surface background of aged asphalt (infrared emissivity of 0.94 and solar absorptivity of 0.85) was assumed for the thermal and radiation modeling. Given the difficulty of predicting soiling on a vehicle that is in use, losses due to soiling were not considered. Vehicles with PVs should be washed regularly to maximize energy production. Predicted total yearly energy production and monthly energy production for the five cities are shown in Figure 6.22. For angle of incidence corrections, the TPV models assumed the conventional thin-film angular dependence from Figure 6.21b and the silicon PV model used the empirical equations from Section 6.2.2.

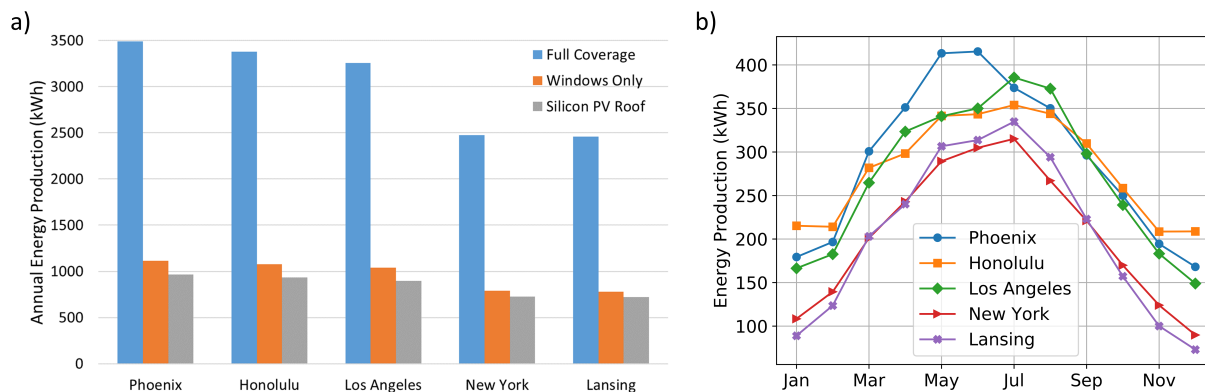


Figure 6.22: a) Predicted total annual energy production in five U.S. cities for three different vehicle-integrated PV systems: TPVs covering entire surface of the vehicle, TPVs only used in windows, and a conventional silicon PV roof module. b) Predicted monthly energy production for the TPV system that covers the entire surface of the vehicle.

Assuming an EV energy efficiency of 26 kWh/100 miles [153], a Jeep Grand Cherokee that is completely covered with 15% efficiency TPVs could drive 13,400 miles a year in Phoenix on solar energy alone. Note that this assumes an idealized scenario where the car is always in non-shaded areas (e.g. parked far away from other vehicles that would block sunlight from reaching the side panels) and kept perfectly clean. If TPVs are only used for the Jeep’s windows (including a sunroof), solar energy could provide up to 4,300 miles of range a year. A conventional silicon PV roof could provide up to 3,700 miles. In locations with less solar irradiance, such as New York or Lansing, the energy production is expected to be about 30% lower than in Phoenix. Rerunning the model of the Jeep with full coverage of TPVs with an improved AOI dependence (the optimized curve from Figure 6.21), results in an approximately 10% increase in predicted annual energy production. This demonstrates the need to include an AOI correction in PV modeling and also provides motivation to develop PV devices with optimized angular dependence. The TAITherm model also predicts that TPVs that cover the entire vehicle’s surface will have an additional benefit of causing a reduction of cabin air temperature by 1-2°C, which would reduce cabin cooling costs during the warm seasons. Of course, the actual driving range will also depend on the influence of temperature on battery performance, HVAC use, and driving conditions (city vs. highway, flat vs. mountainous). In future work, the PV thermal-electrical model could be coupled with electric

vehicle battery, motor, HVAC, and drive-cycle models for more detailed analysis.

### 6.3.3 PV-Battery Systems

Batteries are often used to store energy produced by photovoltaics. When developing PV-battery systems, it is necessary to appropriately select the capacity and type of battery that can store the needed amount of energy and satisfy the charge and discharge rate requirements for the system's application. Batteries that are charged with currents that are a larger proportion of their maximum capacity degrade faster. Additionally, the temperature of a battery during operation must be considered for several reasons. One is to ensure that it stays within the safe operating range for the battery and within any additional temperature restrictions due to the application (e.g. there may be a narrower operating range for batteries installed together with other sensitive electronics). The temperature of a battery also impacts its performance and, therefore, should be considered for an accurate estimate of usable battery capacity and available discharge power. In some applications, passive or active thermal management may be used to maintain the battery within its optimal operating range. Understanding how batteries degrade as functions of time, charge/discharge cycles, and temperature can help extend battery lifetime by optimizing charging and discharging with "smarter" battery management systems (BMSs). This section outlines how one may combine the PV thermal-electrical model presented in this chapter with battery performance and lifetime models.

In this work, the performance and lifetime of a PV-system battery are modeled using a commercial thermal-electrical battery lifetime prediction tool developed by ThermoAnalytics. The model consists of two main parts: a thermal-electrical battery model and a battery lifetime model. The lifetime model is an empirical model with physically justifiable formulas developed by NREL [164]. The NREL lifetime model separates battery degradation into calendar and cycling fade. Calendar fade is degradation that occurs over time and is independent of cycling. Cycling fade is degradation that occurs with the number of cycles and is independent of time. Since calendar and cycling fade are due to internal chemical processes in the battery, their rates depend on battery temperature,

thus requiring a thermal-electrical model, which is run in TAITherm to predict those temperatures. The electrical model uses NREL’s equivalent circuit battery model to calculate the voltage, state of charge (SOC), currents, and heat generation of individual cells within a battery. The calculated heat generation is considered in the thermal model to calculate new temperatures. These temperatures affect the battery’s electrical behavior, which is modeled by temperature-dependence of the resistors in the equivalent circuit model. Figure 6.23 shows a schematic of the thermal-electrical battery model.

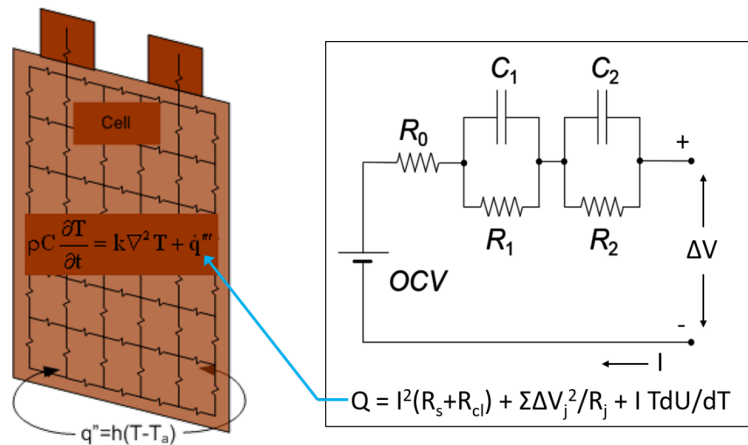


Figure 6.23: Schematic of the thermal-electrical battery model.  $Q$  is the heat generated by the battery, calculated in terms of Joule heating (electrical losses) within the battery equivalent circuit and entropic heating (heat from chemical reactions in the battery). Adapted from [165].

As batteries age, their resistance increases and capacity decreases, influencing the battery’s temperatures and performance. Thus, the lifetime and thermal-electrical battery models are bi-directionally coupled, forming a multi-timescale simulation. The lifetime model’s goal is to describe a battery’s change in resistance and capacity over the course of months and years and therefore uses a one-day time step. The thermal-electrical model’s goal is to describe a battery’s performance at the minute and hour resolution and therefore uses a time step on the order of minutes. ThermoAnalytics’ co-simulation software CoTherm controls the multiple time-scale simulation. First, the thermal-electrical TAITherm model is run for a single day to compute the battery’s temperatures and SOC over time. This information is provided to the lifetime model (integrated into CoTherm), which is run with one-day time-steps for the period of a few months.



After a few months of lifetime simulation, the currently predicted values of battery capacity and resistance are used to update the equivalent circuit coefficients, and the thermal-electrical model is rerun for a single day. This cycle repeats to simulate many years of the battery's life. Figure 6.24 shows the battery lifetime simulation approach.

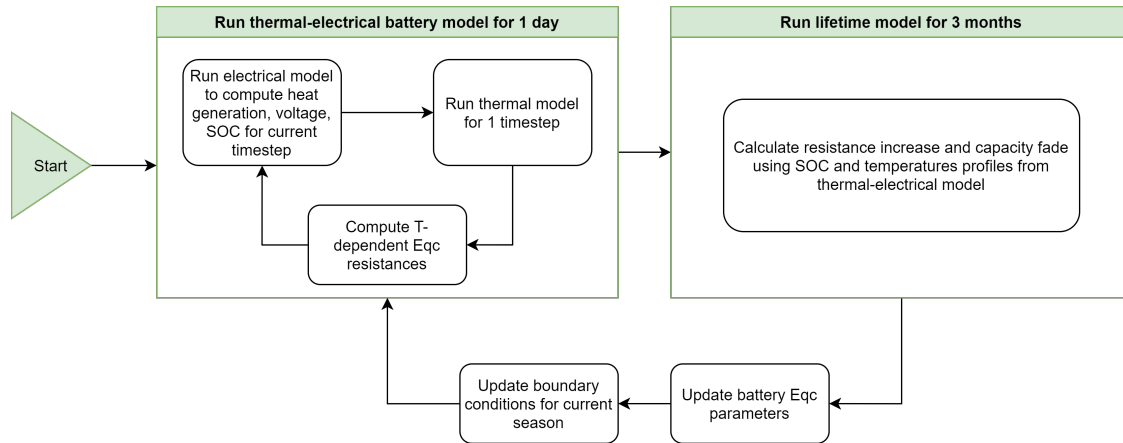


Figure 6.24: Flow diagram of the battery life prediction model. ("Eqc" stands for "equivalent circuit".)

For proof-of-concept modeling, we specified a PV module's photocurrent at maximum power as the charging current of the battery. To compute the photocurrent, we used the validated PV thermal-electrical model to model a single First Solar CdTe Series 4 module located in Phoenix, Arizona. Irradiance and weather for one representative day in each of the four seasons was used to generate four representative photocurrent profiles for input into the battery lifetime model. After every three months of lifetime simulation, the TAItherm thermal-electrical model was rerun using the representative photocurrent for that season. We modeled two PV-battery systems that both use the same CdTe solar module but have different sized batteries for energy storage (30 Ah and 60 Ah). For simplicity, the batteries were assumed to start the day with 20% SOC, charge during the day with the PV module, and be discharged each night back down to 20% SOC. Figure 6.25 shows one such charge/discharge current profile and the corresponding battery SOC. For this simulation, the batteries were assumed to be in a climate-controlled environment maintaining 22°C (natural weather environmental boundary conditions can be specified in the models if desired).

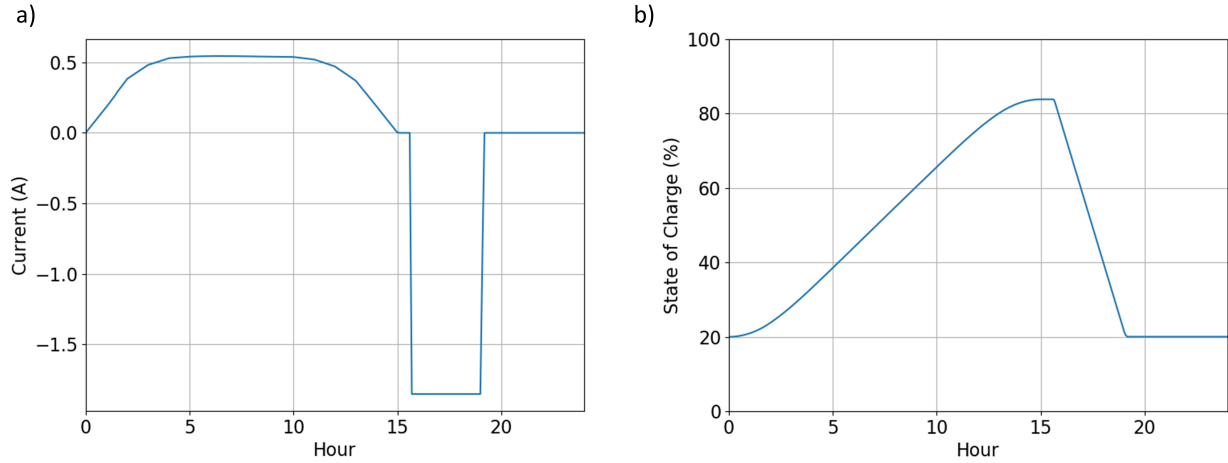


Figure 6.25: a) Battery charge/discharge current over a single summer day. Positive current is defined as charging. b) State of charge of the 30 Ah battery due to the current profile in a).

Figure 6.26 shows the results of the predictions of relative resistance and capacity of the 30 Ah and 60 Ah batteries over their life. Both batteries are oversized for the system, meaning that they are not fully charged/discharged over normal use. This oversizing reduces the cycling fade of the battery, thus increasing the battery lifetime. We see that the larger 60 Ah battery degrades slower than the smaller 30 Ah battery. The financial trade-off between a larger, more expensive battery and longer battery lifetime, reducing the frequency of battery replacement, needs to be considered when designing or purchasing a PV-battery system.

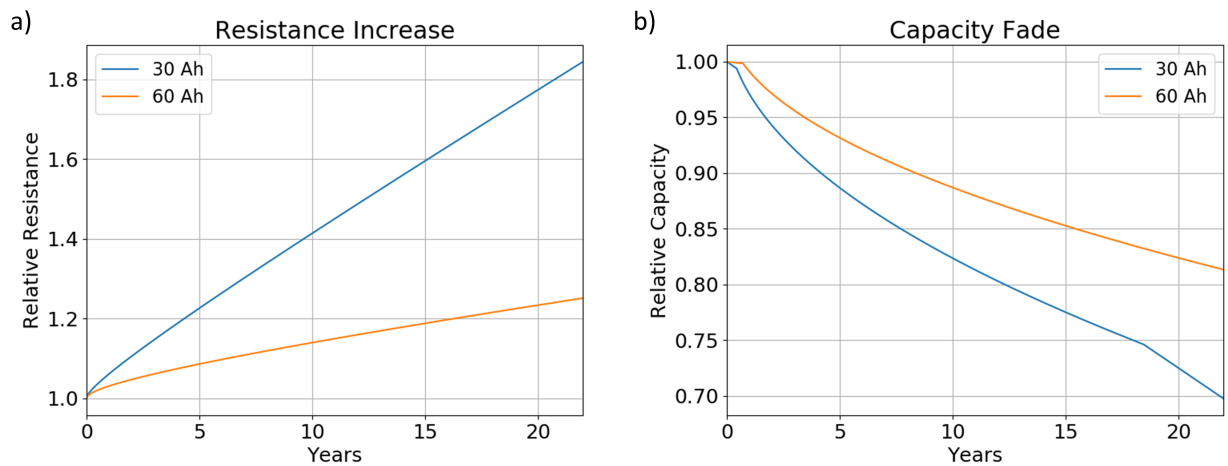


Figure 6.26: Relative resistance (a) and capacity (b) of the 30 Ah and 60 Ah batteries. Values are relative to those of a brand-new battery.

In future work, these simulation approaches could be used to design and model batteries which are optimized for photovoltaic systems [166]. They could also be used to model battery packs (multiple batteries connected in series or parallel to provide a higher energy storage capacity or power) and smart battery management systems which optimize the charging/discharging of these battery packs to extend usable capacity, power, and lifetime of the pack [167]. Figure 6.27 shows one possible approach envisioned for PV-battery and battery management system modeling. The equivalent circuit battery model could be replaced with an electrochemical model if a more detailed and physics-based battery model is desired.

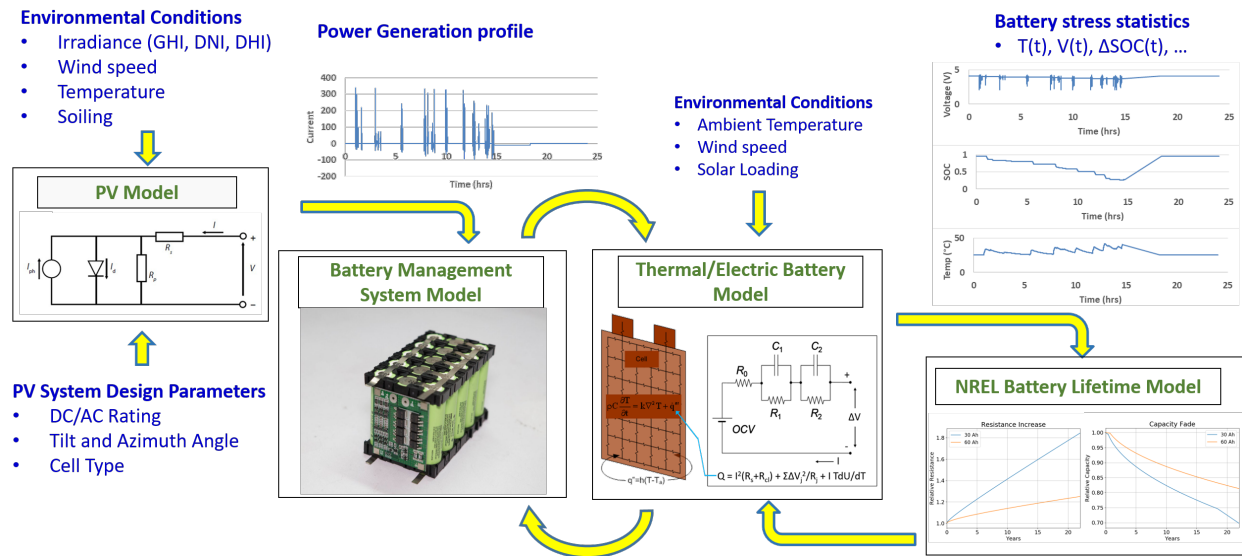


Figure 6.27: PV-battery and battery management system modeling approach.

### 6.3.4 Other Applications

In addition to reducing thermal losses, other photovoltaic applications where coupled thermal-electrical PV models could be an effective simulation approach include:

- Solar cells in space under extreme (both high and low) temperature conditions [168, 169]
- Photovoltaic-thermal technology: a PV panel coupled with a thermal collector [170]
- Photovoltaic collectors and bifacial PV systems [171, 172]

- Temperature-induced solar cell ageing [173]
- Battery management systems for efficient storage of photogenerated energy [174]
- IR imaging of PV-plants [175]
- Melting of snow on heated panels [176]
- Condensation on dusty PV modules and associated formation of mud [177]

## 6.4 Conclusions

In this chapter, we developed coupled thermal-electrical PV system models that consider the effects of temperature on solar panel performance by implementing custom user routines in a commercial heat transfer solver. After validating the modeling approach by comparison with measured data, we developed proof-of-concept modeling examples for residential PV systems and vehicle-integrated solar panels. Through these examples, we showed that consideration of temperature-induced losses is important to avoid overestimating a PV system's potential energy production. Additionally, we developed the foundations for modeling the interactions between solar panels and batteries used for energy storage by coupling the thermal-electrical PV model with a commercial thermal-electrical battery temperature and performance model, and a commercial battery aging model. These models can also be used together with the soiling models developed in Chapter 5. The approaches developed in this chapter, which leverage the power and flexibility of a commercial heat transfer solver, can be applied for computer-aided engineering of a wide range of PV systems, such as vehicle and building-integrated PVs, PVs in space, PV-thermal technology, and battery management systems for PV energy storage.

## CHAPTER 7

### CONCLUSIONS AND OUTLOOK

#### 7.1 Conclusions

In this dissertation, we described the development of computational multi-physics models for photovoltaic devices and systems. We started our modeling with the smallest functional unit in a PV system: a single solar cell. For this goal, we used the computationally efficient yet accurate drift-diffusion approach. We introduced the numerical methods for drift-diffusion modeling in Chapter 2. We also demonstrated that the drift-diffusion model is consistent with the Mott-Gurney law for space-charge-limited currents. In Chapter 3, we investigated the impact of the choice of discretization approach (Scharfetter-Gummel versus Slotboom), iterative solution approach (Gummel versus Newton), and convergence improvement technique (linear versus Pulay mixing) on the convergence behavior of a drift-diffusion model for bilayer organic solar cells. The findings can help in selecting a suitable discretization and iteration approach for each device model. Pulay mixing can be used to improve convergence speed, Newton's method is superior to Gummel's method for situations where the equations become highly coupled, and Slotboom variables can be used to simplify the implementation of the matrix equations.

In Chapter 4, the drift-diffusion model was adapted for planar perovskite solar cells and validated by reproducing literature results. The model was then used to describe recent experimental results for perovskite solar cells that use fullerene layers for electron transport. Through drift-diffusion modeling, poor electron extraction at the perovskite interface was found to be the primary cause of the severe decrease in device performance when there is no  $C_{60}$  layer. We have also found a possible explanation for the S-shaped JV curve seen in the 0 nm  $C_{60}$  devices. The S-shape is likely due to an imbalance of carrier mobilities in the HTL and ETL, which results in charge accumulation and the formation of an interface dipole. The modeling results support the experimental observation and conclusion that while the inclusion of a  $C_{60}$  layer is critical for achieving good performance of

perovskite solar cells that use BCP as their ETL, an ultra-thin  $C_{60}$  is sufficient to improve device performance by enhancing electron extraction.

In the second half of this dissertation, the modeling focus was shifted to the larger scale of PV modules and systems, where each module is made up of many individual solar cells, and each system can be composed of many modules. To improve return-on-investment assessment for solar energy systems, PV models need to accurately predict energy output, including considering losses due to temperature and soiling. In Chapter 5, we explored both semi-physical and machine learning approaches to modeling the soiling of PV panels. We developed a general semi-physical model which is expected to be reasonably applicable globally, provided that the empirical coefficients are fitted on a region-by-region basis. We also developed the methodology for integrating the soiling models with a Python package for PV energy production prediction (PVLIB) and cleaning cycle optimization algorithms, which resulted in the release of a new commercial software tool (PV SoilSayer). Preliminary model validation was performed by comparison to published soiling measurements from an NREL study. Additionally, we demonstrated the feasibility of using multi-linear regression and artificial neural networks for soiling predictions. These approaches were found to be able to both replicate the results of semi-physical soiling accumulation models and predict future soiling losses based on historical measurements of soiling and environmental parameters. The models and software that we developed are expected to provide the PV industry with improved methods for predicting soiling losses and their financial impacts.

Finally, in Chapter 6, we developed coupled thermal-electrical PV system models by implementing custom user routines in a commercial heat transfer solver. The modeling approach was validated by comparison with measured data from a utility-scale PV system. We also developed proof-of-concept modeling examples for residential PV systems and vehicle-integrated solar panels. Additionally, we developed and demonstrated an approach for modeling PV-battery systems by coupling the thermal-electrical PV model with a commercial thermal-electrical battery performance model and a commercial battery aging model. These thermal-electrical PV models are expected to be beneficial for the engineering of a variety of PV systems.

## 7.2 Outlook

There are many possibilities to extend this research. The drift-diffusion model can be adapted to various solar cell architectures to help improve our understanding of the physics in these devices and perform computational experiments that explore the impact of different materials and cell architectures on device efficiency. The models can be extended to consider transient effects and field-dependent carrier mobilities. Additionally, the drift-diffusion model can be extended to simulate light-emitting diodes (LEDs). LEDs that are made of organic materials (OLEDs) are a promising technology for digital displays and lighting. The physics in LEDs is very similar to solar cells, with the main difference being that in solar cells, photogenerated carriers are separated to generate a current, while in LEDs, an external current forces carriers through the device where they recombine and emit light. Two and three-dimensional extensions of the drift-diffusion model can be applied to devices with asymmetry in the carrier transport in the in-plane directions. (Example implementations of extending the drift-diffusion models presented here to 2D and 3D are available<sup>1</sup>). Further fundamental understanding of materials for solar cells and LEDs can be achieved through ab-initio quantum chemistry calculations (e.g. density functional theory). Ab-initio calculations can also guide experimental efforts in developing new devices by helping to select promising candidate materials (e.g. based on calculated bandgaps and carrier mobilities). The convergence improvement methods discussed in Chapter 3 could also be applicable to other systems of equations with similar mathematical properties to the drift-diffusion equations.

The PV soiling models and software developed in Chapter 5 can be applied to help PV system developers, maintainers, engineers, and researchers have a better understanding of soiling losses. With the growing realization of the impact of soiling, the installation of soiling monitoring stations is becoming more widespread, which will lead to the availability of more soiling data. With this soiling data, the correlations between environmental parameters (such as particulate matter, wind speed, and rainfall) and soiling should be analyzed for numerous regions worldwide and used to develop region-specific semi-physical or machine learning models for soiling loss prediction.

---

<sup>1</sup>[https://github.com/tgolubev/Drift-Diffusion\\_models-Cpp\\_Matlab](https://github.com/tgolubev/Drift-Diffusion_models-Cpp_Matlab)

Careful experiments should be conducted to clarify the cleaning effects of rain and attempt to compile a database of regional rainfall thresholds required for effective cleaning. Experiments should also be conducted to further study the influence of wind on soiling accumulation, especially focusing on resuspension, which is currently not well understood. Additionally, the predictions of optimal cleaning cycles should be validated by conducting experiments where panels are cleaned according to different schedules.

In the last part of Chapter 5, we have demonstrated the potential of using MLR and ANN for predicting soiling. However, MLR is unable to capture non-linear effects, and deep learning (i.e. artificial neural networks) is not necessarily the best solution for all datasets since it has many disadvantages such as requiring larger amounts of data and more computational resources to train than other techniques, and being difficult to interpret. Therefore, it is important to explore other ML solutions. Testing multiple ML models for a given dataset is tedious and requires significant knowledge and experience with ML, which limits the ability of photovoltaic engineers and researchers to use ML. The new field of automated machine learning (AutoML) provides methods that automate the process of selecting a suitable ML model and its hyperparameters (user-defined parameters that control the learning process) for a given dataset, thus greatly improving the efficiency of developing an ML model and making ML accessible to non-ML-experts. In future work, open-source AutoML packages such as TPOT (Tree-based Pipeline Optimization Tool), Auto-sklearn, and AutoKeras can be used to select the best ML algorithms and hyperparameters for PV soiling loss models.

The coupled thermal-electrical PV modeling approaches developed in Chapter 6 can be applied for computer-aided engineering of a wide range of PV systems, such as vehicle and building-integrated PVs, PVs in space, PV-thermal collectors, wearable PVs, and battery management systems for PV energy storage. Further validation and refinement of the models should be done in collaboration with experimental PV research. The models can also be improved by coupling with more sophisticated system-level models. For example, a PVT collector can be modeled by coupling the PV models developed here with a computational fluid dynamics software for modeling the fluid



flow in the heat exchanger. Another possible application of system-level modeling is predicting the contribution of vehicle-integrated PVs to electric vehicle (EV) driving range. To develop such a model, one could couple the thermal-electrical PV model with a model of EV batteries that considers the impact of temperature on battery efficiency. One could further couple the PV and battery models with a model of the vehicle's HVAC system and a model of human thermal comfort (such as in [178]) in order to estimate the power needed to preserve the comfort of the vehicle's occupants in different seasons and climate regions. Finally, ML-based reduced-order-modeling where physical models are replaced with ML models that replicate the physical models' behavior should be explored as a way of reducing the computational expense of PV system-level modeling.

## **APPENDICES**

## APPENDIX A

### PV SOILSAYER SOFTWARE DESCRIPTION

A significant portion of the photovoltaics soiling research completed for this dissertation involved developing practical solutions for integrating the various soiling modeling approaches (described in Chapter 5) with an open-source Python package for PV modeling (PVLIB) [129, 179] and the PV cleaning cycle optimization algorithms of a PV startup company (Enlighten Energy, Ltd). The results of this integration was Enlighten Energy's release of PV SoilSayer, a commercial software application for soiling loss calculations and optimal clean cycle forecasts. A description of the software is presented here to illustrate how the soiling models developed in this dissertation were incorporated into a broader PV simulation tool. After writing, this Appendix was adapted to create the first version of the PV SoilSayer User Manual.

#### A.1 Weather

Prediction of a PV system's energy production and soiling losses is dependent on the location-specific weather patterns. PV SoilSayer utilizes annual weather files with an hourly resolution for its predictions. Upon entering the location of their PV system, the user can choose from one of several weather databases: 30-year typical meteorological year (TMY) from Meteonorm [154], actual measured weather from last calendar year (from AccuWeather), next year weather forecast (from AccuWeather), and an alternative precipitation-based TMY that we self-generated based on 10-year historical data (from AccuWeather). Two important parameters for energy and soiling loss prediction, total GHI and total precipitation, are compared graphically to help select a weather resource. The weather station locations relative to the plant locations are displayed on an embedded Google Map (Figure A.1). Note that the Meteonorm TMY resource interpolates the weather for particular coordinates from multiple nearby plants (all shown on the map), while the Accuweather resources select only the closest plant. There are also options to update TMY weather datasets with year-to-date weather and 90 day weather forecasts (from AccuWeather).

Users also have the option of uploading their own weather data. Since precipitation is often measured at a daily, instead of an hourly resolution, there is also an option to upload hourly weather data with daily precipitation. In this case, the daily precipitation will be interpolated to hourly values to use in the forecasting algorithms. Weather parameters used for forecasting are solar irradiance components (GHI, DNI, DHI), relative humidity, wind speed, wind direction, ambient air temperature, and precipitation. Any weather parameters that are not uploaded by the user are taken from Meteornorm TMY.

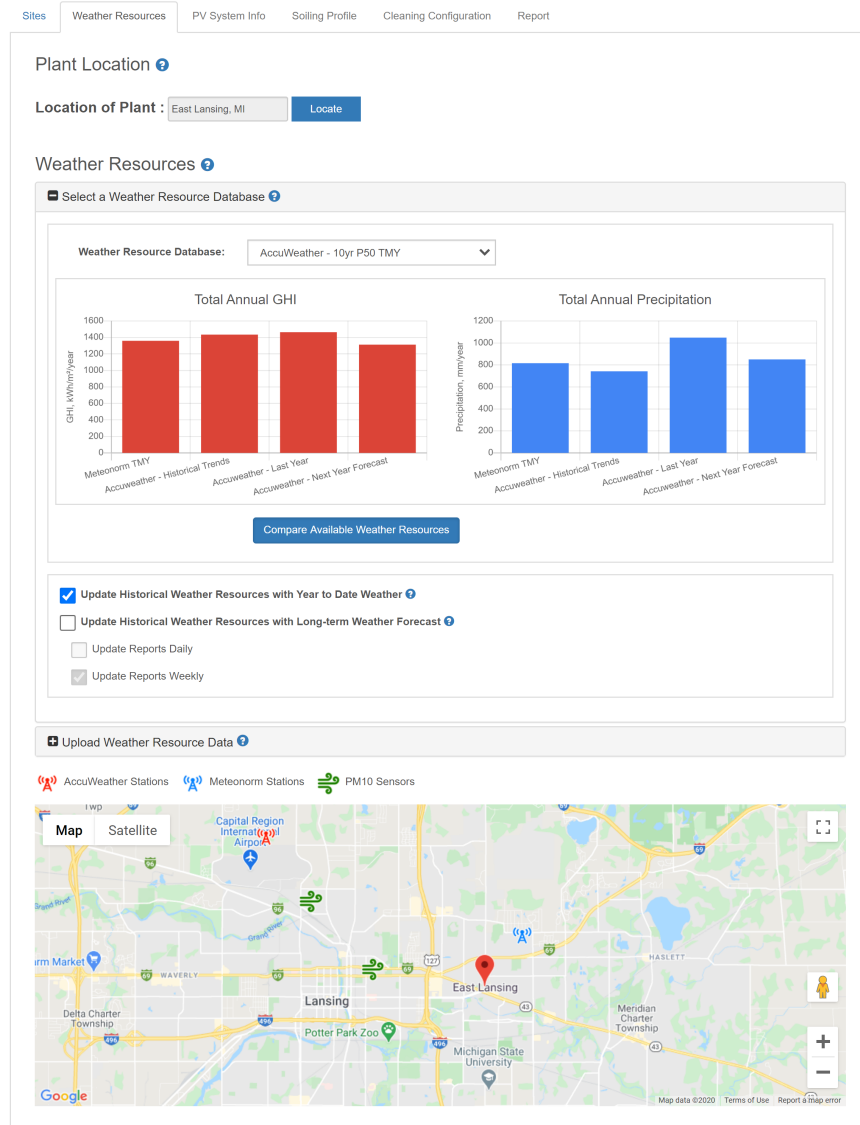


Figure A.1: Weather Resource UI.

Possible advantages of using the Meteonorm 30-year TMY datasets is that this approach is the solar industry-standard for energy prediction. Additionally, their interpolation of weather from multiple nearby stations could yield more representative weather datasets for locations that are not near any weather stations. A potential disadvantage is that due to rapid climate change in many global regions, a 30-year TMY is not necessarily representative of typical weather in the current years. For example, many locations may be seeing higher temperatures and drier or wetter conditions than 20-30 years ago. Therefore, weather resources based on Accuweather that rely on the past ten years of historical data, last year data, or next year forecasts could be preferable. Future versions of the software could allow rerunning the forecast for the same PV system with different historical weather data and calculate a statistical average soiling forecast and uncertainties based on weather variability.

## A.2 PV System Design

The design parameters of a PV system can greatly impact its energy production. This section provides an overview of the main design parameters considered in PV SoilSayer (Figure A.2).

The screenshot shows the 'PV System Design' interface with the following parameters:

- DC System Size: 2000 kWp
- AC System Size: 1700 kWp
- Module Type: Glass/Backsheet
- Cell Type: Mono c-Si
- Array Type: 1-Axis True Tracking
- Max Tracker Angle: 65 deg
- Tracker Stow Angle: 65 deg
- Elevation Angle: 0 deg
- Azimuth Angle: 180 deg
- Albedo: 0.2 (for all months: Jan, Feb, Mar, Apr, May, Jun, Jul, Aug, Sep, Oct, Nov, Dec)

Figure A.2: System Design UI.

### DC and AC System Size

The nominal energy production capability of a PV system is defined by its direct current (DC) and alternating current (AC) power rating (also known as *system size*). These are expressed in kilowatts

peak (kWp) at standard test conditions (STC), meaning the peak kW power production under cell temperature of 25°C, irradiance of 1000 W/m<sup>2</sup>, and AM1.5 solar spectrum. PV systems produce DC power that is then commonly inverted to AC for use in the electric grid. The AC system size describes the peak power that the inverter is capable of outputting. The ratio between DC and AC system size is called *DC-to-AC ratio* or *Inverter Load Ratio* and is often used to describe a PV system [180]. PV systems are generally sized with DC-to-AC ratios of 1.1 – 1.3, meaning that the inverter power output capability is lower than the maximum possible DC power production. This leads to what is known as *inverter clipping* or *clipping loss* where during times of peak production (e.g. sunny day at solar noon), the DC power feeding the inverter is greater than what the inverter can handle, so the extra DC power potential is clipped and lost. The inverter clips by raising the modules' operating voltage to move the array off of its maximum power point and therefore reduce the DC power. Such undersizing of inverters is done to improve project economics (less powerful inverters are less expensive) and to match the AC power output with the grid connection point design's maximum power (e.g. a home's AC panel has a power limit). The clipping losses due to DC-to-AC ratios that are > 1 are small since full STC conditions are rare. STC conditions describe noon on a clear summer day, but the cell temperature is assumed to be 25°C. Actual cell temperatures are commonly significantly higher, resulting in reduced efficiency (see Chapter 6).

### **Inverter Efficiency**

The conversion of DC to AC by the inverter has an associated loss due to imperfect inverter efficiency. PV SoilSayer implements the inverter model described in Version 5 of PVWatts, which is based on an analysis of inverter performance data from the California Energy Commission (CEC) [181]. The inverter performance curve is given in Figure A.1, which scales the efficiency curve to the nominal rated efficiency specified by the user ( $\eta_{nom}$ ). The default nominal efficiency is 0.96. The reference inverter efficiency ( $\eta_{ref} = P_{ac0}/P_{dc0}$ ) from the CEC data for a typical inverter is 0.9637, and the AC nameplate rating ( $P_{ac0}$ ) is determined from the DC rating of the system and

the DC-to-AC ratio.

$$\eta = \frac{\eta_{mon}}{\eta_{ref}} - 0.0162\zeta - \frac{0.0059}{\zeta} + -.9858 \quad (\text{A.1})$$

where

$$\zeta = \frac{P_{dc}}{P_{dc0}} \quad (\text{A.2})$$

and

$$P_{dc0} = \frac{P_{ac0}}{\eta_{nom}} \quad (\text{A.3})$$

When the predicted AC output exceeds the nameplate rating, the output is clipped to the nameplate value. Figure A.3 shows the inverter efficiency curve as a function of load fraction (ratio of power input to the inverter to the inverter's AC rating) for different nominal inverter efficiencies. Note the steep drop in inverter efficiency at very low load fractions, which may result in high inverter losses during low light conditions (e.g. sunrise/sunset).

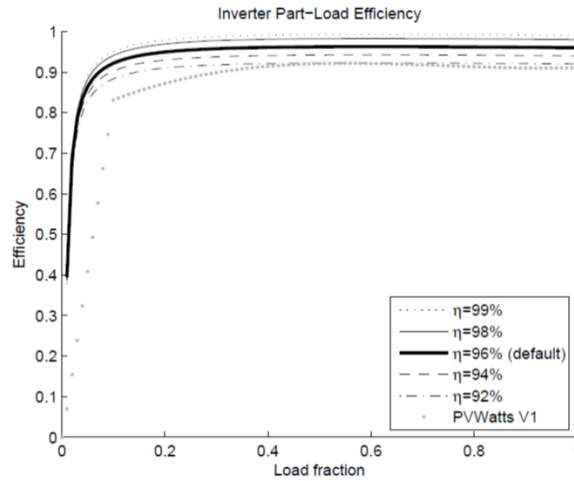


Figure A.3: Inverter partial-load efficiency curve. Adapted from [181].

## Module Type

PV modules come in two main constructions called *glass-glass* and *glass-backsheet*. Glass-Glass modules use glass on both the front and back sides of the module, while glass-backsheet modules use a polymer sheet on the backside. Most PV modules use the glass-backsheet construction, but

glass-glass modules can provide better reliability and durability. The module type impacts the coefficients used in the cell temperature prediction model, which in turn impact the cell efficiency.

Temperature-induced losses are considered without any additional input from the user. Currently, PV SoilSayer uses the Sandia Array Performance Model (SAPM) [182] to calculate cell temperature as implemented in PVLIB. The module temperature is given in terms of POA irradiance ( $E$ ), wind speed ( $WS$ ), ambient air temperature ( $T_a$ ), and two empirical coefficients ( $a$  and  $b$ ).

$$T_m = E \times \exp(a + b \times WS) + T_a \quad (\text{A.4})$$

The cell temperature is calculated from the module temperature by

$$T_C = T_m + \frac{E}{E_0} \Delta T \quad (\text{A.5})$$

with  $\Delta T$  being the empirically-estimated difference between the temperatures of the module's back surface and the cell.

Table A.1 shows the empirical parameters used in the SAPM model.

Table A.1: SAPM temperature model coefficients.

Module Type	a	b	$\Delta T$
Open-Rack Glass-Glass	-3.47	-0.0594	3
Open-Rack Glass-Backsheet	-3.56	-0.075	3
Rooftop Glass-Glass	-2.98	-0.0471	1
Rooftop Glass-Backsheet	-2.81	-0.0455	0

The computed cell temperature impacts the DC power model as described in the section below. Future development of PV SoilSayer could include allowing several temperature models with user-input empirical coefficients, or uploading cell temperatures that were either modeled in an external software or measured. (See Chapter 6 for a discussion of cell temperature modeling).



## DC Power Model

PV SoilSayer currently uses NREL's PVWatts DC power model as implemented in PVLIB [129]. The empirical model predicts a PV module's power output based on incident plane-of-array ( $G_{poa,eff}$ ) irradiance and cell temperature

$$P_{dc} = \frac{G_{poa,eff}}{1000} P_{dc0} (1 + \gamma_{pdc} (T_{cell} - T_{ref})) \quad (\text{A.6})$$

where  $P_{dc0}$  is the DC power output of the modules at STC (*DC System Size* input). PV SoilSayer currently assumes a temperature coefficient of  $\gamma_{pdc} = 0.004/^\circ\text{C}$ .

## Cell Type

The cell type describes the active material of the PV module. The most common cell types used commercially are monocrystalline and polycrystalline silicon, CIGS, and CdTe. The cell type impacts the spectral mismatch model coefficients that are used by PVLIB. The spectral mismatch modifier,  $M$ , is based on precipitable water,  $P_{wat}$ , and absolute (pressure corrected) airmass,  $A_m$  [129]. It describes the effect of variation in spectral irradiance on a module's short-circuit current. The following empirical equation is used

$$M = c_1 + c_2 A_m + c_3 P_{wat} + c_4 A_m^5 + c_5 P_{wat}^5 + c_6 A_m / P_{wat}^5 \quad (\text{A.7})$$

with coefficients given below.

Table A.2: Spectral mismatch modifier coefficients.

Cell Type	c1	c2	c3	c4	c5	c6
CdTe	0.86273	-0.038948	-0.012506	0.098871	0.084658	-0.0042948
Mono-Si	0.85914	-0.020880	-0.0058853	0.12029	0.026814	-0.0017810
Poly Si	0.85914	-0.020880	-0.0058853	0.12029	0.026814	-0.0017810
CIGS	0.85252	-0.022314	-0.0047216	0.13666	0.013342	-0.0008945

## Array Type and Orientation

PV arrays can be free-standing (also known as open-rack) or roof-mounted. Roof-mounted arrays are generally fixed in place. The choice between free-standing and roof-mounted arrays impacts the empirical cell temperature models since free-standing systems have convection on both sides, while roof-mounted systems have limited convection on the back, increasing cell temperatures. Free-standing arrays can be either fixed in place or rotate around one or two axes to track the sun. The rotating arrays are known as *single-axis trackers* and *two-axis trackers*. Figure A.4 shows the three types of free-standing arrays.

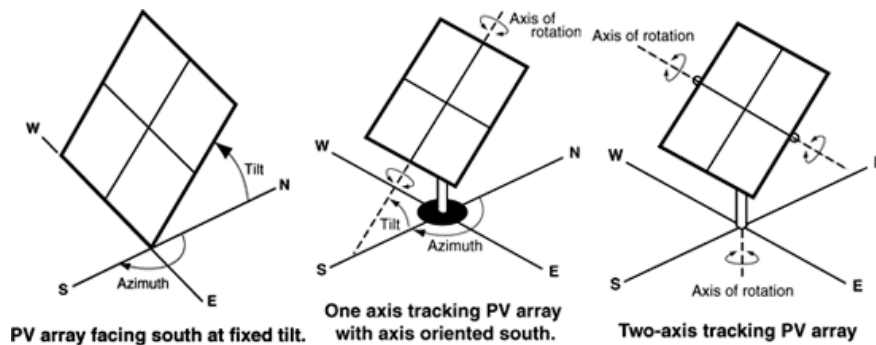


Figure A.4: Array types. Adapted from [183].

The array's orientation determines the amount of irradiance incident on the collector surface and is described by a tilt (also known as *elevation*) angle and azimuth angle, as labeled in Figure A.4. Fixed tilt free-standing array tilt angles are chosen to maximize the total incident irradiance. A common recommendation is to set the tilt angle equal to the absolute value of the system's latitude. Higher tilt angle arrays, while increasing energy production in higher latitudes and during winter months, can have a higher associated cost and may increase the risk of wind damage. Roof-mounted arrays typically have tilt angles equal to the roof pitch. For single-axis trackers, the tilt angle refers to the angle from the horizontal of the tracking axis. Tilt angle does not apply to two-axis trackers since they move to always maintain a normal incidence of the direct normal solar irradiation.

The azimuth angle is the angle clockwise from true north that describes the direction that the array (or axis of rotation for single-axis trackers) faces. Often the azimuth angle is around  $180^\circ$

(south-facing) for locations in the northern hemisphere and  $0^\circ$  (north-facing) for locations in the southern hemisphere. The actual optimal azimuth angle can be slightly different based on local weather patterns. For the northern hemisphere, increasing the azimuth angle favors afternoon energy production, and decreasing the azimuth angle favors morning energy production. The opposite is true for the southern hemisphere [183].

PVLIB allows modeling the motion of single-axis trackers as well as the effect of self-shading<sup>1</sup>. Self-shading is a reduction in the array's output caused by shading of neighboring rows of modules at certain times of day and year when the sun is low on the horizon. Single-axis trackers often use backtracking, which is a self-shading mitigation technique that rotates the array toward the horizontal during early morning and late evening hours. The user can turn on/off backtracking by selecting either a "True Tracking" or Backtracking" array type. The ground cover ratio (GCR) specifies the ratio of module area to land area. Figure A.5 shows the relationship between self-shading and GCR. In the figure,  $\beta$  is the tilt angle,  $z$  measures height along the array, and  $\psi(z)$  is the screening angle, which represents a two-dimensional field-of-view reduction at height  $z$  [184].

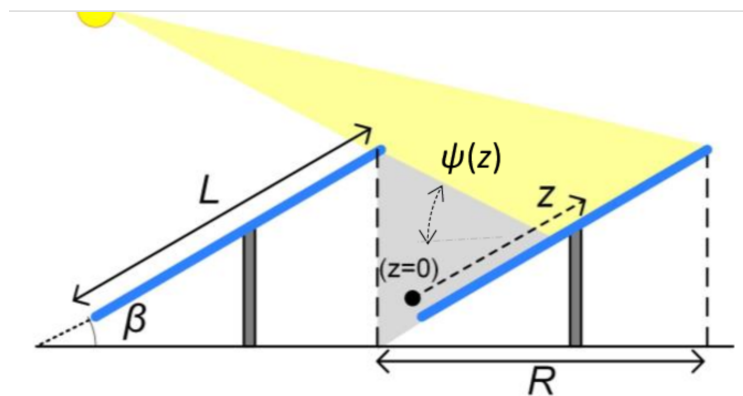


Figure A.5: Ground cover ratio. Adapted from [183].

For single-axis trackers, an additional optional input is the Tracker Stow Angle, describing the tilt angle of the SAT at night. This is needed only for the semi-physical soiling model, which

<sup>1</sup>For fixed-tilt and two-axis trackers, self-shading is not modeled, but its effects can be specified as a percent loss in the Shading input in the PV System Losses UI.

considers the effect of tilt angle on soiling accumulation. Higher stow angles result in lower soiling losses (see Chapter 5).

### Ground Reflection Albedo

The albedo coefficient determines the amount of solar irradiance reflected from the ground surrounding the PV installation, which can contribute to the total irradiance incident on the module. Note that PV SoilSayer currently uses albedo only for mono-facial panels. Common albedo values are presented in Table A.3.

Table A.3: Sample albedo values. From [129].

Surface Type	Albedo
Urban	0.18
Grass	0.20
Fresh Grass	0.26
Soil	0.17
Sand	0.40
Snow	0.65
Fresh Snow	0.75
Asphalt	0.12
Concrete	0.30
Aluminum	0.85
Copper	0.74
Fresh Steel	0.35
Dirty Steel	0.08
Sea	0.06

#### A.2.1 PV System Losses

PV systems have multiple sources of energy losses. Losses other than those due to temperature and soiling, which are computed separately, are accounted for by requesting user-input of annual (and monthly for shading and snow) loss percentage values (Figure A.6).

PV System Losses ?

Mismatch:	<input type="text" value="1"/>	%	Light-Induced Degradation:	<input type="text" value="1.5"/>	%
Wiring:	<input type="text" value="2"/>	%	Nameplate Rating:	<input type="text" value="1"/>	%
Connections:	<input type="text" value="0.5"/>	%	Age:	<input type="text" value="0"/>	%
			Availability:	<input type="text" value="1.5"/>	%

Shading %:	Jan :	Feb :	Mar :	Apr :	May :	Jun :	Jul :	Aug :	Sep :	Oct :	Nov :	Dec :
	<input type="text" value="0"/>	<input type="text" value="0"/>	<input type="text" value="0"/>	<input type="text" value="0"/>	<input type="text" value="0"/>	<input type="text" value="0"/>	<input type="text" value="0"/>	<input type="text" value="0"/>	<input type="text" value="0"/>	<input type="text" value="0"/>	<input type="text" value="0"/>	<input type="text" value="0"/>

Snow %:	Jan :	Feb :	Mar :	Apr :	May :	Jun :	Jul :	Aug :	Sep :	Oct :	Nov :	Dec :
	<input type="text" value="5"/>	<input type="text" value="5"/>	<input type="text" value="0"/>	<input type="text" value="0"/>	<input type="text" value="0"/>	<input type="text" value="0"/>	<input type="text" value="0"/>	<input type="text" value="0"/>	<input type="text" value="0"/>	<input type="text" value="0"/>	<input type="text" value="0"/>	<input type="text" value="3"/>

Inverter Efficiency:	<input type="text" value="96"/>	%	Ground Coverage Ratio:	<input type="text" value="0.4"/>
----------------------	---------------------------------	---	------------------------	----------------------------------

Figure A.6: PV System Losses UI.

The losses calculations follow the simple multiplicative approach of NREL’s free PVWatts software [181] with the exception that PVWatts does not support entering monthly resolution losses for snow and shading. For each month, the net losses percentage (except for temperature and soiling losses) is

$$L_{net} = 100 \left[ 1 - \prod_i \left( 1 - \frac{L_i}{100} \right) \right] \quad (A.8)$$

Since snow and shading losses are highly seasonal, using monthly values gives a more accurate estimate of the seasonal variability of panel losses. System losses that are considered by PV SoilSayer are described briefly below.

**Mismatch Loss** is electrical loss due to slight differences caused by manufacturing imperfections between modules in the array that cause the modules to have slightly different current-voltage characteristics.

**Wiring Loss** is the resistive loss in the DC and AC wires connecting modules, inverters, and other parts of the system.

**Connections Loss** describes the resistive losses in electrical connectors in the system.

**Light-Induced Degradation Loss** accounts for the reduction of power output of a PV module from the manufacturer rating because of light-induced degradation of the photovoltaic cells. A

new PV module's power output often decreases during the first few months of its operation. The module's power stabilizes after this initial period.

**Nameplate Rating Loss** accounts for any inaccuracies in the manufacturer's nameplate rating. Field measurements of the electrical characteristics of photovoltaic modules in the array may show that they differ from their nameplate rating. For example, a nameplate rating loss of 5% would indicate that testing yielded power measurements at Standard Test Conditions (STC) that were 5% less than the manufacturer's nameplate rating.

**Age Loss** accounts for the effect of weathering of the photovoltaic modules on the array's performance over time.

**Availability Loss** describes the reduction in the system's output caused by scheduled and unscheduled system shutdown for maintenance, grid outages, and other operational factors.

**Shading Loss** describes the reduction in the incident solar radiation from shadows caused by faraway features such as large buildings or mountains, objects near the array such as trees, or self-shading. The PVWatts default value of 3% only considers typical observed shading losses due to faraway features. This value should be increased to account for any shading from nearby features and self-shading. For accurate prediction of shading losses using an external shading software or conducting an on-site survey is recommended. Note that PV SoilSayer automatically considers self-shading losses for single-axis trackers; therefore, the self-shading contribution to the overall shading loss should only be included for fixed tilt and two-axis tracker arrays.

**Snow Loss** describes the reduction in the system's annual output due to snow covering the array. The default value is zero, assuming that there is never any snow accumulating on the array or that the array is kept clear of snow.

For reference, Table [A.4](#) shows the default values of annual losses used in PVWatts.

Table A.4: Default annual losses in PVWatts for reference.

Loss Mechanism	Default Value
Mismatch	2%
Wiring	2%
Connections	0.5 %
Light-induced degradation	1.5%
Nameplate rating	1%
Age	0%
Availability	3%
Shading	3%
Snow	0%

### A.2.2 Annual Energy Calculation

The first calculations occur when *Calculate Annual Energy* is clicked at the bottom of the PV System Info tab. Here, the PV System Design and System Losses parameters are used with PVLIB models to estimate the DC and AC energy production for a year for a panel with no soiling losses (perfectly clean). The energy production is calculated with an hourly resolution, and a monthly resolution chart is displayed to allow the user to verify that the production estimates are reasonable before proceeding with the soiling calculations (Figure A.7).

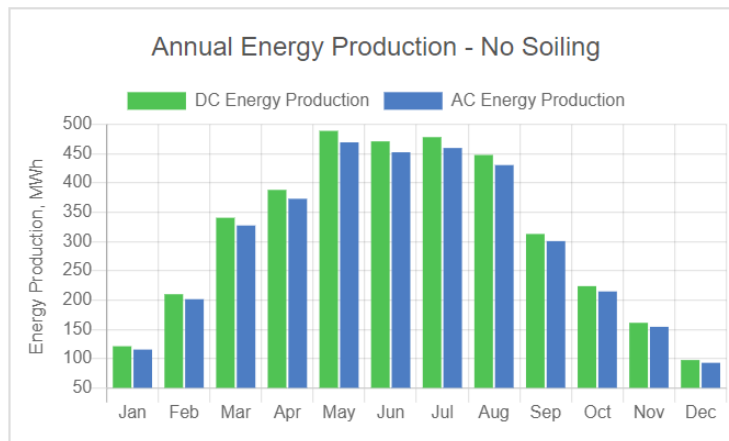


Figure A.7: Monthly energy production chart example.

## A.3 Soiling Profile

### A.3.1 Soiling Loss Calculation/Upload Options

Users have several options for calculating or uploading soiling loss data to be used for soiling loss prediction and clean cycle calculations (Figure A.8). For calculated options, users can specify the month at which to start the year-long forecast and the starting DC soiling ratio (the DC power loss due to soiling).

The screenshot shows a web interface for configuring soiling loss calculations. At the top, there are navigation tabs: Sites, Weather Resources, PV System Info, Soiling Profile (selected), Cleaning Configuration, and Report. The main heading is "Soiling Losses" with a help icon. Below it, a prompt says "Please Select From One of the Following Soiling Loss Calculation Options:". There are three radio button options: "Use the Soiling Loss Calculator to Estimate Soiling Losses Throughout the Year", "Use DC Soiling Losses Measured Over a Dry Period to Estimate Soiling Losses Throughout the Year", and "Use Average Daily Soiling Rates to Calculate Soiling Losses". Below these options are two input fields: "Clean Cycle Start Date" with a date picker set to "01/2020" and "Starting DC Soiling Ratio" with a numeric input set to "0" and a percentage sign. An "OR" separator follows, with a prompt "Please Select From One of the Following Soiling Loss Upload Options:". There are two radio button options: "Upload Measured Hourly Soiling Losses" and "Upload Daily Soiling Losses measured at Solar Noon".

Figure A.8: Soiling loss calculation/upload options.

### Soiling Loss Calculator

The soiling loss calculator utilizes the semi-physical soiling model described in Chapter 5 to estimate soiling losses. The user has an additional option to empirically increase the monthly soiling rate in any month due to any localized soiling that they may observe from sources such as local farming practices, mowing, sheep grazing, and roadways. The localized soiling increases are arbitrary with moderate, heavy, very heavy, and extreme soiling corresponding to 50%, 100%, 150%, and 200% increases in the soiling rate. This feature was added at the request of prospective users who were managing PV plants with abnormally high local soiling that is not representative



of the region’s average air quality, but at the same time did not have daily soiling data available to use the upload option.

	Jan	Feb	Mar	Apr	May	Jun	Jul	Aug	Sep	Oct	Nov	Dec	All
Moderate Soiling:	<input type="checkbox"/>	<input type="checkbox"/>	<input type="checkbox"/>	<input type="checkbox"/>	<input checked="" type="checkbox"/>	<input type="checkbox"/>	<input type="checkbox"/>	<input type="checkbox"/>	<input type="checkbox"/>	<input type="checkbox"/>	<input type="checkbox"/>	<input type="checkbox"/>	<input type="checkbox"/>
Heavy Soiling:	<input type="checkbox"/>	<input type="checkbox"/>	<input type="checkbox"/>	<input type="checkbox"/>	<input type="checkbox"/>	<input checked="" type="checkbox"/>	<input checked="" type="checkbox"/>	<input checked="" type="checkbox"/>	<input type="checkbox"/>	<input type="checkbox"/>	<input type="checkbox"/>	<input type="checkbox"/>	<input type="checkbox"/>
Very Heavy Soiling:	<input type="checkbox"/>	<input type="checkbox"/>	<input type="checkbox"/>	<input type="checkbox"/>	<input type="checkbox"/>	<input type="checkbox"/>	<input type="checkbox"/>	<input type="checkbox"/>	<input type="checkbox"/>	<input type="checkbox"/>	<input type="checkbox"/>	<input type="checkbox"/>	<input type="checkbox"/>
Extreme Soiling:	<input type="checkbox"/>	<input type="checkbox"/>	<input type="checkbox"/>	<input type="checkbox"/>	<input type="checkbox"/>	<input type="checkbox"/>	<input type="checkbox"/>	<input type="checkbox"/>	<input type="checkbox"/>	<input type="checkbox"/>	<input type="checkbox"/>	<input type="checkbox"/>	<input type="checkbox"/>

Figure A.9: Soiling Loss Calculator UI.

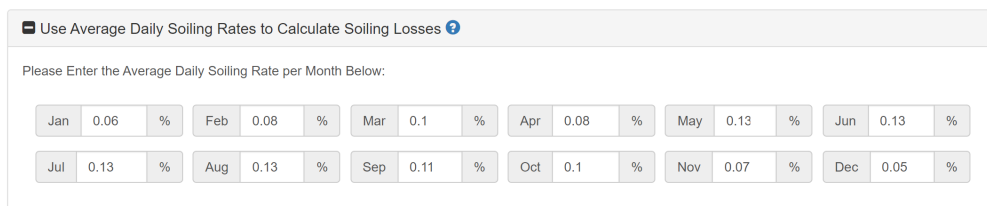
### DC Soiling Losses Over a Dry Period

DC soiling losses measured over a dry period can be used to calculate the hourly losses throughout the year. Measurements over a dry period are correlated with weather resources and interpolated to the hourly resolution to determine hourly soiling losses. The user should input the length (in days) of the dry period and the change in soiling loss over its duration. For example, if one measures that the first day of a dry period has 5% soiling at solar noon and the 30<sup>th</sup> day of the dry period has 10% soiling loss at solar noon, then the Dry Measurement Duration is 30 days, and the Total Change in DC Soiling Loss is 5%.

Figure A.10: DC Loss Over a Dry Period UI.

## Average Daily Soiling Rates

This option is most aligned with the way soiling is treated in other industry-standard software since it treats soiling analogously to the Kimber et al. model with the exceptions that we do not include a Grace Period and allow for different daily soiling rates in each month instead of one annual value (see Section 5.1). Daily average soiling rates for each month should be calculated using data from the longest dry period during each month as the change in soiling loss over the Dry Period divided by the length of the Dry Period in days.



Month	Rate	Unit
Jan	0.06	%
Feb	0.08	%
Mar	0.1	%
Apr	0.08	%
May	0.13	%
Jun	0.13	%
Jul	0.13	%
Aug	0.13	%
Sep	0.11	%
Oct	0.1	%
Nov	0.07	%
Dec	0.05	%

Figure A.11: Daily Soiling Rates UI.

## Upload Measured DC Hourly Soiling Losses

In this option, the forecast uses hourly measured soiling losses throughout the year. The measured soiling losses must exclude any manual cleaning events. The rainfall cleaning calculations (see A.3.3) are not run when this option is used since all cleaning effects of rainfall are assumed to be included in the measured soiling losses.

## Upload Daily Soiling Losses Measured at Solar Noon

In this option, annual hourly soiling losses are estimated from daily soiling losses measured at solar noon. The measured soiling losses must exclude any manual cleaning events. The rainfall cleaning calculations (see A.3.3) are not run when this option is used since all cleaning effects of rainfall are assumed to be included in the measured soiling losses. The algorithm treats the input as a measurement at the hour closest to solar noon (where solar noon is not necessarily at 12 pm but is the time at which the sun is at the highest position in the sky).

If *Calculate Soiling Losses due to Sun Angle* is selected (see Angular Loss below), then the angle of incidence effect on soiling losses will be taken into account as described in Chapter 5.

### Possible Machine Learning Feature

Future releases may offer an optional feature where machine learning models are trained on user-uploaded measured soiling loss and weather data, and applied to predict soiling loss based on TMY or next-year forecast weather data. A proof-of-concept of this approach is presented in Section 5.8.

### A.3.2 Angular Loss

PV SoilSayer utilizes semi-physical models to calculate hourly soiling losses as a function of sun angle and direct and diffuse irradiance throughout the day. Users have the option to turn on/off angle of incidence effects.



Figure A.12: Angular Losses UI.

### A.3.3 Rainfall Cleaning Calculations

PV SoilSayer derates the soiling losses according to rainfall (unless measured soiling losses are uploaded, in which case the effects of rainfall are assumed to be already included in the measurements). Default values are standard based-on available research; however, these values may vary from site to site. Users can configure Rainfall parameters to estimate the cleaning effects of rainfall for a given site's design and location.

The **Minimum Rainfall Clean Amount** and **Maximum Rainfall Clean Amount** specify the amount of rain that is required to clean the panels during the wet season and dry season, respectively. During periods with regular rain, the panels may be easier to clean than after a dry period where

dust and debris have baked onto the panels. Any rainfall below the specified Rainfall Clean Amount is proportioned as a ratio of the Rainfall Clean Amount.

**Minimum Duration of the Dry Period to Set Max Rainfall Clean Amount** is the amount of time between rainfall events required before the Maximum Rainfall Clean Amount is used to calculate a Rainfall Clean Event. The Minimum Rainfall Clean Amount is used until this minimum duration without rainfall events occurs. Essentially, this defines what is considered as a "wet" and "dry" period.

The **Minimum Rainfall Resulting in Performance Recovery** is the amount of rain within 1 hour that will result in a decreased Soiling Ratio (i.e. will result in higher performance of the PV panels). Different values of this quantity can be specified for the dry and wet periods. In some cases, especially with panels at very low tilt angles under approximately  $10^\circ$ , small rainfall amounts will not clean the panels (and may even have a reverse effect, resulting in an increased Soiling Ratio). Panels installed at higher tilt angles and during the wet season may need minimal rainfall to see a decrease in the Soiling Ratio.

It is often the case that while rainfall mostly cleans the panels, some residue remains. The **Rainfall Clean Quality** specifies how clean the panels will be after receiving rainfall equal to the Rainfall Clean Amount. For example, a 1% Rainfall Clean Quality says that an average daily loss of 1% remains directly after each Rainfall Clean Event (i.e. after the Rainfall Clean Amount threshold has been exceeded).

**Minimum Duration of the Soiling Ratio to Set Rainfall Clean Quality** is the amount of time required to maintain a soiling ratio greater than the Rainfall Clean Quality, in order to set the Rainfall Clean Quality. If the Starting Soiling Ratio is less than the Rainfall Clean Quality, the Rainfall Clean Quality will not be applied until the Soiling Ratio defined by the Rainfall Clean Quality is exceeded for the specified number of days. In many cases, the soiling will adhere to the surface of the glass over time, which results in higher rainfall needed to detach the soiling from the panels. This depends on several factors, including the type of glass, the type of soiling, and the weather conditions.

### Rainfall Clean Events [?](#)

Minimum Rainfall Clean Amount (Wet Season):  mm/hr

---

**Advanced**

Minimum Rainfall Resulting in Performance Recovery:  mm/hr

---

Rainfall Clean Quality:  %

---

**Advanced**

Minimum Duration of Soiling Ratio to Set Rainfall Clean Quality:  days

---

Maximum Rainfall Clean Amount (Dry Season):  mm/hr

---

**Advanced**

Minimum Rainfall Resulting in Performance Recovery:  mm/hr

Minimum Duration of Dry Period to Set Max Rainfall Clean Amount:  days

Figure A.13: Rainfall Parameters UI.

### A.3.4 Monthly Average Soiling Losses

After setting the Soiling Profile parameters, clicking *Calculate Soiling Losses* will run a soiling loss calculation and display a preview of the monthly results for a panel that is never manually cleaned. Hovering the mouse over the plot data will display the numerical values for total precipitation and DC and AC soiling loss. Here users can optionally adjust the monthly soiling values to better match any known local conditions.

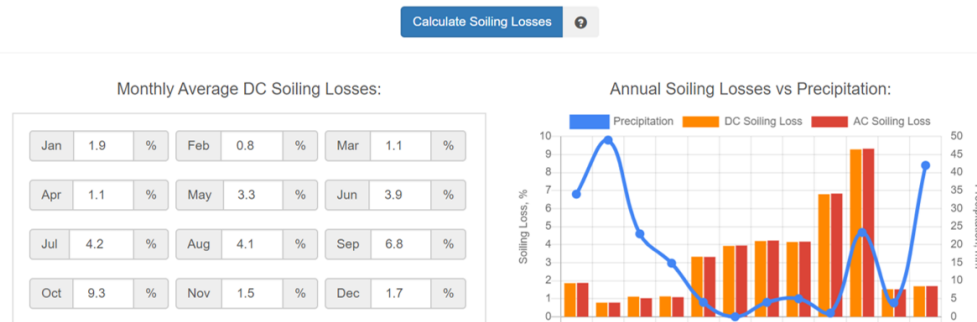


Figure A.14: Sample Monthly Average Soiling Losses Output.

## A.4 Clean Cycle Configuration

The Clean Cycle Configuration (Figure A.15) allows the user to specify which cleaning cycle should be calculated and the parameters defining that cleaning cycle. One can calculate an optimal clean cycle that minimizes cost and maximizes performance, a cleaning cycle that records a cleaning event when specific thresholds (average daily soiling loss, max financial loss, or soiling loss at solar noon) are reached, or manually enter the cleaning dates. This page also contains the user inputs for the Manual Clean Quality (for modeling non-perfect manual cleans) and the number of days needed for cleaning.

Sites Weather Resources PV System Info Soiling Profile **Cleaning Configuration** Report

### Clean Cycle Configurations ?

Please select from one of the following clean cycle configuration options:

- Calculate Optimal Clean Cycle ?
- Calculate Clean Cycle Based-on Specified Thresholds ?
- Calculate Soiling Losses Based-on a Specified Clean Cycle ?

Manual Clean Quality:  %      Number of Days Required to Clean:  days

### Value of Energy ?

- Use Average Annual Price of Energy ?
- Use Average Monthly Price of Energy ?

### Cost of Cleaning ?

- Input the Total Cost of Cleaning per PV System or Power Block ?
- Cost of Cleaning Based-on System Size ?

Proceed

Figure A.15: Clean Cycle Configuration UI.

### A.4.1 Optimal Clean Cycle

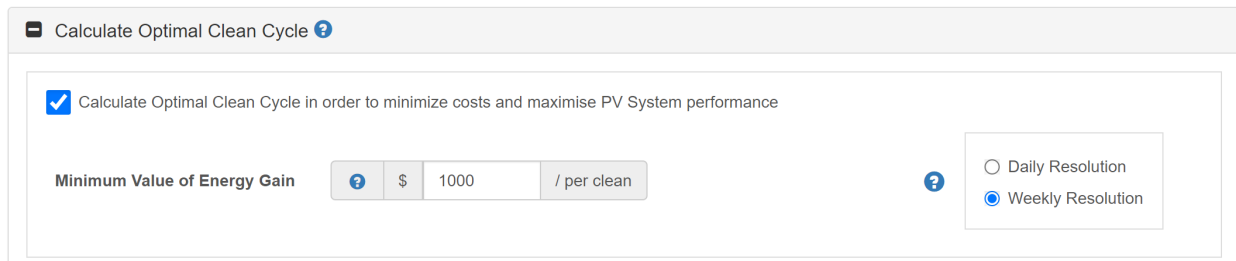
This option calculates the optimal time to clean based on the energy gain from cleaning versus not cleaning the PV panels. The calculation of the optimal clean cycle considers three different scenarios at each hour of the year:

**No Soil:** This scenario calculates the energy production assuming that the panels are always clean.

**No Clean:** This scenario calculates the energy production assuming that the panels are never cleaned manually.

**Clean:** This scenario calculates the optimal days to clean the panels throughout the year in order to maximize revenues.

The result of this calculation is an optimal clean cycle that is expected to yield the maximum return-on-investment (i.e. revenue gain considering the cost of cleaning) over not cleaning the system.



The screenshot shows a web application interface for calculating the optimal clean cycle. At the top, there is a title bar that says "Calculate Optimal Clean Cycle" with a help icon. Below the title bar, there is a checkbox that is checked, labeled "Calculate Optimal Clean Cycle in order to minimize costs and maximise PV System performance". Underneath the checkbox, there is a text input field for "Minimum Value of Energy Gain" with a value of "1000" and a unit of "\$ / per clean". To the right of the input field, there is a radio button selection for "Daily Resolution" and "Weekly Resolution", with "Weekly Resolution" being the selected option.

Figure A.16: Optimal Clean Cycle UI.

The Minimum Value of Energy Gain is calculated as the net revenue gain after subtracting the cost of cleaning the PV plant. The Minimum Value of Energy Gain filters the results to ensure that only the Manual Clean Events above a specified net revenue gain threshold are used. Setting the value too high may result in no cleans. The default value is calculated at 100% of the cleaning cost.

Users have the option to run the Optimal Clean Cycle calculation with a weekly or daily resolution. While both resolutions calculate soiling losses on an hourly resolution, this option selects the precision to which the Manual Clean Events are optimized. The weekly resolution tries to find the optimal weeks to clean the panels, while the daily resolution tries to find the optimal

days.

Calculations at the weekly resolution (default) select the optimal cleaning day with a possible error in the cleaning optimization (independent of soiling and weather prediction errors) of  $\pm 4$  days. This calculation is typically returned within 1-3 minutes and provides users with reasonable estimates of clean cycles and associated costs. Since it may be impractical to schedule cleaning services on a precise day, and since large PV plants take multiple days to clean, the weekly resolution is expected to be sufficient for most applications. Additionally, the errors in soiling and weather prediction may affect the optimal clean events by greater than  $\pm 4$  days, and therefore the weekly optimization provides a good balance between accuracy and computational effort. Calculations at the daily resolution will attempt to find the exact days for manual cleanings. These may result in slightly different calculated Manual Clean Events and resulting revenue. These calculations often require significant additional processing times (e.g. 10-60 minutes); however, automated emails can be configured to be sent upon calculation completion.



#### A.4.2 Clean Based on Specific Thresholds

In these cleaning cycles, Manual Clean Events are triggered by simple thresholds. This option allows users to model common techniques used in the industry for cleaning scheduling and compare the predicted results to results from PV SoilSayer's optimal clean cycle. Users can choose one of several options for triggering manual cleans in order to calculate the resulting clean cycle and associated revenue gains/losses.

The screenshot shows a web interface titled "Calculate Clean Cycle Based-on Specified Thresholds". Below the title, it says "Please choose one of the following thresholds:". There are three main sections, each with a plus icon and a question mark:

- Clean based on an Average Daily Soiling Loss %**: This section is expanded. It contains two radio buttons. The first is selected and labeled "Clean when the Average Daily AC Soiling Loss >". To its right is a text input field containing the number "5" and a percentage sign "%". The second radio button is labeled "Clean when the Average Daily DC Soiling Loss >" and is not selected.
- Clean based on a Max Financial Loss**: This section is collapsed.
- Clean based on the Soiling Loss at Solar Noon**: This section is collapsed.

Figure A.17: Clean Based on Specific Thresholds UI.

**Clean Based on Average Daily Soiling Loss:** A Manual Clean Event is triggered when the average daily soiling loss reaches the specified amount. A soiling loss threshold in terms of AC or DC energy production can be specified.

**Clean Based on Max Financial Loss:** A Manual Clean Event is triggered when the accumulated loss of revenue due to soiling reaches the specified amount.

**Clean Based on the AC Soiling Loss at Solar Noon:** A Manual Clean Event is triggered when the AC soiling loss at solar noon reaches the specified amount.

#### A.4.3 Clean Based on Specified Clean Cycle

In this option, users select the dates or cleaning frequency to clean the system and the resulting energy loss and revenue loss due to the specified Clean Cycle are reported.

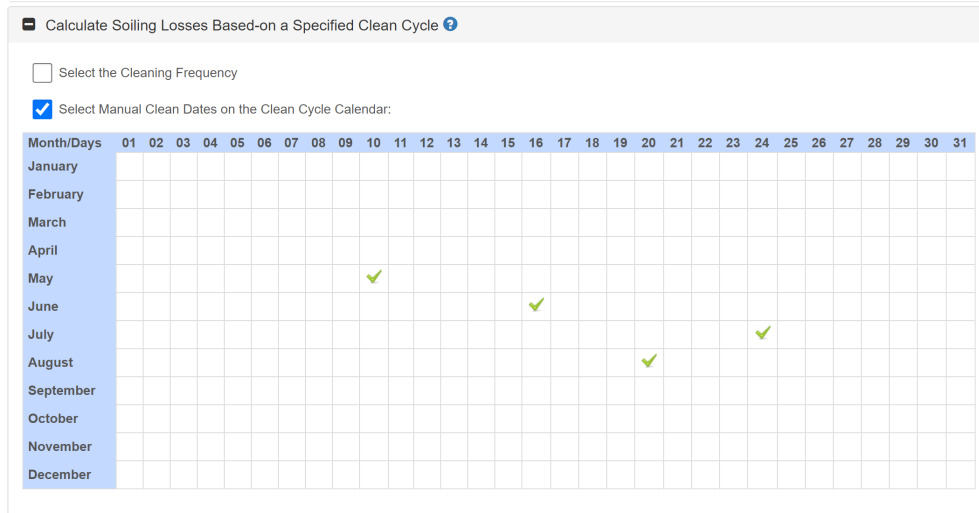


Figure A.18: Clean Based on Specified Cycle UI.

#### A.4.4 Manual Clean Quality and Days Required to Clean

Often cleaning the panels does not remove 100% of the soiling. The **Manual Clean Quality** allows specifying the quality of each manual cleaning in terms of the soiling loss (measured at solar noon) remaining after the cleaning. The **Number of Days Required to Clean** allows to account for extended cleaning procedures that take several days or weeks at larger PV systems. This assumes that the cleaning process is evenly distributed among the days required to clean and accounts for the combination of higher soiling losses experienced by portions of the system that have not been cleaned with the lower soiling losses of portions of the system that have been cleaned.

#### A.4.5 Value of Energy and Cost of Cleaning

Finally, the financial parameters need to be specified. These are the value of energy that is produced (\$/kWh), either as an annual constant rate or as monthly variable rates, and the cost of cleaning, which can be input as a total dollar amount per clean or dollar amount per kilowatt-peak system size rating.

## APPENDIX B

### PV MODULE DATASHEETS

## DOUBLE GLASS



**PERLIGHT**  
Powering Possibilities

### PLM-260M-60DG SERIES

Monocrystalline Silicon Solar Module



### PERLIGHT SOLAR

Founded in 2006, Perlight is a Global Solar Energy provider with a presence in more than 80 countries around the world. More than 1.5GW of Perlight modules have been used in residential, commercial and off-grid systems around the world.

Perlight's success has been built on proven product performance and reliability, state of the art technology and long term partnerships with key customers.

<b>18.0% -20.8%</b> CELL EFFICIENCY	 <b>Improved durability</b> <ul style="list-style-type: none"><li>• PID resistant and free of snail trails</li><li>• Increased module robustness to minimize micro-cracks</li></ul>
<b>12 YEARS</b> PRODUCT WARRANTY	 <b>Enhanced safety</b> <ul style="list-style-type: none"><li>• Fire class A certified by TUV according to fire test IEC 61730-2</li><li>• Certified for fire type 13 (UL 1703)</li></ul>
<b>0 -3%</b> POWER TOLERANCE	 <b>Increased value</b> <ul style="list-style-type: none"><li>• Higher maximum system voltage reduces BOS costs</li><li>• 30 year linear warranty</li><li>• Higher light transmission creates more value for carport and greenhouse applications</li></ul>
<b>POWER WARRANTY</b> <ul style="list-style-type: none"><li> 80% Power Output Warranty</li><li> 90% Power Output Warranty</li><li> Material &amp; Workmanship Warranty</li></ul>	 <b>Certified to withstand the most challenging environmental conditions</b> <ul style="list-style-type: none"><li>• Module coating resistant to sand, acid, and alkali</li><li>• 2400 Pa wind load*      • 5400 Pa snow load*</li><li>• 35mm hail stones at 97km/h</li></ul>

## Mono DOUBLE GLASS, 60-CELL SERIES

### ELECTRICAL PERFORMANCE

Module type	PLM-260M-60DG									
Power output	$P_{max}$	W	260	265	270	275	280	285	290	
Power output tolerances	$\Delta P_{max}$	%	0 - 3							
Voltage at Pmax	$V_{mpp}$	V	31.25	31.55	31.81	32.06	32.30	32.43	32.59	
Current at Pmax	$I_{mpp}$	A	8.32	8.40	8.49	8.58	8.67	8.79	8.90	
Open-circuit voltage	$V_{oc}$	V	38.20	38.31	38.42	38.52	38.65	38.80	38.99	
Short-circuit current	$I_{sc}$	A	8.92	8.99	9.08	9.16	9.24	9.32	9.40	
Solar Module Efficiency	Eff.	%	15.81	16.11	16.40	16.72	17.02	17.33	17.63	

STC: 1000W/m<sup>2</sup> irradiance, 25°C cell temperature, AM 1.5g spectrum according to EN 60904-3.

### ELECTRICAL DATA (NOCT)

Maximum Power- $P_{MAX}$ (Wp)	192.50	196.10	199.80	203.30	206.70	210.00	213.40
Maximum Power Voltage- $V_{MPP}$ (V)	28.50	28.00	28.90	29.00	29.20	29.40	29.60
Maximum Power Current- $I_{MPP}$ (A)	6.76	6.84	6.93	7.00	7.07	7.13	7.20
Open Circuit Voltage- $V_{oc}$ (V)	35.20	35.30	35.40	35.50	35.60	35.70	35.90
Short Circuit Current- $I_{sc}$ (A)	7.22	7.28	7.35	7.41	7.48	7.54	7.61

### MECHANICAL DATA

Solar cells	Multicrystalline 156× 156mm (6 inches)
Cell orientation	60 cells (6× 10)
Module dimensions	1658× 992× 6mm (1658× 992× 25mm with junction box)
weight	23kg
front Glass	2.5mm, High Transmission, AR Coated and Heat Strengthened Glass
EVA	Clear / White
Back Glass	Heat Strengthened Glass, 2.5mm
Frame	Frameless
J-Box	IP 65 or IP rated
Cables	Photovoltaic Technology cable 4.0mm <sup>2</sup> (0.006 inches <sup>2</sup> ), Portrait: 250/130mm, Landscape: 1150/1150mm.
Connector	UTX Amphenol
Fire Type	Type 13

### TEMPERATURE RATINGS

Nominal Operating Cell Temperature (NOCT)	44°C (±2°C)
Temperature Coefficient of $P_{MAX}$	- 0.41%/°C
Temperature Coefficient of $V_{oc}$	- 0.32%/°C
Temperature Coefficient of $I_{sc}$	- 0.05%/°C

### PACKAGING CONFIGURATION

Modules per box: 30 pieces  
Modules per 40' container: 780 pieces



**PERLIGHT**  
Powering Possibilities

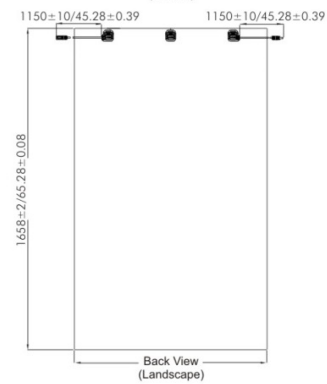
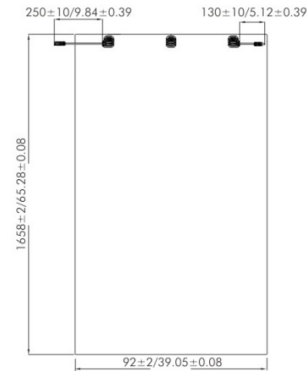
Perlight Partners

### QUALIFICATIONS & CERTIFICATIONS

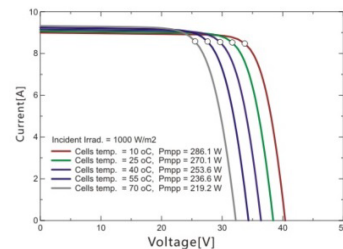
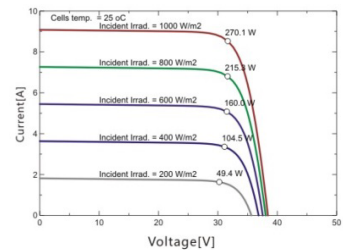
IEC 61215, IEC 61730, CE, IEC 62804 (PID Free), UL 1703, J-PEC, PV CYCLE, IEC/EN 61701, IEC 62716



### Dimensions of Module (unit: mm)



### Electrical Curves:





# First Solar Series 4™ PV Module

ADVANCED THIN FILM SOLAR TECHNOLOGY



**122.5 WATT MODULE  
EFFICIENCY OF 17.0%**

## INDUSTRY BENCHMARK SOLAR MODULES

As a global leader in PV energy, First Solar's advanced thin film solar modules have set the industry benchmark with over 17 gigawatts (GW) installed worldwide and a proven performance advantage over conventional crystalline silicon solar modules. Generating more energy than competing modules with the same power rating, First Solar's Series 4™ and Series 4A™ PV Modules deliver superior performance and reliability to our customers.



### PROVEN ENERGY YIELD ADVANTAGE

- Generates more energy than conventional crystalline silicon solar modules with the same power due to superior temperature coefficient and superior spectral response
- Anti-reflective coated glass (Series 4A™) enhances energy production



### ADVANCED PERFORMANCE & RELIABILITY

- Compatible with advanced 1500V plant architectures
- Independently certified for reliable performance in high temperature, high humidity, extreme desert and coastal environments
- Visit [PlantPredict.com](http://PlantPredict.com) - The only Energy Prediction Software designed for Utility Scale PV



### CERTIFICATIONS & TESTS

- PID-Free, Thresher Test, Long-Term Sequential Test, and ATLAS 25+<sup>1</sup>
- IEC 61215/61646 1500V, IEC 61730 1500V, CE
- IEC 61701 Salt Mist Corrosion, IEC 60068-2-68 Dust and Sand Resistance
- ISO 9001:2015 and ISO 14001:2015
- UL 1703 Listed Fire Performance PV Module Type 10<sup>2</sup>
- CSI Eligible, FSEC, MCS, CEC Listed (Australia), SII, InMetro

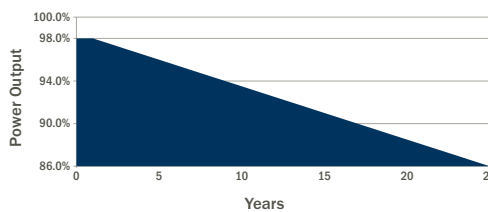


### END-OF-LIFE RECYCLING

- Recycling services available through First Solar's industry-leading recycling program or customer-selected third party.



### MODULE WARRANTY<sup>3</sup>



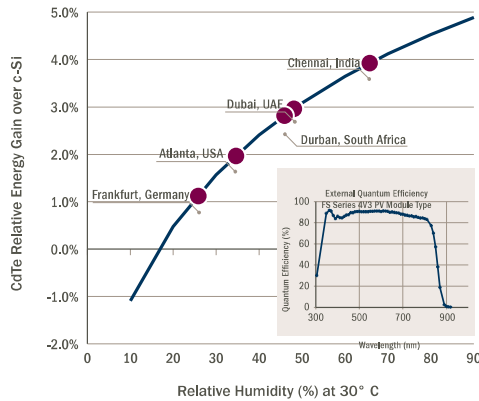
- 25-Year Linear Performance Warranty<sup>4</sup>
- 10-Year Limited Product Warranty

# FIRST SOLAR SERIES 4™ PV MODULE

MECHANICAL DESCRIPTION	
Length	1200mm
Width	600mm
Weight	12kg
Thickness	6.8mm
Area	0.72m <sup>2</sup>
Individual Leadwire	2.5mm <sup>2</sup> , 657mm (minimum from strain relief to connector mating surface)
Connectors	MC4 or MC4-EVO 2 <sup>9</sup>
Bypass Diode	None
Cell Type	Thin-film CdTe semiconductor, up to 216 cells
Frame Material	None
Front Glass	3.2mm heat strengthened
Back Glass	3.2mm tempered
Encapsulation	Laminate material with edge seal
Load Rating	2400Pa <sup>10</sup>

MODULE NUMBERS AND RATINGS AT STANDARD TEST CONDITIONS (1000W/m <sup>2</sup> , AM 1.5, 25°C) <sup>5</sup>							
NOMINAL VALUES		FS-4110-3 FS-4110A-3	FS-4112-3 FS-4112A-3	FS-4115-3 FS-4115A-3	FS-4117-3 FS-4117A-3	FS-4120-3 FS-4120A-3	FS-4122-3 FS-4122A-3
Nominal Power <sup>6</sup> (-0/+5W)	P <sub>MPP</sub> (W)	110.0	112.5	115.0	117.5	120.0	122.5
Voltage at P <sub>MAX</sub>	V <sub>MPP</sub> (V)	67.8	68.5	69.3	70.1	70.8	71.5
Current at P <sub>MAX</sub>	I <sub>MPP</sub> (A)	1.62	1.64	1.66	1.68	1.70	1.71
Open Circuit Voltage	V <sub>OC</sub> (V)	86.4	87.0	87.6	88.1	88.7	88.7
Short Circuit Current	I <sub>SC</sub> (A)	1.82	1.83	1.83	1.83	1.84	1.85
Module Efficiency	%	15.3	15.6	16.0	16.3	16.7	17.0
Maximum System Voltage	V <sub>SYS</sub> (V)	1500 <sup>7,8</sup>					
Limiting Reverse Current	I <sub>R</sub> (A)	4.0					
Maximum Series Fuse	I <sub>CF</sub> (A)	4.0					
RATINGS AT NOMINAL OPERATING CELL TEMPERATURE OF 45°C (800W/m <sup>2</sup> , 20°C air temperature, AM 1.5, 1m/s wind speed) <sup>9</sup>							
Nominal Power	P <sub>MPP</sub> (W)	83.2	85.1	87.0	89.0	90.8	92.7
Voltage at P <sub>MAX</sub>	V <sub>MPP</sub> (V)	63.5	64.5	64.9	65.9	66.3	67.2
Current at P <sub>MAX</sub>	I <sub>MPP</sub> (A)	1.31	1.32	1.34	1.35	1.37	1.38
Open Circuit Voltage	V <sub>OC</sub> (V)	81.6	82.1	82.7	83.2	83.7	83.7
Short Circuit Current	I <sub>SC</sub> (A)	1.47	1.47	1.48	1.48	1.48	1.49
TEMPERATURE CHARACTERISTICS							
Module Operating Temperature Range	(°C)	-40 to +85					
Temperature Coefficient of P <sub>MPP</sub>	γ <sub>K</sub> (P <sub>MPP</sub> )	-0.28%/°C (Temperature Range: 25°C to 75°C)					
Temperature Coefficient of V <sub>OC</sub>	γ <sub>K</sub> (V <sub>OC</sub> )	-0.28%/°C					
Temperature Coefficient of I <sub>SC</sub>	γ <sub>K</sub> (I <sub>SC</sub> )	+0.04%/°C					

## SUPERIOR SPECTRAL RESPONSE



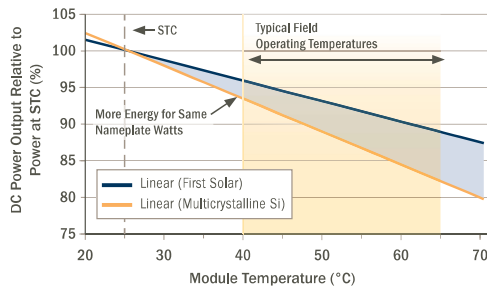
- Device package meets Atlas 25+
- Class A Spread of Flame / Class B Burning Brand. Roof mounted fire rating is established by assessing rack and solar module as a unit
- Limited power output and product warranties subject to warranty terms and conditions
- Ensures 98% rated power in first year, -0.5%/year through year 25
- All ratings ± 10%, unless specified otherwise. Specifications are subject to change
- Measurement uncertainty applies
- UL 1703 1500V Listed / ULC 1703 1000V Listed
- Application Class A for 1000V (class II), Application Class B for 1500V (class 0) with MC4; Application Class A for 1000V and 1500V (class II) with MC4-EVO 2
- Multi-Contact: MC4 (PV-KST4/PV-KBT4) or MC4-EVO 2 (PV-KST-EVO 2 / PV-KBT-EVO 2).
- Higher load ratings can be met with additional clips or wider clips, subject to testing

### Disclaimer

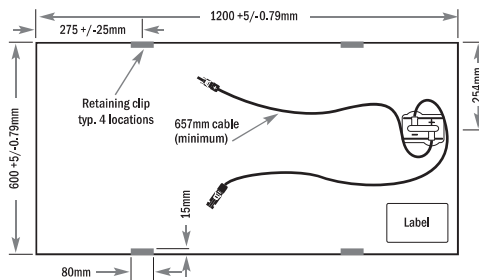
The information included in this Module Datasheet is subject to change without notice and is provided for informational purposes only. No contractual rights are established or should be inferred because of user's reliance on the information contained in this Module Datasheet. Please refer to the appropriate Module User Guide and Module Product Specification document for more detailed technical information regarding module performance, installation and use.

The First Solar logo, First Solar™, and all products denoted with ® are registered trademarks, and those denoted with a ™ are trademarks of First Solar, Inc.

## SUPERIOR TEMPERATURE COEFFICIENT



## MECHANICAL DRAWING



firstsolar.com | info@firstsolar.com

## **BIBLIOGRAPHY**

## BIBLIOGRAPHY

- [1] BP p.l.c. Bp statistical review of world energy 68th edition. Technical report, 2019.
- [2] 2013: Summary for Policymakers IPCC. Climate change 2013: The physical science basis. contribution of working group i to the fifth assessment report of the intergovernmental panel on climate change. Cambridge University Press, Cambridge, United Kingdom and New York, NY, USA.
- [3] Ipc, 2014: Climate change 2014: Mitigation of climate change. In *Contribution of Working Group III to the Fifth Assessment Report of the Intergovernmental Panel on Climate Change*. Cambridge University Press, Cambridge, United Kingdom and New York, NY, USA, 2014.
- [4] George Crabtree Jeff Tsao, Nate Lewis. Solar faqs. US Department of Energy, 2006.
- [5] International Energy Agency. Renewables 2019: Analysis and forecast to 2024. Technical report, 2019.
- [6] Goksin Kavlak, James McNerney, and Jessika E. Trancik. Evaluating the causes of cost reduction in photovoltaic modules. *Energy Policy*, 123:700–710, dec 2018.
- [7] International Energy Agency. Pvps 2019 snapshot of global pv markets. Technical report, 2019.
- [8] Electrical Engineering Students at University of Massachusetts Dartmouth. The p-n junction. <https://rfphotonicslab.org/2020/01/04/the-p-n-junction/>, 2020. Accessed: 2020-10-02.
- [9] L. J. A. Koster. *Device physics of donor/acceptor-blend solar cells*. PhD thesis, University of Groningen, 2007.
- [10] Jenny Nelson. *The Physics of Solar Cells*. Imperial College Press, 2003.
- [11] Junfeng Yan and Brian R. Saunders. Third-generation solar cells: a review and comparison of polymer:fullerene, hybrid polymer and perovskite solar cells. *RSC Adv.*, 4(82):43286–43314, 2014.
- [12] W. Shockley. The theory of p-n junctions in semiconductors and p-n junction transistors. *Bell System Technical Journal*, 28(3):435–489, 1949.
- [13] Arno Smets. *Solar energy: the physics and engineering of photovoltaic conversion, technologies and systems*. UIT Cambridge Ltd, Cambridge, England, 2016.
- [14] Javier Cubas, Santiago Pindado, and Marta Victoria. On the analytical approach for modeling photovoltaic systems behavior. *Journal of Power Sources*, 247:467–474, 2014.
- [15] N. C. Giebink, G. P. Wiederrecht, M. R. Wasielewski, and S. R. Forrest. Ideal diode equation for organic heterojunctions. i. derivation and application. *Physical Review B*, 82(15), 2010.



- [16] Non Thongprong. *Modeling Emerging Solar Cell Materials and Devices*. PhD thesis, Michigan State University, 2017.
- [17] Dragica Vasileska and Stephen M. Goodnick. Computational electronics. *Synthesis Lectures on Computational Electromagnetics*, 1(1):1–216, jan 2006.
- [18] Tibor Grasser, Hans Kosina, Markus Gritsch, and Siegfried Selberherr. Using six moments of boltzmann’s transport equation for device simulation. *Journal of Applied Physics*, 90(5):2389–2396, sep 2001.
- [19] A. Jungel. Mathematical modeling of semiconductor devices (preliminary version). <https://www.asc.tuwien.ac.at/~juengel/scripts/semicond.pdf>. Accessed: 2020-10-31.
- [20] Kausar Banoo. *Direct Solution of the Boltzmann Transport Equation in Nanoscale Si Devices*. PhD thesis, Purdue University, 2000.
- [21] Williams R. Calderón-Muñoz and Cristian Jara-Bravo. Hydrodynamic modeling of hot-carrier effects in a PN junction solar cell. *Acta Mechanica*, 227(11):3247–3260, 2016.
- [22] A Habte, M. Sengupta, and A. Lopez. Developing the next generation of gridded tmys. Technical report, National Renewable Energy Laboratory, 2015.
- [23] Riaz A. Usmani. Inversion of a tridiagonal jacobi matrix. *Linear Algebra and its Applications*, 212-213:413–414, 1994.
- [24] D.L. Scharfetter and H.K. Gummel. Large-signal analysis of a silicon read diode oscillator. *IEEE Trans Electron Devices*, 16(1):64–77, 1969.
- [25] H.K. Gummel. A self-consistent iterative scheme for one-dimensional steady state transistor calculations. *IEEE Transactions on Electron Devices*, 11(10):455–465, 1964.
- [26] P. Farrell, N. Rotundo, D.H. Doan, M. Kantner, J. Fuhrmann, T. Koprucki, and Weierstraß-Institut für Angewandte Analysis und Stochastik. *Numerical Methods for Drift-diffusion Models*. Preprint: Weierstraß-Institut für Angewandte Analysis und Stochastik. Weierstraß-Institut für Angewandte Analysis und Stochastik Leibniz-Institut im Forschungsverbund Berlin e.V., 2016.
- [27] Kanokkorn Pimcharoen. *Modeling of Charge Injection and Transport in Organic Semiconductors with Applications to Conducting Atomic Force Microscopy*. PhD thesis, Michigan State University, 2018.
- [28] Z. B. Wang, M. G. Helander, M. T. Greiner, J. Qiu, and Z. H. Lu. Carrier mobility of organic semiconductors based on current-voltage characteristics. *Journal of Applied Physics*, 107(3):034506, feb 2010.
- [29] Hui Wang. *Simulation of Organic Light-Emitting Diodes and Organic Photovoltaic Devices*. PhD thesis, University of Rochester, 2012.

- [30] Michael C. Heiber and Ali Dhinojwala. Dynamic monte carlo modeling of exciton dissociation in organic donor-acceptor solar cells. *The Journal of Chemical Physics*, 137(1):014903, 2012.
- [31] W Y Liang. Excitons. *Physics Education*, 5(4):226–228, 1970.
- [32] Ala'a F. Eftaiha, Jon-Paul Sun, Ian G. Hill, and Gregory C. Welch. Recent advances of non-fullerene, small molecular acceptors for solution processed bulk heterojunction solar cells. *Journal of Materials Chemistry A*, 2(5):1201–1213, 2014.
- [33] L. J. A. Koster, E. C. P. Smits, V. D. Mihailetschi, and P. W. M. Blom. Device model for the operation of polymer/fullerene bulk heterojunction solar cells. *Physical Review B*, 72(8), 2005.
- [34] Christopher M. Snowden, editor. *Semiconductor Device Modelling*. Springer London, 1989.
- [35] Charles L. Braun. Electric field assisted dissociation of charge transfer states as a mechanism of photocarrier production. *The Journal of Chemical Physics*, 80(9):4157–4161, 1984.
- [36] N. C. Giebink, B. E. Lassiter, G. P. Wiederrecht, M. R. Wasielewski, and S. R. Forrest. Ideal diode equation for organic heterojunctions. II. the role of polaron pair recombination. *Physical Review B*, 82(15), 2010.
- [37] Péter Pulay. Convergence acceleration of iterative sequences. the case of scf iteration. *Chemical Physics Letters*, 73(2):393–398, 1980.
- [38] J.W. Slotboom. Computer-aided two-dimensional analysis of bipolar transistors. *IEEE Transactions on Electron Devices*, 20(8):669–679, 1973.
- [39] Martin A. Green, Anita Ho-Baillie, and Henry J. Snaith. The emergence of perovskite solar cells. *Nature Photonics*, 8(7):506–514, 2014.
- [40] Henry J. Snaith. Perovskites: The emergence of a new era for low-cost, high-efficiency solar cells. *The Journal of Physical Chemistry Letters*, 4(21):3623–3630, 2013.
- [41] Nam-Gyu Park. Perovskite solar cells: an emerging photovoltaic technology. *Materials Today*, 18(2):65–72, 2015.
- [42] Zhen Li, Talysa R. Klein, Dong Hoe Kim, Mengjin Yang, Joseph J. Berry, Maikel F. A. M. van Hest, and Kai Zhu. Scalable fabrication of perovskite solar cells. *Nature Reviews Materials*, 3(4):18017, 2018.
- [43] Zhengqi Shi and Ahalapitiya Jayatissa. Perovskites-based solar cells: A review of recent progress, materials and processing methods. *Materials*, 11(5):729, 2018.
- [44] Nrel best research-cell efficiencies. <https://www.nrel.gov/pv/assets/pdfs/pv-efficiencies-07-17-2018.pdf>. Accessed: 2018-10-12.
- [45] Akihiro Kojima, Kenjiro Teshima, Yasuo Shirai, and Tsutomu Miyasaka. Organometal halide perovskites as visible-light sensitizers for photovoltaic cells. *Journal of the American Chemical Society*, 131(17):6050–6051, 2009.

- [46] Eran Edri, Saar Kirmayer, Sabyasachi Mukhopadhyay, Konstantin Gartsman, Gary Hodes, and David Cahen. Elucidating the charge carrier separation and working mechanism of CH<sub>3</sub>nh<sub>3</sub>pb<sub>3</sub>-xCl<sub>x</sub> perovskite solar cells. *Nature Communications*, 5(1), 2014.
- [47] Tejas S. Sherkar, Cristina Momblona, Lidón Gil-Escrig, Henk J. Bolink, and L. Jan Anton Koster. Improving perovskite solar cells: Insights from a validated device model. *Advanced Energy Materials*, 7(13):1602432, 2017.
- [48] Atsuhiko Miyata, Anatolie Mitioğlu, Paulina Plochocka, Oliver Portugall, Jacob Tse-Wei Wang, Samuel D. Stranks, Henry J. Snaith, and Robin J. Nicholas. Direct measurement of the exciton binding energy and effective masses for charge carriers in organic–inorganic tri-halide perovskites. *Nature Physics*, 11(7):582–587, 2015.
- [49] J. G. Simmons and G. W. Taylor. Nonequilibrium steady-state statistics and associated effects for insulators and semiconductors containing an arbitrary distribution of traps. *Physics Review B*, 4(2):502–511, 1971.
- [50] L. Jan Anton Koster. personal communication.
- [51] Yanjun Fang, Cheng Bi, Dong Wang, and Jinsong Huang. The functions of fullerenes in hybrid perovskite solar cells. *ACS Energy Letters*, 2(4):782–794, 2017.
- [52] Edison Castro, Jesse Murillo, Olivia Fernandez-Delgado, and Luis Echegoyen. Progress in fullerene-based hybrid perovskite solar cells. *Journal of Materials Chemistry C*, 6(11):2635–2651, 2018.
- [53] Dianyi Liu, Qiong Wang, Christopher J. Traverse, Chenchen Yang, Margaret Young, Padmanaban S. Kuttipillai, Sophia Y. Lunt, Thomas W. Hamann, and Richard R. Lunt. Impact of ultrathin c60 on perovskite photovoltaic devices. *ACS Nano*, 12(1):876–883, 2018.
- [54] Takeaki Sakurai, Susumu Toyoshima, Hikaru Kitazume, Shigeru Masuda, Hiroo Kato, and Katsuhiko Akimoto. Influence of gap states on electrical properties at interface between bathocuproine and various types of metals. *Journal of Applied Physics*, 107(4):043707, 2010.
- [55] Hiroyuki Yoshida. Electron transport in bathocuproine interlayer in organic semiconductor devices. *The Journal of Physical Chemistry C*, 119(43):24459–24464, 2015.
- [56] Jeihyun Lee, Soohyung Park, Younjoo Lee, Hyein Kim, Dongguen Shin, Junkyeong Jeong, Kwangho Jeong, Sang Wan Cho, Hyunbok Lee, and Yeonjin Yi. Electron transport mechanism of bathocuproine exciton blocking layer in organic photovoltaics. *Physical Chemistry Chemical Physics*, 18(7):5444–5452, 2016.
- [57] Olga Malinkiewicz, Aswani Yella, Yong Hui Lee, Guillermo Mínguez Espallargas, Michael Graetzel, Mohammad K. Nazeeruddin, and Henk J. Bolink. Perovskite solar cells employing organic charge-transport layers. *Nature Photonics*, 8(2):128–132, 2013.
- [58] Po-Wei Liang, Chu-Chen Chueh, Spencer T. Williams, and Alex K.-Y. Jen. Roles of fullerene-based interlayers in enhancing the performance of organometal perovskite thin-film solar cells. *Advanced Energy Materials*, 5(10):1402321, 2015.

- [59] Chuanliang Chen, Shasha Zhang, Shaohang Wu, Wenjun Zhang, Hongmei Zhu, Zhenzhong Xiong, Yanjun Zhang, and Wei Chen. Effect of BCP buffer layer on eliminating charge accumulation for high performance of inverted perovskite solar cells. *RSC Advances*, 7(57):35819–35826, 2017.
- [60] Ses research: Properties of carbon 60. <https://www.sesres.com/physical-properties/>. Accessed: 2018-03-07.
- [61] Laura M. Herz. Charge-carrier mobilities in metal halide perovskites: Fundamental mechanisms and limits. *ACS Energy Letters*, 2(7):1539–1548, 2017.
- [62] Qingshuo Wei, Masakazu Mukaida, Yasuhisa Naitoh, and Takao Ishida. Morphological change and mobility enhancement in PEDOT:PSS by adding co-solvents. *Advanced Materials*, 25(20):2831–2836, 2013.
- [63] George F. Burkhard, Eric T. Hoke, and Michael D. McGehee. Accounting for interference, scattering, and electrode absorption to make accurate internal quantum efficiency measurements in organic and other thin solar cells. *Advanced Materials*, 22(30):3293–3297, 2010.
- [64] Konrad Wojciechowski, Samuel D. Stranks, Antonio Abate, Golnaz Sadoughi, Aditya Sadhanala, Nikos Kopidakis, Garry Rumbles, Chang-Zhi Li, Richard H. Friend, Alex K.-Y. Jen, and Henry J. Snaith. Heterojunction modification for highly efficient organic–inorganic perovskite solar cells. *ACS Nano*, 8(12):12701–12709, 2014.
- [65] Chen Tao, Stefanie Neutzner, Letizia Colella, Sergio Marras, Ajay Ram Srimath Kandada, Marina Gandini, Michele De Bastiani, Giuseppina Pace, Liberato Manna, Mario Caironi, Chiara Bertarelli, and Annamaria Petrozza. 17.6% stabilized efficiency in low-temperature processed planar perovskite solar cells. *Energy & Environmental Science*, 8(8):2365–2370, 2015.
- [66] G. Horowitz. Tunneling current in polycrystalline organic thin-film transistors. *Advanced Functional Materials*, 13(1):53–60, 2003.
- [67] Ankit Kumar, Srinivas Sista, and Yang Yang. Dipole induced anomalous s-shape i-v curves in polymer solar cells. *Journal of Applied Physics*, 105(9):094512, 2009.
- [68] J.C. Wang, X.C. Ren, S.Q. Shi, C.W. Leung, and Paddy K.L. Chan. Charge accumulation induced s-shape j–v curves in bilayer heterojunction organic solar cells. *Organic Electronics*, 12(6):880–885, 2011.
- [69] Wolfgang Tress, Karl Leo, and Moritz Riede. Influence of hole-transport layers and donor materials on open-circuit voltage and shape of i-v curves of organic solar cells. *Advanced Functional Materials*, 21(11):2140–2149, apr 2011.
- [70] Wolfgang Tress, Annette Petrich, Markus Hummert, Moritz Hein, Karl Leo, and Moritz Riede. Imbalanced mobilities causing s-shaped IV curves in planar heterojunction organic solar cells. *Applied Physics Letters*, 98(6):063301, feb 2011.

- [71] B. Y. Finck and B. J. Schwartz. Understanding the origin of the s-curve in conjugated polymer/fullerene photovoltaics from drift-diffusion simulations. *Applied Physics Letters*, 103(5):053306, 2013.
- [72] Arash Sayyah, Mark N. Horenstein, and Malay K. Mazumder. Energy yield loss caused by dust deposition on photovoltaic panels. *Solar Energy*, 107:576–604, 2014.
- [73] Luxi Zhou, Donna B. Schwede, K. Wyatt Appel, Michael J. Mangiante, David C. Wong, Sergey L. Napelenok, Pai-Yei Whung, and Banglin Zhang. The impact of air pollutant deposition on solar energy system efficiency: An approach to estimate PV soiling effects with the community multiscale air quality (CMAQ) model. *Science of The Total Environment*, 651:456–465, 2019.
- [74] Klemens K. Ilse, Benjamin W. Figgis, Volker Naumann, Christian Hagendorf, and Jörg Bagdahn. Fundamentals of soiling processes on photovoltaic modules. *Renewable and Sustainable Energy Reviews*, 98:239 – 254, 2018.
- [75] Klemens Ilse, Leonardo Micheli, Benjamin W. Figgis, Katja Lange, David Daßler, Hamed Hanifi, Fabian Wolfertstetter, Volker Naumann, Christian Hagendorf, Ralph Gottschalg, and Jörg Bagdahn. Techno-economic assessment of soiling losses and mitigation strategies for solar power generation. *Joule*, 3(10):2303–2321, 2019.
- [76] Greg P. Smestad, Thomas A. Germer, Hameed Alrashidi, Eduardo F. Fernández, Sumon Dey, Honey Brahma, Nabin Sarmah, Aritra Ghosh, Nazmi Sellami, Ibrahim A. I. Hassan, Mai Desouky, Amal Kasry, Bala Pesala, Senthilarasu Sundaram, Florencia Almonacid, K. S. Reddy, Tapas K. Mallick, and Leonardo Micheli. Modelling photovoltaic soiling losses through optical characterization. *Scientific Reports*, 10(1), 2020.
- [77] Leonardo Micheli and Matthew Muller. An investigation of the key parameters for predicting PV soiling losses. *Progress in Photovoltaics: Research and Applications*, 25(4):291–307, 2017.
- [78] Travis Sarver, Ali Al-Qaraghuli, and Lawrence L. Kazmerski. A comprehensive review of the impact of dust on the use of solar energy: History, investigations, results, literature, and mitigation approaches. *Renewable and Sustainable Energy Reviews*, 22:698–733, 2013.
- [79] Marek Jaszczur, Janusz Teneta, Katarzyna Styszko, Qusay Hassan, Paulina Burzyńska, Ewelina Marcinek, and Natalia Łopian. The field experiments and model of the natural dust deposition effects on photovoltaic module efficiency. *Environmental Science and Pollution Research*, 26(9):8402–8417, 2018.
- [80] A. Kimber, L. Mitchell, S. Nogradi, and H. Wenger. The effect of soiling on large grid-connected photovoltaic systems in california and the southwest region of the united states. In *2006 IEEE 4th World Conference on Photovoltaic Energy Conference*. IEEE, 2006.
- [81] R. Hammond, D. Srinivasan, A. Harris, K. Whitfield, and J. Wohlgemuth. Effects of soiling on PV module and radiometer performance. In *Conference Record of the Twenty Sixth IEEE Photovoltaic Specialists Conference*. IEEE, 1997.

- [82] Miguel García, Luis Marroyo, Eduardo Lorenzo, and Miguel Pérez. Soiling and other optical losses in solar-tracking PV plants in navarra. *Progress in Photovoltaics: Research and Applications*, 19(2):211–217, 2010.
- [83] F. Mejia, J. Kleissl, and J.L. Bosch. The effect of dust on solar photovoltaic systems. *Energy Procedia*, 49:2370–2376, 2014.
- [84] Felipe A. Mejia and Jan Kleissl. Soiling losses for solar photovoltaic systems in california. *Solar Energy*, 95:357–363, 2013.
- [85] Benjamin Figgis, Ahmed Ennaoui, Said Ahzi, and Yves Rémond. Review of PV soiling particle mechanics in desert environments. *Renewable and Sustainable Energy Reviews*, 76:872–881, 2017.
- [86] Benjamin Figgis, Dirk Goossens, Bing Guo, and Klemens Ilse. Effect of tilt angle on soiling in perpendicular wind. *Solar Energy*, 194:294–301, 2019.
- [87] B. Figgis and K. Ilse. Anti-soiling potential of 1-axis pv trackers. *36th European Photovoltaic Solar Energy Conference and Exhibition; 1312-1316*, 2019.
- [88] I. M. Peters, S. Karthik, H. Liu, T. Buonassisi, and A. Nobre. Urban haze and photovoltaics. *Energy & Environmental Science*, 11(10):3043–3054, 2018.
- [89] R. R. Cordero, A. Damiani, D. Laroze, S. MacDonell, J. Jorquera, E. Sepúlveda, S. Feron, P. Llanillo, F. Labbe, J. Carrasco, J. Ferrer, and G. Torres. Effects of soiling on photovoltaic (PV) modules in the atacama desert. *Scientific Reports*, 8(1), 2018.
- [90] Wasim Javed, Bing Guo, and Benjamin Figgis. Modeling of photovoltaic soiling loss as a function of environmental variables. *Solar Energy*, 157:397–407, 2017.
- [91] Klemens K. Ilse, Benjamin W. Figgis, Martina Werner, Volker Naumann, Christian Hagedorf, Herbert Pöllmann, and Jörg Bagdahn. Comprehensive analysis of soiling and cementation processes on PV modules in qatar. *Solar Energy Materials and Solar Cells*, 186:309–323, 2018.
- [92] S. Mariraj Mohan. An overview of particulate dry deposition: measuring methods, deposition velocity and controlling factors. *International Journal of Environmental Science and Technology*, 13(1):387–402, 2015.
- [93] Liza Boyle, Holly Flinchpaugh, and Michael Hannigan. Assessment of PM dry deposition on solar energy harvesting systems: Measurement–model comparison. *Aerosol Science and Technology*, 50(4):380–391, 2016.
- [94] Merissa Coello and Liza Boyle. Simple model for predicting time series soiling of photovoltaic panels. *IEEE Journal of Photovoltaics*, 9(5):1382–1387, 2019.
- [95] L Zhang. A size-segregated particle dry deposition scheme for an atmospheric aerosol module. *Atmospheric Environment*, 35(3):549–560, 2001.

- [96] Siming You, Yu Jie Lim, Yanjun Dai, and Chi-Hwa Wang. On the temporal modelling of solar photovoltaic soiling: Energy and economic impacts in seven cities. *Applied Energy*, 228:1136–1146, 2018.
- [97] Bernard Brown. The effect of settling harmattan dust on photovoltaic modules in walewale, northern ghana. Master’s thesis, Kwame Nkrumah University of Science and Technology, 2016.
- [98] Sergey Biryukov. An experimental study of the dry deposition mechanism for airborne dust. *Journal of Aerosol Science*, 29(1-2):129–139, 1998.
- [99] E. Suresh Kumar, Bijan Sarkar, and D.K. Behera. Soiling and dust impact on the efficiency and the maximum power point in the photovoltaic modules. *International Journal of Engineering Research and Technology*, 2(2), 2013.
- [100] Fabian Wolfertstetter, Stefan Wilbert, Felix Terhag, Natalie Hanrieder, Aranzazu Fernandez-García, Christopher Sansom, Peter King, Luis Zarzalejo, and Abdellatif Ghennioui. Modelling the soiling rate: Dependencies on meteorological parameters. In *SOLARPACES 2018: International Conference on Concentrating Solar Power and Chemical Energy Systems*. AIP Publishing, 2019.
- [101] G. Picotti, P. Borghesani, M.E. Cholette, and G. Manzolini. Soiling of solar collectors – modelling approaches for airborne dust and its interactions with surfaces. *Renewable and Sustainable Energy Reviews*, 81:2343–2357, 2018.
- [102] W.G.N Slinn. Predictions for particle deposition to vegetative canopies. *Atmospheric Environment (1967)*, 16(7):1785–1794, 1982.
- [103] E Kim. Dry deposition of large, airborne particles onto a surrogate surface. *Atmospheric Environment*, 34(15):2387–2397, 2000.
- [104] Yu Jiang, Lin Lu, Andrea R. Ferro, and Goodarz Ahmadi. Analyzing wind cleaning process on the accumulated dust on solar photovoltaic (PV) modules on flat surfaces. *Solar Energy*, 159:1031–1036, 2018.
- [105] Lawrence L. Kazmerski, Antonia Sonia A. C. Diniz, Cristiana Brasil Maia, Marcelo Machado Viana, Suellen C. Costa, Pedro P. Brito, Claudio Dias Campos, Lauro V. Macheto Neto, Sergio de Moraes Hanriot, and Leila R. de Oliveira Cruz. Fundamental studies of adhesion of dust to PV module surfaces: Chemical and physical relationships at the microscale. *IEEE Journal of Photovoltaics*, 6(3):719–729, 2016.
- [106] Bing Guo, Wasim Javed, Saadat Khan, Benjamin Figgis, and Talha Mirza. Models for prediction of soiling-caused photovoltaic power output degradation based on environmental variables in doha, qatar. In *American Society of Mechanical Engineers 10th International Conference on Energy Sustainability*, 2016.
- [107] AVCalc LLC. <https://www.aqua-calc.com/page/density-table/substance/sand-coma-and-blank-dry>. Accessed: 2020-05-16.

- [108] [https://www.engineeringtoolbox.com/air-absolute-kinematic-viscosity-d\\_601.html](https://www.engineeringtoolbox.com/air-absolute-kinematic-viscosity-d_601.html). Accessed: 2020-04-12.
- [109] Cheryl McKenna Neuman and Steven Sanderson. Humidity control of particle emissions in aeolian systems. *Journal of Geophysical Research*, 113(F2), 2008.
- [110] Enlighten Energy, Ltd. <https://www.enlighten-energy.net/pv-pss/>. Accessed: 2020-10-02.
- [111] Kipp and Zonen B.V. <https://www.kippzonen.com/Product/419/DustIQ-Soiling-Monitoring-System#.XrlxFmhKhaQ>. Accessed: 2020-10-02.
- [112] Atonometrics, Inc. <http://www.atonometrics.com/products/soiling-measurement-system-for-pv-modules/>. Accessed: 2020-08-10.
- [113] Arizona State University Photovoltaic Reliability Laboratory. <https://pvreliability.asu.edu/asms>. Accessed: 2020-08-10.
- [114] Matthew K. Smith, Carl C. Wamser, Keith E. James, Seth Moody, David J. Sailor, and Todd N. Rosenstiel. Effects of natural and manual cleaning on photovoltaic output. *Journal of Solar Energy Engineering*, 135(3), 2013.
- [115] J. Zorrilla-Casanova, M. Piliouline, J. Carretero, P. Bernaola, P. Carpena, L. Mora-Lopez, and M. Sidrach de Cardona. Analysis of dust losses in photovoltaic modules. In *Proceedings of the World Renewable Energy Congress Sweden, Linköping, Sweden*. Linköping University Electronic Press, 8-13 May, 2011.
- [116] Kudzanayi Chiteka, Rajesh Arora, and S. N. Sridhara. A method to predict solar photovoltaic soiling using artificial neural networks and multiple linear regression models. *Energy Systems*, 11(4):981–1002, 2019.
- [117] T. Mani G. Samy. Waterless web-monitored soiling monitoring station. In *PV Reliability Workshop*, Lakewood, CO, 2018.
- [118] J. John, V. Rajasekar, S. Boppana, S. Tatapudi, and G. Tamizhmani. Angle of incidence effects on soiled PV modules. In Neelkanth G. Dhere, John H. Wohlgemuth, and Rebecca Jones-Albertus, editors, *Reliability of Photovoltaic Cells, Modules, Components, and Systems VII*. SPIE, 2014.
- [119] N. Martín and J. M. Ruiz. A new model for PV modules angular losses under field conditions. *International Journal of Solar Energy*, 22(1):19–31, 2002.
- [120] N. Martin and J.M. Ruiz. Calculation of the PV modules angular losses under field conditions by means of an analytical model. *Solar Energy Materials and Solar Cells*, 70(1):25–38, 2001.
- [121] N. Martín and J. M. Ruiz. Annual angular reflection losses in PV modules. *Progress in Photovoltaics: Research and Applications*, 13(1):75–84, 2004.



- [122] John E. Hay. Calculating solar radiation for inclined surfaces: Practical approaches. *Renewable Energy*, 3(4-5):373–380, 1993.
- [123] José Zorrilla-Casanova, Michel Piliougin, Jesús Carretero, Pedro Bernaola-Galván, Pedro Carpena, Llanos Mora-López, and Mariano Sidrach de Cardona. Losses produced by soiling in the incoming radiation to photovoltaic modules. *Progress in Photovoltaics: Research and Applications*, 21(4):790–796, 2012.
- [124] Leonardo Micheli, Daniel Ruth, Michael G Deceglie, and Matthew Muller. Time series analysis of photovoltaic soiling station data: Version 1.0. Technical report, National Renewable Energy Laboratory, August 2017.
- [125] Manajit Sengupta, Yu Xie, Anthony Lopez, Aron Habte, Galen Maclaurin, and James Shelby. The national solar radiation data base (NSRDB). *Renewable and Sustainable Energy Reviews*, 89:51–60, 2018.
- [126] United States Environmental Protection Agency. <https://www.epa.gov/outdoor-air-quality-data/download-daily-data>. Accessed: 2020-04-04.
- [127] Oregon State University PRISM Climate Group. <http://prism.oregonstate.edu>. Accessed: 2020-06-07.
- [128] Enlighten Energy, Ltd. <https://www.enlighten-energy.net/pv-soilsayer/>. Accessed: 2020-10-02.
- [129] Will Holmgren, Calama-Consulting, Cliff Hansen, Mark Mikofski, Tony Lorenzo, Uwe Krien, bmu, Cameron Stark, DaCoEx, Anton Driesse, Kevin Anderson, konstant\_t, mayudong, Leland Boeman, Ed Miller, Heliolytics, Miguel Sánchez de León Peque, Veronica Guo, Marc A. Anoma, tylunel, jforbess, Cedric Leroy, Alexander Morgan, Todd Hendricks, Oscar Dowson, MLEEFs, Kevin Anderson, Johannes Dollinger, JPalakapillyKWH, and Ahan M R. *pvlib/pvlib-python: v0.7.2*, 2020.
- [130] Bing Guo, W. Javed, B. W. Figgis, and T. Mirza. Effect of dust and weather conditions on photovoltaic performance in doha, qatar. In *2015 First Workshop on Smart Grid and Renewable Energy (SGRE)*. IEEE, 2015.
- [131] Bashar Hammad, Mohammad Al–Abed, Ahmed Al–Ghandoor, Ali Al–Sardeah, and Adnan Al–Bashir. Modeling and analysis of dust and temperature effects on photovoltaic systems’ performance and optimal cleaning frequency: Jordan case study. *Renewable and Sustainable Energy Reviews*, 82:2218–2234, 2018.
- [132] Jun Guo, Xunjian Xu, Weiwei Lian, and Honglu Zhu. A new approach for interval forecasting of photovoltaic power based on generalized weather classification. *International Transactions on Electrical Energy Systems*, 29(4):e2802, 2018.
- [133] Salsabeel Shapsough, Rached Dhaouadi, and Imran Zualkernan. Using linear regression and back propagation neural networks to predict performance of soiled PV modules. *Procedia Computer Science*, 155:463–470, 2019.

- [134] Stack Overflow. <https://tex.stackexchange.com/questions/132444/diagram-of-an-artificial-neural-network>. Accessed: 2020-10-02.
- [135] Swapnil Dubey, Jatin Narotam Sarvaiya, and Bharath Seshadri. Temperature dependent photovoltaic (PV) efficiency and its effect on PV production in the world – a review. *Energy Procedia*, 33:311–321, 2013.
- [136] PVSyst. [https://www.pvsyst.com/help/noct\\_definition.htm](https://www.pvsyst.com/help/noct_definition.htm). Accessed: 2020-05-11.
- [137] Luca Migliorini, Luca Molinaroli, Riccardo Simonetti, and Giampaolo Manzolini. Development and experimental validation of a comprehensive thermoelectric dynamic model of photovoltaic modules. *Solar Energy*, 144:489–501, 2017.
- [138] David Faiman. Assessing the outdoor operating temperature of photovoltaic modules. *Progress in Photovoltaics: Research and Applications*, 16(4):307–315, 2008.
- [139] John Duffie. *Solar engineering of thermal processes*. Wiley, Hoboken, 2013.
- [140] Mathew Muller. Measuring and modeling nominal operating cell temperature (noct). In *PV Performance Modeling Workshop*, Albuquerque, NM, Sept 22-23, 2010.
- [141] ThermoAnalytics, Inc. Taitherm 2020.1.0. <https://www.thermoanalytics.com/taitherm>. Accessed: 2020-10-02.
- [142] Gustav Schon. Numerical modelling of a novel pvt collector at cell resolution. Master’s thesis, KTH School of Industrial Engineering and Management, 2017.
- [143] Nelson Sommerfeldt and Patrik Ollas. Reverse engineering prototype solar PV/thermal collector properties from empirical data for use in TRNSYS type 560. In *Proceedings of SWC2017/SHC2017*. International Solar Energy Society, 2017.
- [144] W. De Soto, S.A. Klein, and W.A. Beckman. Improvement and validation of a model for photovoltaic array performance. *Solar Energy*, 80(1):78–88, 2006.
- [145] Matthew T. Boyd, Sanford A. Klein, Douglas T. Reindl, and Brian P. Dougherty. Evaluation and validation of equivalent circuit photovoltaic solar cell performance models. *Journal of Solar Energy Engineering*, 133(2), 2011.
- [146] Rabeh Abbassi, Abdelkader Abbassi, Mohamed Jemli, and Souad Chebbi. Identification of unknown parameters of solar cell models: A comprehensive overview of available approaches. *Renewable and Sustainable Energy Reviews*, 90:453–474, 2018.
- [147] Yunhua Ding, Margaret Young, Yimu Zhao, Christopher Traverse, Andre Benard, and Richard R. Lunt. Influence of photovoltaic angle-dependence on overall power output for fixed building integrated configurations. *Solar Energy Materials and Solar Cells*, 132:523–527, 2015.
- [148] W. H. McAdams. *Heat Transmission*. McGraw-Hill Kogakusha, Tokyo, Japan, 1954.

- [149] Nuria Martin Chivelet, Jose M Ruiz Perez, and Jose Bionef. *25th European Photovoltaic Solar Energy Conference and Exhibition*. WIP-Renewable Energies, Munich, Germany, 6-9 September 2010.
- [150] ThermoAnalytics, Inc. Taitherm 2020.1.0 materials database.
- [151] <https://solarfeeds.com/wiki/cadmium-telluride-photovoltaic>. Accessed: 2020-06-09.
- [152] U.S. Energy Information Administration. <https://www.eia.gov/tools/faqs/faq.php?id=97&t=3#:~:text=How\much\electricity\does\an,about\914\kWh\per\month>. Accessed: 2020-06-17.
- [153] U.S. Department of Energy: Office of Energy Efficiency and Renewable Energy. [https://www.fueleconomy.gov/feg/bymodel/2019\\_Tesla\\_Model\\_3.shtml](https://www.fueleconomy.gov/feg/bymodel/2019_Tesla_Model_3.shtml). Accessed: 2020-06-17.
- [154] Meteotest AG. <https://meteonorm.com/en/>. Accessed: 2019-01-20.
- [155] Toyota. <toyota-europe.com/new-cars/prius-plugin/>. Accessed: 2020-10-02.
- [156] Hyundai Motor America. <https://www.hyundainews.com/en-us/releases/2640>. Accessed: 2020-02-12.
- [157] Lightyear. <https://lightyear.one/>. Accessed: 2020-02-12.
- [158] Sono Motors GmbH. <https://sonomotors.com/en/sion/>. Accessed: 2020-02-12.
- [159] United States Department of Transportation Federal Highway Administration. <https://www.fhwa.dot.gov/ohim/onh00/bar8.htm>. Accessed: 2020-06-17.
- [160] Christopher J. Traverse, Richa Pandey, Miles C. Barr, and Richard R. Lunt. Emergence of highly transparent photovoltaics for distributed applications. *Nature Energy*, 2(11):849–860, 2017.
- [161] Ubiquitous, Inc. <https://ubiquitous.energy/>. Accessed: 2020-08-21.
- [162] Richard R. Lunt. Theoretical limits for visibly transparent photovoltaics. *Applied Physics Letters*, 101(4):043902, 2012.
- [163] Annick Anctil, Eunsang Lee, and Richard R. Lunt. Net energy and cost benefit of transparent organic solar cells in building-integrated applications. *Applied Energy*, 261:114429, 2020.
- [164] K. Smith, M. Earleywine, E. Wood, and A. Pesaran. Battery wear from disparate duty-cycles: Opportunities for electric-drive vehicle battery health management. Technical report, National Renewable Energy Laboratory, 2012.
- [165] Scott Peck, Aditya Velivelli, and Wilko Jansen. Options for coupled thermal-electric modeling of battery cells and packs. *SAE International Journal of Passenger Cars - Electronic and Electrical Systems*, 7(1):273–284, 2014.

- [166] Carl Johan Rydh and Björn A. Sandén. Energy analysis of batteries in photovoltaic systems. part i: Performance and energy requirements. *Energy Conversion and Management*, 46(11-12):1957–1979, 2005.
- [167] Filippo Spertino, Alessandro Ciocia, Paolo Di Leo, Gabriele Malgaroli, and Angela Russo. A smart battery management system for photovoltaic plants in households based on raw production forecast. In *Green Energy Advances*. IntechOpen, 2019.
- [168] Geoffrey A. Landis, Phillip Jenkins, David Scheiman, and Ryne Rafaele. Extended temperature solar cell technology development. In *AIAA 2nd International Energy Conversion Engineering Conference*, Providence, RI, August 16-19, 2004. AIAA 2nd International Energy Conversion Engineering Conferenc.
- [169] Ilaria Cardinaletti, Tim Vangerven, Steven Nagels, Rob Cornelissen, Dieter Schreurs, Jaroslav Hruby, Jelle Vodnik, Dries Devisscher, Jurgen Kesters, Jan D’Haen, Alexis Franquet, Valentina Spampinato, Thierry Conard, Wouter Maes, Wim Deferme, and Jean V. Manca. Organic and perovskite solar cells for space applications. *Solar Energy Materials and Solar Cells*, 182:121–127, 2018.
- [170] Sourav Diwania, Sanjay Agrawal, Anwar S. Siddiqui, and Sonveer Singh. Photovoltaic–thermal (PV/t) technology: a comprehensive review on applications and its advancement. *International Journal of Energy and Environmental Engineering*, 11(1):33–54, 2019.
- [171] Marc Abou Anoma, David Jacob, Ben C. Bourne, Jonathan A. Scholl, Daniel M. Riley, and Clifford W. Hansen. View factor model and validation for bifacial PV and diffuse shade on single-axis trackers. In *2017 IEEE 44th Photovoltaic Specialist Conference (PVSC)*. IEEE, 2017.
- [172] Bill Marion, Sara MacAlpine, Chris Deline, Amir Asgharzadeh, Fatima Toor, Daniel Riley, Joshua Stein, and Clifford Hansen. A practical irradiance model for bifacial PV modules. In *2017 IEEE 44th Photovoltaic Specialist Conference (PVSC)*. IEEE, 2017.
- [173] Todd Karin, C. Birk Jones, and Anubhav Jain. Photovoltaic degradation climate zones. In *2019 IEEE 46th Photovoltaic Specialists Conference (PVSC)*. IEEE, 2019.
- [174] P. Padmagirisan and V. Sankaranarayanan. Powertrain control of a solar photovoltaic-battery powered hybrid electric vehicle. *Frontiers in Energy*, 13(2):296–306, 2019.
- [175] Ulrike Jahn, Magnus Herz, Marc Kontges, David Parlevliet, and Marco Paggi. Review on infrared anelectroluminescence imagingfor pv field applications. Technical report, IEA International Energy Agency, 2018.
- [176] Ali Rahmatmand, Stephen J. Harrison, and Patrick H. Oosthuizen. Numerical and experimental study of an improved method for prediction of snow melting and snow sliding from photovoltaic panels. *Applied Thermal Engineering*, 158:113773, 2019.

- [177] Abdelhakim Hassabou, Ahmed Abotaleb, and Amir Abdallah. Passive thermal management of photovoltaic modules—mathematical modeling and simulation of photovoltaic modules. *Journal of Solar Energy Engineering*, 139(6), 2017.
- [178] ThermoAnalytics, Inc. Cabin comfort + hvac. <https://www.thermoanalytics.com/cabin-comfort-modeling>. Accessed: 2020-10-02.
- [179] William F. Holmgren, Clifford W. Hansen, and Mark A. Mikofski. pvlib python: a python package for modeling solar energy systems. *Journal of Open Source Software*, 3(29):884, 2018.
- [180] Roberto Faranda, Hossein Hafezi, Sonia Leva, Marco Mussetta, and Emanuele Ogliari. The optimum PV plant for a given solar DC/AC converter. *Energies*, 8(6):4853–4870, 2015.
- [181] Aron P. Dobos. Pvwatts version 5 manual. Technical report, National Renewable Energy Laboratory, 2014.
- [182] J.A. Kratochvill D.L. King, W.E. Boyson. Photovoltaic array performance model. Technical report, Sandia National Laboratories, 2004.
- [183] Anco Blazev. *Photovoltaics for commercial and utilities power generation*. Fairmont Press CRC Press, Lilburn, GA Boca Raton, FL, 2012.
- [184] Matt Donovan Chris Deline, Jenya Meydbray. Photovoltaic shading testbed for module-level power electronics: 2016 performance data update. Technical report, National Renewable Energy Laboratory, 2016.